Facultad de Ciencias
Dpto. Química Inorgánica,
Cristalografía y Mineralogía
UNIVERSIDAD DE MÁLAGA

TESIS DOCTORAL

Catalizadores nanoestructurados con aplicaciones medioambientales. Hidrodesoxigenación de biocombustibles y purificación de hidrógeno

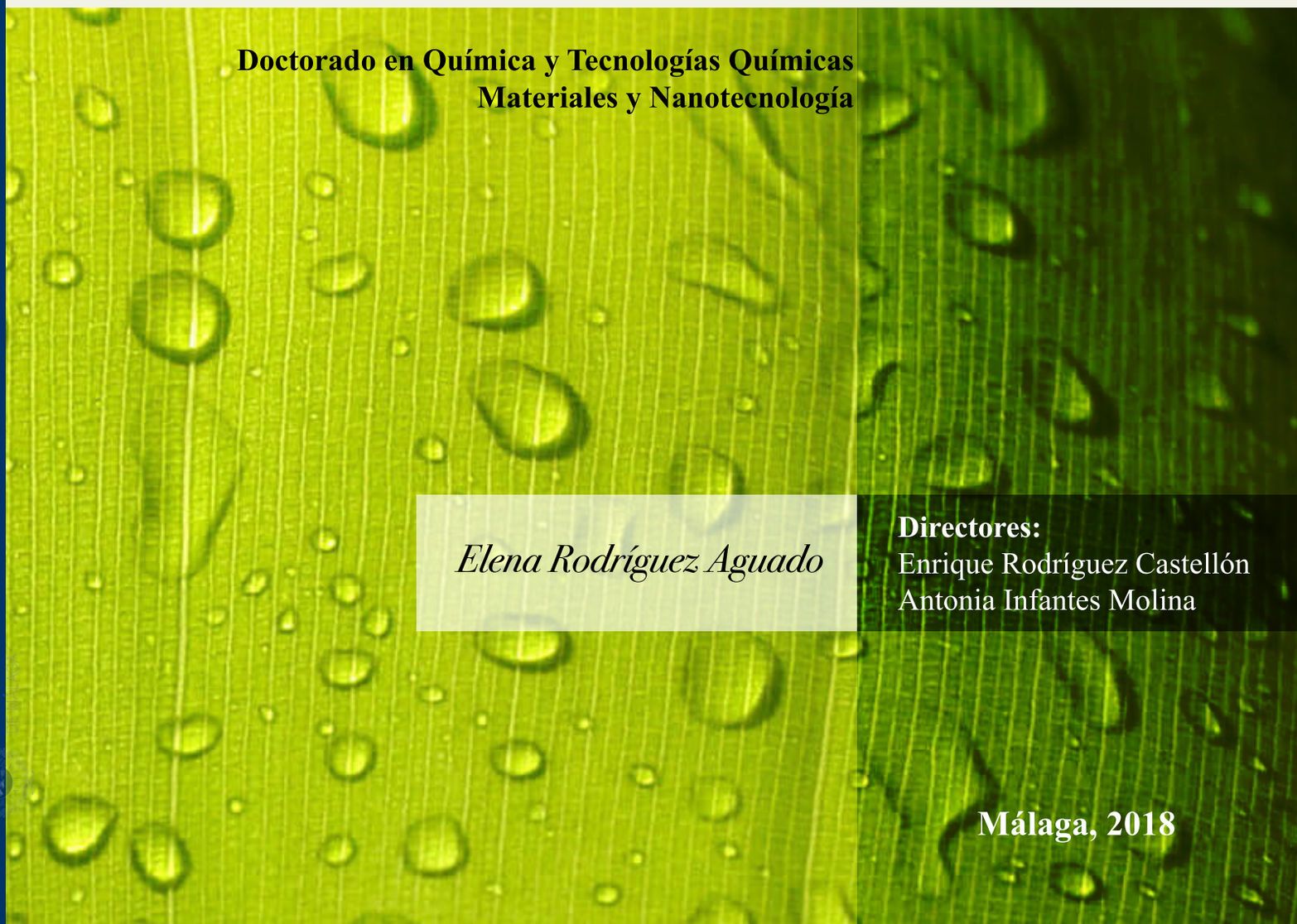

Doctorado en Química y Tecnologías Químicas
Materiales y Nanotecnología

Elena Rodríguez Aguado

Directores:
Enrique Rodríguez Castellón
Antonia Infantes Molina

Málaga, 2018

Tesis Doctoral *Elena Rodríguez Aguado*

2018

UNIVERSIDAD DE MÁLAGA

AUTOR: Elena Rodríguez Aguado

http://orcid.org/0000-0002-9888-5964

EDITA: Publicaciones y Divulgación Científica. Universidad de Málaga

Facultad de Ciencias

Departamento de Química Inorgánica, Cristalografía y Mineralogía

"Catalizadores nanoestructutados con aplicaciones medioambientales. Hidrodesoxigenación de biocombustibles y purificación de hidrógeno"

TESIS DOCTORAL

Elena Rodríguez Aguado

MÁLAGA, 2018

CATALIZADORES NANOESTRUCTURADOS CON APLICACIONES MEDIOAMBIENTALES. HIDRODESOXIGENACIÓN DE BIOCOMBUSTIBLES Y PURIFICACIÓN DE HIDRÓGENO.

MEMORIA presentada por la Licenciada y Máster en Química Dª Elena Rodríguez Aguado para aspirar al grado de Doctor en Ciencias, Sección de Químicas, con la mención de "**Doctorado Internacional**"

Fdo.: Elena Rodríguez Aguado

Los Directores,

Fdo.:

Dra. Dª Antonia Infantes Molina
Investigador Ramón y Cajal
Universidad de Málaga

Fdo.:

Dr. D Enrique Rodríguez Castellón
Catedrático de Química Inorgánica
Universidad de Málaga

D. ENRIQUE RODRÍGUEZ CASTELLÓN, Catedrático de Química Inorgánica perteneciente al Departamento de Química Inorgánica, Cristalografía y Mineralogía de la Facultad de Ciencias de la Universidad de Málaga y Dª ANTONIA INFANTES MOLINA, Investigador Ramón y Cajal, certifican:

Que la presente memoria realizada por Dª Elena Rodríguez Aguado, titulada: "Catalizadores nanoestructurados con aplicaciones medioambientales. Hidrodesoxigenación de biocombustibles y purificación de hidrógeno", ha sido realizada bajo nuestra dirección en el Departamento de Química Inorgánica, Cristalografía y Mineralogía de la Facultad de Ciencias de la Universidad de Málaga. Este trabajo reúne, a nuestro juicio, contenido científico suficiente y las condiciones necesarias para ser presentado y defendido ante el tribunal correspondiente para optar al Grado de Doctor.

Málaga a 2 de Octubre de 2018

Fdo.:

Dra. Dª Antonia Infantes Molina
Investigador Ramón y Cajal
Universidad de Málaga

Fdo.:

Dr. D Enrique Rodríguez Castellón
Catedrático de Química Inorgánica
Universidad de Málaga

D. ENRIQUE RODRÍGUEZ CASTELLÓN, Catedrático de Química Inorgánica de la Universidad de Málaga.

Informa:

Que la presente memoria realizada por Dª Elena Rodríguez Aguado, titulada: "Catalizadores nanoestructurados con aplicaciones medioambientales. Hidrodesoxigenación de biocombustibles y purificación de hidrógeno", ha sido realizada bajo mi dirección y la de la doctora Dª Antonia Infantes Molina del departamento de Química Inorgánica, Cristalografía y Mineralogía de la Universidad de Málaga. Este trabajo constituye la Memoria de Tesis Doctoral de la interesada, cuya presentación autorizo en Málaga a 2 de Octubre de 2018.

Fdo.: D. Enrique Rodríguez Castellón.

AGRADECIMIENTOS

Tras tres años de esfuerzo, constancia y dedicación, llenos de alegrías y sufrimientos, esta etapa llega a su fin. Muchas personas me han ayudado y guiado en este camino y no puedo terminar este periodo sin darles las gracias a todas ellas.

Primero quiero agradecer a mis directores de Tesis, la Dra. Dª Antonia Infantes Molina y al Prof. Dr. D. Enrique Rodríguez Castellón por la gran oportunidad que me habéis brindado, por transmitirme vuestros conocimientos y sobre todo, por vuestra infinita paciencia. A Enrique no podría estar más agradecida por haberme transmitido su amor por la ciencia y por confiar siempre en mí. Su apasionada e incansable forma de trabajar y su actitud positiva me han impulsado a dar lo mejor de mí misma.

A Antonia quiero darle las gracias por su trato cercano, por confiar tanto en mí y por motivarme y enseñarme a no darme por vencida. Gracias por haberme introducido en el mundo de la catálisis y por todo lo que me has enseñado, por tus valiosos consejos y por tu manera ejemplar de luchar y afrontar nuevos retos con valentía.

Quiero dar las gracias también al Ministerio de Economía y Competitividad (proyecto CTQ2015-68951-C3-3-R) por la financiación sin la cual no habría podido realizar este trabajo.

Asimismo agradezco a todos los profesores del departamento por su colaboración y amabilidad. En especial me gustaría agradecer al Profesor Ramón Moreno Tost por su ayuda incondicional y su amabilidad. Al Profesor José Santamaría por sus consejos y su buen humor. Al Profesor José Jiménez por su apoyo incondicional y gentileza. Al Profesor Pedro Maireles por su gran atención y cortesía. Y a D. Antonio Jiménez Morales por su disponibilidad y su sentido del humor.

Mi más sincero agradecimiento a los Doctores Elisa Moretti, Loretta Storaro y Aldo Talon de la Universidad de Ca`Foscari de Venezia por permitirme trabajar en su laboratorio, por transmitirme sus conocimientos y sobre todo, por su excelente trato.

No puedo olvidar agradecer a los técnicos del Servicio Central de Apoyo a la Investigación (SCAI) por su eficiencia y disponibilidad. En especial quiero dar las gracias a la Dra. María del Valle por todos los conocimientos que me ha transmitido y por su simpatía. A la Dra. María Dolores, gracias por su rigurosidad y amabilidad.

A todos los compañeros del departamento por su compañerismo y simpatía. En especial a Jesús, María José, Jose, Sandra, Mercedes, Irene e Inés con los que he compartido breves ratos pero de gran valía.

Y por supuesto a mis compañeros de catálisis, que me han hecho sentir en familia y sin los cuales los largos días de laboratorio no habrían sido igual de llevaderos. Todos a una, siempre ayudándonos y apoyándonos, en las buenas y en las malas. A Juan no podría estar más agradecida por su manera de trabajar y de ser que directa e indirectamente me ha impulsado a superarme a mí misma. Eres el motor del laboratorio, motivando diariamente a todos con tu peculiar personalidad y siendo un gran ejemplo de esfuerzo y constancia. A Cristina millones de gracias por sus magníficos consejos y por ser un espejo donde mirarse, tanto personal como laboralmente. Tu espontaneidad y honestidad me ganaron desde el principio. A Carmen, que siempre ha estado a mi lado desde el principio, quiero darle las gracias por entenderme mejor que nadie, por transmitirme serenidad y confianza y por ser ante todo, una amiga en quien confiar. A Dani, mi compañero de batalla, mil gracias por tu generosidad, tu humildad, tu actitud positiva y pragmática y sobre todo, por tu infinita paciencia. A Ana muchas gracias por tus sabios consejos, por la buena energía que transmites y por tu espíritu valiente y luchador. A Virgina, siempre marcando el ritmo, gracias por tu excelente disposición al trabajo, por tu sentido del humor único y tu alegría contagiosa. A mi querida Raquel, gracias por tu gran pulcritud y organización en el laboratorio, por tu apoyo incondicional y tu mirada cómplice. A Isa, con quien comencé esta andadura, muchísimas gracias por tu compañerismo, tu generosidad, tu empatía y el rigor con el que trabajas. A Inma, gracias por tu dulzura y tu sonrisa, por tu forma de ser única y tu generosidad. A Toni, gracias por tu simpatía y tu gran sentido del humor que tantas risas me ha provocado.

Indudablemente mi infinito agradecimiento a mi maravillosa familia por apoyarme incondicionalmente y creer en mí. Vuestro cariño me ha permitido continuar siempre adelante en todo momento. Gracias a mis padres por ser los mejores ejemplos a seguir en todos los ámbitos, por su humildad, su entrega y esfuerzo diario. Gracias a mis hermanas por estar siempre a mi lado, por motivarme y enseñarme el camino.

Finalmente, gracias a Pato por ser mi mejor compañero de viaje, por sostenerme, entenderme y cuidarme con tanto amor. Millones de gracias por aguantar mi mal humor y transformarlo siempre en sonrisas.

Table of Contents

RESUMEN

La presente tesis se ha planteado desde dos perspectivas distintas que incluyen en ambos casos el desarrollo de sistemas catalíticos para el estudio de reacciones de interés energético y medioambiental. Un primer punto de vista se centra en la síntesis de catalizadores activos en reacciones de hidrodesoxigenación de moléculas modelo presentes en el bio-oil derivado de la pirólisis de biomasa lignocelulósica. La otra perspectiva incluye el desarrollo de fotocatalizadores activos en la reacción de oxidación preferencial de CO en exceso de hidrógeno bajo irradiación solar simulada a temperatura ambiente y presión atmosférica. En primer lugar introduciremos la primera temática junto con los resultados más relevantes derivados de la misma que se incluyen en los capítulos 4-6.

El suministro adecuado y sostenible de energía es uno de los desafíos más importantes a los que se enfrenta la sociedad moderna. La mayoría de las actividades socioeconómicas y conflictos políticos se asocian a la energía. Por lo que el progreso económico y el aumento poblacional, así como la mejora de los estándares de vida para miles de millones de personas están íntimamente relacionados con el desarrollo energético, el cual se ha visto satisfecho mediante el aprovechamiento de combustibles fósiles. Sin embargo, los yacimientos tradicionales de combustibles fósiles se están agotando gradualmente, lo que hace difícil satisfacer la demanda energética actual. Estas fuentes de energía, derivadas del petróleo, carbón y gas natural, constituyen el 80% de la producción mundial de energía. El uso de combustibles fósiles genera ingentes cantidades de CO_2 que van a la atmósfera, siendo la principal causa del efecto invernadero y del calentamiento global según el Panel Intergubernamental sobre el cambio Climático de las Naciones Unidas "UNs Intergovernmental Panel on Climate Change" (IPCC). Por lo tanto, los gobiernos de numerosas naciones han creado estándares de eficiencia y contaminación que junto a legislaciones más restrictivas, pretenden concienciar a los ciudadanos sobre el uso responsable de los combustibles fósiles, así como fomentar el uso de fuentes renovables, especialmente la biomasa, tanto a nivel doméstico como a nivel industrial. Concretamente, los estados miembros de la Unión Europea han establecido como objetivo para el año 2020 un uso mínimo de biocombustibles de un 10%.

Los principales recursos para producir biocombustibles provienen de materiales residuales, productos forestales, cultivos energéticos, azúcar y biomasa acuática. Las energías renovables como la eólica, la solar o la hidráulica también pueden emplearse como alternativa a los combustibles fósiles en el sector de la energía. Sin embargo, en el caso del sector transporte, responsable del 25% de las emisiones, sólo a partir de biomasa lignocelulósica se pueden obtener combustibles líquidos válidos para los motores de combustión interna.

La biomasa es una fuente rica en carbono, que se forma gracias a la fotosíntesis tal y como se muestra en la reacción:

$$CO_2 + H_2O + h\upsilon \rightarrow CH_2O + O_2$$

Este proceso genera dos tipos de metabolitos: primario y secundario. Los productos mayoritarios son metabolitos primarios, constituidos por diferentes tipos de polímeros, principalmente, celulosa, hemicelulosa, almidón y lignina. Todos ellos pueden emplearse para la obtención de biocombustibles. Los metabolitos secundarios, formados minoritariamente, están constituidos por resinas, alcaloides, esteroles y ácidos de plantas. Estos metabolitos secundarios pueden emplearse para la producción de compuestos con alto valor añadido tales como productos farmacéuticos y cosméticos.

Por tanto, los biocombustibles derivados de la biomasa lignocelulósica ofrecen una solución clave para el presente desafío. Dependiendo de su nivel de desarrollo y comercialización se clasifican en tres categorías: biocombustibles de primera, segunda y tercera clasificación. Los biocombustibles de primera generación tales como el biodiesel, bioetanol y el biogás se producen a gran escala principalmente a partir de cultivos agrícolas, considerándose tecnologías establecidas. Sin embargo, el debate social derivado de la competición entre terrenos dedicados al cultivo de alimentos frente a los que se dedican a cultivos energéticos ha impulsado el desarrollo de biocombustibles de segunda y tercera generación. Los biocombustibles de segunda generación, sin embargo, utilizan todo tipo de residuos (agrícolas, industriales, etc) como materias primas para la obtención de biodiesel, bioetanol, biometanol, biogás y biohidrógeno aunque su producción a gran escala aún debe superar muchas barreras tecnológicas. Por último, los biocombustibles de tercera generación emplean biomasa procedente de las algas como materia prima para la obtención de biometanol y bioetanol.

Sin embargo, la conversión eficiente de materiales lignocelulósicos a combustibles líquidos aún supone un gran reto por lo que se requiere tecnología muy avanzada para abordar este propósito. Generalmente, se emplean tres estrategias para la conversión de biomasa a combustibles líquidos: gasificación, pirólisis o licuefacción e hidrólisis. De entre todas ellas la pirólisis es la estrategia más ampliamente usada y establecida para la obtención de biocombustibles. En concreto, la pirólisis rápida se lleva a cabo a presión atmosférica, temperaturas moderadas (753-793 K) en ausencia de O_2 y un tiempo de residencia <2s. Durante el proceso, la biomasa lignocelulósica se descompone térmicamente y sus componentes se fragmentan y despolimerizan. Este proceso logra densificar la materia prima reduciendo así el espacio de almacenamiento y el precio del transporte. El rendimiento de la reacción es del 65-70% en peso de aceite de pirólisis líquido, 15-20% en peso de alquitrán, y gases no volátiles.

Los bio-aceites derivados de la pirólisis rápida de la biomasa lignocelulósica presentan altos contenidos en oxígeno debido a la presencia de fenoles, furanos, ácidos carboxílicos, éteres, alcoholes aromáticos y humedad libre. Estos compuestos oxigenados son los responsables de la alta viscosidad, baja estabilidad, alta volatilidad e inmiscibilidad con los combustibles fósiles. Debido a la alta reactividad de estos compuestos oxigenados, surgen problemas asociados con la estabilidad térmica y el almacenamiento del aceite de pirólisis. A tiempos de almacenamiento

prolongados, tienen lugar reacciones de condensación que inducen a la formación de compuestos más pesados, lo cual ocasiona una separación de fases. Por tanto, con el objetivo de hacer competitivo el proceso de pirólisis de la biomasa frente a la obtención de aceite, el oxígeno del aceite de pirólisis debe eliminarse.

La hidrodesoxigenación se considera el método más eficiente para la mejora del bio-aceite derivado de la pirólisis. Normalmente, la HDO de bio-aceites se lleva a cabo a 300-600 K, con una alta presión de H_2 y en presencia de catalizadores heterogéneos. El consumo de H_2 así como la severidad de las condiciones de reacción requeridas para que la reacción de HDO sea altamente efectiva dependen de la concentración y del tipo de compuestos oxigenados en la alimentación. Durante la hidrodesoxigenación, los compuestos presentes en el bio-aceite se deshidratan formando agua y se hidrogenan formándose enlaces C-C saturados, con el fin de conseguir un biocombustible estable y con mayor contenido energético. La principal reacción que se lleva a cabo es la siguiente:

$$-(CH_2O)- + H_2 \longrightarrow -(CH_2)- + H_2O$$

Este proceso es muy atractivo debido a la alta eficiencia de carbono (eficiencia teórica de C del 100% ya que todos los átomos de carbono se convierten a hidrocarburos sin emisiones de CO_2) y es compatible con la tecnología de hidrotratamiento de petróleo existente (debido a la naturaleza inmiscible del bio-aceite con los productos petrolíferos, se requiere un tratamiento previo). Sin embargo, la distinta reactividad de la multitud de compuestos presentes en el bioaceite de pirólisis hace necesario el estudio de moléculas modelo para simplificar el análisis de mecanismos de reacción, identificación y cuantificación de productos, idoneidad de fases catalíticas, etc. La baja reactividad del fenol y dibenzofurano hace que ambas sean moléculas idóneas para la reacción de hidrodesoxigenación, por lo que se han seleccionado en la presente tesis como moléculas modelo: la primera es representativa del bio-oil procedente de biomasa rica en lignina y la segunda de biomasa rica en celulosa y hemicelulosa.

En lo que respecta a las fases activas en HDO, existe una extensa bibliografía acerca de catalizadores empleados en este proceso, que deja latente la necesidad de preparar un catalizador bifuncional. La bifuncionalidad del catalizador implica, por un lado, la presencia de sitios ácidos para la activación de los compuestos oxigenados, que podría lograrse mediante un catión expuesto, a menudo asociado con el soporte del catalizador. Y por otro, una función metálica con la facilidad para la donación de hidrógeno a los compuestos oxigenados, que tendría lugar en los metales de transición ya que tienen potencial suficiente para activar el hidrógeno. Los catalizadores más estudiados en la reacción de HDO han sido los sulfuros de

metales de transición, pero su progresiva desactivación en reacción, por oxidación de la fase activa, ha impulsado la búsqueda de nuevas fases más resistentes a la oxidación y con buenas propiedades para la transferencia de hidrógeno, como los metales nobles y los fosfuros de metales de transición. Estos últimos son activos a baja temperatura, posibilitando la prevención de reacciones térmicas que conducen a la desactivación del catalizador por formación de coque. Sin embargo, son muy caros y se envenenan fácilmente en presencia de elementos como el azufre y el hierro. Los catalizadores basados en fosfuros de metales de transición son una alternativa prometedora debido a su alta estabilidad y actividad en reacciones de hidrotratamiento. En la última década, los fosfuros de metales de transición han mostrado excelentes rendimientos en reacciones de hidrotratamiento como la hidrodesulfuración (HDS), hidrodesnitrogenación (HDN) e hidrodesoxigenación (HDO). Por tanto, el trabajo de investigación descrito en los capítulos 4-6 se centra en la preparación de catalizadores basados en fosfuros de metales de transición que sean activos en la reacción de HDO de fenol y dibenzofurano. Las observaciones comunes a los tres capítulos se resumen a continuación:

Todos los fosfuros se prepararon mediante el método de impregnación a humedad incipiente y posterior reducción termoprogramada con hidrógeno. El estudio catalítico se realizó en un reactor catalítico de alta presión de acero inoxidable (9.1 mm de diámetro y 230 mm de longitud), lecho fijo y flujo descendente continuo. La alimentación del reactor consistió en una disolución al 1% en peso de fenol en octano y una disolución 2% en peso de dibenzofurano diluido en decalina.

Para poder justificar la actividad presentada por los catalizadores, estos se caracterizaron mediante diversas técnicas experimentales pudiendo establecerse, de este modo, una clara correlación entre las propiedades físico-químicas del catalizador y la actividad que presenta. Las técnicas empleadas para tal fin fueron: difracción de rayos-X (XRD), espectroscopía fotoelectrónica de rayos-X (XPS), microscopía electrónica de transmisión de alta resolución (HRTEM), desorción termoprogramada de amoníaco (NH_3-TPD), desorción termoprogramada de hidrógeno (H_2-TPD), espectroscopía Mössbauer, análisis elemental, fisisorción de N_2 a -196 ºC, quimisorción de CO y espectroscopía infrarroja de CO a baja temperatura.

Las observaciones más relevantes de los capítulos 4-6 son:

- El capítulo 4 se centra en el estudio de fosfuros mono y bimetálicos de hierro y níquel con diferentes relaciones molares Ni/Fe (1/0, 3/1, 2/1, 0/1) en la reacción de HDO de fenol a 1.5 y 3MPa, 300 ºC y a tiempos de contacto diferentes (2.5, 3, 4.5 y 6 s). Las propiedades texturales de los catalizadores revelaron que la fase activa se encuentra altamente dispersa sobre la superficie del soporte, corroborado a su vez mediante XRD,

donde se identificó principalmente la formación de la fase Ni_2P. La dispersión disminuyó con el contenido en Ni en el catalizador (XPS y TEM). La acidez de los catalizadores, determinada mediante DTP-NH_3, se asoció a la presencia de Ni, Fe y P en la superficie, siendo principalmente de naturaleza débil con un aumento de la fortaleza ácida en los fosfuros mixtos. Además, los resultados de XPS sugieren un enriquecimiento superficial de especies P al aumentar el contenido en Ni, asociado principalmente a los grupos P-OH responsables de la acidez. Los resultados de H_2-TPD indicaron que los catalizadores con mayor contenido en Ni presentan una mayor capacidad para activar hidrógeno en la superficie metálica, mientras que el Fe favorece el fenómeno spillover. Los resultados catalíticos reflejaron que a 3MPa, 300 ºC y 6 s de tiempo de contacto, la conversión HDO es cercana al 100%. Como producto mayoritario de reacción se obtuvo ciclohexano para todos los catalizadores en todas las condiciones estudiadas, obteniéndose las mejores selectividades a tiempos de contacto y presiones de trabajo mayores. También se obtuvo ciclohexanol como producto minoritario y al trabajar a presiones y tiempos de contacto menores aumentó la selectividad hacia este producto. Estudios a diferentes tiempos de contacto indicaron que estos materiales reaccionan principalmente vía hidrogenación/hidrogenólisis.

- El capítulo 5 describe el estudio de fosfuros de cobalto soportados sobre sílice con distinta estequiometría (relación molar P/Co = 0.5, 1, 1.5, 2 y 2.5) en la hidrodesoxigenación de fenol y dibenzofurano a diferentes presiones (1.5 y 3 MPa) y temperaturas (275 y 300ºC). Los resultados de difracción de rayos-X evidenciaron la importancia de la relación molar inicial P/Co en la actividad catalítica de los mismos. Los fosfuros con mayor contenido en cobalto, P/Co-0.5 y P/Co-1, presentaron Co_2P como fase mayoritaria, mientras que en los fosfuros con mayor contenido en fósforo, P/Co =1.5, 2, 2.5, se observó CoP como fase mayoritaria. Esta última fase condujo a los mayores valores de conversión para los catalizadores P/Co-1.5 y 2 en ambos estudios y bajo las distintas condiciones de presión y temperatura estudiadas, obteniéndose como productos mayoritarios ciclohexano (HDO fenol) y biciclohexano (HDO DBF). Los resultados de XRD tras DBF HDO reflejaron un aumento de la intensidad de los picos de difracción, debido probablemente a la aglomeración de la fase activa. También se observó la formación de un fosfuro rico en fósforo, CoP_2, en el catalizador con mayor contenido en fórforo. Los resultados de caracterización revelaron que la capacidad hidrogenante, la acidez y la exposición superficial de la fase activa están directamente relacionadas con la relación molar inicial P/Co, y por tanto, con el tipo de fase fosfuro presente en la superficie del catalizador. El estudio comparativo a 1.5 y 3 MPa demostró la fuerte dependencia de la presión en los resultados de conversión total y conversión

HDO. El análisis elemental CNH de los catalizadores tras reacción reflejó que los fosfuros con mayor relación molar P/Co presentan mayor resistencia a la desactivación por formación de coque.

- El capítulo 6 desarrolla el estudio de fosfuros de hierro soportados sobre sílice con distinta relación molar P/Fe = 0.5, 1, 2 y 3 en la reacción de HDO de fenol a 275 ºC, 0.5 y 1.5 MPa de presión. Los resultados de fisisorción de N_2 muestran una notable dispersión de la fase activa sobre la sílice, sufriendo una leve disminución con el aumento del contenido en fósforo. Mediante XRD se ha identificado la presencia de la fase Fe_2P en los catalizadores P/Fe-0.5 y P/Fe-1, desapareciendo con el aumento de P en los catalizadores P/Fe-2 y P/Fe-3, donde se han identificado las fases FeP y FeP_2 en el último caso. Mediante espectroscopía Mösbauer se corroboraron estos resultados y se observó a su vez la presencia de una fase amorfa en todos los casos correspondiente al fosfato de hierro(II). Los resultados de NH_3-TPD muestran un notable aumento de la acidez tipo Brönsted a mayor contenido en P, asociado a la mayor exposición superficial de los grupos P-OH, a su vez corroborado por XPS. Los resultados catalíticos reflejaron que los catalizadores Fe_xP_y/SiO_2 exhibieron una notable respuesta catalítica que puede asociarse a la estequiometría del fosfuro formado. Así pues, se observó que la actividad está relacionada con la fase fosfuro formada observándose la tendencia: $Fe_2P>FeP>FeP_2$.

Abordando ahora la segunda temática y respondiendo al problema de sostenibilidad energética que se ha planteado en un principio, el uso del hidrógeno como combustible es otra de las alternativas que se contempla para evitar la emisión desmesurada de gases de efecto invernadero derivada del uso de combustibles fósiles. De hecho, se espera que el hidrógeno sea uno de los vectores de energía más importantes del futuro, principalmente por su alto contenido energético y especialmente cuando se usa en celdas de combustible en dispositivos móviles. Pese a ser el elemento más abundante del universo, es muy difícil encontrarlo en su forma elemental porque normalmente está combinado con otros elementos como el carbono y el oxígeno, de modo que su disponibilidad para aplicaciones industriales sólo puede ser el resultado de procesos de producción a partir de sustancias que lo contienen. Aun así, cuenta con la ventaja de poder utilizar muchas materias primas como fuente de hidrógeno: combustibles fósiles, biomasa, agua, etc. Pese a estar desarrollándose métodos más sostenibles para su producción, el 85% de la producción mundial aún proviene del reformado con vapor de metano, generándose H_2 y CO según la reacción:

$$CH_4 + H_2O \rightarrow CO + 3H_2$$

Sin embargo, el hidrógeno también se puede obtener a partir de biomasa, como fuente renovable de energía. Así, la gasificación de biomasa da lugar a una mezcla H_2+CO, que bien puede ser utilizada en el proceso Fischer-Tropsch para producir biocombustibles o bien se reduce el contenido de CO mediante la reacción de desplazamiento de agua o water gas shift (WGS) según la reacción:

$$CO + H_2O \rightarrow CO_2 + H_2.$$

Se obtiene así una corriente rica en H_2 pero que aún presenta contenidos considerables de CO para su uso, por ejemplo, en celdas de combustible. El uso de hidrógeno en celdas de combustible posibilita la obtención de energía eléctrica a partir de una reacción química en la que no se generan sustancia tóxicas, sólo H_2O. Concretamente, en el caso de las pilas de combustible de membrana de intercambio protónico (PEM), el hidrógeno que se utiliza como alimento se genera a bordo mediante reformado catalítico de metanol, etanol o biocombustible. La corriente resultante presenta un alto contenido en CO por lo que es necesario someterla a una serie de procesos de purificación para reducir su concentración a niveles inferiores a 10 ppm para evitar el envenenamiento y la posterior desactivación de los electrodos de Pt de la pila de combustible. Las reacciones de purificación más usadas son la WGS seguida de la oxidación preferencial de CO (CO-PROX). La reacción de WGS ocurre en dos etapas consecutivas (de alta y baja temperatura) generándose CO_2 e H_2. Sin embargo, la concentración de CO no convertido oscila entre 0.5-1 % en volumen, cantidad aún muy elevada para las PEM. Por tanto, una unidad adicional CO-PROX es necesaria antes de que la corriente de hidrógeno entre en la pila. La reacción principal que tiene lugar es:

$$CO + 1/2\ O_2 \rightarrow CO_2$$

Paralelamente puede producirse la reacción competidora de oxidación de H_2:

$$H_2 + 1/2O_2 \rightarrow H_2O$$

Además se pueden producir otras reacciones como la metanación de CO y CO_2 o la WGS inversa (RWGS), que no son deseables ya que implican un alto consumo de hidrógeno. Otra reacción indeseable es la de formación de coque que se depositaría en la superficie del catalizador conduciendo a su desactivación. Para evitar que suceda cualquiera de estas reacciones es necesario que los catalizadores sean muy activos y selectivos en la oxidación de CO a CO_2 y que sean resistentes a la desactivación por la presencia de H_2O y CO_2. De entre todos los sistemas catalíticos que se han estudiado, los materiales que han proporcionado una mejor respuesta catalítica incluyen: metales nobles soportados y óxidos metálicos soportados, y más en concreto el sistema CuO-CeO_2. Sin embargo, y ya que esta reacción ha sido ampliamente

estudiada, recientemente se ha propuesto el uso de fotocatalizadores que utilizan radiación solar como fuente de energía, posibilitando entre otros aspectos, trabajar a temperatura y presión atmosférica.

De entre toda la variedad de semiconductores, los sistemas catalíticos basados en TiO_2 han conducido a resultados prometedores en fotocatálisis heterogénea. En este proceso, la luz absorbida por un semiconductor excita los electrones desde la banda de valencia a la de conducción, generándose pares electrón-hueco que si se disocian y difunden a la superficie del material pueden transferirse en ésta al fluido circundante, provocando transformaciones químicas de posible interés. El TiO_2 ha demostrado ser muy adecuado para este tipo de reacciones debido a su capacidad oxidativa, super-hidrofilia, baja toxicidad, alta disponibilidad y excelentes propiedades químicas bajo iluminación. Sin embargo, el uso del TiO_2 puro está limitado por su energía de banda prohibida que puede variar de 3.0 a 3.2 eV dependiendo del polimorfo, por lo que se requiere irradiar con longitudes de onda en el UV cercano (387.5 nm) para una excitación eficiente. Este hecho impide aprovechar de forma eficiente la mayor parte de la radiación solar que llega a la Tierra ya que ésta contiene menos del 5% de radiación UV, mientras que la radiación visible constituye el 43% del total. Otra limitación que presenta es la rápida recombinación del par electrón-hueco lo que limita su actividad catalítica. Con el fin de mejorar estos aspectos, se han desarrollado estrategias para disminuir la energía de la banda prohibida y ralentizar la recombinación par electrón-hueco, posibilitando así ampliar la foto-respuesta del TiO_2 bajo luz visible. Estas estrategias se basan en técnicas de modificación estructural y/o superficial. La modificación estructural consiste en la adición de dopantes principalmente metálicos como V, Nb, Mo o Fe que al ocupar posiciones de sustitución en la red son capaces de desplazar la energía de la banda prohibida a mayores longitudes de onda, aumentando así la ventana de absorción en la región visible. En cuanto a la mejora superficial, una técnica comúnmente utilizada es el depósito de nanopartículas metálicas sobre la superficie de la titania, de forma que el metal actúe como un atrapador de electrones, ralentizando la recombinación del par electrón-hueco y aumentando así la fotoactividad. Recientemente se ha prestado especial atención a aquellos procesos catalíticos y fotocatalíticos que usan nanopartículas (NPs) de oro, debido a su alta reactividad a bajas temperaturas. Concretamente, el depósito de NPs de Pd, Pt, Au, Ag o Cu sobre titania parece ser un método muy efectivo para mejorar la separación de carga proporcionando, por tanto, más sitios catalíticamente activos. Entre los distintos metales nobles, las NPs de Au soportadas sobre TiO_2 han mostrado una fotoactividad sorprendentemente alta en la región visible que puede atribuirse al plasmón de resonancia superficial de las NPs de Au. Este tipo de catalizadores han demostrado ser fotoactivos en la reacción de oxidación total de CO a CO_2. Así pues, el electrón foto-generado en la superficie de las NPs de Au a través de la excitación del plasmón de resonancia superficial

localizado, se inyecta en la banda de conducción de la titania para activar las moléculas de CO. Por tanto, la separación de los portadores de carga podría ayudar a reducir la tasa de recombinación y, por tanto, a aumentar la conversión en la reacción de oxidación preferencial de CO en exceso de H_2. Además de esto, se ha de tener en cuenta, en función de los resultados encontrados en bibliografía, que la fotoactividad del TiO_2 depende de un amplio número de factores tales como la estructura cristalina, el cociente entre las fases anatasa/rutilo, la distribución del tamaño de partícula, el área específica y el tamaño promedio de poro. Es por tanto que en la presente tesis se presenta la síntesis y el estudio de sistemas basados en NPs de Au soportadas sobre distintas estructuras de titania para ser estudiados en la mentada reacción. Las observaciones comunes a los capítulos 7-8 se resumen a continuación:

La síntesis de NPs de oro soportadas sobre titania se ha llevado a cabo mediante el método de depósito-precipitación con NaOH. Este método permite la obtención de nanopartículas de oro del orden de 2-5 nm mediante el control del pH y de la temperatura de calcinación, tamaño idóneo para asegurar una alta actividad en la oxidación de CO. El estudio catalítico se llevó a cabo en un reactor de lecho fijo y flujo continuo a presión atmosférica y temperatura ambiente. El reactor se alimentó con 1.2% CO, 1.2% O_2, 50% H_2 (vol%) y 52.4 % He.

Los catalizadores se caracterizaron mediante diversas técnicas instrumentales con el objetivo de poder relacionar las propiedades físico-químicas con los resultados catalíticos. Las técnicas empleadas para tal propósito son: XRD, XPS, HRTEM, fisisorción de N_2 a -196 ºC, espectroscopía de reflectancia difusa (DRUV-vis), espectroscopía de absorción atómica (AAS), fluorescencia de rayos X (XRF), espectroscopía Raman y dispersión de rayos X a bajo ángulo (SAXS).

Los capítulos 7 y 8 se resumen a continuación:

- El capítulo 7 se centra en el desarrollo de sistemas basados en Au/MTX (MT= titania mesoporosa, X= temperatura de calcinación) en los que la titania se ha preparado mediante un método sol-gel y se ha calcinado a diferentes temperaturas obteniéndose distintas fases cristalinas. Los resultados de difracción de rayos-X revelaron que los catalizadores calcinados a 400 y 500 ºC presentan anatasa como fase única, mientras que en Au/MT600 aparece cierta contribución de fase rutilo (9.8%) que en el catalizador Au/MT800 pasa a ser la fase mayoritaria (98.8%). Los espectros de reflectancia difusa demostraron que la adición de oro reduce la energía de la banda prohibida. Los resultados catalíticos demostraron que a pesar de la baja carga metálica (0.5% en peso determinada por AAS), todos los catalizadores resultaron muy activos en la reacción foto-PROX en condiciones ambientales. Estos resultados se atribuyen en parte al pequeño y óptimo tamaño de las nanopartículas de Au (2-5 nm, confirmado

mediante HRTEM) que, a su vez, están altamente dispersas en la superficie del soporte, proveyendo así de sitios catalíticamente disponibles para coordinarse con CO y O_2. El catalizador Au/MT600 condujo a los mejores resultados de conversión y selectividad bajo irradiación solar simulada. El delicado equilibrio entre tipo de polimorfo, cristalinidad, porosidad y tamaño de las nanopartículas conducen a pensar que la presencia simultánea de anatasa y rutilo favorece la actividad fotocatalítica en la reacción foto-PROX.

- En el capítulo 8 se describe el estudio de sistemas catalíticos basados en NPs de oro soportadas sobre estructuras de titania con forma de nanovarillas. Estos soportes se sintetizaron mediante dos métodos hidrotermales marcadamente ácido y básico y se calcinaron a 500 y 700 ºC. Los resultados de difracción de rayos X reflejaron que los soportes procedentes del tratamiento ácido presentan únicamente la fase rutilo mientras que los que proceden del tratamiento básico presentan anatasa como fase única. Mediante HRTEM se observó que el tamaño de partícula del Au depende principalmente del área superficial y del tipo de polimorfo. Los catalizadores procedentes del tratamiento ácido (AuTNRa), exhiben una distribución de tamaño de partícula entre 2-3.5 nm, mientras que en los procedentes del tratamiento básico (AuTNRb) la distribución del tamaño de partícula oscila entre 1.6-1.9 nm. Los test catalíticos demostraron que todos los catalizadores presentan una alta conversión de CO (>80%) a excepción del AuTNRb7, que por el contrario, resultó ser el más selectivo hacia CO_2 (100%). En el resto de catalizadores, la alta fotoactividad conduce a una disminución de la selectividad hacia CO_2 como resultado de la reacción competitiva de oxidación de H_2 a H_2O.

1. INTRODUCTION

1.1. Energetic context

Sustainable and suitable energy supply is one of the most important challenges that society faces. Most of socioeconomic activities and politic conflicts are associated with energy delivery and manufacturing. The world population is expected to reach 8.5 billion by 2030 and 9.7 billion in 2050. Total world energy consumption grows from 549 quadrillion British thermal units (Btu) in 2012 to 815 quadrillion Btu in 2040, i.e., a 48% increase from 2012 to 2040 [1]. Hence, population and economic growth as well as the improvement on life standards for millions of people are closely related to the energetic development, which has been satisfied by the utilization of fossil fuels. However, traditional fossil fuels supply is being gradually depleted making it difficult to cope with the current energetic demand [2]. Today, the most used energy sources are liquid fuel, coal and natural gas and these constitute 80% of the world's energy production [3].These fossil fuels lead to large CO_2 emissions in the atmosphere, which are the leading reason for global warming. Concretely, the International Energy Agency predicts that the carbon dioxide emissions will increase by 20% in 2035, which may lead to an average temperature of 3.6 K [4]. Furthermore, uncontrolled rise of global atmospheric CO_2 to an alarming level of 406.69 ppm forced the world political leaders to discuss a new global agreement on climate change in United Nations Framework Convention on Climate Change (UNFCCC) summited in Paris, aimed at reducing greenhouse gases emissions; and thereby, bringing about a transitional change from a fossil fuel based economy to a more sustainable carbon-neutral bio-economy [5].

Regarding the abovementioned, it is important to highlight that the sharp increase in human population has also been accompanied with the generation of large amounts of various types of wastes. Investment of energy for waste disposal is not economical but utilization of waste for energy production is promising. Therefore, a renew interest has emerged towards the production and utilization of plant origin fuels or organic wastes for sustainable energy development. In that sense, biomass resources are the only renewable and suitable primary energy resource that can provide various alternative transportation fuels in the short-term [6]. In contrast to fossil fuels, biofuels (or biomass) provide an environmental advantage: they take carbon out of the atmosphere while it is growing, and returns it as it is burned. In other words, the cycle for biomass-based fuels from carbon to CO_2 and back to carbon is much faster than that for conventional fuels. Fossil fuels are formed from material already existing under-ground whereas the biomass needed for biomass-based fuels continuously consumes CO_2 via photosynthesis. This maintains a closed carbon cycle with no net increase in atmospheric CO_2 levels. Since the transportation sector is strongly dependent on petroleum, a lot of research is being performed in the field of alternative energy sources. Vehicles powered by electricity, solar energy, hydrogen fuel cells and biofuels are being actively researched to reduce the dependence on petroleum [7].

In this sense, hydrogen as energy carrier is regarded as another alternative to fossil fuels and will be discussed in sections 1.8 and following.

1.2. From biomass to biofuels

In 2012, the estimated global petroleum consumption was about 89 million barrels per day from which about a half was used for gasoline production. At this rate of consumption, fossil fuel resources will be depleted within the next 50 years [8]. Biofuels offer a key solution for the present challenge since they are produced through renewable biomass resources. According to the FAO definition, biofuels are "fuels produced directly or indirectly from biomass such as fuelwood, charcoal, bioethanol, biodiesel, biogas (methane) or biohydrogen" [9]. Based on the level of development and commercialization, there is a tendency to classify them into three categories: First generation, second generation, third generation and more recently, into fourth generation biofuels. This classification is illustrated in Figure 1.1.

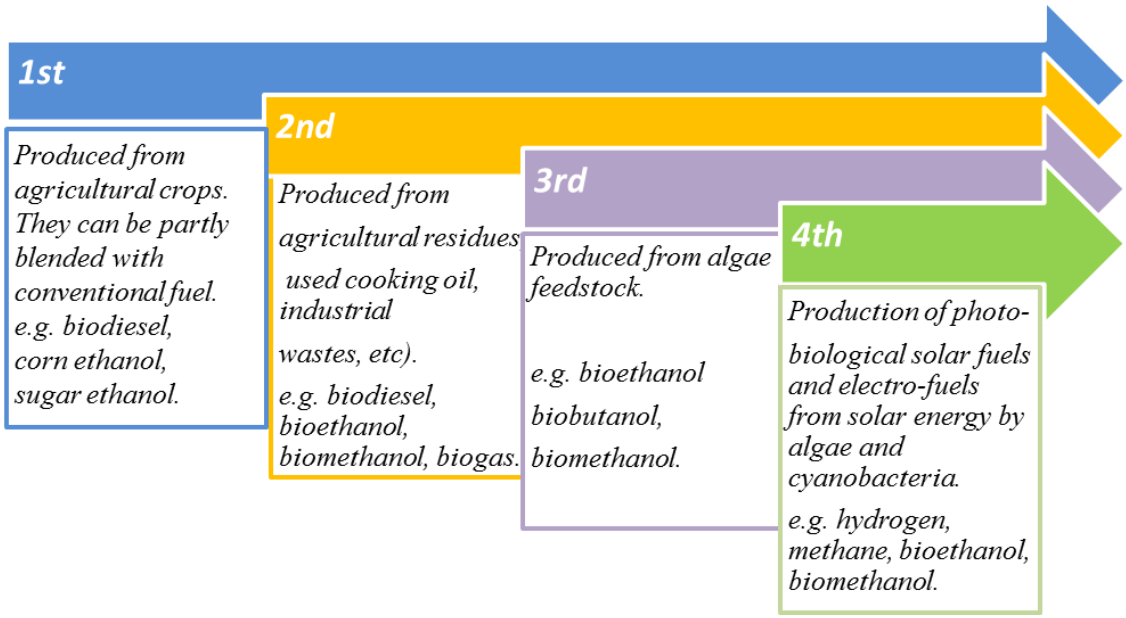

Figure 1.1. Classification of biofuels [10]

First generation biofuels consist of biodiesel, bioethanol and biogas and are generally produced from agricultural crops (sugarcane, sugar beet, wheat, rice, soybean oil, sunflower, palm oil, etc.). These fuels are characterized by their ability to be blended with petroleum-based fuels and have been produced at a large scale worldwide, being considered as "established technologies" [11]. Biodiesel is produced through transesterification of vegetable oils and can be used as substitute of conventional diesel. Bioethanol is produced through fermentation of sugar and starch, and can be used as a substitute for gasoline and feedstock to ethyl tertiary butyl ether. Bioethanol and biodiesel are used commercially with almost 120 and 30 billion liters produced worldwide, respectively. Currently, the three major producers are the United States of America, Brazil and the European Union [12]. There are, however, controversies about first generation

fuels which have generated a great debate because they are competing with food crops and because of their low energy efficiency. The "Food vs Energy" conflict has prompted many researchers to opt for the production of second and third generation biofuels which can be obtained from non-food competing crops.

Second generation biofuels use cheap feedstock such as abundant plant waste, and all parts of plant, such as seeds, barks and leaves. Examples of wastes which can be used for second generation biofuels production are municipal solid wastes, used cooking oil, industrial wastes, agricultural wastes, and sewage sludge. Lignocellulosic materials from the cell walls are used as feedstock in pyrolysis and liquefaction to produce bio-oil and in gasification to produce Fischer-Tropsch oil. Biofuels such as biodiesel, bioethanol, bio-methanol, bio-butanol, biogas, and biohydrogen can be produced from them. The production of second generation fuels is, however, not yet cost effective due to many technological barriers [11].

Third generation biofuels are mainly produced from algae feedstock which is currently considered as the most promising renewable energy resource. Algal biomass is more abundant in nature, mainly grown in various types of wastewater sources from which biofuels such as bioethanol and biomethanol can be obtained [13].

The *Fourth generation biofuels* are just emerging at the basic level and consists of photo biological solar fuel and electrofuels that are expected to bring fundamental breakthroughs in the field of biofuels. Production of these solar biofuels is based on the direct conversion of solar energy into fuel by the use of raw materials which are inexhaustible, cheap and widely available such as algae and cyanobacteria [14-16].

1.2.1. Biomass resources and feedstocks

A wide variety of biomass can be used for biofuel production. The annual global primary production of biomass is about 220 billion tons on dry weight basis that is equivalent to 4500 EJ of solar energy captured each year. From this biomass, an annual bioenergy market of 270 EJ is possible on a sustainable basis [17]. The main biomass resources are wood and wood wastes, agricultural crops and their waste by-products, municipal solid waste, animal wastes, wastes from food processing, aquatic plants and algae. Maximum biomass energy is produced from wood and wood wastes (64%), followed by municipal solid waste (24%), agricultural waste (5%) and landfill gases (5%) [18]. Fast growing species such as poplar, willow or eucalyptus can be harvested after every few years [19]. Waste wood from the forest products industry such as bark, sawdust, board ends etc. are widely used for energy production [20]. Algal biomass is also a promising source especially for production of third generation biofuels like biodiesel. Table 1.1 details different categories of biomass resources. The conversion of lignocellulosic

biomass to liquid hydrocarbons such as alkanes and aromatics has more important practical significance compared to the rest of feedstock types derived from biomass [21].

Table 1.1. Categories of biomass resources [20]

Feedstock type	Resources
Lignocellulosic biomass	Agricultural crop residues, cellulosic crop biomass, food processing wastes, forest residues, mill wastes, urban wood residues, garden residues.
Sugar/starches	Agricultural crops (i.e. wheat, rice, maize, sugarcane etc.), food processing residues containing residual sugars and starches
Solid wastes	Municipal solid waste, furniture construction and demolition wood wastes, non-recycled paper and recycled material.
Bio-oils	Agricultural and forestry oil bearing crops and trees, waste oils/fats/grease, algal oil etc.
Other wastes	Animal wastes, waste from waste water treatment, biogas and landfill gas.

1.2.2. Lignocellulosic biomass. Source and composition

Lignocellulosic biomasses are predominantly derived from corn stover, wheat, rice, barley straw, sorghum stalks, coconut husk, sugarcane bagasse and wood. Among all the by-products, USA produces large amount of corn stover, and wood from Canada, China and New Zealand generates considerable quantity of agricultural and forest residues [22, 23]. After China, India provides around 0.2 billion tons of agricultural residues yearly. Kumar et al [24] estimated that terrestrial plants can produce 1.3×10^{10} metric tons of wood per year (dry weight basis) which is equivalent to 7×10^{9} metric tons of coal energy. In addition, an average 180 million tons of cellulosic feedstock per year is available from agricultural sources [25] . According to a report from the Food and Agricultural Organization (FAO) pulse, oil seed and plantation crops contributed to 2.9×10^{3}, 1.4×10 and 5.4×10^{2} million tons of agricultural waste per year, respectively (FAOSTAT, 2006) [26].

Lignocellulosic biomass as a crop or a residue is largely produced from perennial herbaceous plant species and woody crops and is the most abundant plant material available on our planet.

Agricultural and forest residues and municipal organic wastes (e.g. straw from agriculture and wood from pulp and paper industry) are other major sources of lignocellulosic biomass [27, 28].

1.2.2.1. Composition

This composite material synthesized by plants cells typically consists of 40-50 wt% cellulose, 25-35 wt% hemicellulose, 15-20 wt% lignin and a minor amount of other organics [29]. Certain

differences in content are observed between the three types of lignocellulosic biomass: grasses, softwoods and hardwoods. Chemical composition and structural differences among them affect their amenability to disorganization or deconstruction of the biomass [23, 30] .

Cellulose

Cellulose is a natural organic polymer which is the most abundant (40-50%) and important component in plants, and has the potential to be an inexhaustible source (1.5×10^{12} ton per year as a biomass resource) for raw material to produce chemicals and energy [31]. Cellulose (chemical formula $(C_6H_{10}O_5)n$), is a long chain polymer formed from connection of D-glucose molecules that are linked via -O- group between –OH groups of C4 and C1 carbon atoms (β-(1-4)-glycosidic bonds) as shown in Figure 1.2. The basic repeating unit consists of two glucose anhydride units, called a cellobiose unit. The cellobiose unit is formed via the removal of water from each glucose unit [32]. The degree of polymerization (DP), which varies depending on the source and treatment of the raw materials, determines the chain length of cellulose (between 300 and 150000 units) [33]. As it possesses a not branched crystalline structure, the interaction between the –OH groups by strong hydrogen bonds gives rise to the hierarchical structure of the 3-D cellulose materials which is very difficult to fractionate [34]. Hence, cellulose degradation occurs at 513-623 K, resulting mainly in anhydrocellulose and levoglucosan [32].

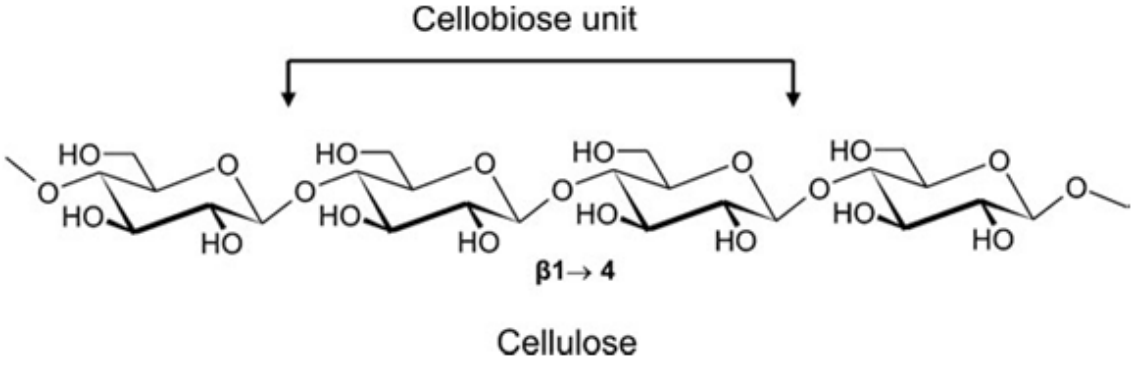

Figure 1.2. Chemical structure of cellulose [31]

Hemicellulose

Hemicellulose representing 15-35% of plant biomass, is a branched substituted polysaccharide located in the plant cell walls contributing to the strength of the cell wall by interaction with cellulose and in some conditions, with lignin [35]. It consists of heterogeneous class of polysaccharides such as glucose, mannose, xylose, arabinose and glucuronic acid residues as seen in Figure 1.3 [32]. Hardwood hemicelluloses are rich in xylan, while softwood hemicelluloses are richer in glucomannan [32]. The degree of polymerization is lower than that of cellulose (70-200) base units [33] resulting in a lower onset temperature of decomposition.

Hemicellulose decomposes at temperatures of 473-533 K and produces more volatiles, less tars and chars than cellulose [32].

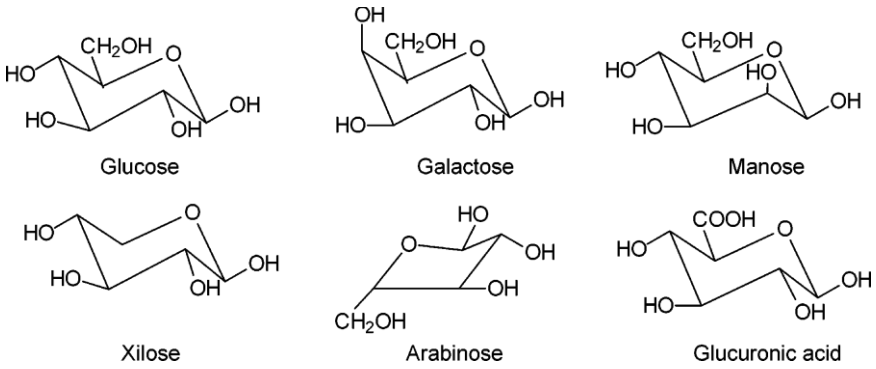

Figure 1.3. Main components of hemicellulose [32]

Lignin

Lignin, a three-dimensional amorphous polymer consisting of methoxylated phenylpropane structures [36], is one of the most abundant organic compounds on earth. From a quarter to a third of the dry mass of wood is comprised of lignin. Furthermore, it contains as much as 30% of non-fossil organic carbon [37]. Lignin holds the lignocellulose material together and locates in the space between cellulose and hemicellulose in the plant cell walls. It consists of variously bonded hydroxyl substituted and methoxy substituted phenylpropane units. It has been widely accepted that three types of phenyl propane units (*p*-coumary alcohol, coniferyl alcohol, sinapyl alcohol), Figure 1.4, polymerize with each other to form lignin [38, 39]. Due to the difference in the relative abundance of the p-coumaryl, coniferyl, and sinapyl alcohols, the composition of softwood and hardwood lignin varies accordingly. The ratio between these building blocks is typically 100:70:7 for hardwood lignin. Softwood lignin contains fewer alcohol units [32].

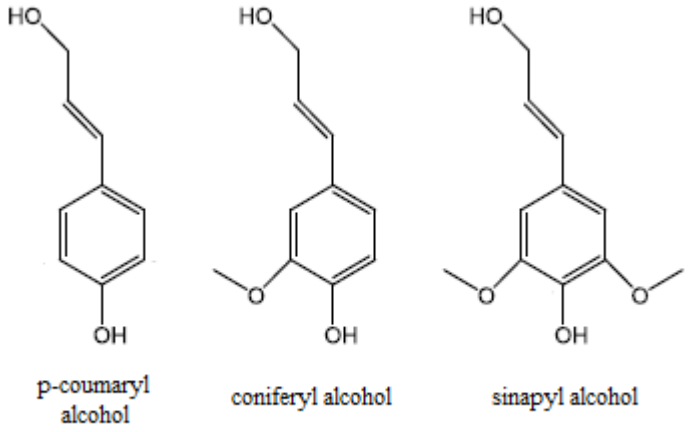

Figure 1.4. Structures of building blocks phenolic compounds present in lignin [40]

Due to the different thermal stabilities of these three alcohols, lignin decomposes over a broad temperature range that goes from 553 K to 1173 K. A maximum rate is observed at 623-723 K, however, around 773 K the conversion of lignin is still limited to 40% [41]

The chemical structure of lignin suggests that it has a great potential to be used as a feedstock for value-added chemicals, such as acids, alcohols, phenols, aldehydes and aromatics (benzene, toluene, xylene). Most lignin derived compounds partition into a non-polar phase due to their lower oxygen content , leading to more thermally stable and higher energy density liquid fuels compared to fuels derived from other biomass components [42].Yet there is relatively little research focused on valorization of lignin relative to cellulose and hemicellulose, especially on the conversion of lignin to liquid transportation fuels.

Other compounds

Besides these three main components, biomass also contains a small fraction of inorganic minerals and organic extractives. Potassium, sodium, phosphorus, calcium and magnesium typically end up in the pyrolysis ash [43] . Organic extractives can be extracted from the biomass with polar (such as water or alcohols) or non-polar solvents (such as toluene or hexane). Examples of extractives are fats, waxes, proteins, simple sugars, pectins, resins, etc.

1.3. Methods for converting lignocellulosic biomass into transportation fuels

Lignocellulosic biomass can be converted to various forms of energy by four strategies, (*i.e.* physical, chemical, biological and thermochemical processes) depending on the raw material characteristics and the type of energy desired. However, nowadays it is still a challenge to convert lignocellulosic materials to liquid fuels with high efficiency. It requires more advanced technology to realize its potential [44]. As a result, a wide variety of conversion schemes has been developed [45, 46]. Among various conversion technologies, thermochemical conversion of biomass offers a convenient way to produce liquid fuels. The liquid products, known as bio-oils have been regarded as promising candidates to replace petroleum fuels for power generation, heat, or for extraction of valuable chemicals. Figure 1.5 shows the three main strategies for converting the lignocellulosic biomass to transportation fuels**:** gasification (to synthesis gas), pyrolysis or liquefaction (to bio-oil) and hydrolysis (to sugar monomers) [46].

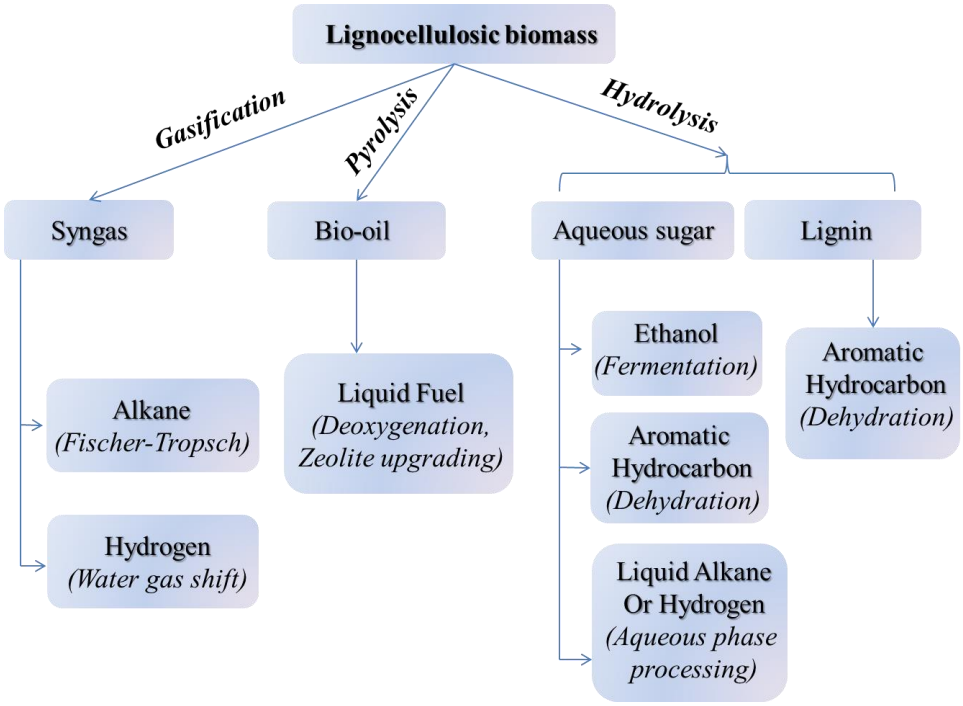

Figure 1.5. Scheme of processes for thermochemical conversion of biomass [46, 47]

Among all the strategies, fast pyrolysis is the most widely applied process for production of bio-oil and will be the only one discussed in the present thesis. Although it is not the purpose of this introduction to give an extensive literature overview on pyrolysis, some relevant characteristics are given as follows.

Fast pyrolysis occurs at moderate temperatures (753-793 K) and rapid heating is conducted in the absence of air, with a short hot-vapor residence time (<2s) in the reaction zone [48]. Today, there are several fast pyrolysis plants operating on full scale, the largest being Ensyn Technologies (USA) which produces 50 t/day [49]. A schematic representation of fast pyrolysis reactor is given in Figure 1.6. The essential features of the process are as follows: the biomass must first be dried and ground to obtain the optimal heat transfer properties, the temperature must be strictly controlled around 773 K, and the produced pyrolysis vapor has to be rapidly cooled to prevent cracking [45]. During the process, fragmentation and depolymerization of hemicellulose, cellulose and lignin-based compounds takes place. The resulting "bio-oil" or "pyrolysis oil", can be produced with yields up to 70 wt% (dry feed basis), and holds the potential to supplement crude oil as a liquid hydrocarbon feedstock.

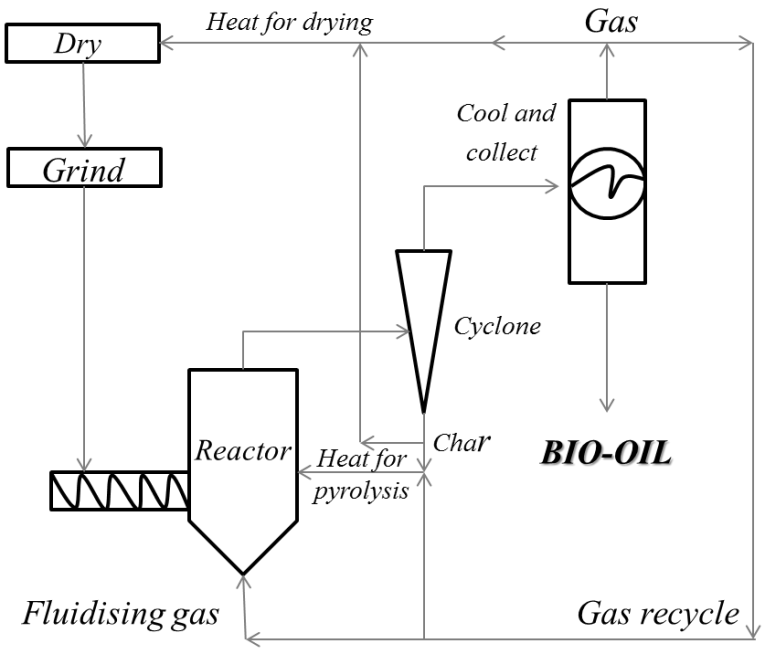

Figure 1.6. Scheme of a pyrolysis reactor [48]

1.3.1. Bio-oil from fast pyrolysis

The so-called pyrolysis oil is a free-flowing liquid with a distinctive smoky odor and dark brown color. More than 300 different compounds have been identified in the bio-oil where the specific composition of the product depends on the feed and process conditions used [50]. Table 1.2 shows a rough characterization of bio-oil from different biomass resources.

Table 1.2. Bio-oil composition in wt% on the basis of different biomass sources and production methods [51]

	Corn cobs [52]	Corn stover [52]	Pine [53]	Softwood [54]	Hardwood [54]
Tª(K)	773	773	793	773	-
Reactor	Fluidized bed	Fluidized bed	Transport bed	Rotating bed	Transport bed
Water	25	9	24	29-32	20-21
Aldehydes	1	4	7	1-17	0-5
Acids	6	6	4	3-10	5-7
Carbohydrates	5	12	34	3-7	3-4
Phenolics	4	2	15	2-3	2-3
Furans	2	1	3	0-2	0-1
Alcohols	0	0	2	0-1	0-4
Ketones	11	7	4	2-4	7-8
Unclassified	46	57	5	24-57	47-58

It is observed that the principal compound of the bio-oil is water, constituting 10-30 wt%, also containing: hydroxyaldehydes, hydroxyketones, sugars, carboxylic acids, esters, furans, guaiacols, and phenolics, among which monomeric or dimeric alkoxyphenols are predominant [51] [49].

Comparison between bio-oil and crude oil is shown in Table 1.3. The main difference between both is the oxygen content that ranges from 28 to 40 wt% in the bio-oil whereas in crude oil it is lower than 1 wt% oxygen [41, 50]. The high water content causes the lower heating value of pyrolysis oil to be only 40-45 wt% of that exhibited by hydrocarbons. Overall, this means that the bio-oil has a polar nature due to the high water content and is therefore immiscible with crude oil [52, 55] . The acidic nature of the bio-oil which is ascribed to the presence of acetic and formic acid constitutes another problem [56]. The low pH, from 2 to 4, will entail the harsh conditions for equipment used for storage, transport and processing. Common construction materials such as carbon steel and aluminium have proven to be unsuitable when operating with bio-oil due to corrosion [55].

Another pronounced problem with bio-oils is the instability during storage ascribed to the presence of highly reactive organic compounds. Olefins are suspected to be active for repolymerization in the presence of air. Furthermore, ketones, aldehydes and organic acids can react via aldol condensation to form ethers, acetals and hemiacetals, respectively. These types of reactions effectively increase the average molecular mass of the oil, the viscosity and the water content. Besides, those reactions are temperature driven and therefore pyrolysis oil has to be stored under room temperature. An overall decrease in the oil quality is therefore seen as a function of storage time, ultimately resulting in phase separation [53].

As an alternative to the tentative first route, literature has reported new upgrading processes that can be tackle within a near context. Mainly when it comes to hemicellulose and cellulose revalorization

As a consequence of all these disadvantages, bio-oil cannot be directly utilized as transportation fuel and, therefore, it has to be upgraded. Petroleum-based jet fuels contain 20% *n*-alkanes, 40% isoalkanes, 20% cyclic alkanes, and 20% of aromatic hydrocarbons. The O/C and H/C ratios of crude bio-oil range from 0 to 0.03 and from 1.6 to 2.1, respectively. In contrast, the O/C and H/C ratios of crude bio-oil range from 0.6 to 0.71 and from 1.0 to 1.35, respectively [57]. Bio-oil upgrading should, therefore, target oxygen removal, carbon preservation and hydrogenation of unsaturated carbon bonds. Production of *n*- or iso-alkanes from lignin-derived bio-oils is not practical due to the inefficiency of aromatic and cycloalkane ring-opening reactions. Instead, upgrading lignin-derived bio-oils into aromatic hydrocarbons and cycloalkanes is preferred.

Table 1.3. Comparison between bio-oil and crude oil [50, 58]

	Bio-oil	Crude oil
Water (wt%)	15-30	0.1
Ph	2.8-3.8	-
ρ(kg/l)	1.05-1.25	0.86
μ_{50^oC} (CP)	40-100	180
HHV (MJ/Kg)	16-19	44
C (wt%)	55-65	83-86
O (wt%)	28-40	<1
H (wt%)	5-7	11-14
S (wt%)	<0.05	<4
N (wt%)	<0.4	<1
Ash (wt%)	<0.2	0.1

1.4. Catalytic upgrading

Catalytic upgrading enhances the properties of the pyrolysis bio-oil by removing oxygen compounds, reducing molecular weight and altering chemical structure to resemble those of fossil fuels [59]. There are three general methods to upgrade bio-oils directly to liquid transportation fuels: (i) catalytic hydrodeoxygenation (HDO) [60], (ii) zeolite cracking (ZC) [45], and (iii) emulsification with diesel fuel. An alternative, indirect fourth pathway involves steam reforming the bio-oil to produce syngas, followed by production of liquid fuels via Fischer-Tropsch or similar chemistry [45]. This fourth pathway is a deviation from upgrading of pyrolysis bio-oil and it is not discussed further here. HDO and ZC are catalytic upgrading approaches, while emulsification of bio-oils into diesel fuel through the use of surfactants does not require a catalytic process and therefore, will not be discussed here either.

During zeolite cracking, different kinds of zeolites (i.e. HZSM-5, H-mordenite, SAPO-11) are used on the deoxygenation process without demanding hydrogen, so operation is performed at atmospheric pressure. However, it results in a low H/C ratio of the oil product not to mention the extensive carbon deposition that leads to very short catalyst lifetime. Overall, oil from zeolite cracking is of a low grade, with heating values of approximately 25% lower than that of crude oil.

Given the different types of C-O bond in bio-oil, each with varying bond strength, the catalytic upgrading of bio-oil actually represents a complex network of many reactions [60]. The process can be somewhat simplified by distinguishing reactions according to the hydrocarbon products and oxygen-elimination products. A combination of decarbonylation, decarboxylation, direct

deoxygenation (hydrogenolysis), dealkoxylation, cracking, hydrocracking, hydrogenation, dealkylation, methyl transfer, and hydrodeoxygenation have been observed during deoxygenation reactions [51]. Figure 1.7 shows example transformations for the most representative reactions.

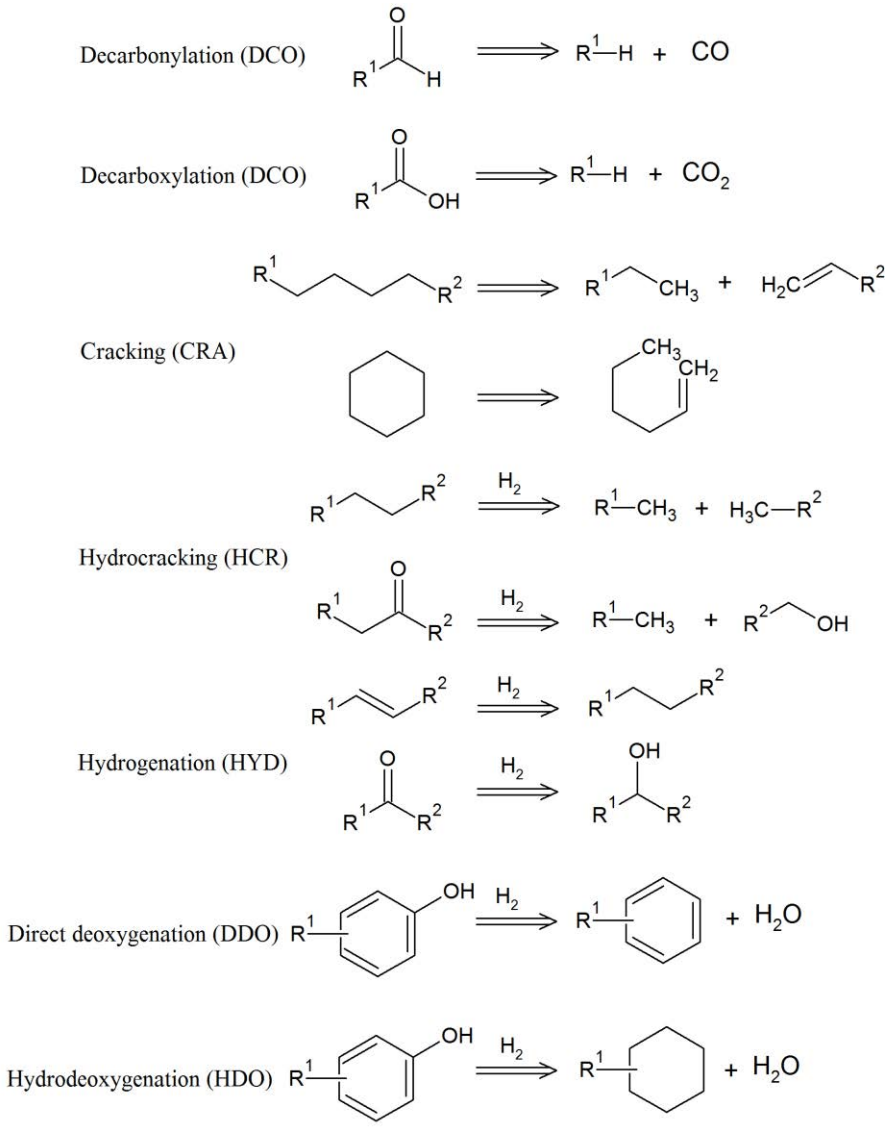

Figure 1.7. Examples of reactions occurring during catalytic bio-oil upgrading [61]

Beside these, carbon formation is a significant side-reaction. Decarbonylation and decarboxylation (DCO) eliminate oxygen as CO and CO_2, respectively. Although these are effective reactions to remove oxygen from aldehydes and carboxylic acids of bio-oil, this partial loss of carbon from the feed ultimately lowers the carbon efficiency of a biomass to fuels process. Cracking (CRA), hydrocracking (HCR), and hydrogenation (HYD) yield alkenes, which are subsequently hydrogenated to alkanes, and can also produce alcohols. Elimination of oxygen via cracking produces CO_2. These are important reactions to reduce the aromatic content and to control both the chain length and degree of branching in the biofuel product (CRA,HCR).

However, high temperatures are needed to achieve deoxygenation, and this increase the cracking rate, leading to degradation of the bio-oil to yield light gases and carbon. Nonetheless, the direct deoxygenation (DDO) and hydrodeoxygenation (HDO) reactions eliminate oxygen as water, and retain all carbon atoms from the original bio-oil. All these reactions are important for the total deoxygenation process, which can be considered as the sum of the individual reactions. This span of potential reactions make evaluation of bio-oil upgrading difficult and such evaluation often restricted to model compounds, as described in greater detail below. But above all these routes, HDO is the preferred one because of its ability to reach high conversion of oxygenated compounds to hydrocarbons with no CO_2 emission as well as its technological compatibility with conventional hydrotreating technology [62].

HDO is therefore evaluated in the present thesis as being a path to fuels in a grade and at a price equivalent to present fossil fuels. However, several tasks that will be discussed below still have to be addressed within this process [51].

1.4.1. HDO process

The removal of oxygen from pyrolysis oil by catalytic reaction with hydrogen is called hydrodeoxygenation (HDO). This is a typical hydrolysis reaction, where the carbon-oxygen bond is cleaved with hydrogen in the presence of a catalyst. All the reactions shown in Figure 1.7 are relevant for HDO but the principal reaction is, as the name implies, the hydrodeoxygenation. Simplifying the overall reaction stoichiometry can be represented by equation down below, where CH_2 refers to unspecified hydrocarbon products [63]. The overall thermochemistry of this reaction is exothermic and simple calculations have shown an average overall heat of reaction in the order of 2.4 MJ/kg when using bio-oil [64].

$$CH_{1.4}\,O_{0.4} + 0.7\,H_2 \rightarrow CH_2 + 0.4\,H_2O$$

Water is formed in the conceptual reaction, so (at least) two liquids phases will be observed as product: one organic and one aqueous. The appearance of two organic phases has also been reported due to the production of organic compounds with densities lower than that of water. The formation of two organic phases is usually observed in instances with high degrees of deoxygenation, which will result in high degree of fractionation in the feed [58].

Due to the similarity with hydrodesulfurization (HDS) and hydrodenitrogenation (HDN), well-studied processes in the petroleum industry, much of the knowledge has been extrapolated from HDS and HDN experience with common cobalt-molybdenum, nickel-molybdenum and their oxides on silica and alumina supports [50, 59, 65]. According to Furimsky [60], the relative heteroatom removal takes place in the order of HDS > HDO > HDN.

Regarding operation conditions, HDO is carried out at elevated temperatures (523-723 K [51, 66, 67] and high pressures (7.5-30 MPa) [41, 51] and a typical range of liquid hourly space velocity of 0.1-1.5 h^{-1}. The high pressure ensures higher solubility of the hydrogen in the pyrolysis oil. Thereby more hydrogen will be available in the vicinity of the catalyst which will enhance the complete hydrogenation of unsaturated hydrocarbon products [67].

Typically, HDO is carried out in two stages as a result of the different reactivity of the molecules and groups present in pyrolysis oil [25, 50, 60]. The first stage is the so-called stabilization stage and is performed below 573 K. This mild hydrotreating step converts reactive oxygen containing groups (for example acids) into less reactive ones (for example alcohols). In other words, the first stage produces a partially deoxygenated, stabilized bio-oil which can be used for heat and electricity generation or stored before further upgrading. Therefore, mild hydrotreating will not always result in a decrease in oxygen content, but rather increases the stability of the oil. Due to more complex bound or sterically hindered oxygen, phenols and furans have lower HDO reactivity. Therefore, the second stage is performed around 623 K to reduce the oxygen content even more, generating fully or deeply deoxygenated fuels [62].

Furimsky [60] has summarized the HDO reactivity of the oxygen groups in the tentative order as shown down below.

alcohols>ketons>alkylethers>carboxylicacids~m-phenols~

p-phenols~napthol>phenol>diarylethers~

o-phenols~alkylfurans>benzofurans>dibenzofurans

HDO reactions can occur in aqueous solvents (e.g. formic or acetic acid), in organic solvents (e.g. tetralin) and in a hydrogen gas atmosphere such as the case of the present thesis [42]. Another important aspect to take into account during HDO reaction is the hydrogen consumption. Hydrogen has two effects in the upgrading of pyrolysis oil: removing oxygen (decreased O/C ratio) and saturating double bounds (increased H/C ratio). Venderbosch *et al* [58] investigated the hydrogen consumption as a function of the deoxygenation rate over a Ru/C catalyst in a fixed bed reactor at 448-673 K and 20-25 MPa. From the experiments, it was clear that the hydrogen consumption increased markedly as a function of the deoxygenation rate. This is the consequence of the different reactivity of the compounds in pyrolysis oil. Highly reactive compounds, such as ketones, are easily converted with low hydrogen consumption. The more stable compounds, such as furans, are first saturated resulting in higher hydrogen consumption at complete deoxygenation. The effect of the degree of deoxygenation (and consequently the hydrogen consumption) on the oil yield was investigated by Samolada *et al* [68] on a Co-MoS_2/Al_2O_3 catalyst. The oil yield decreased as a function of the deoxygenation, which is due to increased water and gas yields. This shows that when harsh conditions are used to remove the

oxygen, a significance decrease in the oil yield occurs. Therefore it is important to evaluate to which extent oxygenates should be removed [51, 68].

1.4.2. Model compounds

The complexity of lignocellulosic biomass, and consequently of fast pyrolysis oil, have prompted the use of several simplified model compounds to study hydrodeoxygenation. These model compounds contain linkages and functional groups that resemble those found in lignocellulosic biomass allowing observation of individual bond cleavage. The removal of oxygen implies breaking several chemical bonds. Often only one type of functional group is contained in a representative compound, simplifying the analysis of the reaction pathways and products identification and quantification. Figure 1.8 shows the most representative model molecules employed in HDO studies of transition metal phosphides [69-73] , among which dibenzofuran (DBF) and phenol (PH) have been tested in the present thesis.

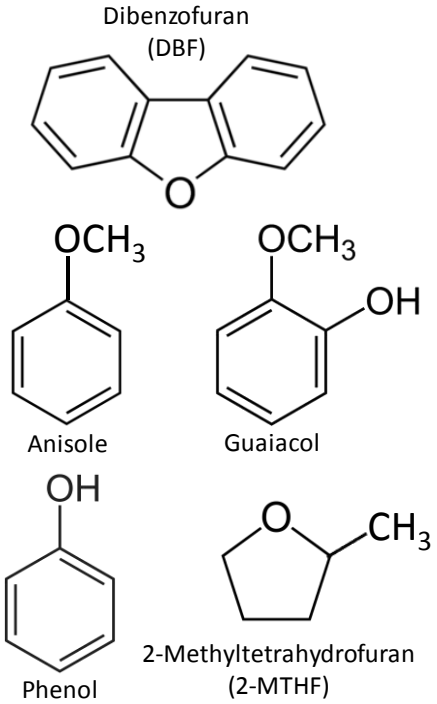

Figure 1.8. Chemical structure of the most studied bio-oil model compounds

Therefore, while real bio-oils provide the true test for HDO process development, model compounds research can elucidate more complicated kinetic mechanisms associated with degrees of deoxygenation, bio-oil component interactions, catalysts suitability and the inherent reasons of coke formation/catalyst deactivation [42].

1.4.3. HDO of phenol

Phenols or phenolic compounds are commonly studied model compounds due to their relatively high presence in pyrolysis oil (up to 55 vol%) [74] and their low HDO reactivity, as abovementioned [42, 60]. Table 1.4 shows the bond dissociation energy of several bonds present in model compounds. Due to the higher bond strength of oxygen attached to the aromatic ring compared to that of oxygen attached to an aliphatic carbon, the elimination of oxygen from phenolic compounds will be more difficult.

Phenol is the simplest monomeric model compound and has attracted considerable attention since it contains a hydroxyl group and a benzene ring, both characteristic of typical lignin-derived compounds [75]. Since phenol and its derivatives are formed as intermediates in the reactions of more complicated lignin-derived model compounds, it is important to understand their reaction network.

Table 1.4. Bond dissociation Energies [60]

Chemical bond	Dissociation Energy ($kJ \cdot mol^{-1}$)
RO-R	339
R-OH	385
RO-Ar	422
Ar-OH	468

The HDO of phenol proceeds through three distinct pathways which are direct deoxygenation route (DDO) [76], hydrogenation-dehydration route (HYD) [77] and tautomerization-deoxygenation route [78], as seen in Figure 1.9. Reaction pathway (1) involves a direct scission of the $C_{AR}(sp^2)$-OH bond by hydrogenolysis to give benzene and water. Partial hydrogenation of benzene yields cyclohexene, which is further hydrogenated to cyclohexane. In the alternative reaction route (2), the aromatic ring is partially hydrogenated to 1-hydroxy-cyclohexene, which is a tautomer of cyclohexanone. Further hydrogenation of 1-hydroxy-cyclohexene results in the formation of cyclohexanol. The hydroxyl group on cyclohexanol can be removed through dehydration, and further hydrogenation is needed to produce cyclohexane. Cyclohexanol can be converted to cyclohexane in one step through hydrogenolysis. The third pathway (3) involves firstly the keto-enol tautomerization of phenol into 3,5-cyclohexadienone. The formation of this highly unstable keto compound will cause its facile C=O hydrogenation and its subsequent dehydration to form a deoxygenated aromatic compound [79].

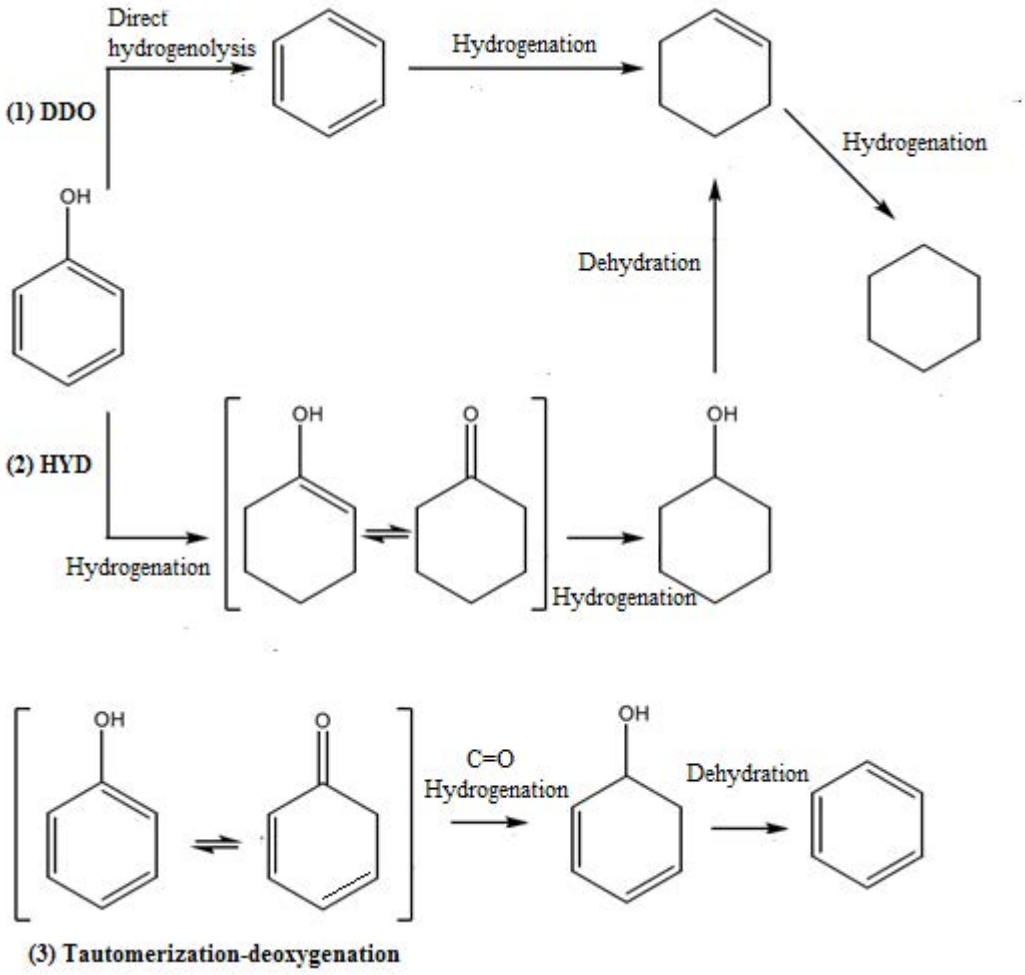

Figure 1.9. Proposed reaction pathways of phenol HDO [47, 79]

1.4.4. HDO of dibenzofuran

Dibenzofuran was also chosen as a model molecule since furanic compounds are some of the oxygenated compounds commonly found in bio-oil as the dehydration products of cellulose and hemicellulose fragments [80]. Although dibenzofuran has not been identified in bio-oil, it contains functional groups resembling those of furans and ,therefore, is among the lowest reactive compounds as classified by Furimsky [60]. The HDO of DBF is more difficult than that of benzofuran and furan due to the high energy bond C_{AR}-C_{AR} bond between two benzene rings. Indeed, the established order of resonance energy: dibenzofuran> benzofuran>furan, indicates that DBF is the most stable and unlikely to be deoxygenated as compared with benzofuran and furan [60].

The HDO of DBF can proceed via three routes as seen in Figure 1.10: hydrogenation (HYD) route (1) involves the hydrogenation of aromatic rings followed by oxygen removal yielding bicyclohexane, (cyclopentylmethyl) cyclohexane and cyclopentylcyclohexane. In reaction pathway (2) the removal of oxygen is preceded by the hydrogenation of a single benzene ring to

produce cyclohexylbenzene, whose C_{AR}-$C_{(sp3)}$ bond is further ruptured to give cyclohexane and benzene. Reaction route (3) is a direct deoxygenation pathway (DDO), involving the direct cleavage of $C_{(sp2)}$-OH to yield biphenyl which eventually yields benzene by $C_{(sp2)}$-$C_{(sp2)}$ scission [47, 72].

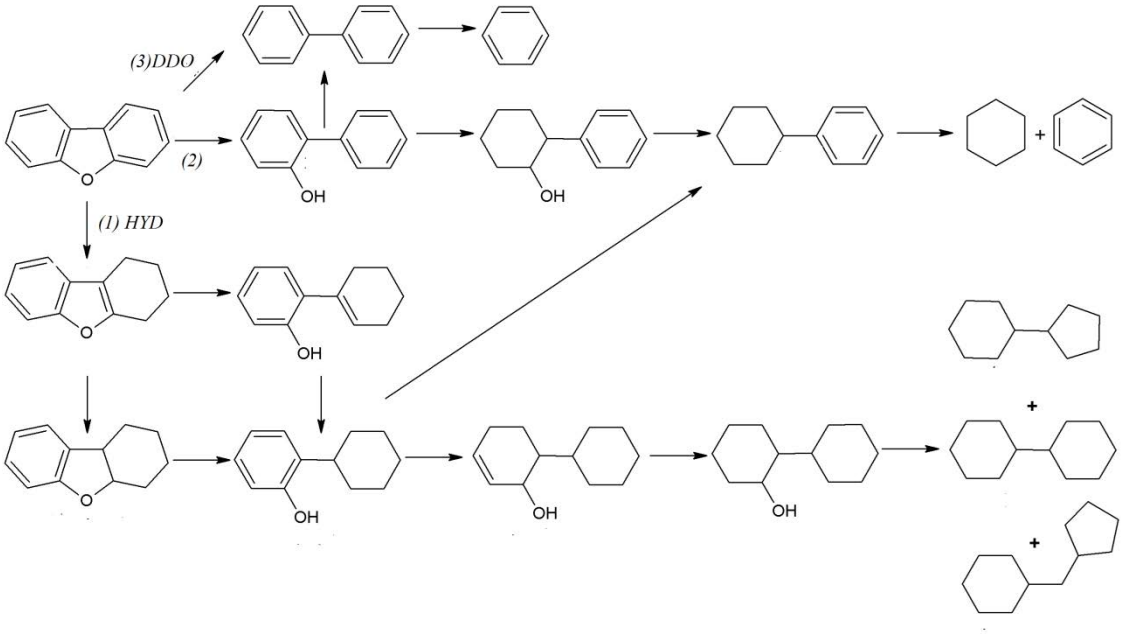

Figure 1.10. Proposed reaction pathways of DBF HDO [72]

1.5. Conventional catalysts for HDO

A great variety of catalysts has been evaluated for HDO of lignin model compounds. So far, no catalyst has dominated in terms of effectiveness [81] . Evaluation of catalyst performance considers, among others: 1) product distribution of target products, 2) reaction condition severity, 3) yield of target deoxygenated products, 4) catalyst deactivation with time on stream, 5) catalyst cost.

Catalysts types that have been investigated include metal oxides, metal sulfides, metal nitrides, metal carbides, transition metals, noble metals and metal phosphides. Some of their most remarkable characteristics and proposed mechanisms in HDO reactions are summarized hereafter; with particular emphasis on metal phosphides as these are object of study in the present thesis.

1.5.1. Transition metal sulfide (TMS) catalysts

Transition metal sulfides are used in every refinery of the world for hydrotreating of petroleum and are the most widely used catalysts in industry on the basis of materials processed per year [82]. These conventional HDS and HDN catalysts such as CoMo or NiMo supported on alumina have therefore been tested on the earliest bi-oil HDO studies due to their hydrogenation and

heteroatom removal capabilities [83-85]. In these catalysts, Co or Ni act as promoters, donating electrons to the molybdenum atoms. Promoters weaken the bond between molybdenum and sulfur and thereby generate sulfur vacancy sites (coordinatively unsaturated sites). These sites, located at the edges of MoS_2 clusters, exhibit Lewis acid character and can adsorb atoms with unpaired electrons being therefore active for C-O bond cleavage [86]. S-H$^-$ species are also present along the edge of the catalyst as these are generated from the H_2 in the feed. Similarly, these groups serve as Brönsted acid sites and donate protons to the attached molecule leading to carbocation formation. This can undergo direct C-O bond cleavage, forming the deoxygenated compound and oxygen is hereafter removed in the formation of water [87]. Mo-H and S-H Brönsted acid groups can also promote hydrogenation of unsaturated carbon bonds to generate cycloalkanes. Overall, these catalysts have shown some exciting performance in HDO processes [87, 88]. Actually, phenol, guaiacol, 2,3-dihydrobenzofuran or anisole are among the main model molecules that have been used for HDO studies on sulfide systems [89]. With respect to the support, γ-Al_2O_3 was initially investigated, although studies using CoMo sulfides supported on mesoporous silicates showed comparatively a much higher catalytic activity [90]. Indeed, the catalytic performance of TMS was found to be strongly influenced by the support morphology, among other properties. For CoMo sulfides, the most effective catalytic behavior was displayed on the cubic mesoporous silica support SBA-16 [90].

However, it is important to point out that during prolonged operation a decrease in activity can occur due to transformation of the catalyst from a sulfide form to an oxide form. In order to avoid this, co-feeding H_2S is necessary to regenerate the sulfide sites and stabilize the catalyst [88, 91]. However, an excessive amount of sulfide deactivates catalysts by decreasing the average degree of active site reduction and the vacancies for hydrogenolysis and hydrogenation of lignin-derived molecules [92] . Furthermore, these catalysts are susceptible to trace amounts of water suffering deactivation by carbon deposition [93]. Risk of sulfur contamination in the final product is another disadvantage that has also been considered to state that these catalysts are not likely to be suitable for HDO of lignin-derived bio-oils [94].

1.5.2. Noble metals

Noble metals have been widely studied for HDO processes because of their efficiency in activating molecular hydrogen [95], their stability and water resistance [96]. In general, noble metals can effectively catalyze oxy-compounds in a hydrogen atmosphere under less severe conditions than other metals [95]. Concerning the HDO over noble metal supported catalysts, it is generally accepted that H_2 is adsorbed, activated and split on the noble metal sites and the hydrogen atoms react with lattice oxygen within the support material to create water and generate oxygen vacancies. Oxygen-containing molecules from lignin-derived bio-oils are adsorbed into the oxygen vacancies and additional hydrogen atoms cleave the C-O bonds in the

adsorbed oxy-compounds. Finally, the deoxygenated molecules desorb from the oxygen vacancies and new oxy-compounds in the feed take their place.

Several nanostructured noble metals, including rhodium [97, 98], ruthenium [99, 100], platinum [101, 102], palladium [103, 104] and bimetallic combinations [105] have been proposed for HDO studies showing some outstanding results. In particular Pt, Pd and Rh supported on zirconia have been reported to present catalytic activities higher than conventional CoMo sulfides supported on alumina [98], with the least carbon deposition observed for Rh, and the highest activity achieved with Pd.

In general, regardless of the support, it is also important to highlight the capacity of Pt on oxygen removal from pyrolysis oil, which is found more effective than NiMo and CoMo sulfide catalysts under the same HDO conditions [89].

In brief, supported noble catalysts are superior to conventional catalysts based on yields, selectivity for desirable products, and the amount of carbon deposition during HDO processes. However, they present several disadvantages such as high costs [106], limited availability, high hydrogen consumption due to high hydrogenation activity, and less resistance to poisoning (iron or sulfur) than conventional sulfide catalysts [96].

1.5.3. Transition metals and metal oxides

Nanostructured metallic systems based on non-noble transition metals and metal oxide catalysts have attracted attention because of their lower costs, higher material availability, and higher selectivity to some desired products compared to noble metals catalysts [107]. Mechanistic speculations for these systems have indicated that the catalysts should be bifunctional, which implies two aspects. On the one hand, activation of oxy-compounds is needed, which likely could be achieve through the valence of an oxide form of a transition metal or on an exposed cation, often associated with the catalyst support. On the other hand, hydrogen donation to oxy-compounds could take place on transition metals, as they have potential to activate hydrogen [108].

Iron, nickel, molybdenum, cobalt, copper, tungsten and boron have been the most commonly studied metals for HDO of lignin-derived molecules with some good results [109].

Among all these, Ni has proved by far to provide the best catalytic performance, which has been demonstrated to be radically affected by the nature and properties of the support, as similarly observed for noble metals. In that sense, oxides appear as the most adequate supports for metal Ni catalysts used in HDO of bio-oil model molecules [75, 110, 111]. Especially good performance for HDO of phenol has been reported on Ni using ZrO_2 as support. Comparatively, meaningless activity was obtained with Ni supported on amorphous carbon (AC) at similar

conditions [75]. However, a negative effect of carbonaceous supports on the HDO catalytic performance of Ni cannot be generalized, since up to 100% conversion of a different model molecule (guaiacol) has been reported using Ni supported on carbon nanotubes (CNT) [112]. The oxide form of Ni has also been studied for HDO purposes [113]. Molybdenum oxides have also been significantly assessed for HDO purposes, alone or combined with other oxides like NiO [113, 114]. Concretely, Moberg et al.[115] studied MoO_3 as catalyst for HDO on the basis of density functional theory (DFT) calculations. These calculations highlighted that for oxide catalysts the activity partly rely on the availability and strength of the Lewis acid sites on the catalyst.

1.5.4. Transition metal carbides and nitrides

Transition metal carbides (TMCs) and nitrides (TMNs) have activities for HDO reactions similar to noble metals [116]. Their low hydrogen consumption, acidic and basic properties, resistance to oxidation, low cost and ease of preparation has drawn considerable attention for catalytic HDO of lignin-derived bio-oil. On the surface of TMCs and TMNs, hydrogen is adsorbed and activated by the unsaturated transition metals. Oxygen atoms within the lignin-derived oxy-compounds simultaneously attach to the C or N sites; this attachment cleaves C-O bonds through hydrogenolysis with the activated hydrogen, resulting in removal of oxygen and formation of water [117].

It is important to highlight the capability of transition metal carbides to exceed the catalytic activity of Pt-group metals (PGMs) for hydrogenation and dehydrogenation reactions [118]. Especially relevant are Mo and W carbides, which have been the most studied for HDO reactions [119, 120]. The carbon from the carbide seems to induce an enhancement in the surface reactivity of the transition metal, which at least in the case of W and Mo has been reported to approach that displayed by PGMs [121]. Indeed, high conversion values have been reported for HDO of model bio-oil molecules using W and Mo carbides [122-124]. However, formation of oxygenate species on the catalyst surface has been claimed to substantially prevent hydrogenation, leading to high selectivity toward aromatic compounds instead of forming the most convenient saturated hydrocarbons. In that sense, W shows stronger oxygen affinity and thus forms a stronger W-O bond compared with Mo [124].

Regarding the interest in the nitrides of transition metals, it arises from their bifunctionality created by the coexistence of acid and basic sites as a result of the significant difference in the electronegativity between the nitrogen and the metal. Although nitrides are scarcely studied, some interesting results, especially on Mo nitride catalysts, can be found [125, 126].

1.6. Transition metal phosphides

Transition metal phosphides have structural aspects and properties in common with sulfide, carbides and nitrides based catalysts [89, 127, 128]. However, the phosphide catalysts generally exhibit a catalytic activity higher than that found for equivalent HDO reactions using the abovementioned conventional catalysts. Beyond the similarities shared by those transition metal-based compounds, the phosphide systems present structural singularities which bestow them unique catalytic reactivity, among other properties.

1.6.1. General properties of metallic phosphides

Phosphorus reacts with most elements of the periodic table to form a diverse class of compounds known as phosphides. The bonding in these materials ranges from ionic for the alkali and alkaline earth metals to metallic or covalent for the transition metal elements and covalent for the main group elements. They can be classified according to their stoichiometry as:

- Metal-rich phosphides (M/P>1)
- Monophosphides (M/P=1)
- Phosphorus-rich phosphides (M/P<1)

Of them all, transition metal phosphides, MP or M_2P, have shown useful properties in hydrotreating reactions. These phosphides have physical properties similar to those of ordinary metallic compounds such as carbides, nitrides, borides and silicides. Thus, they present good metallic and ceramic properties, being therefore, good conductors of heat and electricity, are hard and strong, and have high thermal and chemical stability [129]. Conversely, the phosphorus-rich phosphides are semiconductors and considerably less stable than the metal-rich compounds. Table 1.5 [130] presents the ceramic and metallic properties of the metal-rich phosphides.

Table 1.5. Metallic and ceramic properties of metal-rich phosphides

Metallic properties		**Ceramic properties**	
Electrical resistivity (μΩ·cm)	900-25000	Melting point (K)	1100-1800
Magnetic susceptibility (10^6 emu·mol)	110-620	Microhardness ($kg \cdot mm^{-2}$)	600-1100
Heat capacity ($J \cdot mol^{-1} \cdot K^{-1}$)	20-50	Heat of formation ($kJ \cdot mol^{-1}$)	30-180

The nature, structure and synthesis of phosphides have been described in a number of reviews [131-133]. They highlight that although the physical and chemical properties of phosphides resemble those of carbides and nitrides, they differ substantially in their crystal structure. In the carbides and nitrides, the carbon and nitrogen atoms reside in the interstitial spaces between metal host atoms to form relatively simple lattices: face-centered cubic, hexagonal close-packed, or simple hexagonal. For these compounds, geometric considerations predict stable structures when the ratio of nonmetal (X) to metal (M) (rX/rM) is between 0.41 and 0.59 [134]. For the phosphides, however, the atomic radius of phosphorus (0.109 nm) is substantially larger than that of carbon (0.071 nm) or nitrogen (0.065 nm) and the radius ratio is too large for octahedral coordination around the nonmetal to be favorable. For this reason, in phosphides (as well as in borides and silicides), the nonmetal atom is usually found at the center of a trigonal prism where the metal atoms surround the phosphorus atoms as seen in Figure 1.11 [133, 135]. The latter structure favors more isolation for the non-metallic atom which results in poor P-P interactions into a lattice where metal-metal lengths are found within metallic and covalent bond ranges. Thus, metal-rich TMPs are majorly governed by the metal atoms arrangement which can reach up to 9 metal ligands around the phosphorus in a tricapped trigonal prismatic coordination [131].

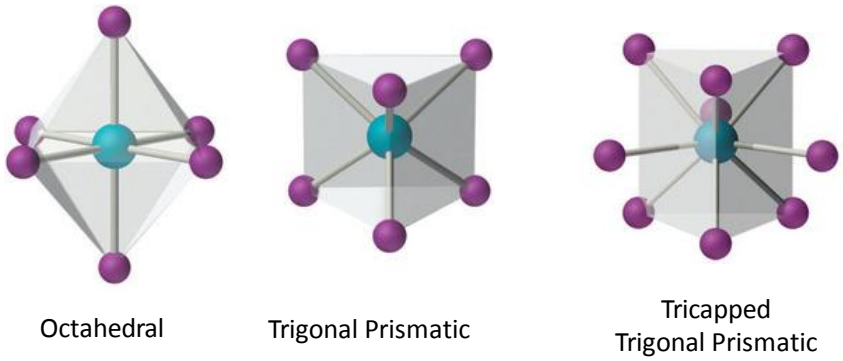

Figure 1.11. 3-D representation of the different geometries in TMP

Metal-metal interactions gain increasing relevance as the metal/phosphorus ratio in the global lattice increases, leading to higher electron delocalization in the metal sublattice of the phosphide. As abovementioned, sulfides also present trigonal prisms as basic crystallographic structures. However, unlike sulfides whose triangular prism units are arranged forming layers in sulfides, in phosphides, those building blocks can grow in all directions forming three-dimensional structures. Consequently, the phosphides present a greater amount of surface atoms without saturated coordination and so, potentially permit greater access to active corner and edge sites on the crystallite surfaces [135]. The globular morphology of Ni_2P and MoP has been demonstrated by electron microscopy [136, 137]. Different arrangements of these building blocks give rise to different structures as compiled in Figure 1.12 [138].

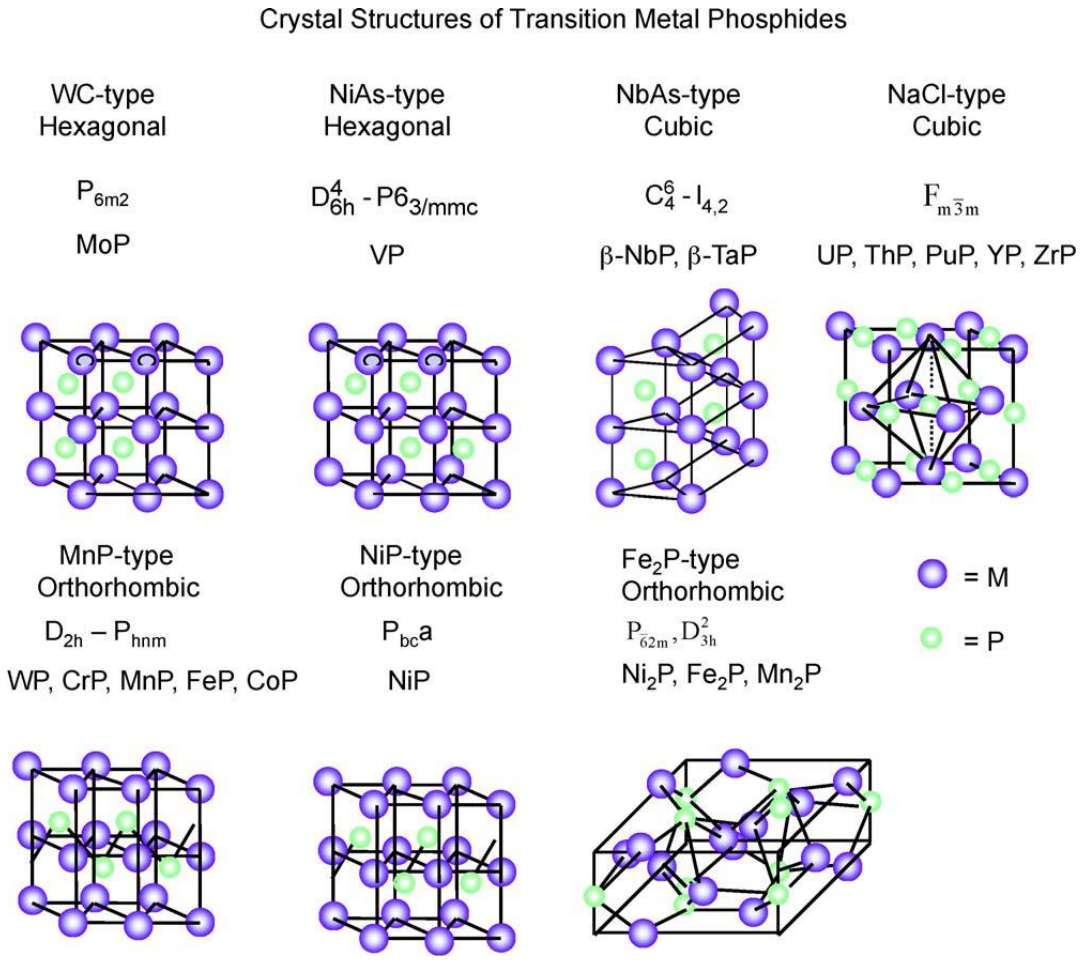

Figure 1.12.Crystallographic structures of more common TMPs [131, 138]

The monophosphide MoP is isostructural with WC, with the nonmetal-containing prisms stacked on top of each other. VP presents the Ni-As structure with the P-prisms displaced laterally one-half a lattice spacing. The monophosphides NbP and TaP adopt the closely related NbAs structure, which just differs from VP in the way the prisms are stacked. The monophosphides of elements of groups 6-10 adopt the MnP and NiP structures which have disorted NiAs structures where the phosphorous atoms form chains (MnP) or pairs (NiP). The structure of Ni_2P and Fe_2P is orthorhombic, with two different types of metallic sites in its unit cell (M-I and M-II) and another two for phosphorus (P-I and P-II) giving rise to different trigonal prisms [139] as seen in Figure 1.13. Although the number of M-I and M-II sites in the unit cell is the same, they present different coordination environments. M-I site is coordinated to four phosphorus atoms with a quasi-tetrahedral structure and to eight metal atoms further away. M-II site is coordinated to five phosphorus atoms with a pyramidal disposal and to six metal atoms [131].

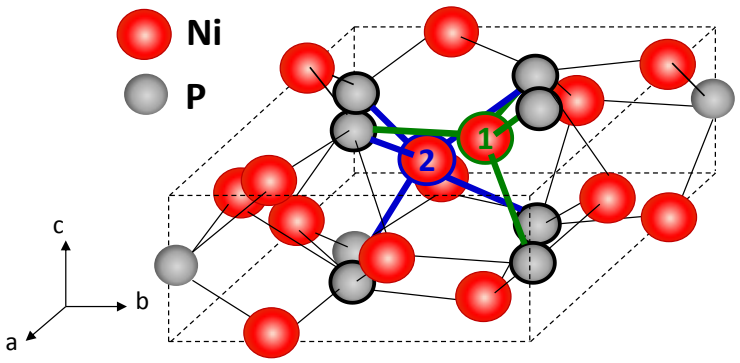

Figure 1.13. Unit cell of Ni_2P structure with coordinations highlighted in green and blue

1.6.2. Synthesis

The synthesis of transition metal phosphides has been carried out by numerous synthetic strategies that are collected in Table 1.6.

Table 1.6. Strategies for the synthesis of TMPs

Method	Reaction
Combination of a metal (M^0) with phosphorus (P^0) [140, 141]	$M^0 + xP^0$ (red) → MPx
Metathesis [129, 142]	MClx + Na_3P → MP + NaCl
Chemical transport [143]	MOx + Al + P^0 (red)→ MPx + Al_2O_3
Molten salt electrolysis [144]	MOx + NaPOy → MP + H_2O
Deprotonation of phosphides [145]	MP_2 + M → 2MP
Vapor deposition of organometallic precursors [146]	$TiCl_4(PH_2C_6H_{11})_2$ → TiP + PH_3 + HCl+ C_6H_{10}
Reduction of phosphorus oxidized species [147, 148]	MPOx + H_2 → MP + xH_2O MPOx + CH4 → MP + xCO_2
Reactions with PH_3 [149]	MOx + PH_3 → MP + H_2O
Solvothermal synthesis [150]	MClx + xP^0 (red) → MPx + HCl MClx + PCl_3 + Na → MPx + NaCl

Many of these synthetic methods are not practical for catalytic purposes since high temperatures and expensive precursors (source materials) are required. Not to mention the obtainment of complex species that can pollute the final product.

Among all the proposed synthetic routes, transition metal phosphides can be easily synthetized by means of hydrogen thermo-programmed reduction of a transition metal phosphate as extensively described by Oyama [135, 151-153], Bussel [136, 137, 154, 155], Wang [156, 157] and Prins [158]. This is a very simple method that only requires moderate temperatures (773-873 K) and the use of low cost precursors. The reduction process in the presence of hydrogen has been described thoroughly in various publications. During the first stage the transition metal is reduced from M^{n+} to M^0 whereas phosphorus is reduced from its form PO_x^{n-} to PH_3. In the last stage, the transition metal reacts with phosphine giving rise to the corresponding phosphide, $M^0 + PH_3 \rightarrow$ MxPy. In the present thesis, all the phosphide type catalysts have been synthetized by a variant of this method developed by the group of Jiménez-López [70]. In this new method, the starting material is a phosphite precursor that avoids a further calcination step simplifying the procedure and minimizing the synthetic cost, accordingly.

Currently, the scientific community is developing new synthetic methods that allow working under lower temperatures and yielding TMPs with lower particle sizes and higher dispersions such as: plasma reduction, sonochemical reactions, dispersive agents assisted synthesis, new sources of phosphorus such as tri-octylphosphine (TOP) forming metal complexes (TOP+MX→ M-TOP) [159].

1.6.3. Phosphides in HDO

Metal phosphides have been extensively studied as catalysts for HDN and HDS [131, 135, 160, 161], but only recently have their deoxygenation properties attracted scientific and technological attention. As reported in literature, the oxygen-containing molecules present in bio-oil can be readily removed via these types of catalysts due to ensemble and/or ligand effects of phosphorus. Thus, the main active phases for TMPs during HDO are metallic sites which are responsible of H_2 activation and acid sites for activation of oxygenated compounds. $M^{\delta+}$, which stands for a transition metal bearing small positive charges, acts as Lewis acid site participating in hydrogenation, hydrogenolysis and demethylation reactions [81, 162]. Incomplete reduction of phosphate species results in Brönsted acid sites, P-OH groups, that donate active hydrogen species, but they are less active as compared to metal sites since the higher *d* electron density is beneficial for a better activity. Based on the literature [162], the mechanism of HDO over TMPs without considering the support contribution is proposed in Figure 1.14.

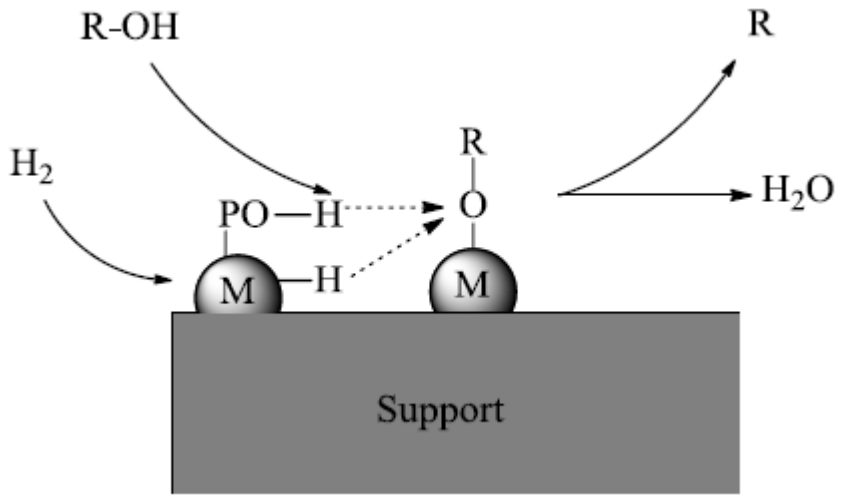

Figure 1.14. Proposed HDO mechanisms over TMPs [62, 162], where M stands for metal.

Oxy-compounds and adsorbed H_2 are activated on the $M^{\delta+}$ sites, and H atoms from both $M^{\delta+}$ and P-OH sites react with the adsorbed oxy-intermediate species producing deoxygenated products.

A wide variety of TMPs has been recently studied in HDO reactions, including Ni_2P, CoP, WP, MoP, FeP, Ru_2P and RuP. Among all, nickel phosphide catalysts, especially those based on Ni_2P, have been reported to be the most promising catalysts for bio-oil upgrading owing to its high activity, superior selectivity, and good stability under hydrotreating conditions [61, 163].

However, it must be pointed out that quantitative comparison of the catalytic activity among HDO catalysts is not straightforward, due to the strong influence, on the results, of many factors which are not kept constant between the different studies. Among these factors is the large number of model molecules, with even different nature, that can be used, or the different and complex composition when comparing actual bio-oil samples. Other important parameters are the support, or the H_2 pressure employed in the catalytic studies which can be found varying within a large range, from atmospheric pressure up to 90 bar. Moreover, the contact time has been proven to strongly influence either the catalytic conversion or the distribution of products, with even a different trend depending on the transition metal phosphide employed as catalysts [164]. The P/Metal molar ratio introduced in the synthesis of TMPs is another parameter to take into account [69]. These are just some of the most representative factors affecting the catalytic behavior, which might present, in turn, interdependencies between them. Most of the times, it is not possible to find the impact of a certain parameter studied for all of the main TMPs.

1.6.4. Nickel, cobalt and iron phosphide catalysts for HDO

As already justifiably discussed above, most of the HDO studies use model samples consisting of only one type of bio-oil representative O-containing molecule. Nevertheless, the effectivity for oxygen content reduction of actual bio-oil samples over Ni_2P based catalysts has also been assessed [165-167]. In this respect, reductions of oxygen content to about half compared to the original levels in pyrolysis bio-oil samples have been reported using Ni_2P catalysts, with catalytic activities, at moderate temperatures (573-623 K) under atmospheric H_2 pressure, exceeding those of nanostructured metal based catalysts such as Ni/SiO_2 or Pd/C, and other commercial catalysts for fluid catalytic cracking (FCC) [167]. In that sense, the presence of phosphorus in Ni-P catalysts has been confirmed to enhance the deoxygenation activity over the cracking activity, the latter leading to lighter hydrocarbons. Cracking activity is practically suppressed on Ni_2P, while comparatively favored in nanostructured Ni metal catalysts [167, 168]. Beyond hydrodeoxygenation and hydrogenation reactions, decarbonylation and hydrolysis have also been experimentally confirmed to occur during bio-oil upgrading employing Ni_2P based catalysts [167].

Furthermore, the superior catalytic behavior of Ni_2P phase has been related to the intrinsic greater presence of P-OH species that is suggested to prevent metal phase oxidation, in turn acting as weak acid sites which can easily react with O-containing species. In addition, P-OH surface species can also act as H-donors to carry out hydrogenation reactions [130, 135, 158], while spillover species would be responsible for cleaning the surface of carbon deposits avoiding deactivation. Anyway, slight deactivation gradually increasing with reaction time has been observed by coke formation on the surface of SiO_2-supported Ni_2P catalysts for HDO of real bio-oil streams [167].

Another factor influencing the size and morphology of Ni_2P crystallites is the nature of the material employed to support them. As a case in point, smaller Ni_2P clusters are reported to be formed on SiO_2 compared with using ZrO_2 and Al_2O_3 supports, leading to a higher activity in H-transfer processes for the SiO_2-supported catalysts [169]. Accordingly, although the initial trend of intrinsic activity dependent on the support, measured for atmospheric HDO of guaiacol as model molecule, was $Ni_2P/SiO_2 < Ni_2P/Al_2O_3 < Ni_2P/ZrO_2$, after the first hour of on-stream reaction, the situation turned over. Henceforth, the higher activity was obtained on the Ni_2P/SiO_2 catalyst which was suggested to be due by a low coke accumulation on the SiO_2-supported catalysts, as well as to a better maintenance of a fully phosphide state favored by a phosphorus excess most likely acting as a reservoir for replenishment of the Ni_2P active phase. Despite the value of absolute catalytic activity, the influence of the support in the catalyst performance of the active phase has proved to exhibit an important role in the hydrodeoxygenation pathway, significantly influencing the selectivity. Thus, depending on the

properties of the support, different reaction pathways are favored, consequently providing distinct distribution of products [169, 170]. As a representative example it is worth to mention the formation of benzene as major product in HDO of the model molecule anisole using Ce_2O as Ni_2P support. The high selectivity to the aromatic product was related to the support-induced electron enrichment of $Ni^{\delta+}$ surface sites that favored the easy desorption of the deoxygenated product (benzene) once formed over the active phase surface. Different reaction routes were also reported to be favored in HDO of guaiacol using Ni_2P supported on ZrO_2, Al_2O_3 or SiO_2 [169]. Among them, SiO_2 was found to promote the most desired direct deoxygenation. Taking into account the additional advantages discussed above, it is not a coincidence that Si_2O is used as a support by default in most of the studies on the parameters influencing the HDO catalytic performance of Ni_2P. Nevertheless, substrates other than Si_2O have been reported to present additional benefits for the HDO catalytic behavior of Ni_2P, eg. using ZSM-5 as support was proved to provide removal of oxygen with higher oil yield compared to SiO_2 under equivalent reaction conditions [167]. Anyway, the nature of the model bio-oil molecule must be also taken into account to consider the eventual effect of the support.

The effect of employing phosphate or phosphite species as phosphorus precursors on the catalytic activity of resulting SiO_2-supported Ni_2P catalysts has also been studied in detail [171]. The standard phosphate method used Ni(II) nitrate and $(NH_4)_2HPO_4$, while $Ni(OH)_2$ and H_3PO_3 were employed for the phosphite method. Selectivity and turn over frequency did not change regardless of the method. However, the total conversion was higher for the catalyst derived from the phosphate, while the opposite was found for the conversion to HDO products, with an 81% vs. the 85% reached on the phosphite-derived catalyst, at 548 K and 1 atm. Furthermore, the catalysts obtained from the phosphite showed around 23% higher surface area (ca. 220 $m^2\ g^{-1}$) and required reduction temperature 30 degrees below that for the corresponding phosphate derived ones.

Cobalt and iron are among the main transition metals other than Ni that form phosphides worth to mention as investigated catalysts for HDO of bio-oils. However, the use of Fe or Co phosphides in the hydrotreating field has been scarce. Zhao et al [73] studied a series of TMPs supported on mesoporous silica in the HDO reaction of guaiacol where the catalytic activity followed the order: Ni_2P>Co_2P>Fe_2P~WP~MoP. Similar results were obtained by Bui et al. [70] in the HDO of 2-methyl-tetrahydrofuran, revealing that CoP phase exhibited a remarkable performance. Cobalt and nickel phosphides supported on silica with a metal loading of 5 wt% were also evaluated in the HDO of DBF at different contact times, H_2 pressures and H_2/DBF molar ratios. Once again, the Ni_2P phase was identified as the most effective catalyst regardless of the operating conditions [72]. More recently, Yuan et al. [172] evaluated the catalytic behavior of FeP and Fe_2P in the HDS of dibenzothiophene, HDN of quinoline and

hydrogenation of tetralin to decalin, obtaining the highest conversions for the FeP based catalysts.

Several studies have also revealed that the incorporation of a second metal into the structure of Ni_2P may provide an enhanced effect on the catalytic properties [173]. In that regard, bimetallic phosphides such as NiCoP and NiFeP have been tested in hydrotreating processes [174, 175]. These researches revealed that the addition of a small amount of Co or Fe to the Ni_2P phase improved the HDO activity of these catalysts, confirming the existence of a synergistic effect between Co, Fe and Ni. Gaudette et al. [176] studied the iron contribution on nickel and iron mixed phosphides. As previously stated in section 1.6.1, Fe_2P and Ni_2P adopt orthorhombic structures with two different metallic coordination sites, M-I and M-II. In unsupported mixed phosphides, Fe preferably occupies M-II sites when it is the majority metal and M-I sites when Ni is in a greater proportion in the mixed phosphides. When supported on SiO_2 and doped with small amounts of iron, it preferably occupies M-I sites, whereas Ni equally occupies M-I and M-II sites. Similarly, Zhao and Oyama [177] studied the nature of the active sites of Ni_2P phase substituted with Fe in the HDS of 4,6-DMDBTF by CO adsorbed infrared spectroscopy, concluding that Fe acts as an electron donor to Ni [178]. They also observed that the incorporation of Fe into Ni_2P slightly decreased the catalytic activity but remarkably increased selectivity to direct desulfurization (DDS), which was associated to the presence of Ni in M-I sites. In view of these results, one of the objectives of the present thesis is to evaluate the effect of adding different amounts of Fe to Ni_2P supported on SiO_2 via the phosphite procedure.

Finally, the effect of Ni loading (from 2.5 to 10 wt.%) in SiO_2-supported Ni_2P catalysts, as well as the influence of the nominal P/Ni ratio in the synthesis for a constant intermediate load of Ni (5 wt.%), were also studied for the HDO of dibenzofuran employing the improved method based on phosphite precursor [69]. Increasingly Ni loadings brought about an enhanced HDO conversion until the sample with 7.5 wt. % from which higher Ni content led to lower catalytic activity. The surface density of acid sites (Brönsted and Lewis), considered as the active sites for hydrogenolysis and hydrogenation processes in HDO reaction [162], increased either with greater Ni loadings or higher P/Ni synthesis ratios. These results were consistent with previous works assigning the presence of acid sites in the final catalysts to either phosphate species incompletely reduced [174, 179] or Ni species undergoing high electron transfer to phosphorus [162]. On the other hand, better dispersion of the active Ni_2P phase, with smaller particle size, was induced by lower Ni loading on the SiO_2 support, as well as by excess of phosphorus in the synthesis, i.e. high P/Ni ratios. Indeed, a phosphorus excess has been reported to favor the formation of the $Ni(HPO_3H)_2$ precursor for the Ni_2P active phase formation. Furthermore, while the SiO_2-supported Ni_2P catalyst prepared with P/Ni molar ratio of 1 undergoes a gradual deactivation from the second hour during the HDO test, those prepared with phosphorus excess

(P/Ni ratios of 2-3) displayed high stability with no deactivation for the time tested (12 h) at 300 ºC bellow $4 \cdot 10^4$ ppm of reactant feed concentration.

Taking into account these findings, although there are some reports concerning the catalytic behavior of cobalt and iron based phosphides, none of them has focused on the effects of the stoichiometry of the phosphide in HDO reactions, which is another of the objectives of the present thesis.

1.7. Future work to develop in HDO

As abovementioned, there are still many barriers that HDO has to face before consolidating as an established technology as in the case of HDS and HDN. The main challenges can be summarized as follows:

1. HDO processes presents high costs and low hydrogen efficiency.
2. The production of high added value chemicals is necessary.
3. Water must be removed after HDO in order to avoid catalyst deactivation.
4. HDO needs adequate and stable catalysts and catalytic systems, where noble metals are considered as a kind of efficient catalysts if their high costs are not considered. Therefore, it is essential to develop cheaper, abundant and non-toxic active phases.
5. HDO process can improve the pyrolysis oil quality, but it generally has low hydrogen utilization efficiency.

Therefore, the use of efficient catalysts is one of the key factors of pyrolysis oil upgrading. Transitional metal phosphides have proven to act like noble metals, being considered as low cost and very stable catalyst systems which can work at relatively low hydrogen pressure. Furthermore, this family of catalysts can be improved with the addition of small amounts of noble metals in order to improve their catalytic performance and with possible scale up in advanced catalytic processes.

1.8. Hydrogen as energy carrier

Addressing now the second subject matter and in response to the energetic sustainability issue raised in the beginning, the use of hydrogen as biofuel is regarded as an alternative to fossil fuels. Hydrogen is the simplest element on the earth and has the highest energy content per unit mass (141.9 MJ/kg) of any other fuel [180]. Therefore, it is expected to be one of the most important energy carriers in the near future [181]. In spite of being the most abundant element on earth, hydrogen does not occur naturally as gas and it is primarily bound into other molecules such as hydrocarbons, fats, carbohydrates or water, and its production requires either catalytic and non-catalytic processes [182].

With many alternative sources of energy becoming available, why should we focus our efforts on developing hydrogen as a source of energy? The answer is because hydrogen can be derived from many different domestic sources of energy by using a wide variety of technologies.

Generation

More than 50 million metric tons of hydrogen is yearly produced worldwide [183], mainly from fossil fuels by thermochemical processes such as steam-reforming (SR), auto-thermal reforming (ATR), thermal partial oxidation (TPOX) and gasification. It can also be obtained from electrolysis of water and from ammonia and hydrogen sulfide [184]. But, as abovementioned, most of the existing production techniques use fossil fuels either as hydrogen source or as a power source. Thus, almost 98% of the annual production of hydrogen comes from the reforming of fossil fuels, mainly from natural gas, accounting for 85% of the total hydrogen produced [184, 185]. During steam-reforming of natural gas, methane reacts with steam in the presence of a nickel catalyst to obtain H_2 and CO [186-188]. The reaction of the process is as follows:

$$CH_4 + H_2O \rightarrow CO + 3H_2 \quad AH^o = 205\ kJ \cdot mol^{-1}$$

This endothermic process is accomplished over a temperature range of 923-1223 K and pressures of 15-40 bar.

As hydrogen contains CO and other compounds, reforming is followed by the water gas shift reaction (WGS) [189]. The WGS reaction is a follow-up method which can be used to further enhance H_2 production and lower CO content in the products of all the above mentioned production technologies. The reaction takes place by mixing the CO with high temperature steam as shown in equation:

$$CO + H_2O \rightarrow CO_2 + H_2 \quad AH^o = -27\ kJ \cdot mol^{-1}$$

However, this approach is not very sustainable due to the limited availability of fossil fuels and the CO_2 production. That is why the development of efficient and environmentally compatible technologies for hydrogen production is a key step towards the generalized development of a sustainable hydrogen economy. Currently, only a small part of the hydrogen (4%) is produced from renewable sources [188]. A special interest is being focused on photochemical processes that are able of harnessing the UV or visible radiation to generate reactive species that catalyze the production of hydrogen more efficiently than the same technology in the absence of radiation [185, 188]. Biogas is also regarded as a promising option to minimize the abovementioned drawbacks because it can be produced through anaerobic digestion of organic materials and can be distributed through the existing natural gas infrastructure [190].

1.8.1. Uses

Hydrogen is used for electricity generation, chemical synthesis and transport [191]. Concretely, most of its uses include: the synthesis of ammonia, petrochemical refining, hydrocarbons purification, methanol production, hydrogenation reactions, production of synthetic fuel, carbon dioxide recycling, etc. Thus, hydrogen is not only an essential chemical compound in many industrial processes but is also considered an attractive clean energy vector for the future, specially combined with efficient fuel cells for both stationary power generation and transportation [184]. These devices transform chemical energy into electrical energy with high efficiency and practically zero emission of pollutants. That is why hydrogen is considered a good alternative to fossil fuels. However, hydrogen presents a low density (0.003 $kg \cdot L^{-1}$ at 350 atm in gaseous state and 0.0708 $kg \cdot L^{-1}$ in liquid state at -251 ºC and 1 atm) which is a significant obstacle for its storage, transport and distribution [192, 193].

Therefore, lack of efficient hydrogen storage intermediate has boosted the development of fuel processor or economic onsite hydrogen production techniques for application to fuel cell promptly.

1.8.1.1. Fuel Cells

A fuel cell is an electrochemical device that converts the chemical energy of fuel without fuel combustion into electricity, water and heat. The scheme of a simplified fuel cell is shown in Figure 1.15 [194]. It consists of an electrolyte layer in contact with two electrodes on either side. The hydrogen fuel is fed continuously to the anode electrode and the oxidant is fed continuously to the cathode electrode. At the anode terminal the hydrogen fuel is decomposed into positive and negative ions. The intermediate electrolyte membrane only permits the positive ions to flow from anode to cathode side and acts as an insulator for electrons. These electrons want to recombine on the other side of the membrane for the system to become stable, for which

the free electrons moved to the cathode side through an external electrical circuit. The recombination of the positive and negative ions with oxidant takes place at the cathode to form depleted oxidant (or) pure water. The chemical reactions involved in the anode and cathode are as follows:

Anode reaction:

$$H_2 \rightarrow 2H^+ + 2e^- \qquad \text{(Eq.1)}$$

Cathode reaction:

$$1/2O_2 + 2H^+ + 2\,e^- \rightarrow H_2O \quad \text{(Eq.2)}$$

Overall reaction:

$$H_2 + ½O_2 \rightarrow H_2O \quad \text{(Eq.3)}$$

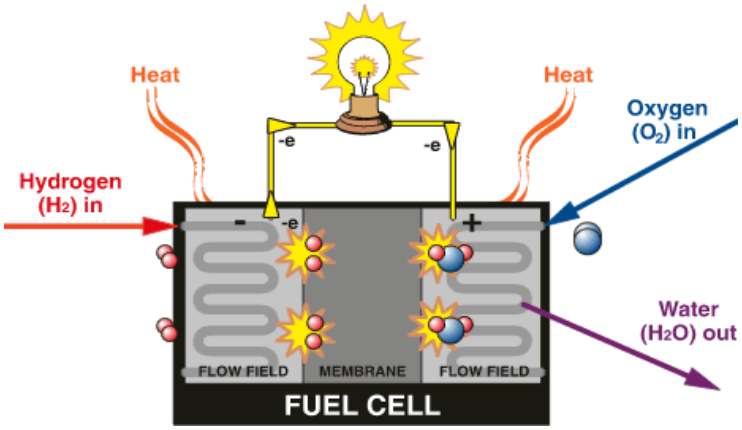

Figure 1.15. Scheme of a PEM fuell cell

As the electrochemical process takes place in a single step, fuel cell is not limited by the Carnot cycle and, therefore, its efficiency is determined by enthalpy (ΔH) and free Gibbs energy (ΔG) values of the reaction.

Advantages of fuel cells in comparison with other types of devices which are producing energy are as follows: higher efficiency, no existence of the mobile parts and as a result lack of sonic pollution, simple design that can be scaled, no emissions of environmental polluting gases such as SOx, NOx, CO_2, CO, etc. On the contrary, the main disadvantages are the high costs and the scarcity of the catalyst (normally platinum) and the poisoning of the electrodes [195].
Fuel cell systems have different variables such as type of the electrolyte, type of the exchanged ion through the electrolyte, type of reactants (e.g. primary fuels and oxidants), operating temperature and pressure, direct and indirect usage of the primary fuels in fuel cell system, etc.

But generally, they are classified and nominated based on the nature of the electrolyte [194]. Table 1.7 summarizes the fuel cells types and their most outstanding characteristic [195, 196].

Table 1.7. Fuel cell types based on the electrolyte used and operating conditions

Fuel Cell type	Electrolyte	Operating temperature (K)	Fuel	Efficiency (%)
PEMFC	Solid polymer membrane (Nafion)	323-373	Pure H_2	40-50
AFC	Liquid solution of KOH	323-473	Pure H_2	~50
PAFC	Phosphoric acid	~473	Pure H_2	40
MCFC	Lithium and potassium carbonate	~923	H_2, CO, CH_4, other hydrocarbons	>50
SOFC	Stabilized solid oxide electrolyte	1073-1273	H_2, CO, CH_4, other hydrocarbons	>50
DMFC	Solid polymer membrane	333-473	CH_3OH	40

Among them, proton exchange membrane (PEM) fuel cells, also known as polymer electrolyte membrane fuel cells (PEMFCs), have received much attention from the transportation industry to drive the first generation of hydrogen fueled vehicles. They were chosen for this application over other fuel cell designs because of their relatively low operating temperature, quick start up, short transient times and the ability to respond quickly to varying loadings, i.e. stop and go driving. In addition, a fuel cell operates far more efficiently than its internal combustion engine counterpart. The gasoline internal combustion engines that power vehicles today operate at an efficiency of approximately 25% as compared to a PEM fuel cell which can operate at around 55%

The low operating temperature of PEMFCs also makes them competitive in mobile applications like laptop computers, bicycle and mobile phones. The hydrogen used as fuel is generated on board by catalytic reforming of methanol, ethanol or biofuel [197].

PEMFCs need to be fueled with an extremely pure source of hydrogen containing less than 10 ppm of carbon monoxide or below 50 ppm for the state of the art Pt-Ru anodes. As the generated hydrogen gas stream presents a high CO content, it has to be minimized in order to protect the platinum anode from poisoning and subsequent deactivation of the fuel cell. After the reforming process, CO is partially converted to CO_2 via the water gas shift (WGS) reaction. The WGS reaction takes place in two consecutive stages: the first one at high temperature (HT-

WGS) at 573-673 K and the second one at low temperature (LT-WGS) at 453-573 K. In this process, carbon monoxide reacts with steam giving raise to CO_2 and H_2, as follows:

$$CO + H_2O \rightarrow CO_2 + H_2 \quad \Delta H^{o}_{298} = -41.1 \text{ kJ·mol}^{-1} \quad \text{(Eq.4)}$$

These two catalytic processes are thermodynamically limited and 0.5–1.0 vol.% of unconverted carbon monoxide remain in the hydrogen fuel downstream after LT-WGS, still very high amount for entering the PEMFCs [198]. Therefore, the additional unit is needed to remove the residual CO in the H_2 generator for PEMFC. For that purpose, there are several technologies which selectively remove or minimize the amount of CO in a hydrogen rich gas stream with minimal loss of hydrogen. Among which are included hydrogen selective membrane purification, pressure swing adsorption, methanation and preferential oxidation (PROX) of CO or CO-PROX [199, 200]. Figure 1.16 illustrates the scheme of one of the most employed process that takes place in several steps as follows.

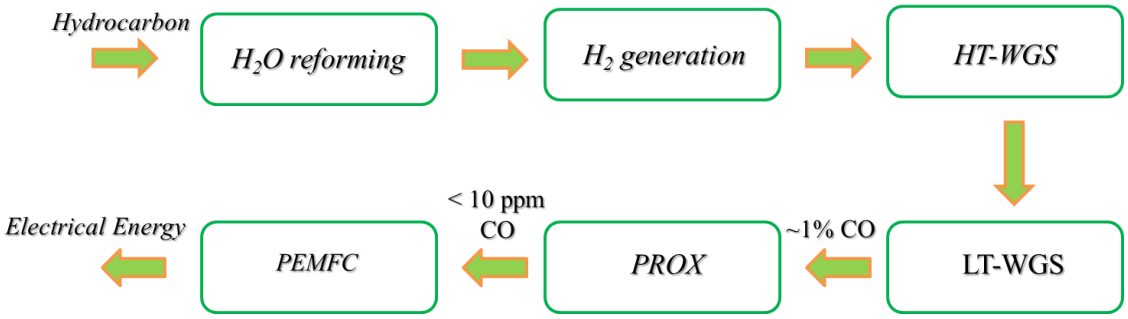

Figure 1.16. Flow diagram of the production and purification of hydrogen process for a PEMFC [200]

1.9. CO-PROX reaction

As abovementioned, the preferential oxidation of CO in H_2 stream (CO-PROX) is considered one of the most effective methods for reducing the concentration of CO to 10 ppm level in the hydrogen generation process before entering PEMFCs. PROX of CO is a reaction to convert CO in a H_2-rich gas mixture to CO_2 with minimal H_2 consumption [201-203]. The reaction that takes place is the following:

$$CO + 1/2O_2 \rightarrow CO_2 \quad \Delta H^{o} = -283 \text{ kJ·mol}^{-1} \quad \text{(Eq.5)}$$

The competitive oxidation reaction of hydrogen can occur simultaneously as follows:

$$H_2 + 1/2O_2 \rightarrow H_2O \quad \Delta H^{o} = -242 \text{ kJ·mol}^{-1} \quad \text{(Eq.6)}$$

The selectivity of the CO-PROX reaction is defined as the ratio between O_2 that reacts with CO and total O_2. As part of the oxygen is consumed in the competitive reaction of hydrogen oxidation (Eq.6), O_2 must be supplied in excess in order to enhance CO-PROX reaction (Eq.5). The oxygen excess is determined by equation 11:

$$\lambda = 2[O_2]/[CO] \qquad \text{(Eq.11)}$$

where λ is the oxygen excess factor and $[O_2]$ and [CO] the respective concentrations of oxygen and carbon monoxide in the feed. In the first step of equation 5 an excess of oxygen of 2 is provided and about 90% of the CO is transformed. In the second step (Eq.5) a substantially higher oxygen excess is used, at a factor of 4, which is then processed with the remaining CO. In order to reduce the CO concentration to less than 10 ppm to also avoid excess CO-fraction loading, the transient operation of a CO adsorber may be important. Equation 6 is highly undesirable due to the oxidation of H_2 to form H_2O, resulting in a loss of H_2 [204]. If dominant over CO oxidation, hydrogen oxidation can suppress the catalytic surface redox cycle and lead to catalyst deactivation.

CO and CO_2 methanation reactions (Eq.7 and Eq.8, respectively) and inverse water gas shift reaction (Eq.9) may occur as well, which is also undesirable due to H_2 consumption:

$$CO + 3H_2 \rightarrow CH_4 + H_2O \qquad \Delta H^o = -206\ kJ\cdot mol^{-1} \qquad \text{(Eq.7)}$$

$$CO_2 + 4H_2 \rightarrow CH_4 + 2H_2O \qquad \Delta H^o = -165.5\ kJ\cdot mol^{-1} \qquad \text{(Eq.8)}$$

$$CO_2 + H_2 \rightarrow CO + H_2O \qquad \Delta H^o = -41.2\ kJ\cdot mol^{-1} \qquad \text{(Eq.9)}$$

Another undesirable reaction such as the coke formation by the Boudouard reaction could also occur:

$$2CO \rightarrow C + CO_2 \qquad \Delta H^o = -173.12\ kJ\cdot mol^{-1} \qquad \text{(Eq.10)}$$

The formed coke is deposited over the catalyst surface, reducing remarkably its conversion and provoking its deactivation.

In order to minimize these undesirable side reactions, catalysts must meet a series of indispensable requirements [204]. One critical point is to find a catalyst that is both highly active and highly selective in the CO oxidation reaction. The operating temperatures should be somewhere in between the low temperature WGS unit (523-573 K) and the temperature of the PEMFC (353-373 K). It also has to present a high resistance to deactivation by the presence of

H_2O and CO_2 in the effluent. Finally, such catalyst should be able to operate under transient conditions since the power demand will vary considerably.

1.10. CO-PROX catalysts

Literature has reported several promising catalysts for CO-PROX reactions that can be classified in three categories. The first category includes supported noble metals such as Pt, Pd, Ir, Ru and Rh and the second one consists of metal oxide catalysts such as $CuO\text{-}CeO_2$. A third category includes the supported gold catalysts, and more specifically supported gold nanoparticles.

Supported noble metal catalysts are very active in the CO-PROX reaction and are stable in the presence of CO_2 and H_2O. However, they favor the oxidation reaction of H_2 which make them less selective. Not to mention their high costs [205-208].

Metal oxide based catalysts, and more specifically the system $CuO\text{-}CeO_2$, are considered a very good alternative to noble metals. These catalysts achieve similar conversions at low temperature to noble metals, being much more selective than these and also more affordable [209-211].

Supported gold catalysts reach remarkably better catalytic results at lower temperatures than noble metals. In fact, low-temperature CO oxidation has served as a prototypical reaction in catalysis by gold [212]. When Au nanoparticles are dispersed on the surface of a reduced oxide support such as TiO_2, the electron density on the surface of Au nanoparticles is increased due to the electron transfer from the titania to Au nanoparticles, which promotes the adsorption of CO at the surface of Au nanoparticles and then the oxidation of CO [213-216]. At temperatures lower than 40 ºC, the selectivity to CO_2 is higher than 80% and decreases gradually when temperature increases, to finally vanish at 300 ºC. This temperature dependence in PROX selectivity is well known [212].

Overall, previous research shows three very important considerations when designing a new catalyst: the surface area of the catalyst to increase catalytic site availability, the substrate material for oxygen transport and the particle size of the catalyst to increase overall catalytic efficiency.

However, as this reaction has been widely studied, the use of photocatalysts has been proposed to replace the conventional thermal sources to input energy to the system. Photocatalysis utilizes high energy and short wavelength light as the energy input for the system. Therefore, unlike a thermal reaction where large amounts of energy are added in the form of heat, the photocatalytic reaction can be performed at standard conditions. Concretely, in 2006 Kamegawa et al.[217] were the first in state that “to the best of our knowledge, no attempt has been made to apply photocatalysis for the PROX reactions”. Since then, several studies have been devoted to the so-called photo-PROX reaction. Dai et al.[218] studied the preferential oxidation of CO in a H_2-rich stream over Au/TiO_2 systems under UV irradiation. The results showed that UV radiation not only promoted the oxidation of CO, but also increased the selectivity of CO oxidation from

35.6% to 37.5%. They also studied the effect of visible radiation in the mentioned reaction at room temperature for the same system prepared again by the deposition-precipitation method. It was found that the visible-light irradiation promoted the adsorption of CO and its activation at the surface of Au species, increasing CO conversion from 29.5% to 38.5% [219]. As it is known that metal oxide supports play an important role on the dispersion of Au nanoparticles and on the adsorbing behavior of reactants, Au/TiO_2 and Au/Al_2O_3 systems were compared [220]. The results reflected that the visible light irradiation promoted the oxidation of CO and its selectivity to CO_2 in the presence of hydrogen over Au/TiO_2, whereas it also promoted the oxidation of CO but suppressed the selectivity of CO oxidation over Au/Al_2O_3. This fact was ascribed to the different electron transfer processes in both systems. For Au/TiO_2, the excited electrons in the Au 6sp band are transferred to the conduction band of TiO_2 with the formation of a transient electron-rich state at Au surface. While for Au/Al_2O_3, the excited electrons are transferred to the HOMO of Al_2O_3 resulting in the formation of a transient electron-deficient state at Au surface, exerting therefore different effects on CO adsorption and oxidation.

Yang et al. [221] also studied a polyaniline (PANI) assembled Au/TiO_2 catalyst aimed at building up a good interface to facilitate electron transfer as an effective way of promoting CO oxidation over Au/TiO_2. The results showed that coupling the LSPR effect of Au nanoparticles and the electron donor effect of PANI led to a better CO-PROX activity under visible light than Au/TiO_2.

More recently, Zhang et al. [222] studied the system Au/ZIF-8-TiO_2, a gold nanoparticle catalyst supported on a metal organic framework modified TiO_2. The results reflected its better performance in CO oxidation than Au/TiO_2 at room temperature in dark or under visible light irradiation, which was ascribed to the higher surface electron density of both Au and TiO_2, attributed to the electron transfer between ZIF-8 and TiO_2.

In view of the good results achieved by gold nanoparticles supported on titania, it would be interesting to evaluate the effect of altering some factors such as the type of crystalline phase and dimensionality on the preferential oxidation of CO from a H_2 rich stream under visible light, room temperature and atmospheric pressure. But first, we will briefly introduce the concept of photocatalyst.

1.11. Photocatalysts

A photocatalyst is defined as a material that is activated by the absorption of photons, helping to accelerate a reaction without being consumed. When it comes to a solid, the band gap energy value is a key parameter which is going to determine the electronic features of the material. The band gap energy is defined as the amount of energy that is needed to promote an electron from its ground state in the valence band to an excited state in the conduction band. If the band gap is greater than 4 eV, the material is a dielectric or insulator, if it is zero or close to zero is called metal or conductor and if it is between 0 and 4 eV is called semiconductor [188]. Solid

semiconductors have proven to be the most active photocatalysts and therefore have been applied to pollutant degradation and environmental remediation, such as water/air purification and contaminant degradation [223-225]. The main processes that occur when a particle of a semiconductor catalyst is irradiated during a photocatalytic process, with energy equal to or greater than the band gap energy, are shown in Figure 1.17.

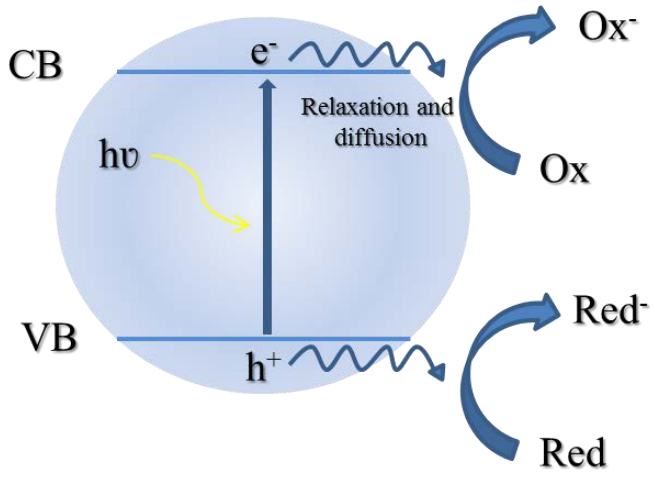

Figure 1.17. Scheme of photocatalytic processes after light absorption.

The absorption of a photon excites an electron from the valence band (VB) to the conduction band (CB), leaving a gap in the VB. This electron promotion creates what are known as charge carriers or "electron hole pairs". An electron hole is the vacancy of an electron in the valence band of an atom, thus giving the valence band a net positive (+) charge. The conduction band, which had a previously neutral charge because it was empty, now is negatively (-) charged due to the presence of the promoted electron. In this way, oxidation reactions occur in the valence band while reduction processes are carried out in the conduction band. However, charge carriers have a relatively short lifetime at which they must migrate to the active sites on the surface to react with the adsorbed reactants. Those charge carriers, that do not react with the adsorbed molecules, are recombined again (in the surface or inside the semiconductor) releasing energy, which can be dissipated as heat or emitting luminescent radiation. Consequently, the overall efficiency of the photocatalytic process decreases and therefore, the optimization of the intermediate steps described above is of vital importance to improve the performance of the photocatalytic reaction [188].

In the present work, TiO_2 has been chosen among the variety of semiconductors catalysts for the reasons detailed below.

1.12. Titania

Since the water splitting breakthrough reported by Fujishima and Honda in 1972 [226], the photocatalytic properties of semiconductor materials have been used to convert solar energy into chemical energy to oxidize or reduce materials to obtain useful materials including

hydrogen and hydrocarbons, and to remove pollutants and bacteria on wall surfaces and in air and water [227-230]. Of the many different photocatalysts, TiO_2 has been the most widely studied and used in many applications because of its strong oxidizing abilities for the decomposition of organic pollutants [231-233], superhydrophilicity [234], chemical stability, long durability, nontoxicity, low cost and transparency to visible light.

As regards its electronic characteristics, TiO_2 is a *n*-type semiconductor with ionic character. The 3d orbitals of Ti^{4+} ($3s^2p^64s^03d^0$) mainly constitute the conduction band while the p orbitals of O^{2-} ($2s^22p^6$) form the valence band. Its photocatalytic properties are derived from the formation of photogenerated charge carriers (holes and electrons) which occurs upon the absorption of ultraviolet light corresponding to the band gap between valence and conduction bands [227, 228]. The photogenerated holes in the valence band diffuse to the TiO_2 surface and react with adsorbed water molecules, forming hydroxyl radicals ($^{\cdot}OH$). The photogenerated holes and the hydroxyl radicals oxidize nearby organic molecules on the TiO_2 surface. Meanwhile, electrons in the conduction band typically participate in reduction processes reacting with molecular oxygen in the air to produce superoxide radical anions ($O_2^{\cdot-}$). However, the main drawback affecting the efficiency of the process is the rapid recombination velocity of the charge carriers, leading to low quantum efficiency. In other words, the competition between charge recombination and interfacial charge transfer between photo-excited TiO_2 and adsorbates appears to limit the overall photocatalytic reaction rate on pure titania surfaces. For example, recombination can occur on the femtosecond timescale, while the transfer of trapped electrons to O_2, can occur over time periods from ms to hours [235]. Besides, the use of this material is limited by its band gap energy, which can vary from 3.0 to 3.2 eV depending on the polymorph, and requires near UV wavelengths (387.5 nm) for efficient excitation. Taking into account that sunlight reaching the Earth's surface contains less than 5% of UV light, while visible light (λ= 400-700 nm) accounts for 43% of the incoming solar energy, engineering the energy band gap of TiO_2 is required in order to expand its photoresponse to longer wavelengths [236]. Therefore, several strategies based on structural and surface modifications have been developed to overcome these issues.

1.12.1. TiO_2 Modifications

One of the most widely used approaches to extend the photocatalytic response into the visible region has been doping with metals and non-metals elements [237]. The introduction of dopants into the structure of titania manages to increase the catalytic activity in several ways: (1) stabilization of the crystalline phase and control of adverse defects such as the existence of Ti^{3+} in the structure; (2) modifications of band edges in order to optimize the light absorption depending on the light source; (3) modification of surface properties such as acidity and basicity

and (4) modification of morphologic properties such as particle size, surface area, etc. [238]. However, the doping approach is characterized by considerable difficulty in reproducing the photocatalytic activity that is frequently dependent on the exact preparation procedure and doping level. Besides, the features of these strategies are out of the scope of this work so they will not be discussed further on.

Surface modification is another of the most important strategies that leads to enhanced photocatalytic efficiency. Surface modifiers can alter the charge transfer process in various ways as follows: (1) creating additional surface traps or charge reservoir sites; (2) altering the intrinsic charge transfer rate reducing the charge recombination; (3) changing reactant adsorption/desorption rates altering the selectivity or the yield of reaction products [239]. The strategies include surface modifications by: donor and acceptor substances [240], organic sensitizers [241], coupling semiconductors [242], insulating oxides[243] and noble metals nanoparticles, which is the case of the study of the present thesis.

1.12.2. AuNPs/TiO_2 systems

Surface modification of titania by depositing noble metal nanoparticles on its surface leads to stable and durable materials due to the chemical inertness, specially, towards photo-oxidation of noble metals. Besides, noble metal nanoparticles have been recognized as a new class of efficient media suitable for harvesting light energy for chemical processes due to their high optical absorption over a wide range of the sunlight spectrum, including both visible and UV light [244, 245]. In the UV region, metallic nanoparticles on the surface of titania can enhance the overall absorptivity, serve as charge traps, and facilitate charge injection into the semiconductor to enhance photocatalytic efficiency. Remarkably, these catalysts also exhibit photocatalytic activity in the visible range due primarily to the plasmonic properties of metallic nanoparticles, as will be described below [235]. In particular, coupling titania with Pd, Pt, Ag or Au NPs, to reduce the electron-hole pair recombination of photogenerated charge carriers, has proven to be an effective way to improve charge separation, providing more catalytic active sites [246-248]. Among noble metals, supported gold nanoparticles show, for several reactions, surprisingly high photocatalytic activity in the visible region at low temperature [249]. Gold nanoparticles exhibit an absorption band in the visible region around 560 nm that is responsible of the brilliant colors observed in gold colloids [250]. These magnificent colors are caused by the localized surface plasmon resonance (LSPR) effect of Au NPs and when supported on TiO_2, the material develops a purple-brown color. The LSPR effect is the resonant photon-induced coherent oscillation of charge at the metal-dielectric interface, established when the photon frequency induced by the incident electromagnetic radiation matches the natural frequency of metal surface electrons oscillating against the restoring force of their positive nuclei. In the

small particle limit, a resonantly enhanced field builds up inside the particle which is homogenous throughout its volume, producing a dipolar field outside the particle as seen in Figure 1.18. This leads to enhanced absorption and scattering cross sections for electromagnetic waves, as well as to a strongly enhanced near field in the immediate vicinity of the particle surface [251, 252]. Therefore, surface plasmon essentially acts as concentrator of the energy of incoming photons in a small volume surrounding the nanostructure, which makes the plasmonic nanostructure of Au NPs very suitable for photocatalytic processes.

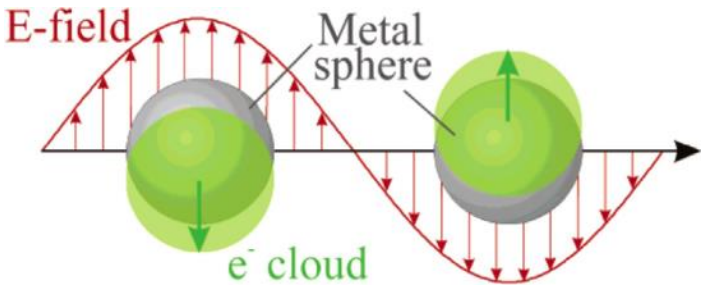

Figure 1.18. Schematic of plasmon oscillation for a sphere, showing the displacement of the conduction electron charge cloud relative to the nuclei [253]

The exact position and shape of the surface plasmon band depends on several factors such as the dielectric constant of the medium, the surrounding environment, the particle size and the shape of Au NPs which are going to determine the light absorption range [254]. As the shape and/or size of the NP changes, the density of the electromagnetic field at the NP surface also changes. These combine to induce a shift in the oscillation frequency of the conduction electrons and a strong field enhancement of the electromagnetic fields near the rough surfaces of Au NPs [253, 255]. There are number of reports on the association of the LSPR effect and NP size, overall, as the particles grow bigger, the absorption band broadens and red-shift to longer wavelengths occur [256].

Visible light excitation of AuNPs/TiO_2

Finally, despite the tremendous research effort to understand Au/TiO_2 catalytic and photocatalytic behavior, there is a need for new studies that can provide a clearer understanding as to precisely which thermal reaction mechanisms, which plasmon decay processes, and which charge transfer phenomena are active under different conditions. Figure 1.19 shows a schematic of the major processes that occur in a plasmonic Au/TiO_2 photocatalyst [257]. Here, the incident visible light excites LSPR in the Au nanoparticle via a coherent oscillation of electrons, which is suggested to excite electrons and holes within TiO_2 by energy transfer and/or charge carrier transfer to TiO_2.

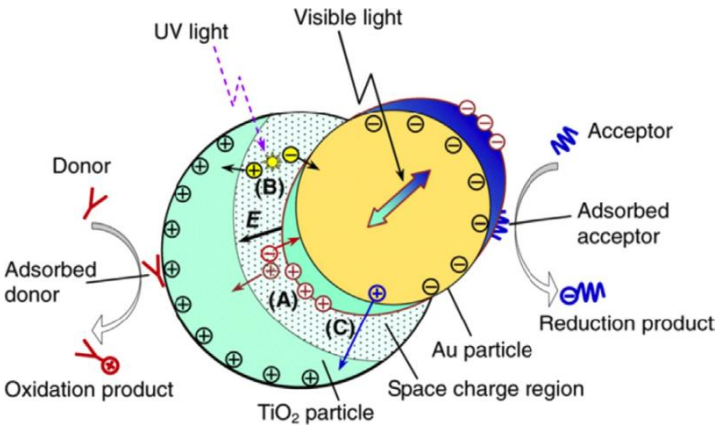

Figure 1.19. Scheme of the major processes in plasmonic photocatalysis [257]

However, as abovementioned, the mechanism by which energy is transferred from gold to TiO_2 still remains as a topic of discussion [258, 259]. Two main mechanisms have been highly cited in the literature regarding plasmonic enhancement of photo catalytic reactions: direct charge transfer and local electric field enhancement. The former proposes a charge transfer mechanism in which an excited plasmon in Au generates conduction band electrons with sufficient energy to traverse the Schotty barrier and enter the conduction band of the adjacent TiO_2 [260].The latter alternative mechanism considers that elevated electric fields (enhanced by plasmonic absorption and concentration) near the interface excite electron-hole pairs in the semiconductor, leading to enhanced photocatalytic activity [258, 259, 261].

CO oxidation over AuNPs/TiO_2

Overall, the photoelectrochemical response of Au/TiO_2 systems in the preferential oxidation of CO under light irradiation can be explained as follows [254, 262]: the generated electron on Au nanoparticles, through the excitation of LSPR by the incident visible light, is injected into the conduction band of TiO_2, leaving a transient electron-rich state at Au surface ($Au^{\delta+}$). The energy of the TiO_2 conduction band is very low and, therefore, easily populated by photoejected electrons. The recombination of these electrons and the positive gold transient is usually very fast, but this recombination can slow down if suitable acceptors can trap the ejected electrons. Consequently, the separation of the charge carriers may slow down the recombination rate and increase the conversion of CO [246]. Furthermore, in agreement to numerous studies, CO is chemisorbed at low-coordinated gold atoms on the Au particles, while O_2 is activated at sites close to the Au/TiO_2 interface [263]. CO binding is fast and strong relative to oxygen binding, thus CO is readily available at or near the active site and O_2 binding and activation is the key kinetic step in the catalysis [264]. As reported in many studies the Au/support interfacial perimeter sites, where a cationic site of the support and one Au atom (or more) are localized at the Au particle perimeter, act as dual adsorption center to bind molecular oxygen in a peroxo-

type configuration. Thus, small Au particles with a high number of interfacial perimeter sites per Au atom will exhibit the highest catalytic activity in the CO oxidation.

1.12.3. Synthesis of AuNPs/TiO_2

In order to control physicochemical parameters such as average particle size, dispersion and loading, several preparation procedures have been developed following a presumably parallelism between catalytic and photocatalytic activity of Au NPs supported on titania. For preparation of a highly active Au/TiO_2 photocatalyst impreganation and deposition-precipitation, are the common methods where the as-prepared state presents mainly Au^{3+} species and should be activated to reduce Au^{3+}. The latter is one of the preferred methods in heterogeneous catalysis. This method leads to very small gold nanoparticles of about 3 nm that are reported to be catalytically active in CO-PROX [237]. Besides, TiO_2 is an amphoteric oxide with an isoelectric point (IEP) of 6, which makes it an excellent candidate for deposition-precipitation in NaOH. In this methodology an aqueous solution of $HAuCl_4$ is brought to the required pH by slowly adding NaOH and then TiO_2 is added to the solution and the resulting suspension stirred for a relatively long time (24h) while the pH is kept constant at the required value. Then, the solid is recovered, exhaustively washed (to remove Cl^- ions completely) and reduced to form Au nanoparticles. The main parameters in the deposition-precipitation method are the pH value of the deposition step because it controls the speciation of Au^{3+} [265]. This method is very simple and convenient, rendering samples with reproducible properties and very small particle size. It is therefore understandable that the World Gold Council uses this method when preparing Au/TiO_2 samples sold commercially as “reference catalyst” type A [237].

Further to this, there are many factors which can exert significant influence on the photocatalytic performance of TiO_2 based materials such as the specific surface area, crystal structure [266], particle size distribution, mean pore size and the exposed surface facets. Structural dimensionality is another factor which can affect the photocatalytic performance and also has a significant impact on the properties of TiO_2 materials. Thus, the development of performance improvements by adjusting some of these factors such as the type of crystalline phase, the ratio between anatase and rutile phases and dimensionality is one of the purposes of the present thesis.

1.13. Influence of crystalline phases

TiO_2 occurs in nature mainly as three different crystalline polymorphs: anatase, rutile and brookite [238]. These three crystallographic forms have the same chemical composition, however, the rutile phase is the most stable whereas anatase and brookite are metastable, transforming into rutile when heated above 500 ºC [267]. The most used phases as

photocatalysts in heterogeneous catalysis are rutile and anatase [268, 269]. Both structures contain slightly distorted TiO_6 octahedra sharing edges. The rutile and anatase bond lengths are similar but the anatase octahedron presents a larger distortion in its bond angles. Consequently, anatase presents a more open structure with a lower density [270, 271].

For pure phases it is generally accepted that anatase exhibits a higher photocatalytic activity compared to rutile, but despite the intensive study of TiO_2 there is no consensus to explain this difference [272-274]. Possible explanations are discussed below:

- Anatase presents a larger band gap than rutile. While this reduces the light that can be absorbed, it may raise the valence band maximum to higher energy levels relative to redox potentials of adsorbed molecules. This increases the oxidation power of electrons and facilitates electron transfer from titania to adsorbed molecules [275].
- Anatase exhibits an indirect band gap that is smaller than its direct band gap. For rutile, on the other hand, its fundamental band gap is either direct or its indirect band gap is very similar to its direct band gap. Semiconductors with indirect band gap generally exhibit longer charge carrier life times compared to direct gap materials. A longer electron-hole pair life in anatase than in rutile would make it more likely for charge carriers to participate in surface reactions. One evidence for longer charge carrier lifetimes in anatase than in rutile comes from transient photoconductivity measurements on single crystalline samples [276].

For mixed phases, literature has reported that the right combination of rutile (10-30 %) and anatase (90-70%) phases is known to have synergistic effects and increased photocatalytic activity if compared to pure phases. That is why commercial catalyst Degussa P25 has been the most used material in photocatalysis so far, and accordingly is considered a reference material. It contains 70-80 wt% of anatase and 30-20 wt% of rutile [269, 270]. A general consensus places the bandgaps of rutile and anatase at 3.03 and 3.20 eV, respectively. Electrochemical impedance analysis established that the flatband potential of anatase is 0.2 eV more negative than that of rutile, indicating that the conduction band of anatase lies 0.2 eV above that of rutile [277]. This band alignment at the interface would favor the transfer of photogenerated electrons from anatase to rutile, and the transfer of holes from rutile to anatase at a clean interface. However, recent results have demonstrated that conduction band of anatase is actually lower than that of rutile [274] and so electrons flow from rutile into anatase, with holes moving in the opposite direction. Regardless of the direction through electrons and holes are preferentially transferred, the charge transfer from one phase to another slows down the recombination of the electron-hole pairs leading to more photocatalytically active systems.

1.14. Influence of the dimensionality

The dimensionality associated with the structure of TiO_2 materials is a factor that can affect its properties and functions, including its surface area, adsorption, reflectance, adhesion, carrier transportation properties and therefore, its photocatalytic performance. Hence, the construction of nanostructures with different dimensionality such as spheres, fibers, tubes, sheets, rods and interconnected structures have been fabricated [225]. Choosing TiO_2 materials with the appropriate dimensionalities enables us to take full advantage of the unique properties offered by TiO_2 materials. For example, a sphere with zero dimensionality has a high surface area, resulting in a higher rate of photocatalytic decomposition of organic pollutants [278]. One dimensional fibers or tubes have advantages with regard to less recombination because of the short distance for charge carrier diffusion [279] and light scattering properties. Two dimensional nanosheets have smooth surfaces and high adhesion [280], whereas three dimensional monoliths may have high carrier mobility as a result of their interconnecting structure.

In the present thesis we evaluate the effects of one-dimensional TiO_2 structures such as nanorods in the studied photocatalytic reaction since it is known that TiO_2 materials with one-dimensional structures can combine unusual and versatile physico-chemical properties with the conventional advantages of titania. One-dimensional nanorods are expected to provide large surface area and a higher length to diameter ratio, enabling a reduction in the hole-electron recombination and a high interfacial charge carrier transfer rate, which are benefitial to facilitating the photocatalytic reaction [281].

1.15. Work to develop in photo-PROX

Important progresses have been carried out in the field of heterogeneous photocatalysis by the use of noble metal nanoparticles (NP) as surface modifiers since they have enhanced the photocatalytic response in the visible region. Nonetheless, the addition of a second metal can lead to efficient charge separation by trapping or removing electrons from TiO_2. Important advances have been made in the application of TiO_2 modified bimetallic NPs, although the development of bimetallic systems is still an attractive research aim.

The most challenging problems are

- The physicochemical properties such as monosize, uniform size, and even distribution of metal nanoparticles over the photocatalyst support, all of these related to the preparation method employed. The preparation of monodisperse and very small monometallic and bimetallic NPs is a very important task [282].
- The preparation of bimetallic-based nanomaterials with a well-controlled shape [283]since it determines surface atomic arrangement as well as the optical properties. In

this regard, nanoarchitecture arrangement (shape and size of metals) as well as the selection of noble metal and titania form may allow to prepare photoactive catalysts under overall solar spectrum.

Anyhow, a photocatalyst with very high efficiency is not practical if the cost of its modification with metals is too high.

1.16. References

1. *International Energy Outlook 2016. Report Number: DOE/EIA-0484*.
2. *U.S.Energy Information Administration, Annual Energy Outlook 2013 With Projections to 2040, 2013.*
3. *Fisher KS, Beitler C, Rueter C, Searcy K, Rochelle DG, Jassim DM, Integrating MEA Regeneration with CO2Compression and Peaking to Reduce CO2 Capture Costs, in, 2005, pp. Medium: ED; Size: 757.*
4. *International Energy, A., World Energy Outlook 2013. 2013*.
5. *NASA, 2017. Global Climate Change. Vital sings of the planet, Retrieved from https://climate.nasa.gov/vital-signs/carbon-dioxide/.*
6. Raslavičius, L., N. Striūgas, and M. Felneris, *New insights into algae factories of the future.* Renewable and Sustainable Energy Reviews, 2018. **81**: p. 643-654.
7. Alonso, D.M., J.Q. Bond, and J.A. Dumesic, *Catalytic conversion of biomass to biofuels.* Green Chemistry, 2010. **12**(9): p. 1493-1513.
8. Arifin, Y., et al., *A Second Generation Biofuel from Cellulosic Agricultural By-product Fermentation Using Clostridium Species for Electricity Generation.* Energy Procedia, 2014. **47**: p. 310-315.
9. *Food and Agriculture Organization of the United Nations (FAO), Introducing the International Bioenergy Platform (IBEP), Rome, 2006.*
10. Kumari, D. and R. Singh, *Pretreatment of lignocellulosic wastes for biofuel production: A critical review.* Renewable and Sustainable Energy Reviews, 2018. **90**: p. 877-891.
11. Jeihanipour, A. and R. Bashiri, *Perspective of biofuels froms wastes: A review*, in *Lignocellulosic-based bioproducts*, K. Karimi, Editor. 2015.
12. *OECD, Biofuels. OECD Publishing.*
13. Chaudhary, L., et al., *Algae as a feedstock for bioethanol production. New entrance in biofuel world.* International Journal of ChemTech Research, 2014. **6**: p. 1381-1389.
14. Aro, E.M., *From first generation biofuels to advanced solar biofuels.* Ambio, 2016. **45 Suppl 1**: p. S24-31.
15. Hays, S.G. and D.C. Ducat, *Engineering cyanobacteria as photosynthetic feedstock factories.* Photosynth Res, 2015. **123**(3): p. 285-95.
16. Naik, S.N., et al., *Production of first and second generation biofuels: A comprehensive review.* Renewable and Sustainable Energy Reviews, 2010. **14**(2): p. 578-597.
17. Demirbas, A., T. Ozturk, and M.F. Demirbas, *Recovery of energy and chemicals from carbonaceous materials.* Journal of Energy sources, 2006. **28**: p. 1473-1482.
18. Deshmukh, S.S., A.M. Jinturkar, and J.S. Gawande, *Comparative experimental study of single basin and stepped type solar still.* J Energy Educ Sci Technol 2008. **20**: p. 79-85.
19. Demirbas, A., *Energy balance, energy sources, energy policy, future developments and energy investments in Turkey.* J Energy Convers Manag 2001. **42**: p. 1239-1258.
20. Chandra, R., H. Takeuchi, and T. Hasegawa, *Hydrothermal pretreatment of rice straw biomass: A potential and promising method for enhanced methane production.* Applied Energy, 2012. **94**: p. 129-140.
21. Han, X., et al., *Catalytic conversion of lignocellulosic biomass into hydrocarbons: a mini review.* Catalysis Today, 2018.
22. Zhang, Y.P., *Reviving the carbohydrate economy via multi-product lignocellulose biorefineries.* J Ind Microbiol Biotechnol, 2008. **35**(5): p. 367-375.
23. Zhu, J.Y. and X.J. Pan, *Woody biomass pretreatment for cellulosic ethanol production: Technology and energy consumption evaluation.* Bioresour Technol, 2010. **101**(13): p. 4992-5002.
24. Kumar, R., S. Singh, and O.V. Singh, *Bioconversion of lignocellulosic biomass: biochemical and molecular perspectives.* J Ind Microbiol Biotechnol, 2008. **35**(5): p. 377-391.
25. Jacobson, K., K.C. Maheria, and A. Kumar Dalai, *Bio-oil valorization: A review.* Renewable and Sustainable Energy Reviews, 2013. **23**: p. 91-106.
26. Hashmi, A.S. and G.J. Hutchings, *Gold catalysis.* Angew Chem Int Ed Engl, 2006. **45**(47): p. 7896-936.
27. Cherubini, F., *The biorefinery concept: Using biomass instead of oil for producing energy and chemicals.* Energy Conversion and Management, 2010. **51**(7): p. 1412-1421.

28. FitzPatrick, M., et al., *A biorefinery processing perspective: treatment of lignocellulosic materials for the production of value-added products.* Bioresour Technol, 2010. **101**(23): p. 8915-22.
29. Taherzadeh, M.J. and K. Karimi, *Pretreatment of lignocellulosic wastes to improve ethanol and biogas production: a review.* Int J Mol Sci, 2008. **9**(9): p. 1621-51.
30. Brandt, A., et al., *Deconstruction of lignocellulosic biomass with ionic liquids.* Green Chemistry, 2013. **15**(3): p. 550.
31. Klemm, D., et al., *Cellulose: fascinating biopolymer and sustainable raw material.* Angew Chem Int Ed Engl, 2005. **44**(22): p. 3358-93.
32. Mohan, D., C.U. Pittman, and P.H. Steele, *pyrolysis of wood biomass for bio-oil. A critical review.* Energy and Fuels, 2006. **20**: p. 848-889.
33. Ragauskas, A.J., et al., *The path forward for biofuels and biomaterials.* Science, 2006. **311**(5760): p. 484-9.
34. Zugenmaier, P., *Zugenmaier, P.: Conformation and packing of various crystalline cellulose fibers. Prog. Polym. Sci. 26, 1341-1417*. Vol. 26. 2001. 1341-1417.
35. Scheller, H.V. and P. Ulvskov, *Hemicelluloses.* Annu Rev Plant Biol, 2010. **61**: p. 263-89.
36. Ragauskas, A.J., et al., *Lignin valorization: improving lignin processing in the biorefinery.* Science, 2014. **344**(6185): p. 1246843.
37. Boerjan, W., J. Ralph, and M. Baucher, *Lignin biosynthesis.* Annu Rev Plant Biol, 2003. **54**: p. 519-46.
38. Lewis, N.G., *A 20th century coaster ride.* Current opinion in plant biology, 1999. **2**: p. 153-162.
39. Goyal, H.B., D. Seal, and R.C. Saxena, *Bio-fuels from thermochemical conversion of renewable resources: A review.* Renewable and Sustainable Energy Reviews, 2008. **12**(2): p. 504-517.
40. Zakzeski, J., et al., *The catalytic valorization of lignin for the production of renewable chemicals.* Chemical Reviews, 2010. **110**: p. 3552-3599.
41. Venderbosch, R.H. and W. Prins, *Fast pyrolysis technology development.* Biofuels, Bioproducts and Biorefining, 2010. **4**(2): p. 178-208.
42. Cheng, F. and C.E. Brewer, *Producing jet fuel from biomass lignin: Potential pathways to alkylbenzenes and cycloalkanes.* Renewable and Sustainable Energy Reviews, 2017. **72**: p. 673-722.
43. Jenkins, B.M., et al., *Combustion properties of biomass.* Fuel Processing Technology, 1998. **54**: p. 17-46.
44. De Bhowmick, G., A.K. Sarmah, and R. Sen, *Lignocellulosic biorefinery as a model for sustainable development of biofuels and value added products.* Bioresour Technol, 2018. **247**: p. 1144-1154.
45. Huber, G.W., S. Iborra, and A. Corma, *<Synthesis of Transportation Fuels from Biomass. Chemistry, Catalysts, and engineering.pdf>*. 2006. **106**: p. 4044-4098.
46. Huber, G.W. and J.A. Dumesic, *An overview of aqueous-phase catalytic processes for production of hydrogen and alkanes in a biorefinery.* Catalysis Today, 2006. **111**(1): p. 119-132.
47. Kay Lup, A.N., et al., *A review on reaction mechanisms of metal-catalyzed deoxygenation process in bio-oil model compounds.* Applied Catalysis A: General, 2017. **541**: p. 87-106.
48. Bridgwater, A.V. and G.V.C. Peacocke, *Fast pyrolysis processes for biomass.* Renewable and Sustainable Energy Reviews, 2000. **4**(1): p. 1-73.
49. Czernik, S. and A.V. Bridgwater, *Overview of Applications of Biomass Fast Pyrolysis Oil.* 2004. **18**: p. 590-598.
50. Zhang, Q., et al., *Review of biomass pyrolysis oil properties and upgrading research.* Energy Conversion and Management, 2007. **48**(1): p. 87-92.
51. Mortensen, P.M., et al., *A review of catalytic upgrading of bio-oil to engine fuels.* Applied Catalysis A: General, 2011. **407**(1-2): p. 1-19.
52. Mullen, C.A., et al., *Bio-oil and bio-char production from corn cobs and stover by fast pyrolysis.* Biomass and Bioenergy, 2010. **34**(1): p. 67-74.
53. Oasmaa, A. and E. Kuoppala, *Fast Pyrolysis of Forestry Residue. 3. Storage Stability.* Energy and Fuels, 2003. **17**: p. 1075-1084.
54. Oasmaa, A. and D. Meier, *Norms and standards for fast pyrolysis liquids.* Journal of Analytical and Applied Pyrolysis, 2005. **73**(2): p. 323-334.
55. Lu, Q., W.-Z. Li, and X.-F. Zhu, *Overview of fuel properties of biomass fast pyrolysis oils.* Energy Conversion and Management, 2009. **50**(5): p. 1376-1383.
56. Oasmaa, A., D.C. Elliott, and J. Korhonen, *Acidity of Biomass Fast Pyrolysis Bio-oils.* Energy & Fuels, 2010. **24**(12): p. 6548-6554.
57. Kleinert, M. and T. Barth, *Towards a Lignincellulosic Biorefinery. Direct One Step Conversion.* Energy and Fuels, 2008. **22**: p. 1371-1379.

58. Venderbosch, R.H., et al., *Stabilization of biomass-derived pyrolysis oils.* Journal of Chemical Technology & Biotechnology, 2010. **85**(5): p. 674-686.
59. Dickerson, T. and J. Soria, *Catalytic Fast Pyrolysis: A Review.* Energies, 2013. **6**(1): p. 514-538.
60. Furimsky, E., *Catalytic hydrodeoxygenation.* Applied Catalysis A: General, 2000. **199**(2): p. 147-190.
61. Ruddy, D.A., et al., *Recent advances in heterogeneous catalysts for bio-oil upgrading via "ex situ catalytic fast pyrolysis": catalyst development through the study of model compounds.* Green Chem., 2014. **16**(2): p. 454-490.
62. He, Z. and X. Wang, *Hydrodeoxygenation of model compounds and catalytic systems for pyrolysis bio-oils upgrading.* Catalysis for Sustainable Energy, 2012. **1**: p. 28-52.
63. de Miguel Mercader, F., et al., *Production of advanced biofuels: Co-processing of upgraded pyrolysis oil in standard refinery units.* Applied Catalysis B: Environmental, 2010. **96**(1-2): p. 57-66.
64. Wildschut, J., *Pyrolysis oil upgrading to transportation fuels by catalytic hydrotreatment.* Ph.D. thesis, Rijksuniversiteit Groningen., 2009. .
65. Saidi, M., et al., *Upgrading of lignin-derived bio-oils by catalytic hydrodeoxygenation.* Energy Environ. Sci., 2014. **7**(1): p. 103-129.
66. Choudhary, T.V. and C.B. Phillips, *Renewable fuels via catalytic hydrodeoxygenation.* Applied Catalysis A: General, 2011. **397**(1-2): p. 1-12.
67. Bu, Q., et al., *A review of catalytic hydrodeoxygenation of lignin-derived phenols from biomass pyrolysis.* Bioresour Technol, 2012. **124**: p. 470-7.
68. Samoladaa, M.C., W. Baldaufb, and I.A. Vasalosa, *Production of a bio-gasoline by upgrading biomass flash pyrolysis liquids via hydrogen processing and catalytic cracking.* Fuel, 1998. **77**: p. 1667-1675.
69. Cecilia, J.A., et al., *Oxygen-removal of dibenzofuran as a model compound in biomass derived bio-oil on nickel phosphide catalysts: Role of phosphorus.* Applied Catalysis B: Environmental, 2013. **136-137**: p. 140-149.
70. Bui, P., et al., *Studies of the synthesis of transition metal phosphides and their activity in the hydrodeoxygenation of a biofuel model compound.* Journal of Catalysis, 2012. **294**: p. 184-198.
71. Cecilia, J.A., et al., *Enhanced HDO activity of Ni2P promoted with noble metals.* Catal. Sci. Technol., 2016. **6**(19): p. 7323-7333.
72. Infantes-Molina, A., et al., *Nickel and cobalt phosphides as effective catalysts for oxygen removal of dibenzofuran: role ofcontact time, hydrogen pressure and hydrogen/feed molar ratio.* Catalysis Science and Technology, 2015. **5**: p. 3403-3415.
73. Zhao, H.Y., et al., *Hydrodeoxygenation of guaiacol as model compound for pyrolysis oil on transition metal phosphide hydroprocessing catalysts.* Applied Catalysis A: General, 2011. **391**(1-2): p. 305-310.
74. Abnisa, F., et al., *Recovery of Liquid Fuel from the Aqueous Phase of Pyrolysis Oil Using Catalytic Conversion.* Energy & Fuels, 2014. **28**(5): p. 3074-3085.
75. Mortensen, P.M., et al., *Screening of Catalysts for Hydrodeoxygenation of Phenol as a Model Compound for Bio-oil.* ACS Catalysis, 2013. **3**(8): p. 1774-1785.
76. Boullosa-Eiras, S., et al., *Catalytic hydrodeoxygenation (HDO) of phenol over supported molybdenum carbide, nitride, phosphide and oxide catalysts.* Catalysis Today, 2014. **223**: p. 44-53.
77. Zhao, C., et al., *Aqueous-phase hydrodeoxygenation of bio-derived phenols to cycloalkanes.* Journal of Catalysis, 2011. **280**(1): p. 8-16.
78. Nie, L. and D.E. Resasco, *Kinetics and mechanism of m-cresol hydrodeoxygenation on a Pt/SiO2 catalyst.* Journal of Catalysis, 2014. **317**: p. 22-29.
79. de Souza, P.M., et al., *Role of Keto Intermediates in the Hydrodeoxygenation of Phenol over Pd on Oxophilic Supports.* ACS Catalysis, 2015. **5**(2): p. 1318-1329.
80. Resasco, D.E. and S.P. Crossley, *Implementation of concepts derived from model compound studies in the separation and conversion of bio-oil to fuel.* Catalysis Today, 2015. **257**: p. 185-199.
81. Hicks, J.C., *Advances in C–O Bond Transformations in Lignin-Derived Compounds for Biofuels Production.* The Journal of Physical Chemistry Letters, 2011. **2**(18): p. 2280-2287.
82. Prins, R., *Hydrotreating.* Wiley-VCH, Weinheim, Germany2008.
83. Massoth, F.E., et al., *Catalytic Hydrodeoxygenation of Methyl Substituted Phenols. Correlations of Kinetic.* Journal of physical Chemistry B, 2006. **110**: p. 14283-14291.

84. Girgis, M.J. and B.C. Gates, *Reactivities, Reaction Networks, and Kinetics in High-pressure.* Industrial and Engineering Chemistry Research, 1991. **30**: p. 2021-2058.
85. Bui, V.N., et al., *Hydrodeoxygenation of guaiacol.* Applied Catalysis B: Environmental, 2011. **101**(3-4): p. 246-255.
86. Senol, O.I., *Hydrodeoxygenation of aliphatic and aromatic oxygenates on sulphided catalysts for production of second generation biofuels.* Department of Chemical Technology,Helsinki University of Technology, Espoo, Finland., 2007( ): p. 59.
87. Romero, Y., F. Richard, and S. Brunet, *Hydrodeoxygenation of 2-ethylphenol as a model compound of bio-crude over sulfided Mo-based catalysts: Promoting effect and reaction mechanism.* Applied Catalysis B: Environmental, 2010. **98**(3-4): p. 213-223.
88. Badawi, M., et al., *DFT study of furan adsorption over stable molybdenum sulfide catalyst under HDO conditions.* Comptes Rendus Chimie, 2009. **12**(6-7): p. 754-761.
89. Si, Z., et al., *An Overview on Catalytic Hydrodeoxygenation of Pyrolysis Oil and Its Model Compounds.* Catalysts, 2017. **7**(6): p. 169.
90. Nava, R., et al., *Upgrading of bio-liquids on different mesoporous silica-supported CoMo catalysts.* Applied Catalysis B: Environmental, 2009. **92**(1): p. 154-167.
91. Ryymin, E.-M., et al., *Insight to sulfur species in the hydrodeoxygenation of aliphatic esters over sulfided NiMo/γ-Al2O3 catalyst.* Applied Catalysis A: General, 2009. **358**(1): p. 42-48.
92. Ferrari, M., et al., *Influences of the Hydrogen Sulfide Partial Pressure and of a Nitrogen Compound on the Hydrodeoxygenation Activity of a CoMo/Carbon Catalyst.* Journal of Catalysis, 2001. **198**(1): p. 47-55.
93. Laurent, E. and B. Delmon, *Influence of water in the deactivation of a sulfided catalyst during hydrodeoxygenation.* Journal of Catalysis, 1994. **146**: p. 281-291.
94. Viljava, T.R., R.S. Komulainen, and A.O.I. Krause, *Effect of H2S on the stability of CoMo Al2O3 catalysts during hydrodeoxygenation.* Catalysis Today, 2010. **60**: p. 83-92.
95. Smith, G.V., Notheisz, F., *Heterogeneous Catalysis in Organic Chemistry.* Academic Press, San Diego., 1999.
96. Elliott D, N.G., Hart T, Hu J, Solana A, Cao C, Bridgwater A, and B. D., *Hydrogenation of bio-oil for chemicals and fuels production.* Bridgwater AV, Boocock DGB, editors. Science in thermal and chemical biomass conversion. UK: CPL press Newbury., 2006: p. 1536-1546.
97. Centeno, A., R. Maggi, and B. Delmon, *USE OF NOBLE METALS IN HYDRODEOXYGENATION REACTIONS*, ed. G.F.F.a.P.G. B. Delmon. 1999.
98. Ardiyanti, A.R., et al., *Hydrotreatment of wood-based pyrolysis oil using zirconia-supported mono- and bimetallic (Pt, Pd, Rh) catalysts.* Applied Catalysis A: General, 2011. **407**(1-2): p. 56-66.
99. Lee, C.R., et al., *Catalytic roles of metals and supports on hydrodeoxygenation of lignin monomer guaiacol.* Catalysis Communications, 2012. **17**: p. 54-58.
100. Chen, L., et al., *Aqueous-phase hydrodeoxygenation of carboxylic acids to alcohols or alkanes over supported Ru catalysts.* Journal of Molecular Catalysis A: Chemical, 2011. **351**: p. 217-227.
101. Li, N. and G.W. Huber, *Aqueous-phase hydrodeoxygenation of sorbitol with Pt/SiO2–Al2O3: Identification of reaction intermediates.* Journal of Catalysis, 2010. **270**(1): p. 48-59.
102. Wang, Y., et al., *Hydrodeoxygenation of dibenzofuran over noble metal supported on mesoporous zeolite.* Catalysis Communications, 2011. **12**(13): p. 1201-1205.
103. Sitthisa, S. and D.E. Resasco, *Hydrodeoxygenation of Furfural Over Supported Metal Catalysts: A Comparative Study of Cu, Pd and Ni.* Catalysis Letters, 2011. **141**(6): p. 784-791.
104. Sitthisa, S., et al., *Conversion of furfural and 2-methylpentanal on Pd/SiO2 and Pd–Cu/SiO2 catalysts.* Journal of Catalysis, 2011. **280**(1): p. 17-27.
105. Yohe, S.L., et al., *High-pressure vapor-phase hydrodeoxygenation of lignin-derived oxygenates to hydrocarbons by a PtMo bimetallic catalyst: Product selectivity, reaction pathway, and structural characterization.* Journal of Catalysis, 2016. **344**: p. 535-552.
106. Procházková, D., et al., *Hydrodeoxygenation of aldehydes catalyzed by supported palladium catalysts.* Applied Catalysis A: General, 2007. **332**(1): p. 56-64.
107. Savva, P.G., et al., *Benzene hydrogenation over Ni/Al2O3 catalysts prepared by conventional and sol–gel techniques.* Applied Catalysis B: Environmental, 2008. **79**(3): p. 199-207.
108. Yakovlev, V.A., et al., *Development of new catalytic systems for upgraded bio-fuels production from bio-crude-oil and biodiesel.* Catalysis Today, 2009. **144**(3-4): p. 362-366.
109. Olcese, R.N., et al., *Gas-phase hydrodeoxygenation of guaiacol over Fe/SiO2 catalyst.* Applied Catalysis B: Environmental, 2012. **115-116**: p. 63-73.

110. Shafaghat, H., P.S. Rezaei, and W.M.A.W. Daud, *Catalytic hydrodeoxygenation of simulated phenolic bio-oil to cycloalkanes and aromatic hydrocarbons over bifunctional metal/acid catalysts of Ni/HBeta, Fe/HBeta and NiFe/HBeta.* Journal of Industrial and Engineering Chemistry, 2016. **35**: p. 268-276.
111. Alessio, Z., I. Francisco, and L. Rafael, *Advances in Nanocatalyst Design for Biofuel Production.* ChemCatChem, 2018. **10**(9): p. 1968-1981.
112. Dongil, A.B., et al., *Hydrodeoxygenation of guaiacol over Ni/carbon catalysts: effect of the support and Ni loading.* RSC Advances, 2016. **6**(4): p. 2611-2623.
113. Selvaraj, M., et al., *Hydrodeoxygenation of Guaiacol over MoO3-NiO/Mesoporous Silicates: Effect of Incorporated Heteroatom.* Energy & Fuels, 2014. **28**(4): p. 2598-2607.
114. Ranga, C., et al., *Effect of composition and preparation of supported MoO3 catalysts for anisole hydrodeoxygenation.* Chemical Engineering Journal, 2018. **335**: p. 120-132.
115. Moberg, D.R., et al., *Mechanism of Hydrodeoxygenation of Acrolein on a Cluster Model of MoO3.* Journal of physical Chemistry C, 2010. **114**: p. 13782-13795.
116. Djéga-Mariadassou G, B.M., Bugli G, Sayag C., *Modification of the surface composition of molybdenum oxynitride during hydrocarbon catalysis.* catalysis Letters, 1995. **31**: p. 411-420.
117. Ramanathant, S. and S.T. Oyama, *New Catalysts for Hydroprocessing. Transition Metal Carbides and Nitrides.* Journal of Physical Chemistry, 1995. **99**: p. 16365-16372.
118. Hwu, H.H. and J.G. Chen, *Surface Chemistry of Transition Metal Carbides.* Chemical Reviews, 2005. **105**(1): p. 185-212.
119. Wang, H., J. Male, and Y. Wang, *Recent Advances in Hydrotreating of Pyrolysis Bio-Oil and Its Oxygen-Containing Model Compounds.* ACS Catalysis, 2013. **3**(5): p. 1047-1070.
120. Levy, R.B. and M. Boudart, *Platinum-Like Behavior of Tungsten Carbide in Surface Catalysis.* Science, 1973. **181**(4099): p. 547-549.
121. Frühberger, B. and J.G. Chen, *Reaction of Ethylene with Clean and Carbide-Modified Mo(110): Converting Surface Reactivities of Molybdenum to Pt-Group Metals.* Journal of the American Chemical Society, 1996. **118**(46): p. 11599-11609.
122. Lee, W.-S., et al., *Selective vapor-phase hydrodeoxygenation of anisole to benzene on molybdenum carbide catalysts.* Journal of Catalysis, 2014. **319**: p. 44-53.
123. Chen, C.-J., W.-S. Lee, and A. Bhan, *Mo2C catalyzed vapor phase hydrodeoxygenation of lignin-derived phenolic compound mixtures to aromatics under ambient pressure.* Applied Catalysis A: General, 2016. **510**: p. 42-48.
124. Lu, Q., et al., *Ordered Mesoporous Metal Carbides with Enhanced Anisole Hydrodeoxygenation Selectivity.* ACS Catalysis, 2016. **6**(6): p. 3506-3514.
125. Ghampson, I.T., et al., *Guaiacol transformation over unsupported molybdenum-based nitride catalysts.* Applied Catalysis A: General, 2012. **413-414**: p. 78-84.
126. Sepúlveda, C., et al., *Hydrodeoxygenation of 2-methoxyphenol over Mo2N catalysts supported on activated carbons.* Catalysis Today, 2011. **172**(1): p. 232-239.
127. Furimsky, E., *Metal carbides and nitrides as potential catalysts for hydroprocessing.* Applied Catalysis A: General, 2003. **240**(1): p. 1-28.
128. Bu, Q., et al., *A review of catalytic hydrodeoxygenation of lignin-derived phenols from biomass pyrolysis.* Bioresource Technology, 2012. **124**: p. 470-477.
129. Ripley, R.L., *The preparation and properties of some transition phosphides.pdf.* JOURNAL OF THE LESS-COMMON METALS, 1962. **4**: p. 496-503.
130. Oyama, S.T., *Transition Metal Carbides, Nitrides, and Phosphides*, in *Handbook of Heterogeneous Catalysis*. 2008.
131. Oyama, S.T., et al., *Transition metal phosphide hydroprocessing catalysts: A review.* Catalysis Today, 2009. **143**(1-2): p. 94-107.
132. Baudler, M., Angew Chem Int Ed Engl, 1987. **26**: p. 419.
133. B.Aronsson, T.L., S. Rundqvis, *Borides, Silicides and Phosphides.* Methuen, London and Wiley, New York., 1965.
134. Hägg, G.Z., Phys. Chem., 1931. **12**: p. 33.
135. Oyama, S.T., *Novel catalysts for advanced hydroprocessing: transition metal phosphides.* Journal of Catalysis, 2003. **216**(1-2): p. 343-352.
136. Phillips, D.C., et al., *Synthesis, Characterization, and Hydrodesulfurization Properties of Silica-Supported Molybdenum Phosphide Catalysts.* Journal of Catalysis, 2002. **207**(2): p. 266-273.
137. Sawhill, S., *Thiophene hydrodesulfurization over supported nickel phosphide catalysts.* Journal of Catalysis, 2003. **215**(2): p. 208-219.
138. Rundqvist, S., Colloq. Int. Cent. Nat. Rech. Sci. , 1967. **157**: p. 85.

139. S.Rundqvist, Acta Chem. Scand, 1962. **16**: p. 992.
140. Rundqvist, S., Nature, 1966. **211**: p. 847.
141. West, A.R., *Solid State Chemistry and its applications* Wiley, Chichester., 1992.
142. Hector, A.L. and I.P. Parkin, Inorg. Chem., 1994. **33**: p. 1727.
143. Martin, J. and R. Gruehn, Sol. Stat. Ion, 1990. **43**: p. 19.
144. Lewis, G. and C.E. Myers, Journal of Physical Chemistry, 1993. **67**: p. 1289.
145. Fjellvag, H., A. Kjekshus, and A.F. Andresen, Acta Chem. Scand A, 1984. **38**: p. 711.
146. Lewkebanadara, T.S., J.W. Proscia, and C.H. Winter, Chem. Mater., 1995. **7**: p. 1053.
147. Li, W., B. Dhandapani, and S.T. Oyama, Chemical Letters, 1998. **27**: p. 207.
148. Burns, S., J.S.J. Hargreaves, and S.M. Hunter, Catalysis Communications, 2007. **8**: p. 931.
149. Yang, S., C. Liang, and R. Prins, Studies in Surface Science and Catalysis, 2006. **162**: p. 307.
150. Lui, Z., et al., Ceram. Int., 2010. **36**: p. 1155.
151. Wang, X., P. Clark, and S.T. Oyama, *Synthesis, Characterization, and Hydrotreating Activity of Several Iron Group Transition Metal Phosphides.* Journal of Catalysis, 2002. **208**(2): p. 321-331.
152. Oyama, S., *Effect of Phosphorus Content in Nickel Phosphide Catalysts Studied by XAFS and Other Techniques.* Journal of Catalysis, 2002. **210**(1): p. 207-217.
153. Oyama, S.T., et al., *Active phase of Ni2P/SiO2 in hydroprocessing reactions.* Journal of Catalysis, 2004. **221**(2): p. 263-273.
154. Sawhill, S., et al., *Thiophene hydrodesulfurization over nickel phosphide catalysts: effect of the precursor composition and support.* Journal of Catalysis, 2005. **231**(2): p. 300-313.
155. Burns, A.W., et al., *Understanding the relationship between composition and hydrodesulfurization properties for cobalt phosphide catalysts.* Applied Catalysis A: General, 2008. **343**(1-2): p. 68-76.
156. Wang, A., et al., *Hydrodesulfurization of dibenzothiophene over siliceous MCM-41-supported nickel phosphide catalysts.* Journal of Catalysis, 2005. **229**(2): p. 314-321.
157. Duan, X., et al., *Role of sulfur in hydrotreating catalysis over nickel phosphide.* Journal of Catalysis, 2009. **261**(2): p. 232-240.
158. Stinner, C., R. Prins, and T. Weber, *Binary and Ternary Transition-Metal Phosphides as HDN Catalysts.* Journal of Catalysis, 2001. **202**(1): p. 187-194.
159. Prins, R. and M.E. Bussell, *Metal Phosphides: Preparation, Characterization and Catalytic Reactivity.* Catalysis Letters, 2012. **142**(12): p. 1413-1436.
160. Cecilia, J.A., et al., *Dibenzothiophene hydrodesulfurization over cobalt phosphide catalysts prepared through a new synthetic approach: Effect of the support.* Applied Catalysis B: Environmental, 2009. **92**(1-2): p. 100-113.
161. Cecilia, J.A., et al., *A novel method for preparing an active nickel phosphide catalyst for HDS of dibenzothiophene.* Journal of Catalysis, 2009. **263**(1): p. 4-15.
162. Li, K., R. Wang, and J. Chen, *Hydrodeoxygenation of Anisole over Silica-Supported Ni2P, MoP, and NiMoP Catalysts.* Energy & Fuels, 2011. **25**(3): p. 854-863.
163. Li, X., et al., *Heterogeneous sulfur-free hydrodeoxygenation catalysts for selectively upgrading the renewable bio-oils to second generation biofuels.* Renewable and Sustainable Energy Reviews, 2018. **82**: p. 3762-3797.
164. Infantes-Molina, A., et al., *Nickel and cobalt phosphides as effective catalysts for oxygen removal of dibenzofuran: role of contact time, hydrogen pressure and hydrogen/feed molar ratio.* Catalysis Science & Technology, 2015. **5**(6): p. 3403-3415.
165. Guo, C., et al., *Hydrodeoxygenation of fast pyrolysis oil with novel activated carbon-supported NiP and CoP catalysts.* Chemical Engineering Science, 2018. **178**: p. 248-259.
166. Zarchin, R., et al., *Hydroprocessing of soybean oil on nickel-phosphide supported catalysts.* Fuel, 2015. **139**: p. 684-691.
167. Koike, N., et al., *Upgrading of pyrolysis bio-oil using nickel phosphide catalysts.* Journal of Catalysis, 2016. **333**: p. 115-126.
168. Lan, X., *Transition metal phosphides : synthesis and catalytic properties in hydrodesulfurization and hydrodeoxygenation Eindhoven*. 2018, Technische Universiteit Eindhoven.
169. Wu, S.-K., et al., *Atmospheric Hydrodeoxygenation of Guaiacol over Alumina-, Zirconia-, and Silica-Supported Nickel Phosphide Catalysts.* ACS Sustainable Chemistry & Engineering, 2013. **1**(3): p. 349-358.
170. Pitakjakpipop, P., *Effects of support for Ni2P catalysts on hydrogenation of bio-oil using anisole as guaiacol as model compounds*. 2016, The Pennsylvania State University: Pennsylvania (U.S.).
171. Bui, P., et al., *Studies of the synthesis of transition metal phosphides and their activity in the hydrodeoxygenation of a biofuel model compound.* Journal of Catalysis, 2012. **294**: p. 184–198.

172. Yuan, Y., et al., *Preparation of Fe 2 P and FeP catalysts for the hydrotreating reactions.* Catalysis Communications, 2017. **100**: p. 202-205.
173. De, S., et al., *Ni-based bimetallic heterogeneous catalysts for energy and environmental applications.* Energy & Environmental Science, 2016. **9**(11): p. 3314-3347.
174. Abu, I.I. and K.J. Smith, *HDN and HDS of model compounds and light gas oil derived from Athabasca bitumen using supported metal phosphide catalysts.* Applied Catalysis A: General, 2007. **328**(1): p. 58-67.
175. Burns, A.W., A.F. Gaudette, and M.E. Bussell, *Hydrodesulfurization properties of cobalt–nickel phosphide catalysts: Ni-rich materials are highly active.* Journal of Catalysis, 2008. **260**(2): p. 262-269.
176. Gaudette, A.F., et al., *Mössbauer spectroscopy investigation and hydrodesulfurization properties of iron–nickel phosphide catalysts.* Journal of Catalysis, 2010. **272**(1): p. 18-27.
177. Zhao, H., et al., *Nature of active sites in Ni 2 P hydrotreating catalysts as probed by iron substitution.* Applied Catalysis B: Environmental, 2015. **164**: p. 204-216.
178. Fang, M., et al., *Performance of Ni-rich bimetallic phosphides on simultaneous quinoline hydrodenitrogenation and dibenzothiophene hydrodesulfurization.* Fuel Processing Technology, 2015. **129**: p. 236-244.
179. Lee, Y.-K. and S.T. Oyama, *Bifunctional nature of a SiO2-supported Ni2P catalyst for hydrotreating: EXAFS and FTIR studies.* Journal of Catalysis, 2006. **239**(2): p. 376-389.
180. Pedersenmjaanes, H., L. Chan, and E. Mastorakos, *Hydrogen production from rich combustion in porous media.* International Journal of Hydrogen Energy, 2005. **30**(6): p. 579-592.
181. Li, X., et al., *Engineering heterogeneous semiconductors for solar water splitting.* Journal of Materials Chemistry A, 2015. **3**(6): p. 2485-2534.
182. Schoegl, I., S.R. Newcomb, and J.L. Ellzey, *Ultra-rich combustion in parallel channels to produce hydrogen-rich syngas from propane.* International Journal of Hydrogen Energy, 2009. **34**(12): p. 5152-5163.
183. Montini, T., et al., *H2 production by photocatalytic reforming of oxygenated compounds using TiO2-based materials.* Materials Science in Semiconductor Processing, 2016. **42**: p. 122-130.
184. V, D., *Steam reforming of sunflower oil for hydrogen gas production.* Helia, 2007. **30**(46): p. 103-132.
185. Dal Santo, V., et al., *Bimetallic heterogeneous catalysts for hydrogen production.* Catalysis Today, 2012. **197**(1): p. 190-205.
186. Christoforidis, K.C. and P. Fornasiero, *Photocatalytic Hydrogen Production: A Rift into the Future Energy Supply.* ChemCatChem, 2017. **9**(9): p. 1523-1544.
187. Colón, G., *Towards the hydrogen production by photocatalysis.* Applied Catalysis A: General, 2016. **518**: p. 48-59.
188. Chiarello, G.L., M.H. Aguirre, and E. Selli, *Hydrogen production by photocatalytic steam reforming of methanol on noble metal-modified TiO2.* Journal of Catalysis, 2010. **273**(2): p. 182-190.
189. Simpson, A.P. and A.E. Lutz, *Exergy analysis of hydrogen production via steam methane reforming.* International Journal of Hydrogen Energy, 2007. **32**(18): p. 4811-4820.
190. Rasi, S., J. Läntelä, and J. Rintala, *Trace compounds affecting biogas energy utilisation – A review.* Energy Conversion and Management, 2011. **52**(12): p. 3369-3375.
191. Yoong, L.S., F.K. Chong, and B.K. Dutta, *Development of copper-doped TiO2 photocatalyst for hydrogen production under visible light.* Energy, 2009. **34**(10): p. 1652-1661.
192. Sharma, S. and S.K. Ghoshal, *Hydrogen the future transportation fuel: From production to applications.* Renewable and Sustainable Energy Reviews, 2015. **43**: p. 1151-1158.
193. Belmont, E.L., S.M. Solomon, and J.L. Ellzey, *Syngas production from heptane in a non-catalytic counter-flow reactor.* Combustion and Flame, 2012. **159**(12): p. 3624-3631.
194. Peighambardoust, S.J., S. Rowshanzamir, and M. Amjadi, *Review of the proton exchange membranes for fuel cell applications.* International Journal of Hydrogen Energy, 2010. **35**(17): p. 9349-9384.
195. Sharaf, O.Z. and M.F. Orhan, *An overview of fuel cell technology: Fundamentals and applications.* Renewable and Sustainable Energy Reviews, 2014. **32**: p. 810-853.
196. Kirubakaran, A., S. Jain, and R.K. Nema, *A review on fuel cell technologies and power electronic interface.* Renewable and Sustainable Energy Reviews, 2009. **13**(9): p. 2430-2440.
197. Lindström, B. and L.J. Pettersson, *Hydrogen generation by steam reforming of methanol over copper-based catalysts for fuel cell applications.* International Journal of Hydrogen Energy, 2001. **26**(9): p. 923-933.

198. Takenaka, S., T. Shimizu, and K. Otsuka, *Complete removal of carbon monoxide in hydrogen-rich gas stream through methanation over supported metal catalysts.* International Journal of Hydrogen Energy, 2004. **29**(10): p. 1065-1073.
199. Alstrup, I., *On the Kinetics of Co Methanation on Nickel Surfaces.* Journal of Catalysis, 1995. **151**(1): p. 216-225.
200. Mishra, A.P., R., *A Review on Preferential Oxidation of CarbonMonoxide in Hydrogen Rich Gases.* Bulletin of Chemical Reaction Engineering &Catalysis, 2011. **6**: p. 1-14.
201. Morse, J.D., *Micro-fuel cell power sources.* Int. J. Energ. Res., 2007. **31**: p. 576-602.
202. Trimm, D.L., *Minimisation of carbon monoxide in a hydrogen stream for fuel cell application.* Applied Catalysis A: General, 2005. **296**(1): p. 1-11.
203. Zhang, Y., et al., *Three-dimensionally ordered macro-porous CuO–CeO2 used for preferential oxidation of carbon monoxide in hydrogen-rich gases.* Catalysis Communications, 2009. **10**(10): p. 1432-1436.
204. Avgouropoulos, G., et al., Catalysis Letters, 2001. **73**: p. 1.
205. Mariño, F., C. Descorme, and D. Duprez, *Noble metal catalysts for the preferential oxidation of carbon monoxide in the presence of hydrogen (PROX).* Applied Catalysis B: Environmental, 2004. **54**(1): p. 59-66.
206. Chin, S.Y., O.S. Alexeev, and M.D. Amiridis, *Preferential oxidation of CO under excess H2 conditions over Ru catalysts.* Applied Catalysis A: General, 2005. **286**(2): p. 157-166.
207. Galletti, C., et al., *CO preferential oxidation in H2-rich gas for fuel cell applications: Microchannel reactor performance with Rh-based catalyst.* International Journal of Hydrogen Energy, 2008. **33**(12): p. 3045-3048.
208. Bera, P., et al., *Ionic Dispersion of Pt and Pd on CeO2 by Combustion Method: Effect of Metal–Ceria Interaction on Catalytic Activities for NO Reduction and CO and Hydrocarbon Oxidation.* Journal of Catalysis, 2000. **196**(2): p. 293-301.
209. Marbán, G. and A.B. Fuertes, *Highly active and selective CuOx/CeO2 catalyst prepared by a single-step citrate method for preferential oxidation of carbon monoxide.* Applied Catalysis B: Environmental, 2005. **57**(1): p. 43-53.
210. Skårman, B., et al., *Carbon Monoxide Oxidation on Nanostructured CuOx/CeO2 Composite Particles Characterized by HREM, XPS, XAS, and High-Energy Diffraction.* Journal of Catalysis, 2002. **211**(1): p. 119-133.
211. Avgouropoulos, G., et al., *A comparative study of Pt/γ-Al2O3, Au/α-Fe2O3 and CuO–CeO2 catalysts for the selective oxidation of carbon monoxide in excess hydrogen.* Catalysis Today, 2002. **75**(1): p. 157-167.
212. G.C.Bond, C.L., D.T. Thompson *Catalysis by Gold, Imperial Press, London 2007*
213. Yi, N. and M. Flytzani-Stephanopoulos, *The making of a robust catalyst for fuel processing and hydrogen production, in catalysis by materials with well-defined structures*, A. Elsevier, Editor. 2015. p. 133-158.
214. Haruta, M., et al., *Low-Temperature Oxidation of CO over Gold Supported on TiO2, α-Fe2O3, and Co3O4.* Journal of Catalysis, 1993. **144**(1): p. 175-192.
215. Schubert, M.M., et al., *CO Oxidation over Supported Gold Catalysts—"Inert" and "Active" Support Materials and Their Role for the Oxygen Supply during Reaction.* Journal of Catalysis, 2001. **197**(1): p. 113-122.
216. Zepeda, T.A., et al., *Preferential CO oxidation in excess of hydrogen over Au/HMS catalysts modified by Ce, Fe and Ti oxides.* Applied Catalysis B: Environmental, 2010. **100**(3): p. 450-462.
217. T. Kamegawa, R.T., M. Matsuoka, M. Anpo, *Characterization of Mo/SiO2 and Mo/Al2O3 and their photocatalytic reactivity for the selective oxidation of CO with O2 in the presence of H2.* 11th International Symposium on Hybrid Nano Materials toward Future Industries. Nagaoka, Japan. 3-5 February 2006.
218. Dai, W., et al., *The promoted effect of UV irradiation on preferential oxidation of CO in an H2-rich stream over Au/TiO2.* Journal of Power Sources, 2009. **188**(2): p. 507-514.
219. Liu, J., et al., *The promoted oxidation of CO induced by the visible-light response of Au nanoparticles over Au/TiO2.* Catalysis Communications, 2012. **26**: p. 136-139.
220. Yang, K., et al., *Comparative study of Au/TiO2 and Au/Al2O3 for oxidizing CO in the presence of H2 under visible light irradiation.* Journal of Catalysis, 2014. **317**: p. 229-239.

221. Yang, K., et al., *Promoted effect of PANI on the preferential oxidation of CO in the presence of H2 over Au/TiO2 under visible light irradiation.* International Journal of Hydrogen Energy, 2014. **39**(32): p. 18312-18325.
222. Zhang, Y., et al., *The promoted effect of a metal-organic frameworks (ZIF-8) on Au/TiO2 for CO oxidation at room temperature both in dark and under visible light irradiation.* Applied Catalysis B: Environmental, 2018. **224**: p. 283-294.
223. Bai, H., et al., *Enhanced adsorbability and photocatalytic activity of TiO2-graphene composite for polycyclic aromatic hydrocarbons removal in aqueous phase.* Colloids Surf B Biointerfaces, 2017. **150**: p. 68-77.
224. Litter, M.I., *Heterogeneous photocatalysis Transition metal ions in photocatalytic systems.* Applied Catalysis B: Environmental, 1999. **23**: p. 89-114.
225. Nakata, K. and A. Fujishima, *TiO2 photocatalysis: Design and applications.* Journal of Photochemistry and Photobiology C: Photochemistry Reviews, 2012. **13**(3): p. 169-189.
226. Fujishima, A. and K. Honda, *Electrochemical Photolysis of Water at a Semiconductor Electrode.* Nature, 1972. **238**: p. 37.
227. Fujishima, A., T.N. Rao, and D.A. Tryk, *Titanium dioxide photocatalysis.* Journal of Photochemistry and Photobiology C: Photochemistry Reviews, 2000. **1**: p. 1-21.
228. Fujishima, A., X. Zhang, and D. Tryk, *TiO2 photocatalysis and related surface phenomena.* Surface Science Reports, 2008. **63**(12): p. 515-582.
229. Inoue, T., et al., *Photoelectrocatalytic reduction of carbon dioxide in aqueous suspensions of semiconductor powders.* Nature, 1979. **277**: p. 637.
230. McCullagh, C., et al., *The application of TiO2 photocatalysis for disinfection of water contaminated with pathogenic micro-organisms: a review.* Research on Chemical Intermediates, 2007. **33**(3): p. 359-375.
231. Nosaka, Y., et al., *Singlet oxygen formation in photocatalytic TiO2 aqueous suspension.* Physical Chemistry Chemical Physics, 2004. **6**(11): p. 2917-2918.
232. Nosaka, A.Y., et al., *Photoinduced Changes of Adsorbed Water on a TiO2 Photocatalytic Film As Studied by 1H NMR Spectroscopy.* The Journal of Physical Chemistry B, 2003. **107**(44): p. 12042-12044.
233. Fujishima, A., X. Zhang, and D.A. Tryk, *Heterogeneous photocatalysis: From water photolysis to applications in environmental cleanup.* International Journal of Hydrogen Energy, 2007. **32**(14): p. 2664-2672.
234. Wang, R., et al., *Light-induced amphiphilic surfaces.* Nature, 1997. **388**.
235. Panayotov, D.A. and J.R. Morris, *Surface chemistry of Au/TiO2: Thermally and photolytically activated reactions.* Surface Science Reports, 2016. **71**(1): p. 77-271.
236. Kubacka, A., M. Fernandez-Garcia, and G. Colon, *Advanced nanoarchitectures for solar photocatalytic applications.* Chem Rev, 2012. **112**(3): p. 1555-614.
237. Primo, A., A. Corma, and H. Garcia, *Titania supported gold nanoparticles as photocatalyst.* Phys Chem Chem Phys, 2011. **13**(3): p. 886-910.
238. Puga, A.V., *Review.* Coordination Chemistry Reviews, 2016. **315**(C): p. 1-66.
239. Xiang, Q., et al., *Microwave-hydrothermal preparation and visible-light photoactivity of plasmonic photocatalyst Ag-TiO2 nanocomposite hollow spheres.* Chem Asian J, 2010. **5**(6): p. 1466-74.
240. Zhang, X., et al., *Efficient photodegradation of 4,4'-(propane-2,2-diyl)diphenol over biomolecule modified titanium dioxide under visible light irradiation.* Catalysis Communications, 2011. **16**(1): p. 7-10.
241. Xu, S.B., et al., *The influence of the oxidation degree of poly(3-hexylthiophene) on the photocatalytic activity of poly(3-hexylthiophene)/TiO2 composites.* Solar Energy Materials and Solar Cells, 2012. **96**(1): p. 286-291.
242. Bessekhouad, Y., D. Robert, and J.V. Weber, *Photocatalytic activity of Cu2O/TiO2, Bi2O3/TiO2 and ZnMn2O4/TiO2 heterojunctions.* Catalysis Today, 2005. **101**(3): p. 315-321.
243. Libanori, R., et al., *Effect of TiO2 surface modification in Rhodamine B photodegradation.* Journal of Sol-Gel Science and Technology, 2008. **49**(1): p. 95-100.
244. Kamat, P.V., *Photophysical, Photochemical and Photocatalytic Aspects of Metal Nanoparticles.* The Journal of Physical Chemistry B, 2002. **106**(32): p. 7729-7744.
245. Watanabe, K., et al., *Photochemistry on Metal Nanoparticles.* Chemical Reviews, 2006. **106**(10): p. 4301-4320.
246. Sarina, S., E.R. Waclawik, and H. Zhu, *Photocatalysis on supported gold and silver nanoparticles under ultraviolet and visible light irradiation.* Green Chemistry, 2013. **15**(7): p. 1814.

247. Ke, X., et al., *Selective reductions using visible light photocatalysts of supported gold nanoparticles.* Green Chem., 2013. **15**(1): p. 236-244.
248. Kozlova, E.A., et al., *Influence of the method of platinum deposition on activity and stability of Pt/TiO2 photocatalysts in the photocatalytic oxidation of dimethyl methylphosphonate.* Catalysis Communications, 2011. **12**(7): p. 597-601.
249. Haruta, M., *Spiers Memorial Lecture : Role of perimeter interfaces in catalysis by gold nanoparticles.* Faraday Discussions, 2011. **152**: p. 11.
250. Orendorff, C.J., T.K. Sau, and C.J. Murphy, *Shape-dependent plasmon-resonant gold nanoparticles.* Small, 2006. **2**(5): p. 636-9.
251. Link, S. and M.A. El-Sayed, *Shape and size dependence of radiative, non-radiative and photothermal properties of gold nanocrystals.* International Reviews in Physical Chemistry, 2000. **19**(3): p. 409-453.
252. Cottancin, E., et al., *Optical Properties of Noble Metal Clusters as a Function of the Size: Comparison between Experiments and a Semi-Quantal Theory.* Theoretical Chemistry Accounts, 2006. **116**(4): p. 514-523.
253. Kelly, K.L., et al., *The Optical Properties of Metal Nanoparticles: The Influence of Size, Shape, and Dielectric Environment.* The Journal of Physical Chemistry B, 2003. **107**(3): p. 668-677.
254. Du, L., et al., *Plasmon-Induced Charge Separation and Recombination Dynamics in Gold-TiO2 Nanoparticle Systems: Dependence on TiO2 Particle Size.* Journal of Physical Chemistry, 2009. **113**: p. 6454-6462.
255. Eustis, S. and M.A. El-Sayed, *Why gold nanoparticles are more precious than pretty gold: Noble metal surface plasmon resonance and its enhancement of the radiative and nonradiative properties of nanocrystals of different shapes.* Chemical Society Reviews, 2006. **35**(3): p. 209-217.
256. Alvarez, M.M., et al., *Optical Absorption Spectra of Nanocrystal Gold Molecules.* Journal of Physical Chemistry, 1997. **101**: p. 3706-3712.
257. Zhang, X., et al., *Plasmonic photocatalysis.* Rep Prog Phys, 2013. **76**(4): p. 046401.
258. Linic, S., P. Christopher, and D.B. Ingram, *Plasmonic-metal nanostructures for efficient conversion of solar to chemical energy.* Nat Mater, 2011. **10**(12): p. 911-21.
259. Hou, W. and S.B. Cronin, *A Review of Surface Plasmon Resonance-Enhanced Photocatalysis.* Advanced Functional Materials, 2013. **23**(13): p. 1612-1619.
260. Tian, Y. and T. Tatsuma, *Mechanisms and Applications of Plasmon-Induced Charge Separation at TiO2 Films Loaded with Gold Nanoparticles.* Journal of the American Chemical Society, 2005. **127**(20): p. 7632-7637.
261. Ingram, D.B., et al., *Predictive Model for the Design of Plasmonic Metal/Semiconductor Composite Photocatalysts.* ACS Catalysis, 2011. **1**(10): p. 1441-1447.
262. Hasobe, T., et al., *Quaternary Self-Organization of Porphyrin and Fullerene Units by Clusterization with Gold Nanoparticles on SnO2 Electrodes for Organic Solar Cells.* Journal of the American Chemical Society, 2003. **125**(49): p. 14962-14963.
263. Bond, G.C. and D.T. Thompson, *Gold-catalysed oxidation of carbon monoxide.* Gold Bulletin, 2000. **33**(2): p. 41-50.
264. Powell, C.D., et al., *CO Adsorption on Au/TiO2 Catalysts: Observations, Quantification, and Explanation of a Broad-Band Infrared Signal.* The Journal of Physical Chemistry C, 2017. **121**(44): p. 24541-24547.
265. Moreau, F., G.C. Bond, and A.O. Taylor, *Gold on titania catalysts for the oxidation of carbon monoxide: control of pH during preparation with various gold contents.* Journal of Catalysis, 2005. **231**(1): p. 105-114.
266. Kato, K., et al., *Crystal structure of TiO2 thin coatings prepared from the alkoxide solution via the dip-coating.* Journal of materials science, 1994. **29**: p. 5911-5915.
267. Smith, S.J., et al., *Heat capacities and thermodynamic functions of TiO2 anatase and rutile: Analysis of phase stability.* American Mineralogist, 2009. **94**(2-3): p. 236-243.
268. Sang, L., Y. Zhao, and C. Burda, *TiO2 nanoparticles as functional building blocks.* Chem Rev, 2014. **114**(19): p. 9283-318.
269. Hurum, D.C., et al., *Recombination Pathways in the Degussa P25 Formulation of TiO2: Surface versus Lattice Mechanisms.* The Journal of Physical Chemistry B, 2005. **109**(2): p. 977-980.
270. Kubacka, A., M. Fernández-García, and G. Colón, *Advanced Nanoarchitectures for Solar Photocatalytic Applications.* Chemical Reviews, 2012. **112**(3): p. 1555-1614.
271. Allen, N.S., et al., *The effect of crystalline phase (anatase, brookite and rutile) and size on the photocatalytic activity of calcined polymorphic titanium dioxide (TiO2).* Polymer Degradation and Stability, 2018. **150**: p. 31-36.

272. Kislov, N., et al., *Photocatalytic Degradation of Methyl Orange over Single Crystalline ZnO: Orientation Dependence of Photoactivity and Photostability of ZnO.* Langmuir, 2009. **25**(5): p. 3310-3315.
273. Morris Hotsenpiller, P.A., et al., *Orientation Dependence of Photochemical Reactions on TiO2 Surfaces.* The Journal of Physical Chemistry B, 1998. **102**(17): p. 3216-3226.
274. Scanlon, D.O., et al., *Band alignment of rutile and anatase TiO(2).* Nat Mater, 2013. **12**(9): p. 798-801.
275. Batzill, M., *Fundamental aspects of surface engineering of transition metal oxide photocatalysts.* Energy & Environmental Science, 2011. **4**(9): p. 3275-3286.
276. Xu, M., et al., *Photocatalytic Activity of Bulk ${\mathrm{TiO}}_{2}$ Anatase and Rutile Single Crystals Using Infrared Absorption Spectroscopy.* Physical Review Letters, 2011. **106**(13): p. 138302.
277. Kavan, L., et al., *Electrochemical and Photoelectrochemical Investigation of Single-Crystal Anatase.* Journal of the American Chemical Society, 1996. **118**(28): p. 6716-6723.
278. Liu, B., et al., *Mesoporous TiO2 Core–Shell Spheres Composed of Nanocrystals with Exposed High-Energy Facets: Facile Synthesis and Formation Mechanism.* Langmuir, 2011. **27**(13): p. 8500-8508.
279. K. Nakata, B.L., Y. Ishikawa, M. Sakai, H. Saito, T. Ochiai, H. Sakai, T. Murakami, and K.T. M. Abe, A. Fujishima, *Fabrication and photocatalytic properties of TiO2 nanotube arrays modified with phosphate.* Chem. Lett., 2011. **40**(): p. 1107–1109.
280. Katsumata, K.-i., et al., *Preparation and Characterization of Self-Cleaning Glass for Vehicle with Niobia Nanosheets.* ACS Applied Materials & Interfaces, 2010. **2**(4): p. 1236-1241.
281. Almquist, C.B. and P. Biswas, *Role of Synthesis Method and Particle Size of Nanostructured TiO2 on Its Photoactivity.* Journal of Catalysis, 2002. **212**(2): p. 145-156.
282. Zielińska-Jurek, A., *Progress, Challenge, and Perspective of Bimetallic TiO2-Based Photocatalysts.* Journal of Nanomaterials, 2014. **2014**: p. 1-17.
283. Gu, J., Y.W. Zhang, and F.F. Tao, *Shape control of bimetallic nanocatalysts through well-designed colloidal chemistry approaches.* Chem Soc Rev, 2012. **41**(24): p. 8050-65.

2. OBJECTIVES

2. Objectives

As previously stated, the present thesis is raised from two perspectives that imply in both cases the development of catalytic systems for the study of reactions of energetic and environmental interest. On the one hand, transition metal phosphides based catalysts have been studied in hydrodeoxygenation reactions of model molecules present in the bio-oil from lignocellulosic biomass. On the other hand, gold nanoparticles supported on titania structures have been tested in the preferential oxidation of CO in excess of H_2 under simulated solar light irradiation at room temperature and atmospheric pressure. Hence the main objectives of chapters 4-6 are summarized as follows:

- Synthesis of mono and bimetallic nickel and iron phosphides supported on silica with different Ni/Fe molar ratios (0/1, 2/1, 3/1 and 1/0). Evaluation of the role of iron in the catalytic response of phenol HDO reaction.
- Synthesis of cobalt phosphides catalysts supported on silica with different stoichiometry (P/Co molar ratios= 0.5, 1, 1.5, 2 and 2.5). Evaluation of composition effects in the HDO reaction of phenol and dibenzofuran.
- Synthesis of iron phosphides catalysts supported on silica with P/Fe molar ratios= 0.5, 1, 2 and 3. Evaluation of the stoichiometry effects in the catalytic activity of phenol HDO.

The common objectives in the three chapters are as follows:

- Synthesis by the incipient wetness impregnation method and subsequent hydrogen thermo-programmed reduction. Evaluation of structural, textural, compositional and acidic properties, among others, by means of a wide range of characterization techniques such as XRD, XPS, HRTEM, N_2 Physisorption, NH_3-TPD, H_2-TPD, CO chemisorption, Mösbauer spectroscopy, Infrared spectroscopy and elemental analysis in order to gain a greater understanding of the catalytic results.

The main objectives of chapters 7 and 8 are summarized below:

- Deposition-precipitation of gold nanoparticles over mesoporous titania supports, previously synthesized by a sol-gel type method and calcined at different temperatures, placing special attention on the effects of TiO_2 polymorph.
- Synthesis of gold nanoparticles supported on titania nanorods based structures, previously synthetized by two hydrothermal methods (basic and acid one) and calcined at different temperatures, by the deposition-precipitation method.

The common objectives of both chapters are:

- Study of the photo-response of Au/TiO_2 based systems in the preferential oxidation of CO in a H_2-rich stream under simulated solar light irradiation at room temperature and atmospheric pressure. Characterization of their structural, chemical and optical properties by means of XRD, XPS, HRTEM, DRUV-Vis, AAS, XFR, N_2 physisorption, SAXS.

3. EXPERIMENTAL

3.1. Chemical reagents for HDO

All the reagents required for the synthesis of the catalysts for the HDO study are compiled in Table 3.1.

Table 3.1. Chemical reagents used for the synthesis of the catalysts

Reagents	Molecular formula	Purity (%)	Trading house
Silica, fumed(silicon dioxide amorphous)	SiO_2	100	Sigma-Aldrich
Phosphorous acid	H_3PO_3	99	Analytical
Nickel(II) hydroxide	$Ni(OH)_2$	100	Aldrich
Iron(II) nitrate nonahydrate	$Fe(NO_3)_2 \cdot 9H2O$	98	Alfa Aesar
Cobalt(II) hydroxide	$Co(OH)_2$	99	Aldrich
Nitric acid	HNO_3	65	VWR Chemicals

The gases used during the characterization and catalytic study of the synthetized catalysts are shown in Table 3.2.

Table 3.2. Gases used for characterization and catalytic study

Reagents	Purity (%)	Trading house
Helium	99.999%	Air Liquid
Nitrogen	99.999%	Air Liquid
Hydrogen	99.999%	Air Liquid
Ammonia	99.9%	Air Liquid
Argon	99.999%	Air Liquid
Synthetic Air ($20\%O_2/80\%N_2$)	99.999%	Air Liquid
$0.5\%O_2/99.5\%N_2$	99.999%	Air Liquid
Carbon monoxide	99.9%	Air Liquid

The organic feed, solvents and the internal standard pumped into the reactor are detailed in Table 3.3 below.

Table 3.3. Reagents used as solvents and organic feed

Reagents	Molecular formula	Purity (%)	Trade house
Phenol	C_6H_6O	99	Amresco
n-octane	C_8H_{18}	95	VWR Chemicals
Dibenzofuran	$C_{12}H_8O$	98	Alfa Aesar
Decalin	$C_{10}H_{18}$	98	Alfa Aesar
n-nonane	C_9H_{20}	95	Alfa Aesar

3.2. Synthesis of HDO catalysts

The precursors of the catalysts for the HDO study have been synthesized by the incipient wetness impregnation method. This method consists on the impregnation of the support with a certain volume of a metal solution in such a way as to ensure a homogenous distribution among the support pores. The minimum volume required for the total impregnation of the support was determined by slowly adding distilled water over a known amount of SiO_2 until it is completely moistened. The required volume was 1.8 ml of H_2O per gram of SiO_2.

Once the impregnation volume was known, necessary amount of phosphorous acid was dissolved jointly with the required amount of transition metal salts and subsequently impregnated over the support. The impregnation was performed by adding the precursor solution drop by drop and milling homogeneously. The impregnated support was then dried at 60 ºC in the oven for one day. The activated precursors were then pelletized with a particle size between 0.85-1.00 mm as described below. First, the impregnated support was subjected to a pressure of 7-8 ton cm^{-2} by means of a hydraulic press obtaining thick tablets that eventually were milled and sieved. The sieves diameters were chosen as a function of the catalytic reactor bed dimensions. As a general rule, the particle size of the catalyst must be ten times less than the inner diameter of the catalytic reactor in order to avoid diffusional limitations. That is to say, in order to favor heat and mass transfer.

Finally, the pelletized precursors were reduced by hydrogen temperature-programmed reduction (H_2-TPR) under different temperature, gas flow and heating ramp conditions that will be discussed in more detail below.

The followed route for the synthesis of these transition metal phosphides has been developed by our research group. This route involves the reduction of a phosphite type precursor which is formed by adding stoichiometric amounts of the metallic salts and phosphorous acid giving rise to the dihydrogenphosphite metallic precursor $M(HPO_3H)_2$ [1]. This precursor is subjected to a

TPR-H_2 giving rise to the corresponding transition metal phosphide MxPy as described in section 1.6.2 of the Introduction.

3.2.1. Synthesis of bimetallic nickel and iron phosphides

Nickel and iron mono- and bimetallic phosphides were synthetized as abovementioned but the specific synthetic conditions are detailed now. Phosphorus, nickel and iron were introduced by the incipient wetness impregnation method by dissolving stoichiometric amounts of $Ni(OH)_2$ and $Fe(NO_3)_3 \cdot 9H_2O$ with H_3PO_3, and these solutions were used to impregnate silica. First, phosphorous acid was dissolved at 70 ºC followed by nickel(II) hydroxide dilution, also at 70 ºC. Lastly, the iron salt was dissolved at room temperature. As $Ni(OH)_2$ is poorly water soluble, 200 µL of HNO_3 was added in order to favor its dissolution. Once impregnated, the solids were air-treated at 60 ºC for 24 h in the oven. Finally, the precursors (0.5 g) were reduced in a tubular reactor by heating over two linear temperature ramps, 10 ºC·min^{-1} and 3 ºC·min^{-1}, in flowing hydrogen (100 mL·min^{-1}) from room temperature to 300 ºC and then from 300 to 620 ºC (2h), respectively. Once reduced, the catalysts were kept in cyclohexane in sealed vials to prevent oxidation of the phosphide phase. The weight load for the Ni_2P catalyst was adjusted to 5 wt% of Ni and the weight loads for the rest of the metal phosphide catalysts were adjusted to a final metal content of 5wt%. They will be referred to as Ni_2P, NiFeP3:1, NiFeP2:1 and FeP, where the ratios are the nominal Ni/Fe molar ratios. All these parameters along with P/M molar ratio are compiled in Table 3.4.

Table 3.4. Chemical composition of mono and bimetallic iron nickel phosphides

Nomenclature	Metal loading (%)	P/M[a]	Ni/Fe[b]
Ni_2P	5	2	-
NiFeP3:1	5	2	3
NiFeP2:1	5	2	2
FeP	5	2	-

[a]*Phosphorus/Metal molar ratio.* [b]*Nickel/iron molar ratio*

3.2.2. Synthesis of cobalt phosphides

Similarly, the synthesis of the cobalt phosphide catalysts was carried out following the same procedure. $Co(OH)_2$ and H_3PO_3 were added as cobalt and phosphorus sources, respectively, and fumed silica was used as support. H_2-TPR was performed ex-situ under a hydrogen flow of 100 mL·min^{-1} (heating rates of 10 and 3 ºC min^{-1}) from r.t. to 300 ºC and from 300 to 700ºC (2h). Once reduced, the catalysts were kept in cyclohexane in sealed vials to prevent oxidation of the phosphide phase. The catalysts will be referred to as P/Co-x, where the x is the initial P/Co molar ratio present on each sample (x=0.5, 1, 1.5, 2 and 2.5). Table 3.5 shows the nomenclature of the catalysts, metal loading and P/M molar ratio.

Table 3.5. Chemical composition for the synthesis of cobalt phosphides

Nomenclature	Metal loading (%)	P/M[a]
P/Co-0.5	5	0.5
P/Co-1	5	1
P/Co-1.5	5	1.5
P/Co-2	5	2
P/Co-2.5	5	2.5

[a]*Phosphorus/metal initial molar ratio*

3.2.3. Synthesis of iron phosphides

A series of iron phosphide catalysts was synthesized likewise by the same procedure using $Fe(NO_3)_3 \cdot 9H_2O$ as iron source and H_3PO_3 as phosphorus source. The precursors were reduced ex-situ under a hydrogen flow of 100 $mL \cdot min^{-1}$ in a tubular reactor by heating from r.t. to 300 ºC over a linear heating ramp of 10 $ºC \cdot min^{-1}$ and from 300 to 700 ºC (3 $ºC \cdot min^{-1}$) remaining 2 h at that temperature. After reduction, the iron phosphide based catalysts were cooled to room temperature under He flow and then passivated under 100 $mL \cdot min^{-1}$ of 0.5%O_2/N_2 flow for 4 h at room temperature. Thus, the prepared catalysts will be referred to as P/Fe-x, where x is the P/Fe molar ratio (x=0.5,1,2 and 3).

Table 3.6. Chemical composition for the synthesis of iron phosphides

Nomenclature	Metal loading (%)	P/M[a]
P/Fe-0.5	15	0.5
P/Fe-1	15	1
P/Fe-2	15	2
P/Fe-3	15	3

[a]*Phosphorus/Metal molar ratio*

3.3. HDO catalytic tests

The HDO of phenol and dibenzofuran were chosen as model reactions to evaluate the catalytic activity of the synthesized catalysts. These reactions were performed in a high-pressure fixed-bed continuous-flow stainless steel catalytic reactor (9.1 mm in diameter and 230 mm in length), operated in the down-flow mode. Figure 3.1 shows a scheme of the reactor. The reaction temperature was measured with an interior placed thermocouple in direct contact with the catalytic bed.

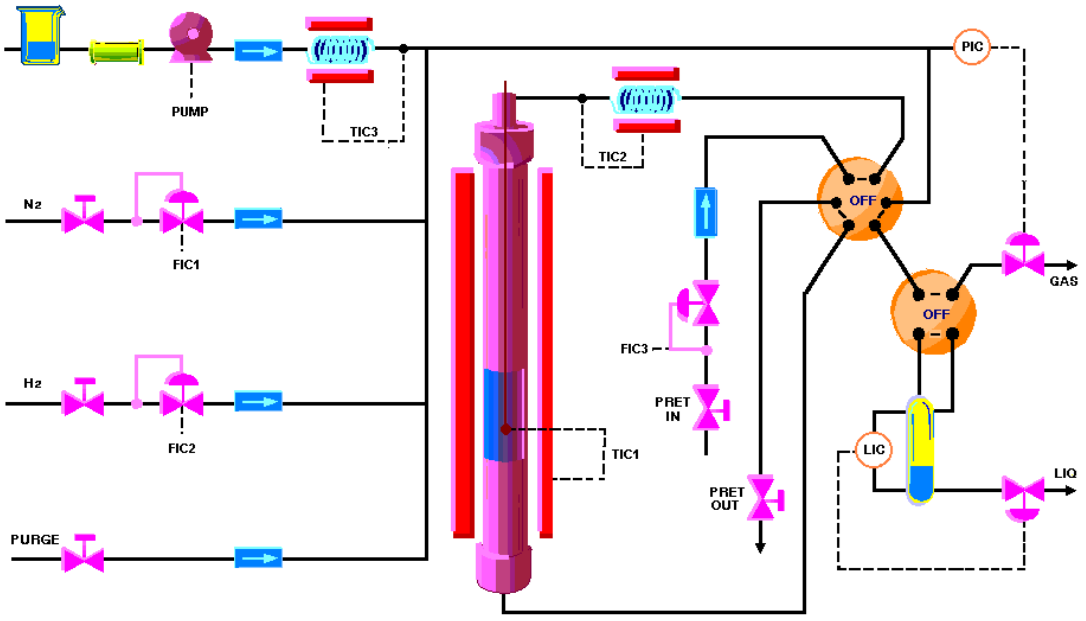

FIC= Mass flow PIC= Pressure meter; TIC= Thermocouple; LIC= Liquid Condenser

Figure 3.1. Scheme of the HDO reactor.

The organic feeds consisted of a solution of phenol (1 wt%) in octane and a solution of dibenzofuran (2 wt%) in decalin. Each solution was supplied by means of a Gilson 307SC piston pump (model 10SC). For the activity test, 0.25 g of catalyst were reduced ex-situ as described in section 3.2 and transferred in an inert solvent (cyclohexane) or passivated (the iron phosphide series) into the catalytic bed preloaded with silicon carbide to a total volume of 3 cm^3 (particle size 0.85-1.18 mm). Prior to the activity test, samples were treated in-situ at atmospheric pressure with a hydrogen flow of 100 $mL \cdot min^{-1}$ by heating from r.t. to 400 ºC (2 h) at a rate of 3 $ºC \cdot min^{-1}$.This pretreatment has the aim of ensuring the total reduction of the passivation layer on the surface of both catalysts kept in cyclohexane and passivated after reduction. The evolution of the reaction was monitored by collecting liquid samples which were kept in sealed vials and subsequently analyzed by gas chromatography (Shimadzu GC-14B, equipped with a flame ionization detector and a capillary column, TBR-14, coupled to an automatic Shimadzu AOC-20i injector). The catalytic studies were performed under different operating conditions which are detailed in Table 3.7. Besides temperature and pressure other parameters such as the weight hourly space velocity (WHSV), liquid hourly space velocity (LHSV) gas hourly space velocity (GHSV) and contact time are considered. In the industry, the WHSV is more frequently used being defined as the weight of feed flowing per unit weight of the catalyst per hour.

Table 3.7. Operating conditions of the studied catalysts during HDO process

Catalyst/ Reaction	T (ºC)	Pressure (MPa)	H_2 flow (ml/min)	Organic Feed (ml/min)	H_2 contact time (s)	GHSV (h^{-1})	WHSV (h^{-1})	LHSV (h^{-1})
NiFeP series/ HDO phenol	300	1.5-3.0	70-60-40-30	0.25	2.5-3-4.5-6	1400-1200-800-600	1-0.42-1-0.42	5
CoP series/ HDO phenol	300	3	30	0.25	6	600	0.42	5
CoP series/ HDO DBF	275	1.5-3	30	0.5	6	600	0.77	10
FeP series/ HDO phenol	275	0.5-1.5	30	0.15	6	600	0.3	3

The HDO conversion was calculated by the following equation:

$$\textit{HDO Conv. (\%)} = \frac{CF.Ini - CF.Fin - C\ Int}{CF.Ini} \times 100$$

Where CF.Ini is the phenol/dibenzofuran concentration in the feed, CF.Fin is the phenol/dibenzofuran concentration in the liquid product and C Int is the concentration of the O-containing intermediates.

Selectivity was calculated considering all the reaction products by using the following equation:

$$\mathbf{Si}\ (\%) = \frac{\mathbf{Ci}}{\mathbf{\Sigma Ci}} \times \mathbf{100}$$

Where Si is the selectivity of i-compound and Ci is the concentration of iproduct.

The turnover frequency number (TOF) was calculated from the formula:

$$\boldsymbol{TOF} = \frac{\boldsymbol{F/W}}{\boldsymbol{M}} \times \boldsymbol{ln}(\mathbf{1} - \boldsymbol{x})$$

Where F is the molar rate of the reaction ($mol \cdot min^{-1}$), W is the catalyst weight (g), X is the conversion factor and M is the number of sites loaded ($mol \cdot g^{-1}$). This formula was used because the conversion values were close to 100%, which is far from differential conditions making an integral analysis necessary.

3.4. Chemical reagents for CO Photo-PROX

All the reagents required for the synthesis of the catalysts for the CO photo-PROX study are compiled in Table 3.8.

Table 3.8. Chemical reagents used for the synthesis of the catalysts

Reagents	Molecular formula	Purity (%)	Trading house
Titanium (IV) isopropoxide	$[Ti(OC_3H_7)_4]$	97	Aldrich
Ethanol	C_2H_5OH	100%	Merck
Gold (III) chloride trihydrate	$HAuCl_4 \cdot 3H_2O$	99.9	Aldrich
Sodium hydroxide	NaOH	99	Merck
Silver nitrate	$AgNO_3$	99	Aldrich
Titanium dioxide P25	TiO_2		Degussa
Sulfuric acid	H_2SO_4	95	VWR Chemicals
Ammonium nitrate	NH_4NO_3	99.9	Sigma-Aldrich
Barium chloride	$BaCl_2$	99.9	Sigma-Aldrich
Nitric acid	HNO_3	65	VWR Chemicals

The gases used to feed the photo-PROX reactor are detailed in Table 3.9.

Table 3.9. Gases used to feed the reactor

Reagents	Purity (%)	Trading house
(5%CO/5%O_2)	99.999	Air Liquid
Hydrogen	99.999	Air Liquid
Helium	99.999	Air Liquid

3.5. Synthesis of CO photo-PROX catalysts

3.5.1. Synthesis of the ordered mesoporous TiO_2 support

First, titanium (IV) isopropoxide was dissolved in anhydrous ethanol and then this solution was added to deionized water (molar ratio of TTIP:EtOH:H_2O= 1:3:60) at room temperature under vigorous stirring for 1 h. The white slurry product was then ultrasonicated for 2h, followed by aging in a closed beaker for 24 h. After that, the sample was dried at 100ºC overnight, later it was grounded and finally split into four fractions. Each fraction was calcined in air flow for 4h at a given temperature (400, 500, 600 and 800ºC/heating ramp 10ºC·min^{-1}) to obtain MTX supports. The acronyms MTX mean: M= mesoporous, T= titania and X= temperature of calcination. Therefore, synthetized supports will be referred to as MT400, MT500, MT600 and MT800.

3.5.2. Synthesis of nanorods of TiO_2 supports

The synthesis of nanorods of titania as supports was conducted by two hydrothermal methods with markedly acid and basic treatments. In the former,10 g of titanium dioxide P25 were dispersed into 100 mL of 15wt% H_2SO_4 solution and transferred into a sealed Teflon stainless steel autoclave kept at 200ºC for 15 days [2]. The obtained product was filtered and washed several times: firstly with deionized water, secondly with NH_4NO_3 0.1 M and finally with hot deionized water until pH=7. The absence of sulfate ions was verified by the $BaCl_2$ test. The obtained product was dried at 100 ºC overnight and calcined at 500 and 700 ºC (2h, 5ºC/min) to obtain TNRaX supports, where TNR= titania nanorods, a= acid treatment and X= calcination temperature. TNRa5 and TNRa7 samples, respectively**.**

In the basic treatment, 5 g of Degussa P25 TiO_2 was dispersed into 400 ml of 10 M NaOH aqueous solution under stirring for 1h. Then the suspension was transferred into a Teflon autoclave and heated at 130 ºC for 20h [3]. The obtained product was filtered and washed several times: 1º with deionized water, 2º with HNO_3 0.1 M (~ 200ml) until pH=1, 3º with hot deionized water until pH=7. Finally, it was dried at 80 ºC overnight and calcined at 500 and 700 ºC (5h, 5ºC/min) to obtain TNRbX supports where TNR= titania nanorods, b= basic treatment and X= calcination temperature. TNRb5 and TNRb7 samples, respectively. The absence of nitrate ions in the sample was verified before calcination by FT-IR.

3.5.3. Synthesis of Au-NPs/TiO_2 photocatalysts

The synthesis of gold nanoparticles supported on titania based structures was carried out by the deposition-precipitation method. In this method the gold precursor, chloroauric acid, is brought out of solution in the presence of a suspension of the support by raising the pH in order to precipitate $Au(OH)_3$. The surface of the support acts as a nucleating agent so that if the method is properly performed, and local high concentrations of alkali are avoided, the active precursor is selectively deposited on the support surface.

Regardless of the support employed for the synthesis, the followed procedure was as described below in all cases. Before gold deposition, the support was pretreated by heating at 100 ºC in an oven overnight. First, the required amount of a 0.01M solution of $HAuCl_4 \cdot 3H_2O$ (5.07 ml) to obtain 1wt% of Au loading was dissolved in 100 mL of Milli-Q water in a round bottomed flask under stirring. The pH value was slowly raised to 9.0 by adding an aqueous solution of NaOH 0.1 M by means of a syringe pump with a flow of $1mL \cdot h^{-1}$. Once the pH stabilized around 9 the titania support was added under vigorous stirring. The resulting suspension was heated in an oil bath for 2 h, monitoring the pH and keeping it about 9 by adding diluted NaOH or HNO_3. The suspension was filtrated and washed several times with Milli-Q water until disappearance of chloride ions. The absence of chloride ions was verified by the $AgNO_3$ test and dried at 100 ºC overnight. The obtained samples were kept in vials recovered with an opaque material in order

to protect them from exposure to light. And finally, before characterization and catalytic test, the samples were pre-treated ex situ at 200 ºC under flowing filtered atmospheric air for 4 h. Table 3.10 compiles the prepared photocatalysts nomenclature.

Table 3.10. Catalysts nomenclature

Sample	Support	Calcination T of the support (ºC)
Au/MT400	Mesoporous TiO_2	400
Au/MT500	Mesoporous TiO_2	500
Au/MT600	Mesoporous TiO_2	600
Au/MT800	Mesoporous TiO_2	800
AuTNRa5	Titania nanorods	500
AuTNRa7	Titania nanorods	700
AuTNRb5	Titania nanorods	500
AuTNRb7	Titania nanorods	700

3.6. CO photo-PROX catalytic tests

The preferential CO oxidation in a H_2-rich stream under simulated solar light irradiation was carried out in a laboratory flow apparatus with a fixed bed reactor operating at atmospheric pressure. Figure 3.2 shows the scheme of the catalytic system. The catalyst (0.15 g) was placed in a quartz cell with a cooling water system. Before the catalytic experiments, the sample was pre-treated in situ at 200°C under flowing filtered atmospheric air for 4 h. The gas hourly space velocity, GHSV, was 22000 h^{-1}. The feed consisted of 1.25% CO, 1.25% O_2 and 50% H_2 (vol.%) balanced with He. The temperature of the quartz cell was controlled at about 30 °C (measured by a thermocouple placed inside the catalyst bed). During the testing process, a visible light (Sunlight Solar Simulator, AM1.5G filter, 100 watt Xenon arc lamp, Abet Technologies) was introduced into the surface of the quartz cell. For testing the thermocatalytic activity of catalyst under dark, the quartz cell was wrapped with Al foils to shut down light irradiation.

The carbon monoxide and oxygen conversions were calculated based on the CO and O_2 consumption, respectively:

$$CO\ Conversion\ (\%) = \frac{n_{CO}^{in} - n_{CO}^{out}}{n_{CO}^{in}} \cdot 100$$

$$O_2\ Conversion\ (\%) = \frac{n_{O_2}^{in} - n_{O_2}^{out}}{n_{O_2}^{in}} \cdot 100$$

The selectivity towards CO_2 was estimated from the oxygen mass balance as follows:

$$Selectivity\ (\%) = \frac{n_{CO}^{in} - n_{CO}^{out}}{2(n_{O_2}^{in} - n_{O_2}^{out})} \cdot 100$$

The excess of oxygen factor (λ) used was 2 because this value was previously found optimal for CO-PROX [4]

$$\lambda = 2 \times \frac{n_{O_2}^{in}}{n_{CO}^{in}}$$

Turnover frequency (TOF) was expressed in mmol of CO or H_2 oxidized $gcat^{-1} \cdot h^{-1}$.

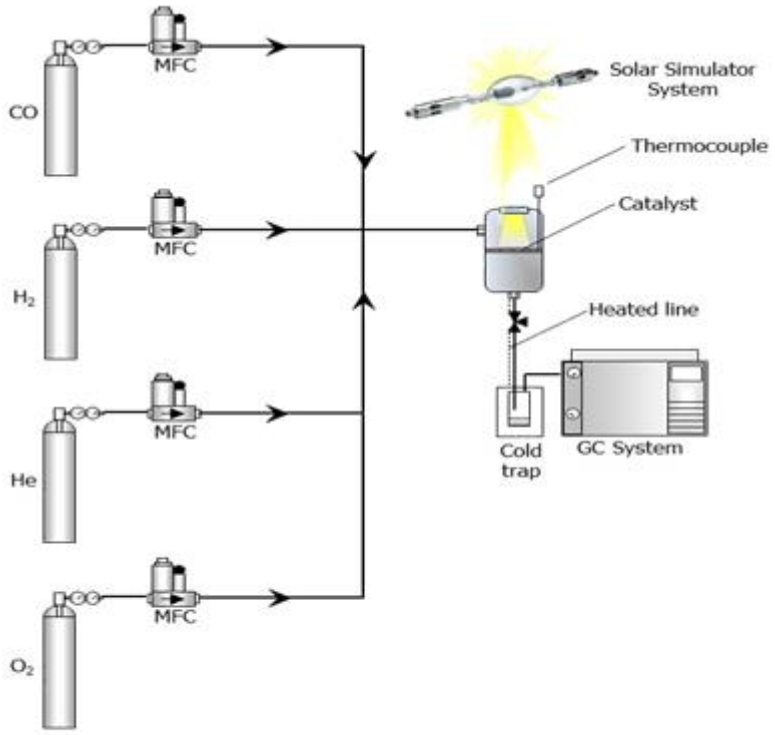

Figure 3.2. Scheme of the CO photo-PROX system

3.7. Characterization techniques

Characterization techniques have the aim of providing all kinds of information related to the physicochemical nature of the synthetized catalysts. This information will allow us to evaluate the nature of the processes and the catalysts behavior.

3.7.1. N_2 adsorption-desorption at -196ºC

The gases physisorption technique is the most commonly used to determine the specific surface area of the catalysts. This technique allows the detection of pores, the evaluation of its morphology, connectivity and size distribution as a function of the physicochemical nature of

the material as well as the range of pore size distribution within the valid range of the method, which is determined by the existence or not of physicochemical phenomena associated with it. The importance of this analysis becomes evident if considering that solid catalyzed reactions are developed over the catalysts surface. The specific surface area as well as the pore size distribution has been determined by means of N_2 adsorption-desorption at -196ºC. The adsorption process, within the context of gas-solid interface, indicates the enrichment or depletion of one or more components in the interfacial face. Thus, measurements of gas adsorption may give information about the surface area and the porous structure of the solid. Isotherms were measured by means of a Micromeritic ASAP 2020. After nitrogen adsorption, samples were summited to a cleaning treatment. For that purpose, samples were outgassed at 200 ºC for 10 hours under a pressure of 1.33×10^{-2} Pa. In order to reach the temperature of -196ºC, the specimen holder was thermostatically controlled with a liquid nitrogen containing Dewar. Adsorption-desorption nitrogen isotherms were built from volume data of adsorbed nitrogen at different relative pressures.

The most common way of determining the surface area of a solid is to find the monolayer value from the Brunauer, Emmet and Teller equation (1398) Equation 3.1 [5]. This equation considers the solid surface as a distribution of adsorption sites in equilibrium with the adsorbate (N_2), where the velocity of the condensation of molecules over vacancy sites is the same than the evaporation velocity of the molecules in the occupied sites.

$$\frac{P}{V(P_0 - P)} = \frac{1}{V_m \cdot C} + \frac{C - 1}{V_m \cdot C} \cdot \frac{P}{P_0} \qquad \text{(Ec 3.1)}$$

P_0 corresponds to the vapour saturation pressure of the adsorbed gas, V_m is the adsorbate volume (N_2) per gram necessary to cover the solid with a monolayer, V is the adsorbed gas volume per gram of solid for a pressure P and C is the BET constant related to the adsorption heat.

This equation is lineal in the range of relative pressures $0.005 < P/P_0 < 0.35$. Vm and C are calculated from the slope and intercept values. Once the monolayer volume is determined the specific surface BET (SBET) is obtained by the equation 3.2 :

$$S_{BET} = \frac{V_m \cdot N \cdot A}{V_0} \qquad \text{(Ec.3.2)}$$

Where N is the Avogadro number, A is the transversal section of nitrogen (16.2Å) and V_0 is the molar volume.

The study of the pore size distribution has been evaluated by the Barret, Johner and Halenda method (BJH) applied to the desorption branch.

3.7.2. Carbon monoxide chemisorption

The dispersion of a compound can be defined as the number of surface atoms with respect to the total number of atoms of a supported compound. Selective chemisorption of a suitable gas over the surface of an active component is the most commonly used method to measure dispersion. The measure of dispersion from chemisorption isotherms is based on the specificity of the interactions adsorbent-adsorbate and on the supposition that a monolayer is formed, in order to determine the expose metallic surface [6].

CO chemisorption measurements were carried out in a Micromeritics ASAP2010 apparatus under static volumetric conditions. Samples were reduced ex situ, transferred in inert atmosphere, and pre-treated in flowing H_2 (60 mL·min^{-1}) at 400 ºC for 1 h. The chemisorption isotherm was obtained by measuring the amount of adsorbed CO for pressures varying from 10 to 600 mmHg. After completing this initial analysis, the reversibly adsorbed gas was evacuated and the analysis was repeated to measure chemisorbed molecules only. Metal dispersion was calculated by equation 3.3:

$$\text{Dispersion (\%)} = \frac{\text{CO Uptake (mmoles/g)}}{\text{Metal loading (mmoles/g)}} \quad \text{(Ec. 3.3)}$$

3.7.3. X-ray photoelectron spectroscopy (XPS)

X-ray photoelectron spectroscopy is one of the most widely used analytical surface techniques. This technique is characterized for its high surface sensibility, allowing it to be applied to a wide range of study fields. This spectroscopy is based, as all the spectroscopies are, on the interaction between matter and photons. And in this particular case, the photoelectric effect is the physic principle applied (Hertz, 1887) [7]. When a sample is irradiated with photons of greater energy than the binding energy of the electrons of the atoms, electrons emerge from the sample with a kinetic energy which is equal to the excess of the incident photon energy. Kinetic energy is measured by means of the hemispheric detector as a function of the photon energy, the binding energy of the electron and the working function of the spectrometer Φ_{espec} which in turn can be approximated to a constant for each device and its value has to be periodically demonstrated. Therefore, kinetic energy can be expressed by the following equation:

$$E_c = h\nu - E_B - \Phi_{\text{espec}}$$

factor Φ_{espec} represents the working function of the spectrometer and E_B is the binding energy which is the ionization energy of the electron in its energetic level. A typical XPS spectrum shows the number of electrons accounts versus the binding energy of the inner levels of the atoms present in the solid [7]

Every element gives a unique and characteristic spectrum, in a way that kinetic energies measurements provide an elemental analysis, since any modification in E_B will be reflected in the Ec. This technique is able to analyze all the elements of the Periodic Table of elements excepting nitrogen and helium. Spectral peaks from a mixture of different components correspond, approximately, to the sum of the single peaks of each element in a way that elements on the surface of the sample can be identified. Detailed analysis of the photoelectron spectra reveals the correlation between the kinetic energy and the chemical state of the element and its compounds. This means that in some way there is a charge transfer through the chemical bound with the vicinity atom, provoking a variation of the observed kinetic energy. Therefore, a qualitative analysis of the test sample can be carried out where we can have information of the present elements, oxidation state and even the coordination environment of the atom. Quantitative analysis is also able through the measurement of the area of the photoelectron peaks.

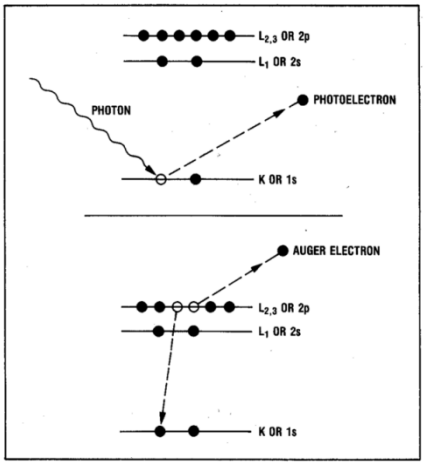

Figure 3.3. Scheme of photoelectron and auger electron emissions [8]

XPS technique allows the study of the surface because although X-Ray radiation penetrates inside the matter in the order of 1-10 μm, the free mean path of photoelectrons is very little, between 0.5 and 4 nm. Therefore, photoelectrons from the sample come exclusively from the

most superficial atomic layers, in such a way that the technique gives information of the first layers of the solid.

As well as spectral peaks originated by primary photoemission processes, other peaks corresponding to diverse electronic processes are observed. Among them, it should be noted the Auger effect, Figure 3.3. When a photoelectron is emitted an inner hole is generated which is occupied by an electronic transition from an outer layer. The energy associated to this transition can be dissipated by the emission of an electron from a third layer, which is known as Auger effect [8].

The measurements of the studied catalysts were carried out by means of a Physical Electronics PHI 5701 spectrometer with non-monocromatic Al Kα or Mg Kα (300 w, 15 Kv and 1486.6 eV or 1253.6 eV) using a multi-channel detector. Spectra of the samples are registered in a constant pass mode of 29.35 eV of energy with a diameter of analysis area of 720 μm, during data acquisition the residual pressure of the ionization chamber was kept at 1.33×10^{-7} Pa. Binding energy was determined with an accuracy of ± 0,1 eV and adventitious carbon was used as referent (C 1*s* at 284.8 eV). For data acquisition software *PHI ACCESS ESCA-V6.0 F* was employed. The spectrum was adjusted by Gauss-Lorentz curves in order to determine the binding energy of the inner level of the various elements. Samples were directly analyzed without previous treatment.

3.7.4. X-ray diffraction (XRD)

X-ray diffraction is the main analytic and non-destructive technique for the investigation of bulk structure. It gives us information about different phases formed during the preparation of an enormous variety of materials. This characterization technique, not only gives qualitative analysis, but also permits to know the quantity of formed phases. X-ray diffraction phenomenon is due to the elastic dispersion process that takes place when monochromatic electromagnetic radiation, with wavelength in the order of interplanar distance, impacts on a crystalline solid.

In a diffraction pattern from a crystal lattice, a number of reflections are generated, each one being associated to a lattice plane (identified by the Miller indices h,k,l) and occurring at an angular position (2Θ) depending on the related interplanar spacing (d(hkl)) and the X-ray wavelength (λ), as defined by the Bragg's Law [9]:

$$2 \cdot d \cdot \text{sen}\Theta = n \cdot \lambda$$

Where n is an integer called the order of reflection, λ is the wavelength of X-rays and d is the characteristic spacing between the incident beam and the normal to the reflecting lattice plane (Figure 3.4). By measuring the angles, Θ, under which the constructively interfering X-ray leave the crystal, the interplanar spacing, d, of every single crystallographic phase can be determined.

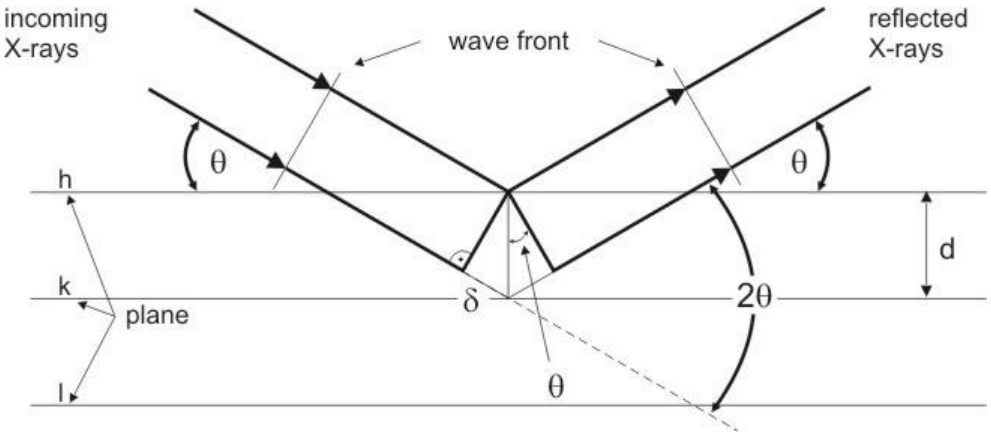

Figure 3.4. X-ray diffraction phenomenon

A diffraction pattern contains a lot of structural information: the angular position of the reflection is related to the size and shape of the unit cell, while the intensities reflect the lattice symmetry and the electron density within the unit cell. As X-ray diffraction is a property of the crystalline structure of matter, every crystalline compound has specific interplanar spacings, then, its identification is feasible through this key parameter in a reliable manner. In order to identify an unknown substance, the powder diffraction pattern is recorded with the help of a camera or a diffractometer and a list of *d*-values and the relative intensities of the diffraction line is prepared. These data are compared with the standard line patterns available for various compounds in the Powder Diffraction File (PDF) database. In practice the appearance of three most intense characteristic lines from the standard PDF line pattern is a sufficiently convincing evidence of the existence of a crystalline phase in either a homogeneous substance or even in a multicomponent mixture. Clear diffraction peaks are only observed when the sample possesses adequate long range order. Diffraction lines from perfect crystals are very narrow. For crystallite sizes below 100 nm, line broadening occurs due to incomplete destructive interference in scattering directions where the x-rays are out of phase.

This technique also allows measuring the crystalline domain size by the Scherrer equation. This formula relates the thickness of the crystallites, that is, the number of planes, to the breadth of peaks in the PXD pattern:

$$D = \frac{(0.94\lambda)}{\beta_{hkl} cos\theta}$$

Where D is the average domain size in the direction perpendicular to h,k,l , λ is the wavelength of Cu $K\alpha$ radiation (1.5418 Å), Θ is the diffraction Bragg angle and β_{hkl} is the width of the diffraction peak at half height.

X ray Patterns of the samples were obtained with a X´Pert PRO MPD Philips diffractometer (PANanalytical), using monochromatic CuKα radiation (P=1.5406 Å). The Kα radiation was selected with a Ge (111) primary monochromator. The X-ray tube was set at 45 kV and 40 mA.

3.7.5. Transmission electron microscopy (TEM)

Transmission electron microscopy is a technique which allows obtaining "local" information of the studied material. The interaction of electrons with matter allows the observation of very weak diffraction phenomena that in many cases are not detected by X-ray or neutrons diffraction. However, transmission electron microscope uses a beam of accelerated electrons under a difference of potential of several hundred kilovolts (20-200 kV) [7] oriented by electromagnetic condenser lenses conducting the intensity and the exact impact point of electrons. When the beam penetrates the sample leads to elastic and inelastic processes that generate various signals related with the atomic structure of the material. During elastic processes, incident electrons are dispersed without energy loss whereas in inelastic processes, incident electrons give part of their energy to the inner electrons of the material (see Figure 3.5).

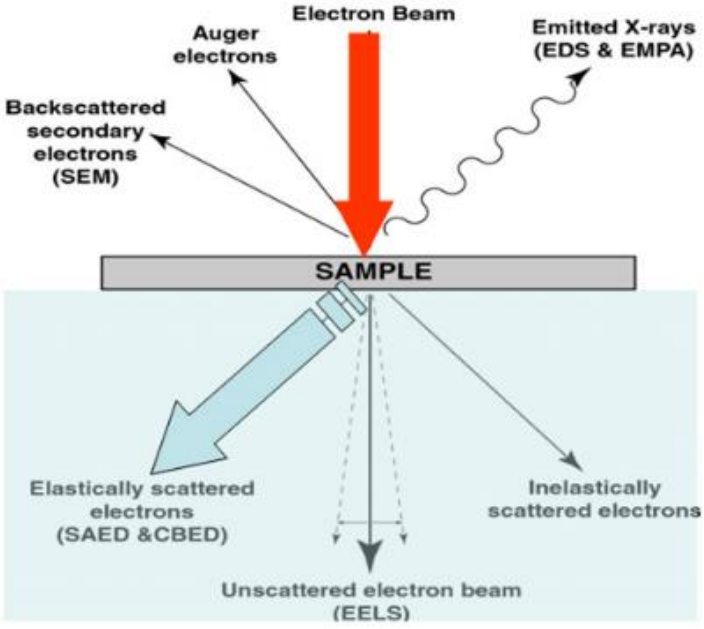

Figure 3.5. TEM radiative processes

These signals are analyzed separately in order to obtain different transmission conventional images. Dark field and high resolution images provide information about morphology, internal structure, dimension and crystalline distribution, interfaces and crystallographic defects of the atomic network. In the present thesis, this technique has been used to visualize the shape and the degree of dispersion of the active sites over the support.

This technique also allows obtaining a characteristic spectrum of the sample composition as well as determining the presence of specific chemical elements in the sample and their approximate composition in micrometric areas. Micrographs of the studied materials were recordered by using a TALOS F200x instrument. HRTEM analyses were performed at 200 kV and 5.5 μA. Scanning transmission electron microscopy (STEM) was performed with a HAAD detector at 200 kV and 200 nA. The microanalysis was carried out with an EDX Super-X system with four X-ray detectors and an X-FEG beam. For the sample preparation, a small amount of material was put on a lacey carbon-coated Cu grid. ImageJ software was employed to measure particle sizes.

3.7.6. Ammonia temperature-programmed desorption (NH_3-TPD)

NH_3-TPD is a technique used to determine the surface acidity of a material. NH_3 molecule has high basicity and small size, being able of quantitatively measure the available acidic sites of a solid. Furthermore, this molecule neutralizes Lewis and Brönsted acid sites at once.

Ammonia thermo-programmed desorption profiles of studied catalysts were obtained by placing 80 mg of catalyst into a tubular reactor connected to the carrier gas feed (He) and to a Shimadzu GC-14A with a TCD detector. The quartz reactor was placed into a tubular reactor with programmable heating velocity. Firstly, the catalyst was reduced as described in section 3.2. Once reduced, the sample was cooled in He flow (60 $ml \cdot min^{-1}$) to 100 ºC and adsorption of ammonia was performed at that temperature (10 min). A He flow (35 $ml \cdot min^{-1}$) was then passed to eliminate the physisorbed ammonia. Finally, thermo-programmed desorption was carried out by heating from 100 to 800 ºC at a heating rate of 10$ºC \cdot min^{-1}$. The evolved ammonia was analyzed by on-line chromatograph (Shimadzu GC-14A) provided with a TCD.

In order to quantify the amount of desorbed ammonia, the equipment was previously calibrated by measuring the corresponding signals of the thermal decomposition of known amounts of hexaaminenickel(II) chloride $[Ni(NH_3)_6]Cl_2$.

3.7.7. Hydrogen temperature-programmed desorption (H_2-TPD)

Hydrogen temperature-programmed desorption is a technique used to study the surface heterogeneity of a catalyst [10], providing information about the hydrogen activation ability of

the sample. It also studies the spillover effect by quantifying the reverse-spillover, a term which describes the processes where hydrogen widespread over the support surface leaves the sites where it was stable and recombines forming molecular hydrogen which is eventually detected.

Hydrogen molecules coming into contact with the catalyst surface are adsorbed lowering their energy. This binding energy varies with the adsorbate and the surface type. When increasing the temperature, transmitted energy to adsorbed molecules provokes the desorption phenomena. Three areas of adsorption are distinguished depending on the desorption temperature:

- Hydrogen interacting with metallic surface is desorbed at low temperatures.
- Hydrogen interacting with the interface metal-support is desorbed at intermediate temperatures.
- Hydrogen spillover, adsorbed and widespread over the support is desorbed at high temperatures.

H_2-TPD measurements were performed in a similar way than NH_3-TPD experiments and in the same device. 80 mg of catalyst precursor were reduced by the procedure described in section 3.2. Once reduced, the sample was cooled under flowing He from the reduction temperature to 100 ºC and then was exposed to H_2 gas at a flow rate of 60 $ml \cdot min^{-1}$ while the temperature was held constant at 100 ºC for 30 min. This step was followed by flushing with Ar for another 30 min in order to remove the physisorbed hydrogen. The chemisorbed hydrogen was eventually analyzed by heating in Ar up to 800 ºC and the evolved gas was analyzed by GC coupled to a thermal conductivity detector. A cold trap of isopropanol and liquid nitrogen was used in order to avoid water entrance into the GC.

3.7.8. Mössbauer Spectroscopy.

Mösbauer spectroscopy is a versatile technique based on the Mösbauer effect that can be used to provide very precise information about the chemical, structural and magnetic properties of a material.

A solid sample is exposed to a beam of gamma radiation, and a detector measures the intensity of the beam transmitted through the sample. The atoms in the source emitting the gamma rays must be of the same isotope as the atoms in the sample absorbing them. In our case, the source consists of a ^{57}Fe nucleus that is accelerated through a range of velocities using a linear motor to produce a Doppler effect and scan the gamma ray energy through a given range. In the resulting spectra, gamma ray intensity is plotted as a function of the source velocity. At velocities corresponding to the resonant energy levels of the sample, a fraction of the gamma rays are absorbed, resulting in a drop in the measured intensity and a corresponding dip in the spectrum.

The number, positions and intensities of the dips (also called peaks; dips in transmitted intensity are peaks in absorbance) provide information about the chemical environment of the absorbing nuclei and can be used to characterize the sample.

Mössbauer data for the iron containing catalysts were recorded at room temperature in the transmisson mode using a conventional constant acceleration spectrometer equipped with a ^{57}Co(Rh) source. An effective absorber thickness of 5 mg cm^{-2} of natural iron was used for all the samples. The velocity scale was calibrated using a 6 μm thick α-Fe foil. All the spectra were computer-fitted and the isomer shifts were referred to the centroid of the spectrum of α-Fe at room temperature.

These measurements were carried out at the Instituto de Química-Física Rocasolano del CSIC in Madrid.

3.7.9 Fourier transform infrared spectroscopy (FT-IR)

Infrared spectroscopy has been a workhorse technique for materials analysis for many years. An infrared spectrum represents a fingerprint of a sample with absorption peaks which correspond to the frequencies of vibrations between the bonds of the atoms making up the material. Because each different material is a unique combination of atoms, no two compounds produce the exact same infrared spectrum. Therefore, infrared spectroscopy can result in a positive identification (qualitative analysis) of every different kind of material. In addition, the size of the peaks in the spectrum is a direct indication of the amount of material present. FT-IR is the preferred method of infrared spectroscopy because it overcomes the limitations encountered with dispersive instruments by using an interferometer. The interferometer produces a unique type of signal which has all the infrared frequencies "encoded" into it. The signal can be measured very quickly, usually on the order of one second or so [11].

The Fourier transform infrared spectra were carried out with a Nicolet Nexus instrument, using a conventional cell connected to a gas-handling system. Prior to each adsorption, pressed disks of powder samples with a diameter of 1.5 cm (ca. 20 mg) were thermally treated within the cell at 400 ºC under H_2 (40 kPa) for 1h. Then, the samples were outgassed at 400 ºC and cooled to carry out the spectrum at rt between 4000 and 400 cm^{-1} using 200 scans and a resolution of 2 cm^{-1}. CO adsorption (0.13 kPa) experiments were performed at -140 ºC and the spectra were recorded in the range of -140 to 10 ºC while degassing.

These measurements were carried out at il Dipartimento di Ingegneria Civile, Chimica e Ambientale, Università degli Studi di Genova, Italia.

3.7.10. Diffuse reflectance UV-vis Spectroscopy (DRUV-vis)

Reflectance spectroscopy is very closely related to UV-vis spectroscopy in that both of these techniques use visible light to excite valence electrons to empty orbitals. The difference in these techniques is that in UV-vis spectroscopy one measures the relative change of transmittance of light as it passes through a solution, whereas in diffuse reflectance, one measures the relative change in the amount of reflected light of a surface. A solution that is completely clear and colorless effectively reflects 100 % of all visible wavelengths of light that interacts with it. However, if the material has electronic energy levels that are separated by energy in the visible region, then it may absorb light of that energy to move electrons from the conduction band to the valence band. This causes a relative decrease in the amount of light at that particular energy, relative to a reference source. In other words, the % of reflectance will decrease and this drop will allow measuring the band gap between valence and conduction band.

Therefore, this technique has been used to measure the band gap of titania based materials. The diffuse reflectance UV-vis spectra were collected with a Perkin Lambda 35 UV-vis spectrophotometer. The absorption coefficient (α) was calculated as follows: $\alpha = ln(1/T)/d$, where T is the measured transmittance and d is the optical path length. Band gap energy, Eg, was determined thoroughly the value (m^{-1}) from a plot of $(\alpha h\nu)^{1/2}$ versus photon energy $(h\nu)$, where h is Planck's constant and ν is the frequency (s^{-1}). The intercept of the tangent to the absorption curves was used to estimate the band gap (Eg) value.

These measurements were carried out at il Dipartimento di Scienze Molecolari e Nanositemi, Università Ca'Foscari di Venezia, Italia.

3.7.11. X-ray fluorescence spectroscopy (XRF)

X-ray fluorescence spectroscopy is a widely used technique for elemental and chemical analysis, applied since the 1970s as a versatile tool to many analytical problems. The analysis of major, minor and trace elements in various kinds of samples can be performed qualitatively and quantitatively. The working principle is based on the excitation of the sample atoms by high energy X-rays, followed by the emission of characteristic photons with certain energy, well correlated to the atomic number Z of each element (Moseley's law). The determination of the energy (or wavelength) of the emitted photon allows qualitative analysis and the determination of the number of emitted characteristic photons allows quantitative analysis [12].

Quantitative analysis of elemental bulk gold composition of the photocatalysts was performed with wavelength dispersive X-ray fluorescence spectrometer (ARL ADVANTXP) and a UNIQUANT software. The X-ray tube was set at 60Kv.

3.7.12. Atomic absorption spectroscopy (AAS)

Atomic absorption spectroscopy is a very common technique for determination of single elements in compounds such as metal and metalloids. It involves measuring the absorption of light by vaporized ground state atoms and relating the absorption to concentration. The incident light beam is attenuated by atomic vapor absorption according to Beer's law. The process involves two steps: atomization of the sample and absorption of radiation from a light source by the free atoms (typically a hollow-cathode lamp). The sample, either a liquid or a solid (such is our case), is atomized in either a flame or a graphite furnace. Upon the absorption of specific ultraviolet or visible light, the free atoms undergo electronic transitions from the ground state to excited electronic states. The light produced by the hollow-cathode lamp is emitted from atoms of the same element which is to be determined. Therefore, the radiant energy corresponds to the wavelength which is absorbable by the atomized sample. Thus, this method provides both sensitivity and selectivity since other elements will not interfere with the measurement.

Elemental analysis of gold content in photocatalysts was performed by using a Perkin-Elmer 3100 instrument equipped with a D2-lamp for background correction and Au mono-hollow cathode lamp as light source.

3.7.13. Small-angle X-ray scattering (SAXS)

Small-angle X-ray scattering is a technique by which nanoscale density differences in a sample can be quantified. This means that it can determine nanoparticle size distributions, determine pore sizes and characteristic distances of partially ordered materials. This is achieved by analyzing the elastic scattering behavior of X-rays when travelling through the material, recording their scattering at small angles (typically o.1-10º). Depending on the angular range in which a clear signal can be recorded, SAXS is capable of delivering structural information of dimensions between 1 and 100 nm, and of repeat distances in partially ordered systems of up to 150 nm [13].

SAXS measurements of studied photocatalysts were performed on a D8 DISCOVER-Bruker diffractometer working at 40 kV and 40 mA. Powder patterns were recorded in capillary-transmission configuration by using a Göbel mirror (Cu Kα1 radiation) and the LYNXeye detector. The powder patterns were recorded between 0.2 and 10º in 2Θ with a total measuring time of 120 minutes.

3.7.14. Raman spectroscopy

Raman spectroscopy is a technique that provides a structural fingerprint by which molecules can be identified. It relies on inelastic scattering of monochromatic light, usually a laser in the

visible, near infrared, or near ultraviolet range. The laser light interacts with molecular vibrations, phonons or other excitations in the system, resulting in the energy of the laser photons being shifted up or down. The shift in energy gives information about the vibrational modes in the system.

Raman spectra with excitation laser at 633 nm were collected by using a micro-Raman JASCO NRS-5100 spectrometer. Raman spectra with excitation laser at 785 and 532 nm were collected in a Bruker Senterra microscope by averaging spectra during 60-90 min with a resolution of 3-5 cm^{-1}. A CCD camera at -50ºC was used for the Raman detection.

3.8. References

1. Bui, P., et al., *Studies of the synthesis of transition metal phosphides and their activity in the hydrodeoxygenation of a biofuel model compound.* Journal of Catalysis, 2012. **294**: p. 184-198.
2. Li, H. and P. Afanasiev, *On the selective growth of titania polymorphs in acidic aqueous medium.* Materials Research Bulletin, 2011. **46**(12): p. 2506-2514.
3. Camposeco, R., et al., *Synthesis, characterization and photocatalytic activity of TiO2 nanostructures: Nanotubes, nanofibers, nanowires and nanoparticles.* Catalysis Today, 2016. **266**: p. 90-101.
4. Arango-Díaz, A., et al., *Preferential CO oxidation (CO-PROX) catalyzed by CuO supported on nanocrystalline CeO2 prepared by a freeze-drying method.* Applied Catalysis A: General, 2014. **477**: p. 54-63.
5. Brunauer, S., P.H. Emmett, and E. Teller, *Adsorption of gases in Multimolecular Layers.* Journal of American Chemical Society, 1938. **60**: p. 309-319.
6. Richardson, J.T. and T.S. Cale, *Interpretation of hydrogen chemisorption on nickel catalysts.* Journal of catalysis, 1986. **102**(2): p. 419-432.
7. Faraldos, M. and C. Goberna, *Técnicas de análisis y caracterización de materiales.* Consejo Superior de Investigaciones Científicas, 2002.
8. Moulder, J.F., et al., *Handbook of X-ray photoelectron spectroscopy*. 1992: Perkin-Elmer Corporation.
9. Weller, M.T. and N.A. Young, *Characterisation methods in inorganic chemistry*. 2017: Oxford.
10. Znak, L. and J. Zieliński, *Effect of support on hydrogen adsorption/desorption on nickel.* Applied Catalysis A: General, 2008. **334**: p. 268-276.
11. Griffiths, P.R. and J.A. Haseth, *Fourier Transfrom Infrared Spectroscopy.* Wiley-Interscience (Second Edition), 2007: p. 1-18.
12. Streli, C., P. Wobrauschek, and P. Kregsamer, *X-ray fluorescence spectroscopy, applications.* . Encyclopedia of spectroscopy and spectrometry (Second Edition), 1999: p. 3000-3009.
13. Walenta, E., *Small angle X-ray scattering*. Vol. 36. 1985. 296.

4. Ni and Fe mixed phosphides for phenol HDO

4.1. Abstract

The present chapter describes the study of a series of silica-supported mono and bimetallic nickel and iron phosphides with different Ni/Fe molar ratios (1:0, 3:1, 2:1, 0:1) on the HDO of phenol. These catalysts were synthesized by means of temperature-programmed reduction of the corresponding precursors $Ni(HPO_3H)_2$ and $Fe(HPO_3H)_2$ supported on silica with a metal loading of 5 wt%. The nomenclature of these catalysts is Ni_2P and FeP for the monometallic phosphides and NiFeP3:1 and NiFeP2:1 for the bimetallic ones, where the ratios are the nominal Ni/Fe initial molar ratios.

The catalysts were evaluated in the HDO of phenol under different pressures and contact times. Characterization results detailed down below were obtained by means of different techniques in order to know structure, texture, acidity, ability to activate hydrogen and composition.

4.2. Characterization results

4.2.1 X-ray diffraction (XRD)

The crystalline phases of the reduced catalysts have been studied by X-ray powder diffraction. The X-ray diffraction profiles are shown in Figure 4.1. In all diffractograms, no well-defined diffraction peaks are observed. This fact is related to the low metallic loading as well as the high dispersion of the active phases over the support. Besides, it is known that silica support promotes the formation of phosphides with very small particle size [1].

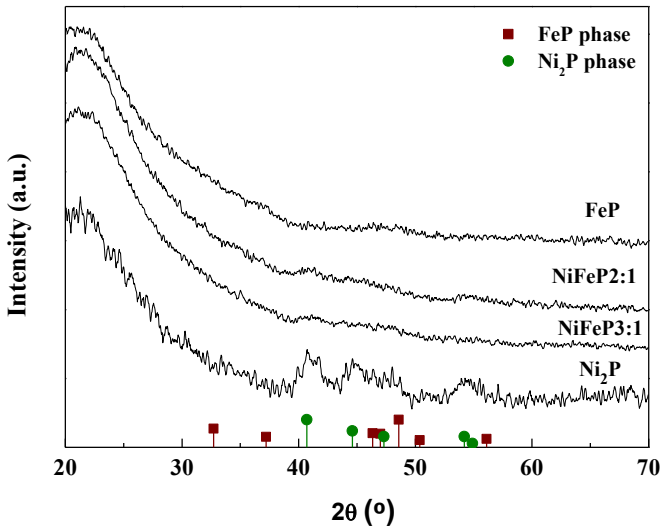

Figure 4.1. X-ray diffraction profiles of reduced catalysts

In general, all the diffractograms show a broad band between 23 and 25º ascribed to amorphous silica. In spite of the noisy diffractograms, Ni_2P, NiFe3:1 and NiFeP2:1 samples show weak diffraction peaks located at 2Θ (º) = 40.7, 44.6, 47.4, 54.2 and 55.0 attributed to Ni_2P phase (JPCDS, PDF card no. 01-089-4864). However, the diffractogram of the FeP catalyst does not present well defined peaks as to distinguish the stoichiometry of the iron phosphide phase formed because, as will be discussed later, this active phase is highly dispersed and indeed, iron fluorescence also hinders the acquisition of the crystallographic peaks [2]. In order to elucidate the stoichiometry of the iron phosphide phase, a catalyst with 15 wt% of iron with the same molar ratio (P/Fe=2) was synthesized. Diffraction results revealed the formation of FeP as unique phase, as seen in Figure 6.1 of Chapter 6. Therefore, we infer that the main phase formed after reduction is FeP due to the great excess of P used in the preparation method. Cho et al. [3] also found diffractions peaks ascribed to FeP phase for a catalyst with higher metal loading and the same molar ratio P/Fe=2.

4.2.2 Textural properties and CO chemisorption

The textural properties of the support and the reduced catalysts were evaluated by N_2 adsorption-desorption isotherms at -196ºC and the corresponding results are compiled in Table 4.1 along with CO chemisorption results. As observed in this Table, a slight decrease in the S_{BET} values is noticeable. The porosity of the support is due to the interparticle space among the various silica spheres so it is expected that after the impregnation with the active phases, the S_{BET} values of the catalysts suffered a decrease.

Table 4.1. Textural properties and CO chemisorption values of the support and reduced catalysts

Sample	S_{BET} ($m^2 \cdot g^{-1}$)	Vp ($cm^3 \cdot g^{-1}$)	CO ($\mu mol \cdot g^{-1}$)
SiO_2	217	0.51	-
Ni_2P	155	0.66	68
NiFeP3:1	152	0.48	52
NiFeP2:1	159	0.60	44
FeP	138	0.56	15

The corresponding isotherms are observed in Figure 4.2. All isotherms are of type II, characteristic of solids with pores of diameters in the range of meso and macropores and generally attributed to interparticle voids as aforesaid. Incorporation of the active phase leads to the blockage of the pore structure provoking the mentioned decreased in the S_{BET} values. However, this decrease is slight enough as to consider that active phases are well dispersed on the support surface. Considering now the pore volume values there is no a defined trend as to

deliver any conclusion. But it clearly seems that the textural properties of the support barely change after the incorporation of the active phases.

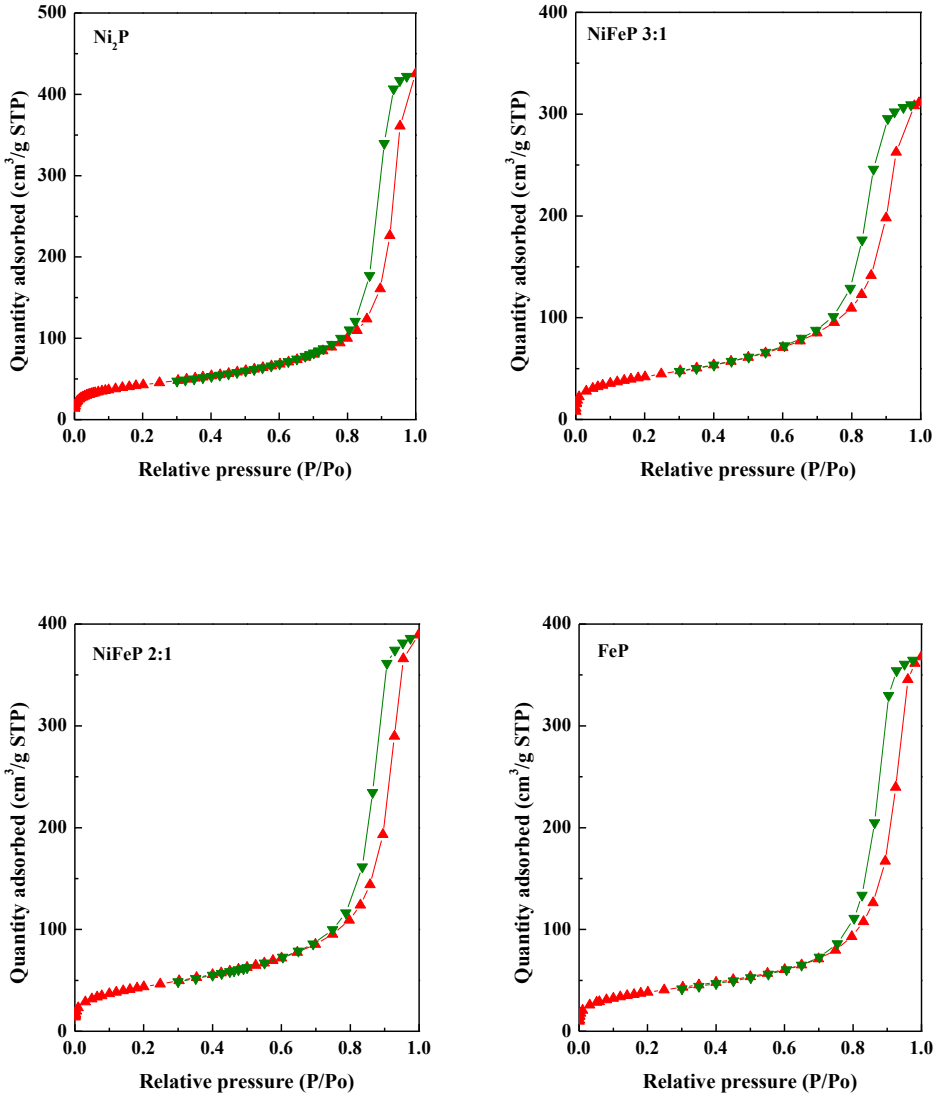

Figure 4.2. N_2 Adsorption-desorption isotherms of reduced catalysts. Red plots correspond to the adsorption branch and green plots to the desorption branch

The estimation of the number of active centers was carried out by CO chemisorption experiments. At first sight, it is noticeable that the amount of chemisorbed CO diminishes with the Fe content. Similar results have been reported for Ni-Fe phosphides [4] and Ni-Fe catalysts [5], where incorporation of iron lowered the amount of chemisorbed CO. Therefore, it is quite risky to use this technique to perform a real estimation of the density of active sites because Fe centers have much more affinity to oxygenated compounds than to CO molecules. The lower amount of chemisorbed CO could also indicate the formation of an alloy where iron occupies part of the nickel surface [3].

4.2.3 Transmission electron microscopy (TEM)

TEM analysis of the studied catalysts was performed to estimate the distribution of the active phase on the support surface. In order to reach a better contrast, analysis was also accomplished in STEM mode enabling the distinction of metallic particles (not shown). In Figure 4.3, images show a good dispersion of the active phase in all catalysts and indeed that the incorporation of iron into the Ni_2P phase improves the distribution of the nanoparticles. The particle size distribution was measured by statistical evaluation of about 500 particles. Histograms show that distribution of particle size is within a narrow range where the average particle size is also included. The FeP catalyst shows the broadest distribution of particle size with an average value of 4.6 nm followed by Ni_2P, with an average particle size of 4 nm. However, in bimetallic phosphides the incorporation of iron provokes a decrease of the particle size being the observed trend: FeP>Ni_2P>NiFeP3:1>NiFeP2:1. In other words, dispersion increases with iron content in bimetallic phosphides which does not match with CO chemisorption values that indicate the opposite trend. Thus, once again CO chemisorption results cannot be used to measure the dispersion. On the whole, TEM results indicate a good dispersion of the active phase which is in accordance with XRD results.

Additionally, the chemical composition of the catalysts was estimated by EDX and included in Table 4.2 along with the nominal composition of the catalysts. The results indicate that the initial excess of phosphorus in all the catalysts is partially lost during the reduction process.

Table 4.2. Metal/Phosphorus atomic ratios calculated by EDX

Sample	Ni/P[a]	Fe/P[a]	(Ni+Fe)/P[a]	Ni/P	Fe/P	(Ni+Fe)/P
FeP	-	0.33	0.33	-	-	-
NiFeP 2:1	0.29	0.14	0.43	0.71	0.41	1.12
NiFeP 3:1	0.33	0.11	0.44	0.82	0.28	1.02
Ni_2P	0.5	-	0.5	1.20	-	1.20

[a]***Nominal composition***

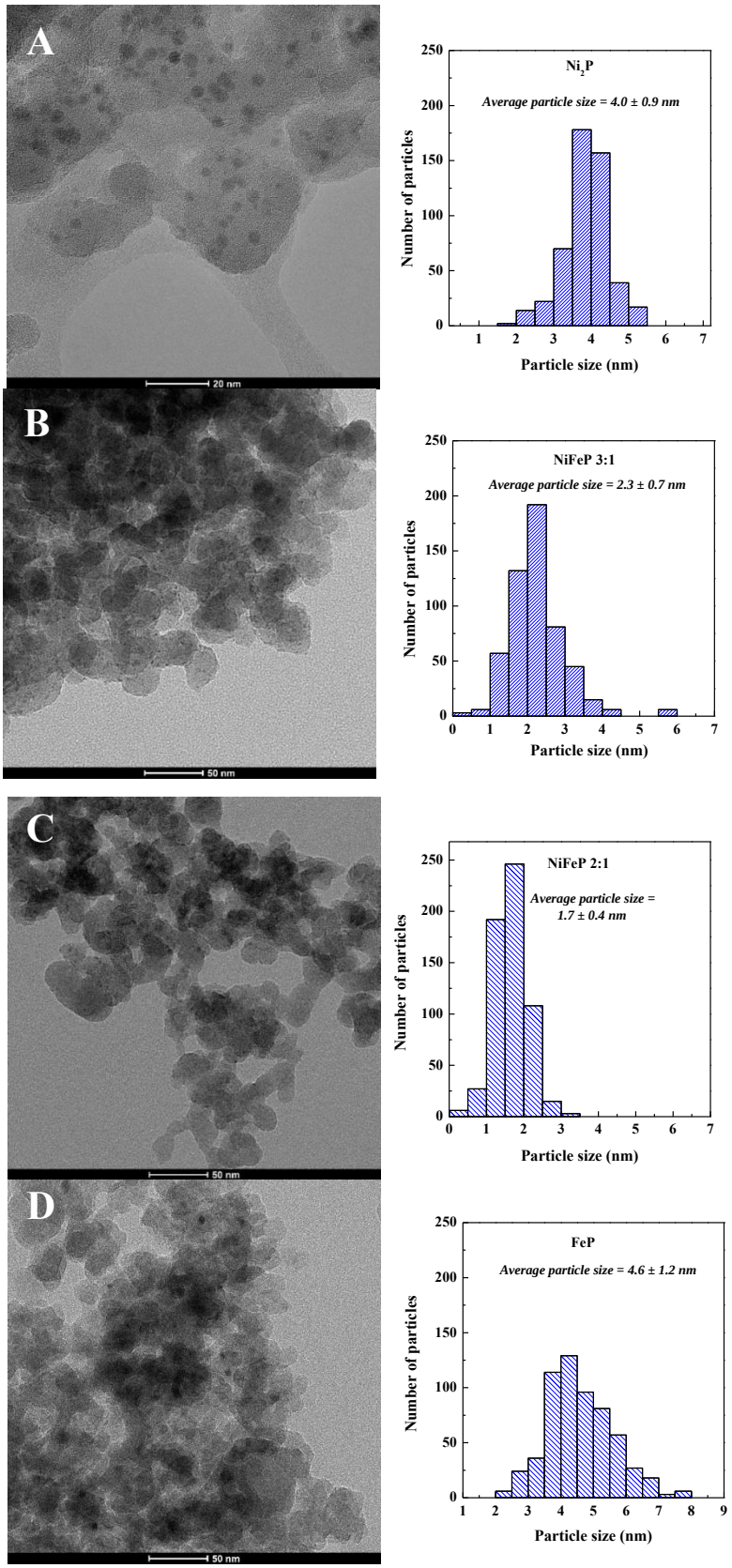

Figure 4.3. TEM micrographs of reduced catalysts and distribution of particle size histograms A) Ni_2P B) NiFeP 3:1 C) NiFeP 2:1 and D) FeP

4.2.4 X-ray photoelectron spectroscopy (XPS)

XPS was performed to determine the chemical composition of the catalysts surface as well as the chemical state of the constituent elements. Again, the low metal loading hinders the acquisition of the spectra, so the Ni 2*p* and Fe 2*p* core-level spectra are not well defined as seen in Figure 4.4. Even though, the Ni 2*p* core-level spectra show distinguishable peaks, concretely the contributions appearing at 852.0 and 853.2 eV are attributable to $Ni^{\delta+}$ species belonging to the Ni_2P phase. Signals at 856.0 and 856.6 eV are ascribed to Ni^{2+} species that interact with oxygen as a result of surface passivation [6]. In the case of the bimetallic phosphides the spectra are difficult to analyze. On the one hand, it is reported that electronic transfer from iron to nickel compensates the partial positive charge of nickel [3]. On the other hand, bimetallic phosphides have a nickel content which is even lower than in monometallic one, being therefore more difficult to distinguish. The Fe 2*p* core-level spectrum of the FeP sample allows the most clear assignment of the photoelectronic peaks finding an intense and asymmetric peak at 711 eV which is ascribed to the FeP phase, in accordance with XRD results.

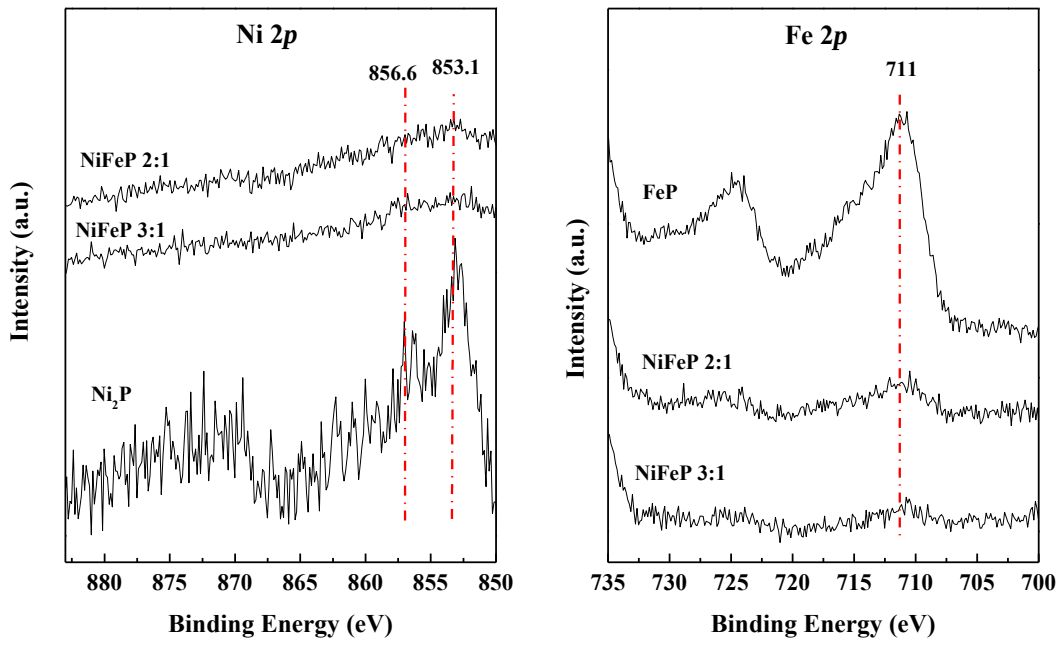

Figure 4.4. Ni 2*p* and Fe 2*p* core-level spectra of reduced catalysts

In the case of bimetallic phosphides, the spectra suffer a slight shift to lower binding energies, likely again due to electron transfer from iron to nickel. The P 2*p* core-level spectra, Figure 4.5, show two contributions of the main component P $2p_{3/2}$ at 129.0 and 134.4 eV. The first one is assigned to $P^{\delta-}$ species present in the phosphide phase. At greater binding energy, the second component is ascribed to P-OH species, which are attributable to the coexistence of unreduced $H_2PO_3^-$ and PO_4^{2-} species resulting from surface oxidation [7]. Table 4.3 compiles Metal/P and

Metal/Si atomic surface ratios which have also been calculated to estimate the degree of metallic exposure on the surface. Metal exposure decreases with nickel content whereas phosphorous exposure increases. Thus, P/Me ratios are lower than that of the theoretical value of 2.0 except for Ni_2P. Those ratios increase with Ni content which indicates a surface enrichment of phosphorous species. Additionally, Me/Si ratios followed the order NiFeP2:1>NiFeP3:1>Ni_2P, which corroborates TEM results in terms of dispersion.

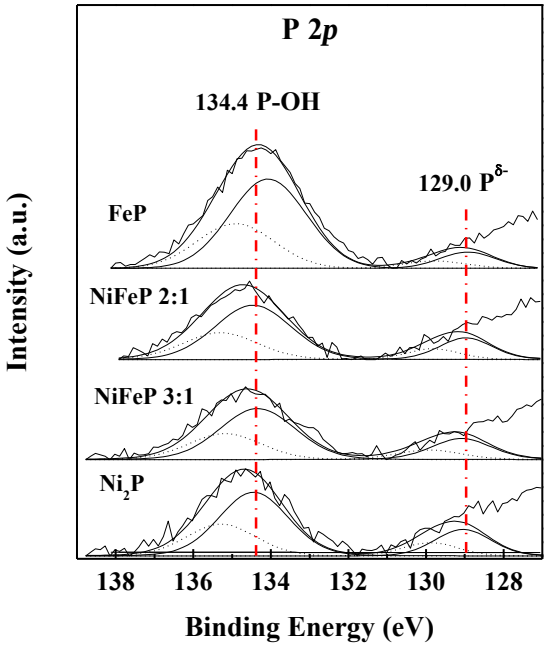

Figure 4.5. P 2*p* core-level spectra of reduced catalysts

Table 4.3. Atomic surface concentration (%) and atomic ratios of reduced catalysts

	Si 2*p*	O 1*s*	Ni 2*p*	Fe 2*p*	P 2*p*	Me/P	Me/Si	P/Si
FeP	31.74	65.48	-	1.17	1.61	0.73	0.036	0.051
NiFeP 2:1	32.12	66.17	0.42	0.23	1.07	0.61	0.020	0.033
NiFeP 3:1	33.80	64.53	0.43	0.19	1.05	0.59	0.018	0.031
Ni_2P	36.50	64.70	0.35	-	0.85	0.41	0.014	0.022

4.2.5 Ammonia temperature-programmed desorption (NH_3-TPD)

Total acidity of the studied catalysts was measured by means of ammonia temperature-programmed desorption (NH_3-TPD). The acidic sites are classified as a function of desorption temperatures as weak (T<300ºC), medium (300ºC<T≤500ºC) or strong (500ºC<T≤700ºC). The bare support has also been studied but only adsorbs a negligible amount of ammonia indicating that the adsorption process is mainly due to the presence of the active phases. Table 4.4 compiles total acidity results for each studied catalyst. Samples with a greater nickel content present higher total acidity values.

Table 4.4. Acidity values expressed in µmol $NH_{3\ desorbed/g\ catalyst}$

Sample	Total acidity[a]	Weak acidity[b]	Medium[c]	Strong acidity[d]
FeP	275	245	26	4
NiFeP2:1	442	304	65	78
NiFeP3:1	419	266	69	85
Ni_2P	489	360	125	4

[a] µmol $NH_{3\ desorbed/g\ catalyst}$ [b] T:100-300 ºC [c] T: 300-500 ºC [d] T:500-700 ºC

The nature of the acidity can be estimated by the desorption curves as mentioned before, therefore, monometallic phosphides exhibit a weak acidic character presenting a single desorption curve below 300 ºC. TPD profiles of bimetallic catalysts, Figure 4.6, reveal the presence of weak acidic sites as well as desorption curves beyond 500 ºC, pointing out to the existence of strong acid sites in both samples. This acidity is originated from Ni sites with partial positive charge acting as Lewis sites and from P-OH groups acting as Brönsted centers [8, 9].

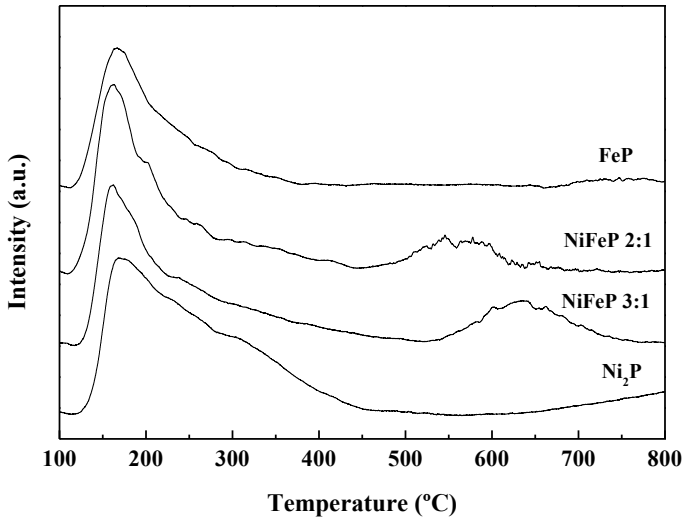

Figure 4.6. NH_3-TPD profiles of reduced catalysts

However, quantification in order to measure the extent of the kind of acidity present in each sample has not been determined. In this regard, Pan et al. [10] reported that Brönsted sites display weak strength and Lewis sites exhibit medium strength. On the whole, NH_3-TPD results point to the same direction than XPS results did, by noting that P-OH groups can be a source of hydrogen species, enhancing the spillover effect. In addition, Lewis sites can be explained as a result of the electronic transfer from nickel to phosphorous justifying the superior acidity found in Ni_2P phase. Therefore, the decreasing acidity in bimetallic phosphides in relation to the Ni_2P phase also can be understood as the decreasing number of $Ni^{\delta+}$ species whose charge is compensated by electron transfer from iron.

4.2.6 Hydrogen temperature-programmed desorption (H_2-TPD)

The nature of the interactions between hydrogen and the catalysts surface was studied by hydrogen temperature-programmed experiments. These interactions are classified as a function of the temperature desorption range in three areas. Area I, corresponding to hydrogen coming from the metallic surface which is desorbed at temperatures below 250ºC. Area II, which is assigned to hydrogen from the metal-support interface at temperatures between 250 and 450ºC. An area III, associated to the hydrogen from the spillover effect on the surface of the support at temperatures beyond 450ºC. The existence of the spillover effect on silica supported Ni_2P as well as on other phosphides has been previously observed, demonstrating that hydrogen species are associated to P-OH groups on the Ni_2P particle, the Ni_2P particle-SiO_2 interface as well as the SiO_2 surface close to the Ni_2P particles[9, 11-14].

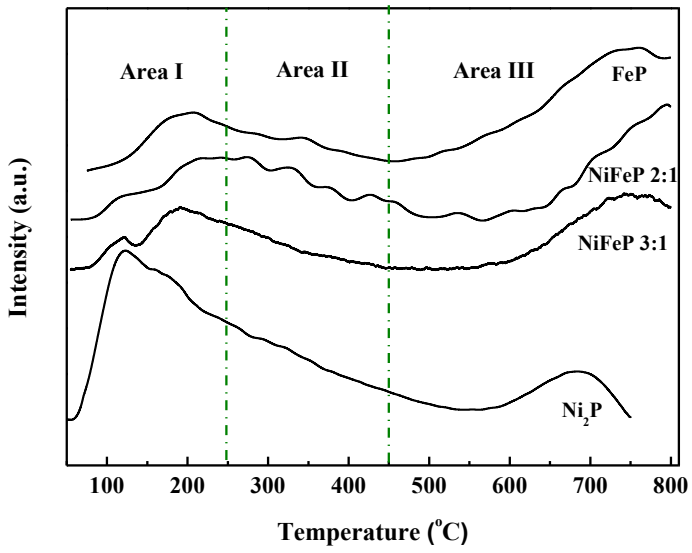

Figure 4.7. H_2-TPD profiles of reduced catalysts

Figure 4.7 includes desorption curves of the support and the studied catalysts. The Ni_2P hydrogen desorption curve presents its main desorption band at temperatures below 400 ºC with a maximum around 100 ºC. It also shows a minor contribution at 650 ºC which corresponds to the hydrogen from the metal-support interface and from the spillover process. Liu et al.[15] observed similar hydrogen desorption profiles by studying Ni_2P-based materials, concluding that H_2 species are mainly located on the surface of the catalyst. However, the desorption curve of FeP shows its main band at 750 ºC with a minor contribution at 200 ºC. Meanwhile, bimetallic phosphides show hydrogen desorption profiles which are intermediate between both phases, where hydrogen comes from both the metallic surface and from hydrogen spillover. Similarly to Ni_2P, NiFeP3:1 curve presents a maximum at 120 ºC and other maximum at 200 ºC just like the FeP profile. As iron content increases in NiFeP2:1 sample, the desorption profile becomes more similar to that of the FeP phase. Therefore, desorption at 100 ºC is ascribed to the presence of nickel while the desorption peak centered at 200 ºC is associated to hydrogen from iron containing catalysts.

On the whole, NH_3-TPD and H_2-TPD results show the existence of both metal sites which are involved in hydrogenation, hydrogenolysis and decarbonylation reactions as well as acid sites which are involved in hydrolysis and dehydration processes.

4.3. Catalytic results

The synthesized catalysts have been evaluated in the HDO reaction of phenol at 300 ºC and 1.5 and 3.0 MPa of H_2 (see Table 4.5).

Table 4.5. Conversion (X%) and Selectivity (S%) values after 6 h on stream at 3.0 and 1.5 MPa, WHSV=0.42 h^{-1} (CH: cyclohexane, CHO: cyclohexanol, CH=:cyclohexene)

	P= 3.0(MPa) Contact time= 6s				P= 1.5 (MPa) Contact time= 3s				
	X_{Total}	X_{HDO}	S_{CH}	S_{CHO}	X_{Total}	X_{HDO}	S_{CH}	S_{CHO}	$S_{CH=}$
FeP	75.5	75.5	100	0	19.5	19.2	35.5	-	64.5
NiFeP2:1	100	94.6	96.9	3.1	75.5	60.1	64.6	28.5	-
NiFeP3:1	100	85.3	88.0	12.6	61.5	41.4	50.8	45.6	-
Ni_2P	100	100	100	0	87.5	78.9	70.2	24.7	-

The results at 3.0 MPa reveal the following tendency in terms of HDO activity: Ni_2P > NiFeP2:1 > NiFeP3:1 > FeP. Ni_2P clearly displays the most outstanding behavior reaching activities up to 100% for both total and HDO conversion. The FeP catalyst is the least active one but, even though, reaches conversion values of 75% after 6 h on stream. Total and HDO conversion reaches relatively equal values in both samples, indicating a high selectivity to deoxygenated products, specifically cyclohexane. Bimetallic catalysts exhibit an intermediate catalytic behavior but more similar to that of Ni_2P sample. After 6 h on stream, NiFeP2:1 and NiFeP3:1 reach 95 and 85% of HDO conversion, respectively. This implies that the greatest part of phenol is converted to deoxygenated products with a minor formation of oxygenated compounds, concretely cyclohexanol.

These results do not show sharp differences among the catalysts as to analyze how the properties assessed before affect the catalytic behavior. So, in order to find greater differences in the product distribution, the Ni_2P catalyst was chosen to perform experiments at different contact times (2.5, 3, 4.5 and 6 s) by adjusting the gas volume flow. Figure 4.8 shows that conversion and contact time are directly related. Even though, remarkable conversion values are attained working at 2.5 s of contact time. Figure 4.8 also shows that contact time and selectivity to deoxygenated products is indirectly related.

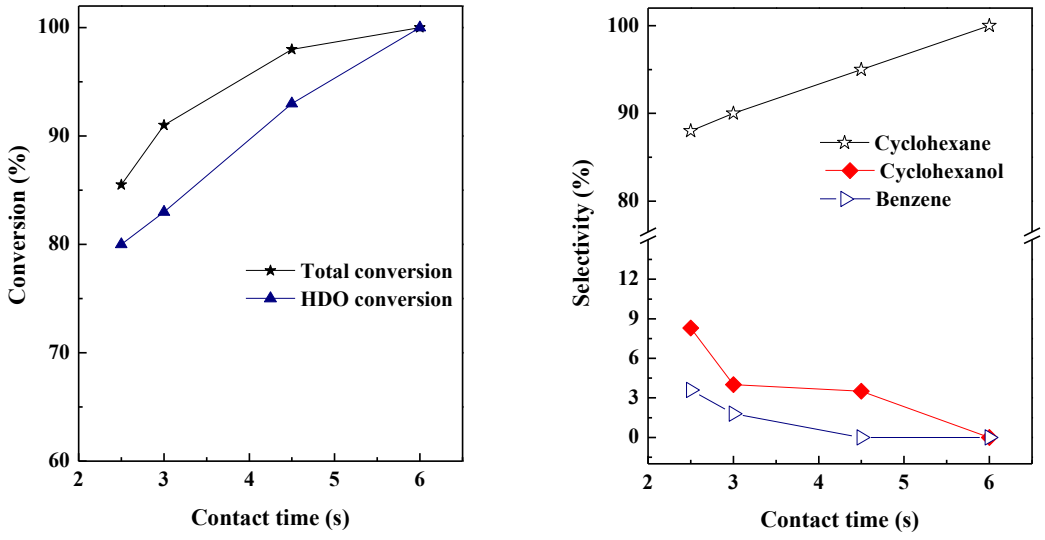

Figure 4.8. Evolution of conversion and selectivity versus contact time

Based on these results, further experiments were carried out at 3 s of contact time and 1.5 MPa of H_2 since it is known that milder pressures hamper the deoxygenation process. These conditions lead to remarkable differences in conversion and product distribution, especially in the case of bimetallic catalysts as seen in Figure 4.9. But their catalytic performance trend remains the same as when working at 3.0 MPa and 6 s of contact time. Figure 4.9 also shows

the evolution of the conversion versus time on stream where it can be seen that after six hours on stream the samples achieved constant conversion values. Again, monometallic catalysts are fairly selective to deoxygenated products, especially the FeP sample, also being the catalyst which leads to the lowest conversion results.

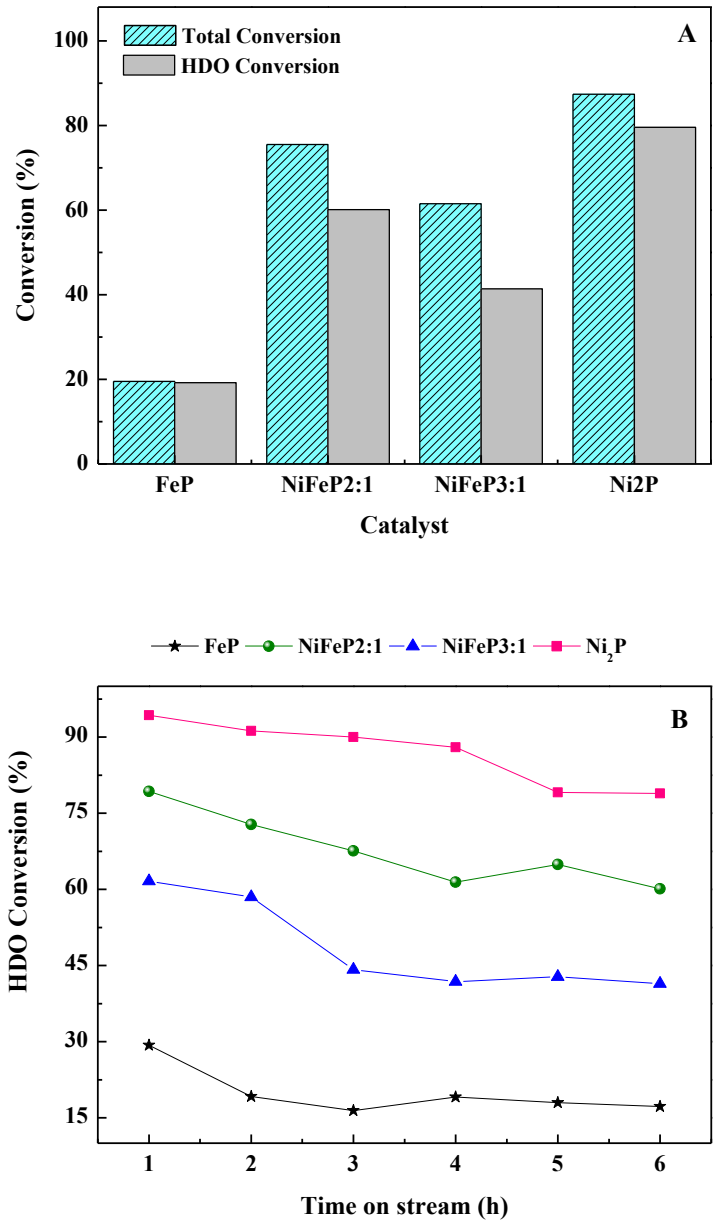

Figure 4.9. A)Total and HDO conversion after 6 h on stream and B) HDO conversion versus time on stream. Reaction conditions: T=300 ºC, P=1.5 MPa, WHSV= 0.42h^{-1},H_2 contact time= 3 s, H_2/phenol=72.1

With regard to the reaction products, the HDO of phenol can proceed through three distinct pathways suggested in the literature, as seen in Scheme 4.1 [16-18] . Reaction pathway (1) is a

direct deoxygenation route (DDO) which involves the direct scission of the C_{AR} (sp^2)-OH bond by hydrogenolysis to give benzene. Partial hydrogenation of benzene yields cyclohexene, which can be further hydrogenated to cyclohexane. In the alternative reaction route (2), the hydrogenation-dehydration route (HYD), the aromatic ring is partially hydrogenated to 1-hydroxy-cyclohexene, which is a tautomer of cyclohexanone. Further hydrogenation of 1-hydroxy-cyclohexene results in the formation of cyclohexanol. The hydroxyl group on cyclohexanol can be removed through dehydration, and further hydrogenation is needed to produce cyclohexane. Cyclohexanol can also be converted to cyclohexane in one step through hydrogenolysis. The third pathway (3), known as tautomerization-deoxygenation route, involves the keto-enol tautomerization of phenol into 3,5-cyclohexadienone. The formation of this highly unstable keto compound will cause its facile C=O hydrogenation and its subsequent dehydration to form benzene [19].

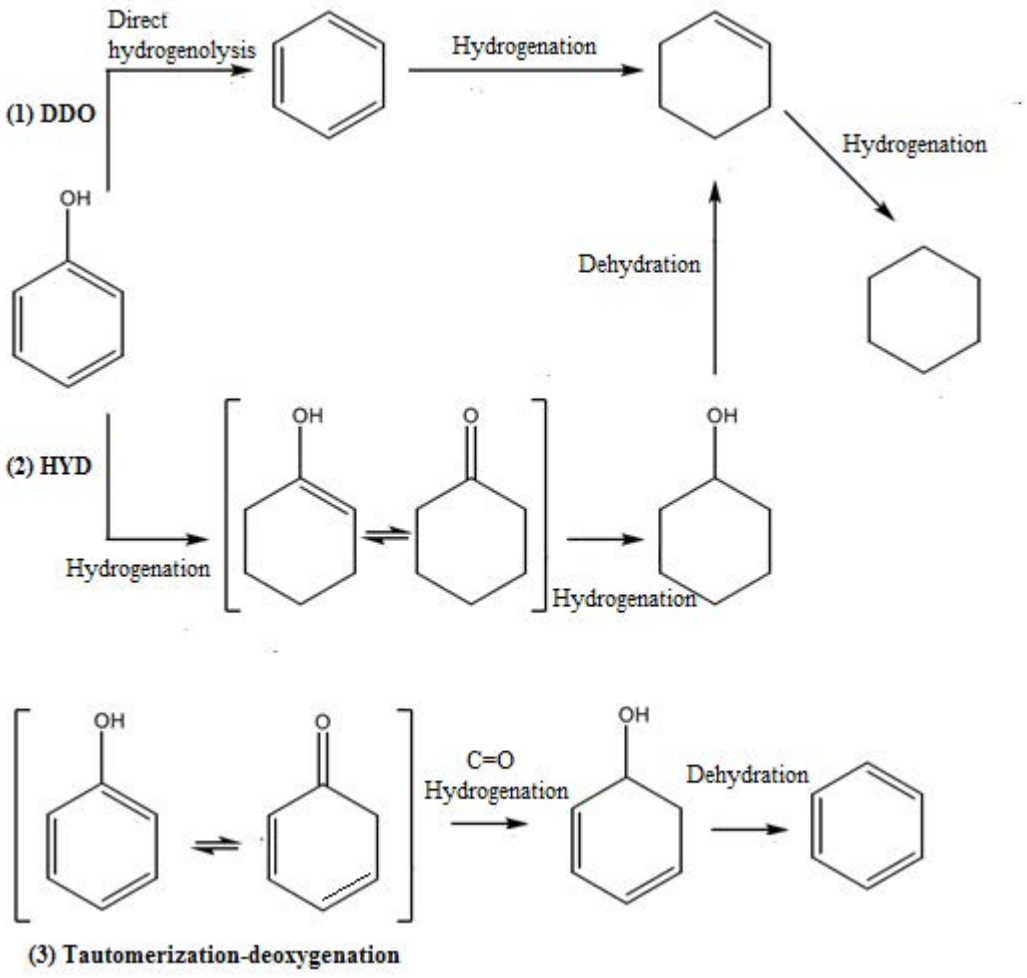

Scheme 4.1. Proposed reaction pathways for phenol HDO [19, 20]

It has also been reported that hydrogenation of phenol over Ni catalysts generates cyclohexanone as the primary product; however, the subsequent hydrogenation of cyclohexanone to cyclohexanol takes place at much higher rate so cyclohexanone might not be detected as it is the case [21].

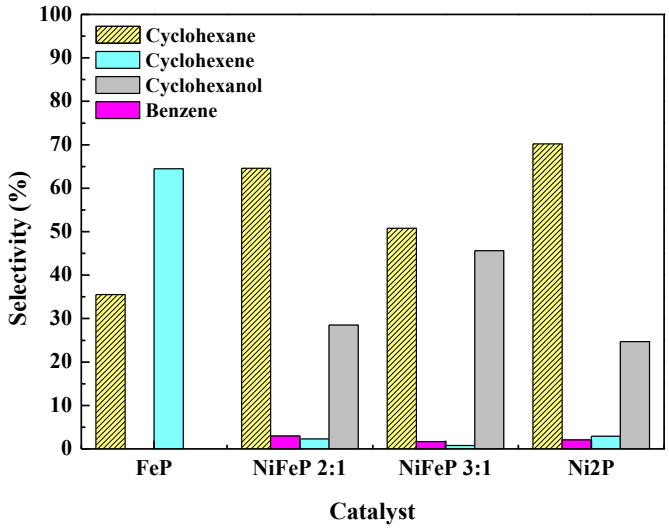

Figure 4.10. Selectivity at 300ºC and 1.5 MPa after 6 h on stream, WHSV=0.42 h^{-1}

As seen in Figure 4.10, all catalysts are highly selective to cyclohexane except for the FeP sample which gives cyclohexene as main reaction product. This striking result seems to indicate that hydrogenation of cyclohexene is a limiting step. In the case of nickel-containing catalysts, the use of milder conditions provokes a decrease in phenol conversion with cyclohexane as the main product, although its selectivity decreased with time on the stream, whereas cyclohexanol selectivity increased. Thus, the degree of hydrogenation of the aromatic ring strongly depends on the reaction pressure employed and the contact time between the feed and the catalyst. This fact suggests that the step to convert cyclohexanol to cyclohexene is the rate limiting step for obtaining deoxygenated products with Ni containing catalysts. Previously, it was reported that deoxygenation takes place more easily from a saturated ring than from an unsaturated ring, which is related to the dissociation energy of the C- O bond [21]. Our results are in line with this finding, since HDO is presumably achieved through the hydrogenation-dehydration route (HYD). In addition, trace amounts of benzene (approximately 10%) are also observed for the Ni_2P sample during the first 3 h. Taking into account the high selectivity of these catalysts to cyclohexane and the relatively low temperature employed for the dehydrogenation reaction, it is expected that benzene formation would occur by DDO of phenol. But it also could take place by the tautomerization-deoxygenation route, despite not having detected 3,5- cyclohexadienol

among the reaction products. Low selectivity values to benzene were also observed at similar reaction temperatures for other phases[22].

4.4. Discussion

The fact that bimetallic catalysts present the greatest selectivity to cyclohexanol can be correlated to the synergetic effect observed in NH_3-TPD experiments. These results point to the presence of strong acid sites in both catalysts which are responsible of retaining cyclohexanol molecules on the surface, hindering the dehydration of cyclohexanol to cyclohexane. In addition, as observed by H_2-TPD, these catalysts show different hydrogen activation capability, which also contributes to this fact.

If TOF values were calculated from CO chemisorption measurements at P = 1.5 MPa and contact time = 3s, the activity per active site would follow the trend NiFeP2:1 (106.9 $10^{-3}s^{-1}$) > Ni_2P (80.2 $10^{-3}s^{-1}$) > NiFeP3:1 (73.710$^{-3}s^{-1}$) > FeP (71.4 $10^{-3}s^{-1}$). These results indicate that the activity per active site is higher in the case of the NiFeP2:1 sample, although other data such as hydrogen activation capability and acidity should also be considered to explain the catalytic behaviour. These results point to the synergy effect of bimetallic catalysts being selective to non-deoxygenated products. From the CO chemisorption results, it is suggested that the number of active sites increases with the nickel content and therefore dispersion seems to be promoted. However, TEM results indicate the opposite trend showing a greater dispersion with the iron content. As a result, it can be estimated that CO is mainly chemisorbed on Ni sites. Despite the Ni_2P catalyst has greater CO chemisorption values and is the most active in terms of conversion, there is not a clear correlation between phenol conversion and chemisorption results. The activity of the prepared catalysts in this study can also be explained by considering the acidity, hydrogen activation capability as well as the active phase dispersion. All of the catalysts have acidic centers associated with the presence of Ni, Fe and P on surface. This acidity is mainly weak in nature and ascribed to the presence of Lewis and Brönsted acid sites. In mixed phosphides, the acid strength increases from NiFeP3:1 to NiFeP2:1, which is attributable to the modification of the electronic state of nickel in the presence of iron. Dandford et al.[23] observed this effect from IR of adsorbed CO in $Ni_{2-x}Fe_xP/SiO_2$ systems. Also noting that as the nickel content increased, the amount of hydrogen desorbed from the metal surface was greater and the temperature required for this process was lower. That is, in the presence of Ni the catalyst is better able to active hydrogen on its surface. In fact, XPS results indicate that the concentration of phosphorus species on surface is greater when increasing nickel content. These surface P-OH groups contribute to the hydrogen spillover effect as observed in H_2-TPD experiments.

The structure of Ni_2P and FeP phases have both been described previously [4]. In mixed phosphides of Ni and Fe, Cho et al.[3] observed that increasing the amount of Fe in the Ni_2P phase changed the lattice parameters towards the formation of bulk FeP. The sites that Fe can occupy in the Ni_2P structure have been determined by Mössbauer spectroscopy [2] and EXAFS [24] concluding that are dependent on the catalyst composition. If Fe substituted Ni at M(2) sites, which are consider to be more active, the lower activity of bimetallic samples could be explained. In the present chapter bimetallic phosphides with higher Fe content are slightly more active, which is associated to the preferential location of Fe in one site or another. Although further research is necessary to understand the role of Fe during HDO in these systems, FeP/SiO_2 sample has shown remarkable HDO activity at high temperatures and has proven to be highly selective to O-free compounds. Previously, a FeP/KUSY [3] sample showed minimal CO uptake capability and had the lowest conversion levels (2-methyltetrahydrofuran) relative to nickel-containing samples. These authors attributed this behaviour to the strong Fe-P bond that avoids the presence of open coordination sites. There are several differences between that work and ours, but mainly their reaction pressure was 0.5 MPa while we have used 3.0 and 1.5 MPa. In the present work, we observed that FeP sample required higher H_2 pressures than Ni_2P samples, which is attributable to its lower H_2 activation capability as determined from H_2-TPD experiments.

4.5. Conclusions

The main conclusions extracted from the present chapter are:

- Silica-supported catalysts based on mono and bimetallic nickel and iron phosphides prepared from phosphite-type precursors displayed good catalytic performance in the removal of oxygen from phenol.
- Deoxygenated compounds were the main observed reaction products in all cases. Particularly, cyclohexane was the main deoxygenated product obtained for Ni-containing samples.
- Catalytic activity decreased upon incorporation of Fe into Ni_2P structures and this result was independent of the dispersion of the active phase.
- Monometallic samples were more selective to O-free compounds, indicating that bimetallic samples present a synergistic effect that increases their selectivity for O-containing intermediates.

4.6 References

1. Cecilia, J.A., et al., *Dibenzothiophene hydrodesulfurization over cobalt phosphide catalysts prepared through a new synthetic approach: Effect of the support.* Applied Catalysis B: Environmental, 2009. **92**(1-2): p. 100-113.
2. Wang, X., P. Clark, and S.T. Oyama, *Synthesis, Characterization, and Hydrotreating Activity of Several Iron Group Transition Metal Phosphides.* Journal of Catalysis, 2002. **208**(2): p. 321-331.
3. Cho, A., et al., *Ligand and Ensemble Effects in Bimetallic NiFe Phosphide Catalysts for the Hydrodeoxygenation of 2-Methyltetrahydrofuran.* Topics in Catalysis, 2012. **55**(14-15): p. 969-980.
4. Zhao, H., et al., *Nature of active sites in Ni 2 P hydrotreating catalysts as probed by iron substitution.* Applied Catalysis B: Environmental, 2015. **164**: p. 204-216.
5. Fang, H., et al., *Product tunable behavior of carbon nanotubes-supported Ni–Fe catalysts for guaiacol hydrodeoxygenation.* Applied Catalysis A: General, 2017. **529**: p. 20-31.
6. Bui, P., et al., *Studies of the synthesis of transition metal phosphides and their activity in the hydrodeoxygenation of a biofuel model compound.* Journal of Catalysis, 2012. **294**: p. 184-198.
7. Cecilia, J.A., et al., *A novel method for preparing an active nickel phosphide catalyst for HDS of dibenzothiophene.* Journal of Catalysis, 2009. **263**(1): p. 4-15.
8. Lee, Y. and S. Oyama, *Bifunctional nature of a SiO2-supported Ni2P catalyst for hydrotreating: EXAFS and FTIR studies.* Journal of Catalysis, 2006. **239**(2): p. 376-389.
9. Chen, J., et al., *Deoxygenation of methyl laurate as a model compound to hydrocarbons on transition metal phosphide catalysts.* Applied Catalysis B: Environmental, 2014. **144**: p. 870-884.
10. Pan, Z., et al., *Effect of a second metal (Co, Fe, Mo and W) on performance of Ni2P/SiO2 for hydrodeoxygenation of methyl laurate.* Journal of Energy Chemistry, 2016. **25**(3): p. 418-426.
11. Chen, J., et al., *A facile approach to enhancing activity of Ni2P/SiO2 catalyst for hydrodechlorination of chlorobenzene: promoting effect of water and oxygen.* Catalysis Science & Technology, 2015. **5**(5): p. 2670-2680.
12. Cecilia, J.A., et al., *Influence of the silica support on the activity of Ni and Ni2P based catalysts in the hydrodechlorination of chlorobenzene. Study of factors governing catalyst deactivation.* Journal of Molecular Catalysis A: Chemical, 2013. **368-369**: p. 78-87.
13. Wang, L., et al., *Hydrodeoxygenation of dibenzofuran over SiO2, Al2O3/SiO2 and ZrO2/SiO2 supported Pt catalysts.* Catal. Sci. Technol., 2015. **5**(1): p. 465-474.
14. Yan, K., et al., *Effect of preparation method on Ni2P/SiO2 catalytic activity for NaBH4 methanolysis and phenol hydrodeoxygenation.* International Journal of Hydrogen Energy, 2015. **40**(46): p. 16137-16146.
15. Liu, X., J. Chen, and J. Zhang, *Hydrodechlorination of Chlorobenzene over Silica-Supported Nickel Phosphide Catalysts.* Industrial and Engineering Chemistry Research, 2008. **47**: p. 5362-5368.
16. Zhao, C., et al., *Aqueous-phase hydrodeoxygenation of bio-derived phenols to cycloalkanes.* Journal of Catalysis, 2011. **280**(1): p. 8-16.
17. Boullosa-Eiras, S., et al., *Catalytic hydrodeoxygenation (HDO) of phenol over supported molybdenum carbide, nitride, phosphide and oxide catalysts.* Catalysis Today, 2014. **223**: p. 44-53.
18. Nie, L. and D.E. Resasco, *Kinetics and mechanism of m-cresol hydrodeoxygenation on a Pt/SiO2 catalyst.* Journal of Catalysis, 2014. **317**: p. 22-29.
19. de Souza, P.M., et al., *Role of Keto Intermediates in the Hydrodeoxygenation of Phenol over Pd on Oxophilic Supports.* ACS Catalysis, 2015. **5**(2): p. 1318-1329.
20. Kay Lup, A.N., et al., *A review on reactivity and stability of heterogeneous metal catalysts for deoxygenation of bio-oil model compounds.* Journal of Industrial and Engineering Chemistry, 2017. **56**: p. 1-34.

21. Mortensen, P.M., et al., *Screening of Catalysts for Hydrodeoxygenation of Phenol as a Model Compound for Bio-oil.* ACS Catalysis, 2013. **3**(8): p. 1774-1785.
22. Infantes-Molina, A., et al., *Effect of Ir and Pt Addition on the HDO Performance of RuS2/SBA-15 Sulfide Catalysts.* Topics in Catalysis, 2015. **58**(4-6): p. 247-257.
23. Danforth, S.J., et al., *Probing hydrodesulfurization over bimetallic phosphides using monodisperse Ni 2-x M x P nanoparticles encapsulated in mesoporous silica.* Surface Science, 2016. **648**: p. 126-135.
24. Oyama, S.T., et al., *Transition metal phosphide hydroprocessing catalysts: A review.* Catalysis Today, 2009. **143**(1-2): p. 94-107.

5. Co phosphides for phenol and dibenzofuran HDO

5.1. Abstract

The present chapter develops the study of a series of cobalt phosphides supported on silica (5wt%) with different stoichiometry in the HDO of phenol and dibenzofuran. As in the previous chapter, the catalysts were prepared by means of temperature-programmed reduction of $Co(HPO_3H)_2$. The initial P/Co molar ratio values (0.5, 1, 1.5, 2 and 2.5) were chosen in order to obtain phosphides with different stoichiometry and thereby, be able to assess the influence of the formed phase on the catalytic results. They will be referred to as P/Co-x, where x is the phosphorus/cobalt initial molar ratio.

The catalysts were evaluated by a wide range of techniques and were tested in the HDO of two model molecules under different temperatures and reaction conditions. Characterization measurements were carried out before and after the catalytic tests for both model molecules.

5.2. Characterization results

5.2.1 X-ray diffraction (XRD)

The crystalline phases of the studied materials have been evaluated by means of X-ray powder diffraction of the reduced catalysts. Figure 5.1 shows the diffraction profiles of fresh catalysts before the catalytic test. Diffraction lines are difficult to distinguish which is expected if taking into account the low metal loading and its high dispersion over the support surface [1].

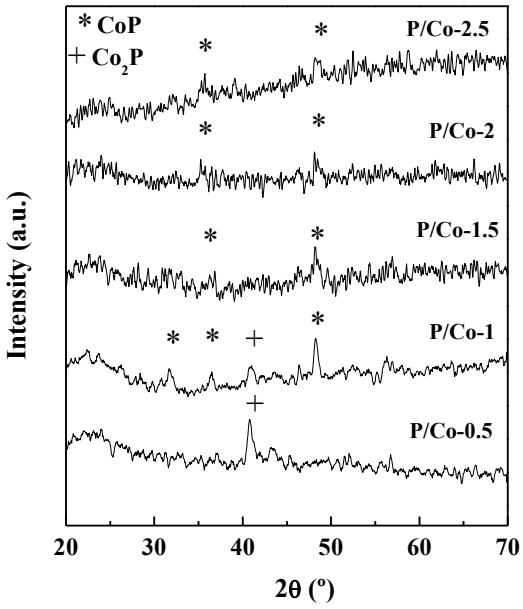

Figure 5.1. X-ray diffractograms of fresh catalysts before the catalytic essays

Furthermore, the intensities of the signals suffer a slight decrease as P content increases, which is indicative of a better dispersion of the active phase. Even so, different phosphides phases can

be distinguished as a function of the initial P/Co molar ratio. Thus, the sample P/Co-0.5 with the lowest initial P/Co ratio presents the main diffraction signal at 2θ = 40.8° (JCPD No. 00-054-0413) which corresponds to a metal rich phosphide, Co_2P. As the phosphorous content increases, P/Co-1 sample, it is observed new emerging diffraction lines located at 2θ = 48.1° and 36° (JCPD No.03-065-2593) corresponding to a phase with greater P content, the CoP phase. Therefore, in P/Co-1 catalyst both phases coexist. For the rest of catalysts with P/Co ≥1.5, CoP is the only observable phase.

As seen hereafter, a new crystalline phase appears after the catalytic test. Figure 5.2 shows X-ray diffractograms of catalysts after the HDO reaction of phenol and dibenzofuran. Again, after HDO of phenol, diffraction profiles do not show clear diffraction lines although phase identification is barely possible. Instead, after HDO reaction of dibenzofuran, all diffraction patterns show an increased intensity of the peaks and the appearance of new diffraction peaks. After both catalytic tests, the samples P/Co-0.5 and P/Co-1 keep on presenting the same phosphide phases than before the essays. But, as mentioned before, a new phosphorus enriched phase, CoP_2 (JCPD No 98-003-8316), appears in catalysts P/Co-2 and P/Co-2.5. This phase was not detected before the test. These results might explain the most outstanding performance of P/Co-1.5, presenting CoP as the major phase which is regarded as the most active one in hydrotreating reactions [1, 2]

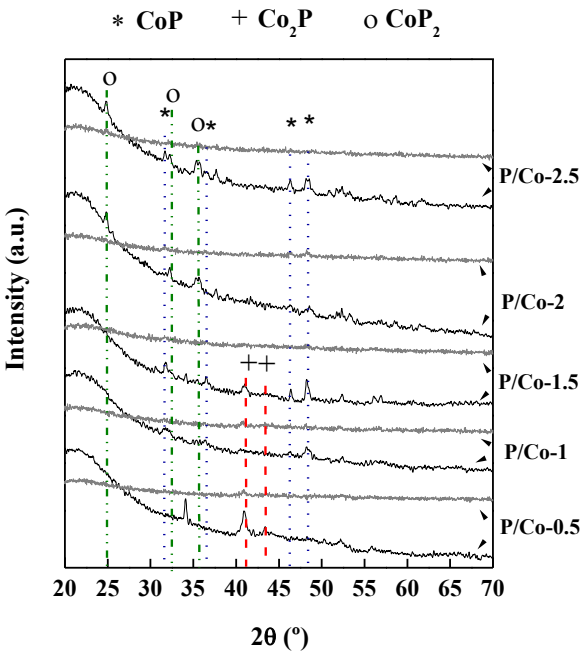

Figure 5.2. X-ray diffractograms of spent catalysts after HDO of phenol (grey lines) and after HDO of DBF (black lines)

5.2.2 Textural properties

Textural properties of the support and fresh catalysts have been evaluated by N_2 adsorption-desorption at -196 ºC. Table 5.1 compiles the specific surface area, pore volume and pore diameter data. As seen in the previous chapter, incorporation of the active phase provokes a decrease on the specific surface area. Specifically, as the P/Co ratio increases, S_{BET} values decrease as a consequence of surface P excess, which causes the blockage of the pores [3].

Table 5.1. Textural properties of fresh catalysts

Sample	$S_{BET}(m^2 \cdot g^{-1})$	$Vp(cm^3 \cdot g^{-1})$	Dp(nm)
SiO_2	217	0.51	14.8
P/Co-0.5	165	0.41	9.1
P/Co-1	139	0.37	9.3
P/Co-1.5	157	0.48	10.7
P/Co-2	148	0.53	12.5
P/Co-2.5	127	0.44	11.6

Although the loss on textural properties is barely noticeable if compared to the bare support, it becomes sharper for catalysts with higher phosphorus content. Anyhow, these results indicate that after metal incorporation the textural properties of the bare support do not suffer a sharp decrease.

5.2.3 Transmission electron microscopy (TEM)

The distribution of the active phase on the support surface has been evaluated by TEM analysis. Micrographs of each catalyst are quite similar showing a good dispersion of the metallic phosphide phase. Figure 5.3 shows the micrographs corresponding to P/Co-1.5, which is the catalyst with the most homogeneous particle size distribution. Statistical quantification of particle sizes has also been accomplished by measuring different regions of several micrographs of each catalyst. In all cases, a distribution of particle sizes ranging from 3 to 10 nm is observed. Bigger particles are also detected but without a clear trend. The mean particle sizes range from 5 to 6.5 nm. Figure 5.3 also includes the histogram of P/Co-1.5 sample with an average particle size of 6.3 nm. The similarity of these results suggests that the particle sizes are not affected by the initial P/Co ratio used.

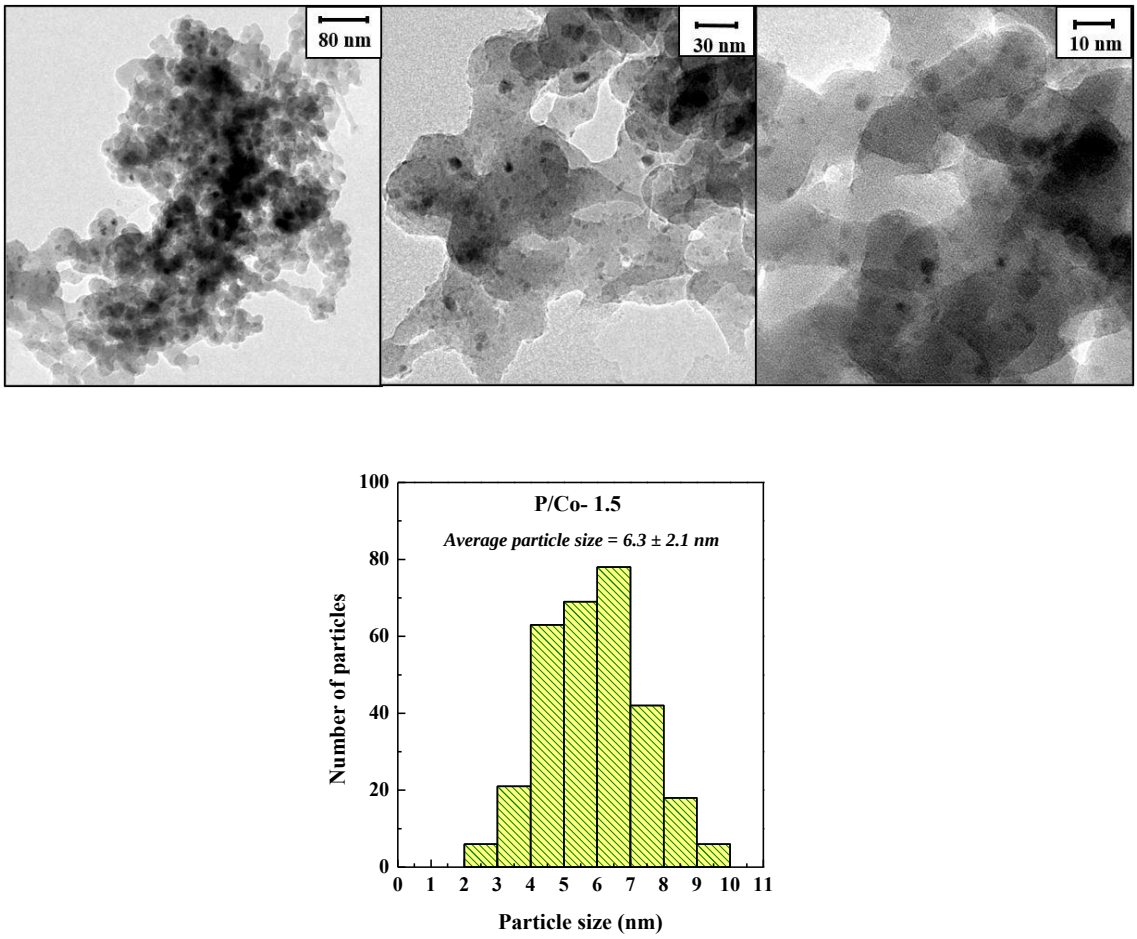

Figure 5.3. TEM micrographs of fresh P/Co-1.5 sample and particle size distribution

5.2.4 Ammonia temperature-programmed desorption (NH_3-TPD)

Acidic properties of fresh catalysts have been evaluated by means of NH_3-TPD experiments. Concentration of acid sites expressed as µmol of desorbed NH_3 per gram of catalyst, are compiled in Table 5.2.

Table 5.2. Acidic values expressed as µmol$NH_3 \cdot g^{-1}$ catalyst

Sample	Total acidity	Weak acidity	Strong acidity
SiO_2	-	-	-
P/Co-0.5	61	36	8
P/Co-1	98	71	16
P/Co-1.5	182	115	36
P/Co-2	258	205	27
P/Co-2.5	445	328	105

The support has also been evaluated and, as seen in the previous chapter, commercial silica does not present acid sites, therefore the acidity can be entirely ascribed to the presence of

phosphorus and cobalt as previously reported [4]. In addition, the presence of Lewis acid sites is ascribed to unreduced M^{2+} species whereas Brönsted centers are attributed to P-OH species as reported in literature [5]. Since the high reduction temperature prevents the presence of unreduced Co^{2+} and HPO_3H^- species, desorption of ammonia comes from both CoP and Co_2P phase. Therefore, Lewis acidity cannot be attributed to single Co^{2+} atoms, but to coordinative unsaturated Co^{2+} sites acting as a kind of new Lewis centers [3].

As seen in Table 5.2, the acidic nature of these materials is weak in character since ammonia is mainly desorbed at temperatures below 300 ºC. Figure 5.4 shows the desorption profiles of each catalyst along with a representation of initial P/Co ratio versus desorbed ammonia. This representation shows how the acidity directly increases with the initial P/Co ratio, likely due to a major concentration of P-OH species acting as Brönsted acid sites.

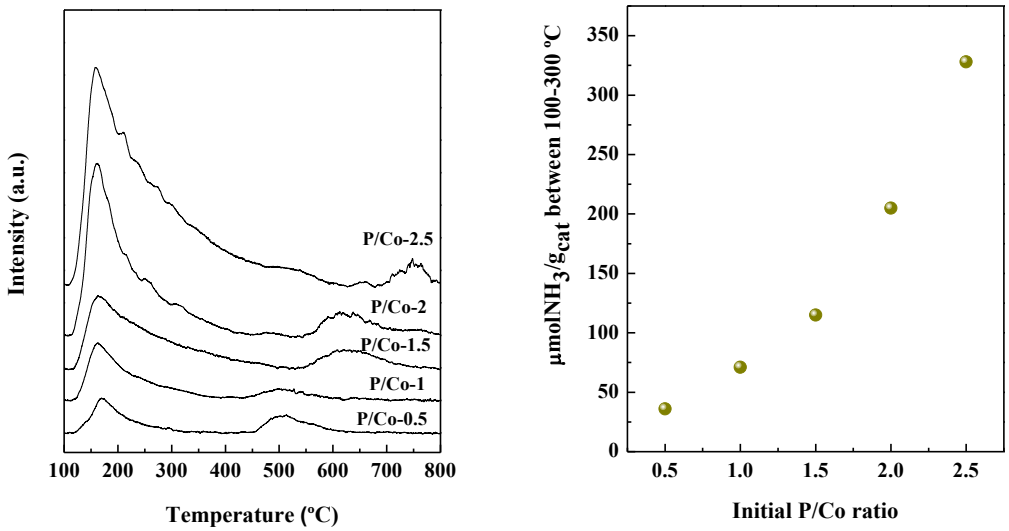

Figure 5.4. NH_3-TPD profiles of studied catalysts and weak acidity versus initial P/Co molar ratio

5.2.5 X-ray photoelectron spectroscopy (XPS)

The chemical composition of the catalysts surface and the chemical state of the constituent elements has been determined by XPS. Figure 5.5 shows the Co 2*p* and P 2*p* core-level spectra of the studied catalysts and Table 5.3 compiles the binding energy values. In all cases, the Co 2*p* signal present two contributions located at 778.0 and 781.5 eV. The first contribution is ascribed to $Co^{\delta+}$ species present in the phases CoP and Co_2P. The second contribution is attributed to the presence of Co^{2+} from the partial oxidation of the surface. The P 2*p* core-level spectra present two contributions of the P 2 $p_{3/2}$ component. First contribution centered at 129.1 eV is assigned to $P^{\delta-}$ species present on both CoP and Co_2P phases. The second one is assigned to PO_4^{3-} species

derived from surface passivation. Atomic surface concentrations have also been measured and surface atomic ratios of the different elements are included in Table 5.3. From the observed tendency in Co/P and Co/Si molar ratios it follows that surface cobalt exposure increases with increasing phosphorus content. In other words, in spite of the incorporation of a greater amount of phosphorous (keeping constant cobalt amount), surface is enriched with cobalt species.

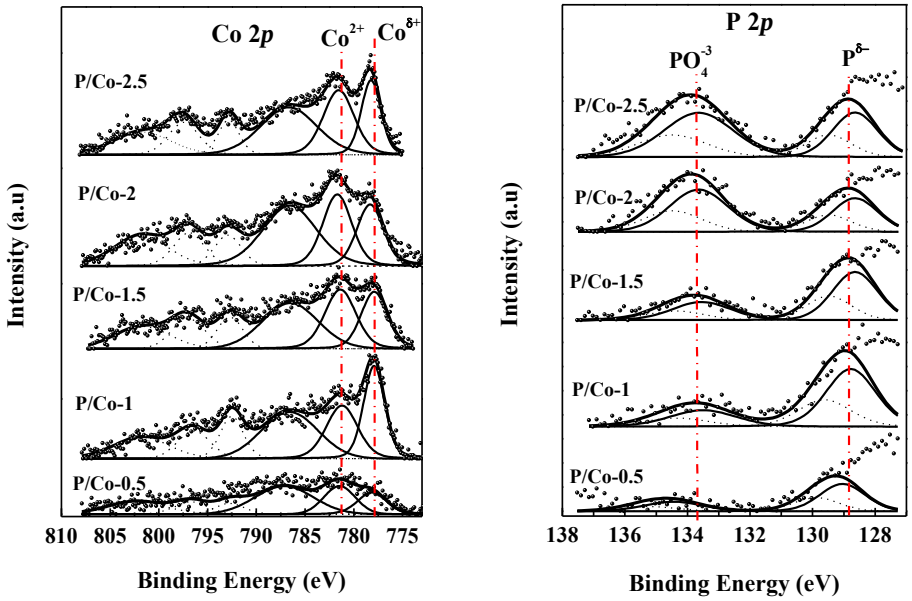

Figure 5.5. Co *2p* and P *2p* core level spectra of fresh catalysts

Table 5.3. Binding energy values and surface atomic ratios of fresh catalysts

Sample	Binding Energy (eV)				Surface Atomic ratio				
	Co $2p_{3/2}$		P $2p_{3/2}$		Co/P	Co/Si	$Co^{\delta+}$/Si	$Co^{\delta+}/Co^{2+}$	PO_4^{3-}/Si
	Co^0/ $Co^{\delta+}$	Co^{2+}	PO_4^{3-}	$P^{\delta-}$					
P/Co-0.5	778.0	781.5	134.4	129.0	1.028	0.012	0.0025	0.27	0.0036
P/Co-1	777.9	781.2	133.5	128.8	1.437	0.029	0.0093	0.48	0.0101
P/Co-1.5	777.9	781.4	133.5	128.6	1.605	0.028	0.0078	0.37	0.0099
P/Co-2	778.2	781.5	133.6	128.6	1.691	0.040	0.0098	0.33	0.0147
P/Co-2.5	778.3	781.6	133.6	128.6	1.194	0.039	0.0099	0.35	0.0198

However, any of the molar ratios included in Table 5.3 follows a clear trend as to state that the concentration of phosphide species on the surface does not change by increasing P/Co. Only the sample with the lowest phosphorous content, P/Co-0.5, shows a low concentration of phosphorus on surface while the sample P/Co-2.5 evidences that the surface is enriched with phosphorus if compared with the rest of the samples. Considering now the $PO4^{3-}$/Si ratios, it is observed that the results match with NH_3-TPD data, indicating that these species are responsible of the acidity of the studied samples. Figure 5.6 includes the Co $2p_{3/2}$ spectra of spent catalysts after HDO reaction of phenol and DBF. A similarity among the spectra is observed with the exception of the signal corresponding to the cobalt phosphide phase ($Co^{\delta+}$), which is less intense also suffering a chemical shift to higher binding energy values when P content is higher. This might be related to the formation of a phosphide with a modified stoichiometry, which seems to be richer in a non-metal, provoking a chemical shift to greater binding energy values. This fact occurs independently of the catalytic reaction studied. However, the signals are less defined after HDO reaction of phenol which was also noticed by XRD. This suggests that the active phase remains highly dispersed during on stream operation of phenol if compared to fresh sample spectra.

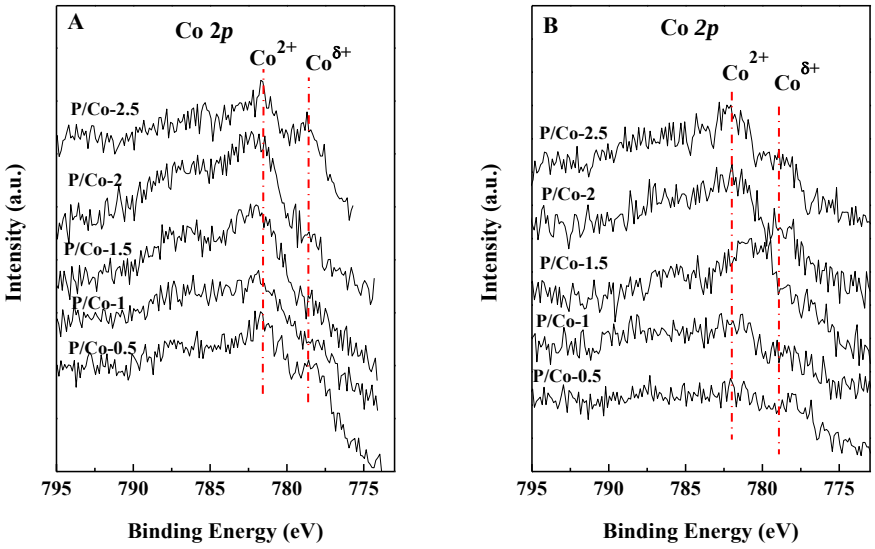

Figure 5.6. Co *2p* core level spectra of spent catalysts after HDO of A) DBF and B) phenol

Figure 5.7 shows the decomposed spectra of the Co *2p* and P *2p* core level spectra of the P/Co-2.5 catalysts, the only one presenting the CoP_2 phase after reaction as seen by XRD. Considering the P $2p_{3/2}$ and P $2p_{1/2}$ signals, it is observed that the intensity of both contributions suffer a remarkable increase, which point out to a phosphorus surface enrichment as a consequence of the formation of the aforesaid phase after the catalytic process. Likewise, Table 5.4 compiles the binding energy values and the corresponding surface atomic ratios. If the Co/Si

ratio is considered, Co surface exposure decreases after the catalytic process as well as Co/P atomic ratio that goes from 1.19 to 0.83. These results confirm, as seen by XRD, the formation of a new phase with a greater P content, CoP_2.

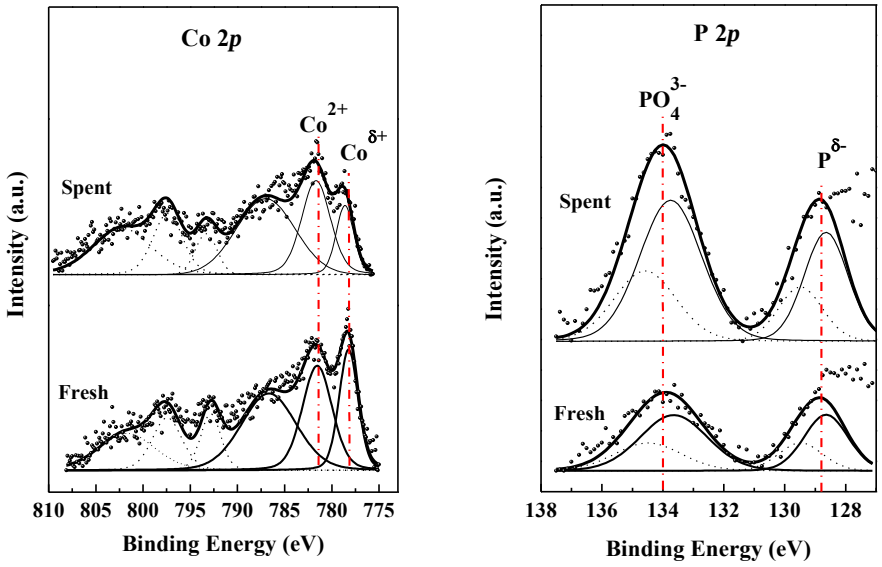

Figure 5.7. Co *2p* and P *2p* core level spectra of fresh versus spent P/Co-2.5 catalyst before and after HDO reaction of DBF

Table 5.4. Binding energy values and surface atomic ratios of fresh and spent P/Co-2.5 catalyst before and after DBF HDO

	Binding Energy (eV)				Surface atomic ratio	
Sample	**Co $2p_{3/2}$**		**P $2p_{3/2}$**		**Co/P**	**Co/Si**
	$Co^{\delta+}$	**Co^{2+}**	**PO_4^{3-}**	**$P^{\delta+}$**		
Fresh	778.3	781.6	133.6	128.6	1.194	0.039
Spent	778.6	781.7	133.7	128.6	0.834	0.029

5.3. Catalytic results

5.3.1 HDO of Dibenzofuran

The catalytic performances of P/Co-x catalysts have been firstly evaluated in the HDO reaction of DBF as a model molecule given its low reactivity, as aforesaid. The essays have been accomplished under 1.5 and 3.0 MPa of hydrogen pressure using 2wt% of DBF solution diluted in decalin as organic feed. Catalytic results in terms of total and HDO conversion are represented in Figure 5.8 for both pressures in order to have an overall comparison. As

expected, results are directly related to the H_2 pressure. Conversion being higher at 3.0 MPa, reaches HDO values up to 80% for P/Co-1.5 and P/Co-2 catalysts. Working under 1.5 MPa, both total and HDO conversion decrease but the highest values are again obtained by the same catalysts with intermediate P/Co ratios. All catalysts display values relatively close to the conversion data, having high yields. This fact suggests that the first step in the HDO reaction of DBF can be limiting and that, once the oxygenated intermediates are formed, the reaction proceeds more readily.

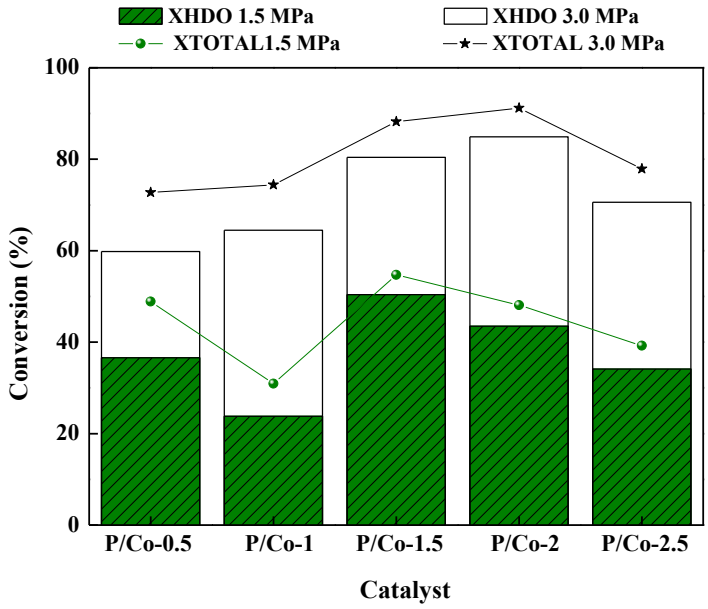

Figure 5.8. DBF total and HDO conversion versus P/Co ratio at 275ºC and 1.5 and 3.0 MPa of H_2, WHSV = 0,77 h^{-1}

In addition, previous research established that the HDO reaction of DBF can take place via different routes which depend on several parameters among which hydrogen pressure and reaction temperature are key factors [6-8]. Scheme 5.1 shows different routes through which the reaction can proceed. Via *I* takes place by direct hydrogenation of the aromatics rings and subsequent oxygen removal from saturated rings. In Via *II* the oxygen removal is preceded by the hydrogenation of a single benzene ring. And Via *III* occurs by direct deoxygenation pathway; oxygen removal takes place first by direct cleavage of oxygen to aromatic carbons followed by excision of Csp^2-Csp^2. In practice, bicyclohexane (BCH) is obtained as majority product along with minor quantities of cyclohexylbenzene (CHB), benzene (B), cyclopentylcyclohexane (C-PE-CH) and cyclopentylmethylcyclohexane (C-PE-ME-CH). With regard to the O-intermediated products, the presence of 2,3,4,9 tetrahydrodibenzofuran(THDBF), 2,3,4,4a,9a, hexahydrodibenzofuran(HHDBF) and 1-

1`bi(cyclohexan)-3-en-2-ol (BCH-3-en-2-ol) is noticeable, although these products are obtained to a much lesser extent than the oxygenated ones.

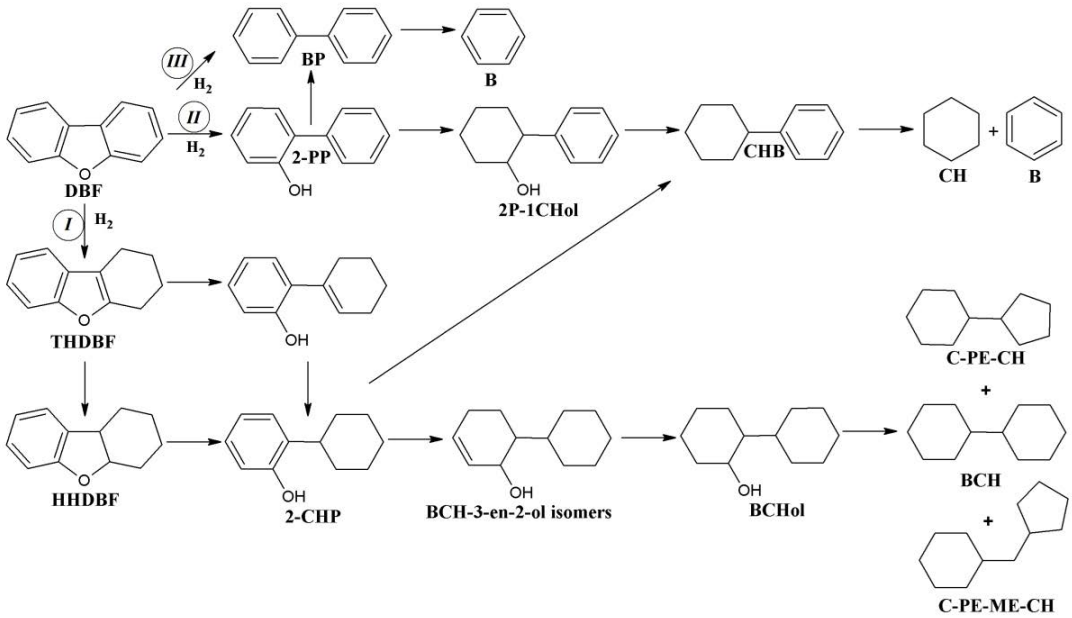

DBF: Dibenzofuran, **THDBF**: 2,3,4,9 Tetrahydrodibenzofuran, **HHDBF**: 2,3,4,4a,9,9a Hexahydrodibenzofuran, **2-CHP**: 2-cyclohexylphenol, **BCH-3-en-2-ol isomers**: 1-1'bi(cyclohexan)-3-en-2-ol, **BCHol**: By(cyclohexan)-2ol, **BCH**: Bicyclohexane, **C-PE-CH**: Cyclopentylcyclohexane, **C-PE-ME-CH**: (Cyclopentylmethyl)cyclohexane, **2-PP**: 2-phenylphenol, **2P-1CHol**: 2-Phenyl-1-cyclohexanol, **CHB**: Cyclohexylbenzene, **CH**: Cyclohexane, **B**: Benzene, **BP**: Biphenyl

Scheme 5.1. Proposed routes for dibenzofuran HDO [6]

The selectivity distribution to deoxygenated compounds and oxygenated intermediates (Figure 5.9.A) present a Gaussian distribution with the highest selectivity values in the range 1≤P/Co≤2, achieving a maximum to HDO products around 90% for P/Co-1.5 catalyst. On the opposite, the catalyst with the lowest P content only reaches 66% of selectivity to deoxygenated compounds. In Figure 5.9.B, the product distribution after 6 h on stream shows that selectivity to CHB, C-PE-CH, C-PE-MECH and B is independent of the active phase due to similar results are obtained for all P/Co-x catalysts. However, the selectivity to BCH is directly correlated to the P/Co molar ratio, maintaining the volcano-type distribution with a maximum of 56% for the P/Co-1.5 catalyst. Selectivity to BCH remains unaffected along the time on stream for all catalysts with the exception of P/Co-0.5 sample, which shows a drastic decrease from 40% after 1 h of ToS to 20% after 6 h of ToS. It follows that the presence of phosphorous species has a beneficial effect on the stability of the P/Co-x catalysts. From these observations it can be inferred that BCH, coming from via I, is sensitive to the active phase while products coming from dehydrogenation (CHB), isomerization (C-PE-CH and C-PE-ME-CH) or cracking (Benzene) are less affected by the stoichiometry of the phosphide and are more dependent on the reaction conditions.

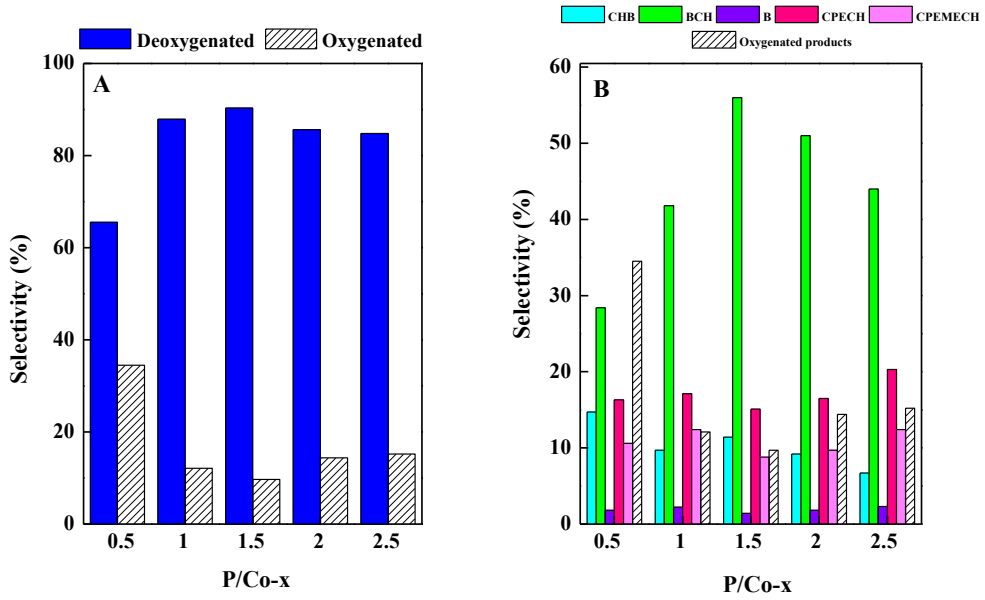

Figure 5.9. A) Selectivity to deoxygenated versus oxygenated products and B) selectivity product distribution after 6 h on stream. Reaction conditions = T=275 ºC, P=1.5 MPa, WHSV =0.77h^{-1}

As O-containing intermediates, THDBF, HHDBF and BCH-3-en-2-ol are attained among which THDBF reaches selectivity values ranging from 5 to 12%. With regard to HHDBF and BCH-3-en-2-ol, all catalysts follow a similar trend except for the P/Co-0.5 whose selectivity to both products increases with ToS. As aforesaid, the use of lower P content in the active phase seems to retain the reaction in earlier steps either by deactivation of the active phase or by adsorption on surface preventing the accessibility to active centers. Figure 5.10.A shows the selectivity values for the catalytic results at 3.0 MPa where a similar trend to that previously described at 1.5 MPa is observed.

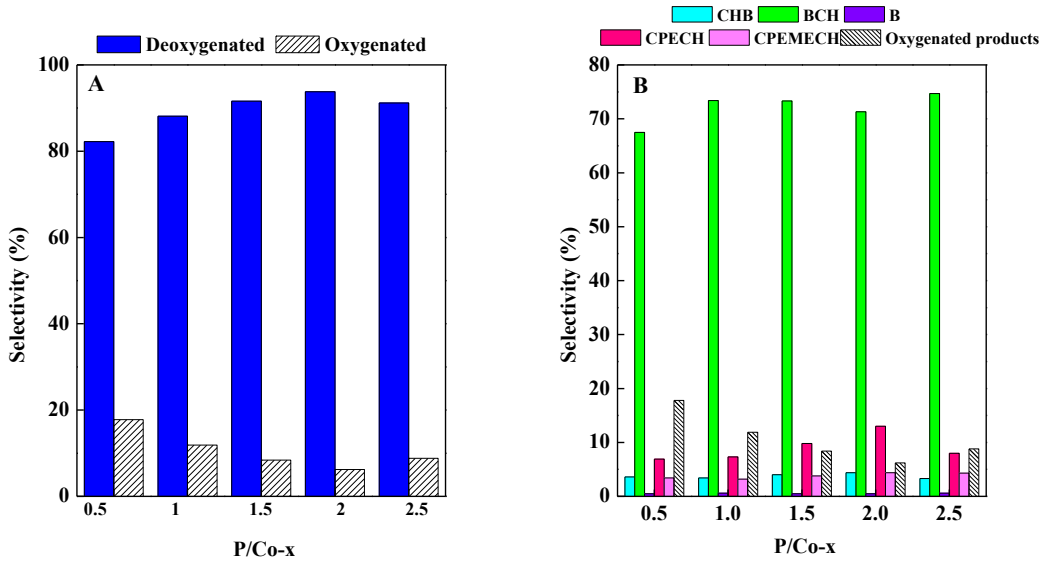

Figure 5.10. A) Selectivity to deoxygenated versus oxygenated products and B) selectivity product distribution after 6 h on stream. Reaction conditions: T=275 ºC, 3 MPa, WHSV=0.77 h^{-1}

Again, the maximum selectivity values are obtained for P/Co-1.5 and P/Co-2 samples. The use of higher hydrogen pressure barely provokes an increase of the selectivity to deoxygenated products, but the selectivity to BCH increases in all cases at expenses of CHB, C-PE-CH and C-PE-ME-CH as seen in Figure 5.10.B. It is also worth noting that under higher pressure, the P/Co-0.5 sample performance is much more similar to the trend observed for the rest of catalysts bringing to light how pressure affects the catalytic results.

5.3.2 HDO of Phenol

The catalytic activity of the cobalt phosphide catalysts have also been assayed in the HDO reaction of phenol. The catalytic performances have been evaluated at 300ºC under 3.0 MPa of hydrogen pressure. Total and HDO conversion after 6 hours are depicted in Figure 5.11.A and selectivity to the reaction products are included in Figure 5.11.B.

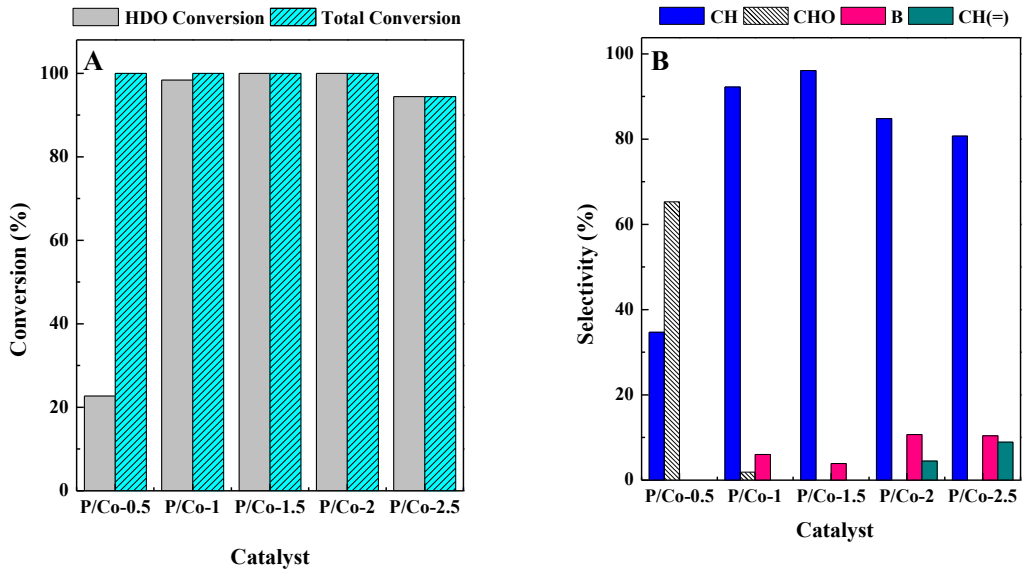

Figure 5.11. A) Total and HDO conversion of phenol and B) selectivity results after 6 h on stream. Reaction conditions: P=3 MPa, T= 300ºC, WHSV = 0.42 h^{-1}

From representation A, it is observed that all catalysts are highly active reaching HDO conversion values up to 100%. Again, as seen in the HDO of DBF the catalyst with the lowest P content (P/Co-0.5) shows a different behavior. Also achieving total conversion values up to 100% but being less active in the oxygen removal process.

With regard to the detected reaction products, Scheme 5.2 depicts three distinct pathways already discussed in the preceding chapter [9-11] . Reaction pathway (1) is a direct deoxygenation route (DDO) which involves the direct scission of the C_{AR} (sp^2)-OH bond by hydrogenolysis to give benzene. Partial hydrogenation of benzene yields cyclohexene, which can be further hydrogenated to cyclohexane. In the alternative reaction route (2), the

hydrogenation-dehydration route (HYD), the aromatic ring is partially hydrogenated to 1-hydroxy-cyclohexene, which is a tautomer of cyclohexanone. Further hydrogenation of 1-hydroxy-cyclohexene results in the formation of cyclohexanol. The hydroxyl group on cyclohexanol can be removed through dehydration, and further hydrogenation is needed to produce cyclohexane. Cyclohexanol can also be converted to cyclohexane in one step through hydrogenolysis. The third pathway (3), known as tautomerization-deoxygenation route, involves the keto-enol tautomerization of phenol into 3,5-cyclohexadienone. The formation of this highly unstable keto compound will cause its facile C=O hydrogenation and its subsequent dehydration to form benzene [12].

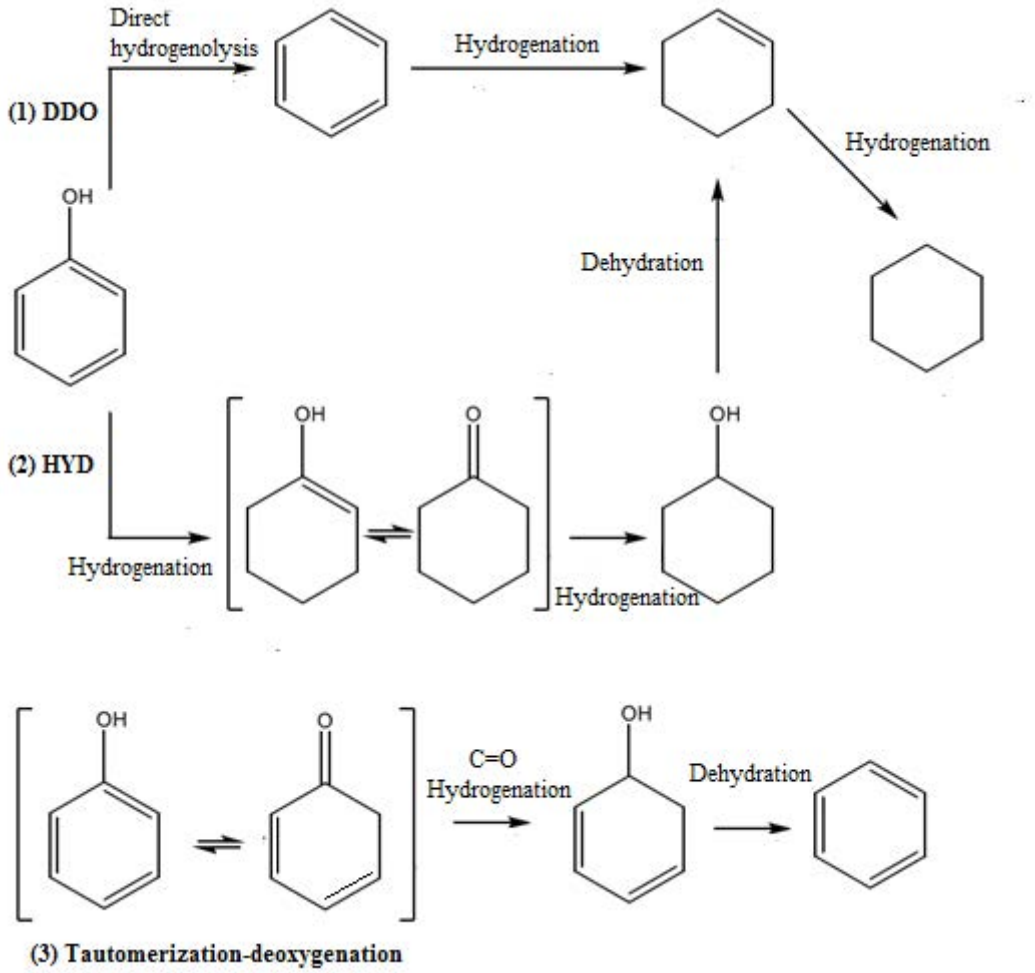

Scheme 5.2. Proposed reaction pathways for phenol HDO [12, 13]

Figure 5.11.B reveals cyclohexane as the main reaction product along with small proportions of benzene and cyclohexene, which are mainly detected for catalysts with higher phosphorous content (P/Co-2 and P/Co-2.5). As aforesaid, P/Co-0.5 catalyst exhibits different selectivity pattern with cyclohexanol as majority product, about 65%, and cyclohexane as the main

deoxygenated compound with a selectivity of only 35%. The low catalytic activity of the P/Co-0.5 catalyst together with the high cyclohexanol content detected suggests that the reaction takes place by the hydrogenation-dehydration route.

As previously reported, coordinatively unsaturated metal sites (CUS) located on the oxide surface can act as Lewis acid sites, while oxygen on the surface acts as Lewis basic center [14]. It has also been proposed that the phenol activation can proceed through heterolytic dissociation of the O-H bond on the SiO_2 surface, where the hydrogen from the phenol molecule is adsorbed on an oxygen site in the oxide surface layer and the phenoxide ion is stabilized by a metal vacancy center [15]. In that sense, Liu et al. have pointed out that phenol is adsorbed on Lewis acid centers which interact with the electronic cloud of the aromatic ring that possesses high nucleophilicity [16]. Lewis sites are attributed to the presence of Co^{2+} species as well as to the existence of defects in the grain boundary that are favored in small crystals [17]. Then, cobalt species interact with phenoxide molecules favoring the hydrogenation of the aromatic ring, leading to cyclohexanone, which evolves quickly to cyclohexanol (see Scheme 5.3). After that, cyclohexanol is adsorbed on the cobalt surface through the hydroxyl group leading to the deoxygenation by a dehydration process, forming cyclohexene and water. Cyclohexene is eventually hydrogenated to form cyclohexane [18].

5.4. Discussion

Previous research investigations have pointed out that catalysts with initial P/Co molar ratios in the range 1.5-2.0 have shown high catalytic activity in the hydrodechlorination of polychlorinated compounds [3, 19]. In the same vein, Burns et al. also evaluated the catalytic performance of cobalt phosphides with different P/Co molar ratios in the hydrodesulfuration of thiophene [2]. Similarly to the data obtained in the present chapter, the catalyst with the lowest P/Co molar ratio displays worse catalytic behavior than those catalysts with higher P content, being P/Co-1.5, the one which led to the best results. In addition, either BCH, C-PE-CH and C-PE-ME-CH present an added value due to their potential use as jet or diesel fuel [20].

The use of DBF as model molecule has been hardly studied in HDO reactions due to its low reactivity. Noble metals such as Pt, Pd or Ru have been tested in the HDO reaction of DBF. From data reported in literature, it can be deduced that the use of supports with low acidity, such as SBA-15, retains the reaction in oxygenated intermediates [21]. Therefore, supports with relatively high acidity such as zeolite [22, 23], Nb_2O_5 [24]or mixed oxides (SiO_2/Al_2O_3 or SiO_2/ZrO_2) [25] have been tested to active the hydrogenating behavior of the phases, obtaining BCH, C-PE-CH, C-PE-ME-CH and CH as deoxygenated products, depending on the reaction conditions. It is well recognized that the presence of acidity in a catalyst promotes the

hydrogenation, although the cracking can also be favored [26]. In addition, the existence of acids sites favors the dehydration and isomerization reactions that could cooperatively function with metal catalyzed hydrogenation and turn promote HDO reaction [27].

According to the literature, the HDO reaction of DBF must take place between cobalt metal surface and one of the benzene rings by the partial or whole hydrogenation of sp^2 C–O bond to sp^3 C–O bond [28, 29] to favor the later dehydration on the acid sites (P-OH or Co^{2+}), obtaining the oxygenated intermediates. After that, a similar procedure must be occurring in the other aromatic ring to obtain BCH. As previously indicated, the presence of these necessary acid sites also causes secondary reactions, such as cracking or isomerization. Furthermore, the direct hydrogenolysis of the sp^2 C-O bond must be discarded since the cleavage of the aromaticity under the mild reaction conditions used in this study, is energetically disfavored due to the stability of the delocalized out of plane O-lone pair orbital. Studies in the HDO of benzofuran reported that the conversion of 2-ethylphenol to deoxygenated compounds are inhibited by the presence of benzofuran or 2,3-dihydrobenzofuran in the active site [30]. In the case of the HDO of dibenzofuran a similar event could take place, where DBF, THDBF or HHDBF can interact strongly with the metal sites inhibiting the conversion of BCH-3-en-2-ol into deoxygenated products. The incorporation of phosphorus into the active phase diminishes the metallic character of the cobalt species, facilitating desorption of these oxygenated intermediates. In fact, the catalyst with the lowest P content, and subsequent higher metallic character, displays higher BCH-3-en-2-ol selectivity probably due to the adsorption of DBF, THDBF or HHDBF that hinders the conversion of BCH-3-en-2-ol to BCH. By increasing the P-content, new phases with lower metallic character are obtained and being more active in this reaction.

Focusing now in the HDO of phenol, there have been several research investigations that have studied the catalytic activity of diverse active phases. Concretely, Yang et. al [31] evaluated the gas phase catalytic activity of CoMo and CoMoP sulfides supported on MgO at 300-450 ºC and 5 MPa, pointing out that HDO yield increases with the temperature, obtaining benzene as the main deoxygenated product. In addition, these authors have established that the direct deoxygenation occurs by the inhibition in the transfer of the substrate hydroxyl group into a coordinatively unsaturated metal site. Boullusa-Eiras et al. have evaluated the catalytic activity of phenol using molybdenum based catalysts in gas phase at 350-450 ºC and H_2 pressure of 2.5 MPa, obtaining benzene as main product along with cyclohexane, cyclohexene and methylcyclopentane as deoxygenated products [10]. Berenguer et al. [32] used Ni_2P and Co_2P as active phase by using milder reaction temperature 220 ºC ,observing that phenol HDO is retained in earlier steps, obtaining cyclohexanol as main product. Echeandia et. al. [33] have evaluated the catalytic activity of NiW/C at 300 ºC and 1.5 MPa, with CH as the main deoxygenated product.

Considering the catalytic data reported in the literature and those shown in the present chapter, it seems that phenol is hydrogenated in an earlier step to obtain cyclohexanol, through the coexistence of CUS and metallic sites. Then, cyclohexanol suffers dehydration in the metallic sites yielding CH (Scheme 5.3). The use of more severe pressure and temperature conditions causes the dehydrogenation of the aromatic ring leading to the formation of cyclohexene and benzene [28, 34]. The amount of benzene formed in the present work is low, and the reaction conditions soft. It is expected that it will come from the DDO route. This fact has been previously observed in the deoxygenation of DBF, where bicyclohexane is the main product at 300 ºC; however an increase of the temperature favors the presence of cyclohexylbenzene and biphenyl [35]. The absence of methylcyclopentane discards the existence of isomerization reactions, which were previously observed in the HDO of DBF.

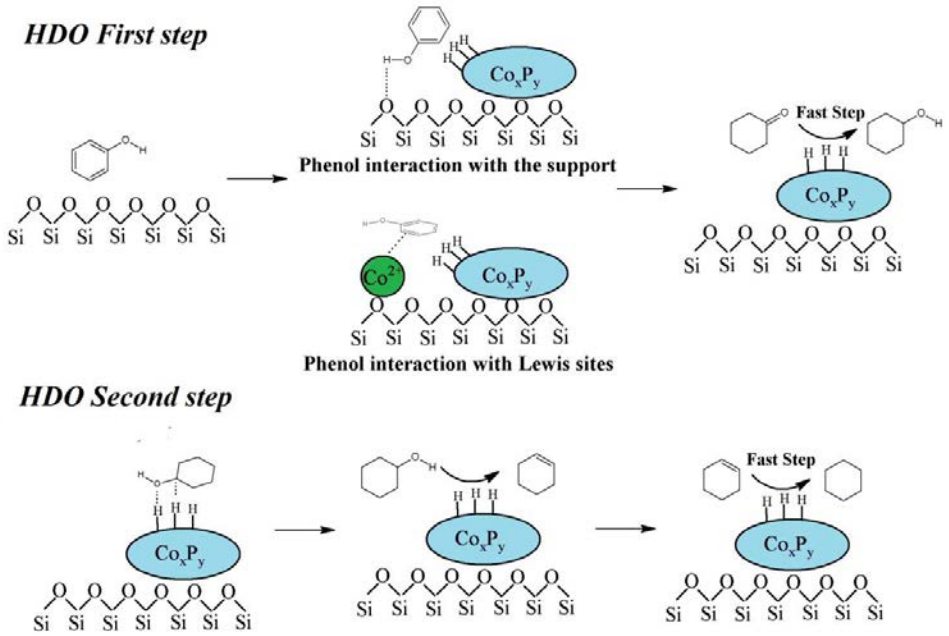

Scheme 5.3. Proposed HDO reaction scheme of phenol over silica supported CoxPy catalysts

In that sense, the analysis of C content after both catalytic reactions (Table 5.5) shows that the amount of C decreases with the P content and after DBF HDO the remaining carbon is higher. The catalytic performance of the studied phases cannot be related to the carbon content in the spent catalysts with the exception of the P/Co-0.5 catalyst, which exhibited greater amount of surface carbon and the lowest catalytic activity. This could be associated to intermediate species adsorbed on the catalyst surface. However, it is worth noting that as the P content increases the stability of the catalysts seem to be improved. Likewise, the descent of the exposure of the active centers prevents from catalyst deactivation by coke formation.

Table 5.5. Carbon content (%) of spent catalysts

Sample	DBF	Phenol
P/Co-0.5	3.4	2.2
P/Co-1	4.2	2.1
P/Co-1.5	2.3	1.5
P/Co-2	1.9	0.4
P/Co-2.5	2.0	0.5

The catalysts exposed here are supported on a non-acidic support, however the catalytic behavior observed in both reactions seems to be linked to the stoichiometry of the active phase formed. In the case of transition metal phosphides, coexists metal sites to activate hydrogen, as well as, $M^{\delta+}$ species that provide Lewis acid sites, respectively, which are required in the case of catalysts for HDO reactions [36, 37]. However, the stoichiometry of the phosphide formed is important to assess a good catalytic response. From the results exposed here, where Co_2P, CoP and CoP_2 species are observed, those catalysts containing CoP as the main phase exhibit the most remarkable catalytic behavior. Berenguer et al. synthesized cobalt phosphide catalysts in the form of CoP_2 for HDO reactions [32], obtaining high total conversion values, although the HDO yield was only between 15-20 %, evidencing the low activity of such phase in these reactions such as the results obtained with P/Co-2.5.

5.5. Conclusions

The main conclusions extracted from the present chapter are summarized as follows:

- $CoxPy/SiO_2$ catalysts have demonstrated good catalytic properties in HDO reactions which have been correlated with the stoichiometry of the phosphide phase formed.
- As the initial P/Co molar ratio increased, Co_2P, CoP and CoP_2 phases were formed, where CoP was found to be the most active among all.
- All catalysts followed the hydrogenation-dehydration route in both reactions obtaining cyclohexane and byciclohexane as main reaction products.
- The hydrogenation capability improved by decreasing the metallic character of the phosphide, i.e., less O-containing intermediates are observed by incorporating phosphorous into the structure.

5.6. References

1. Cecilia, J.A., et al., *Dibenzothiophene hydrodesulfurization over cobalt phosphide catalysts prepared through a new synthetic approach: Effect of the support.* Applied Catalysis B: Environmental, 2009. **92**(1-2): p. 100-113.
2. Burns, A.W., et al., *Understanding the relationship between composition and hydrodesulfurization properties for cobalt phosphide catalysts.* Applied Catalysis A: General, 2008. **343**(1-2): p. 68-76.
3. Cecilia, J.A., et al., *Gas phase catalytic hydrodechlorination of chlorobenzene over cobalt phosphide catalysts with different P contents.* J Hazard Mater, 2013. **260**: p. 167-75.
4. Cecilia, J.A., et al., *The Influence of the Support on the Formation of Ni2P Based Catalysts by a New Synthetic Approach. Study of the Catalytic Activity in the Hydrodesulfurization of Dibenzothiophene.* J. Phys. Chem. B, 2009. **113**: p. 17032–17044.
5. Abu, I.I. and K.J. Smith, *HDN and HDS of model compounds and light gas oil derived from Athabasca bitumen using supported metal phosphide catalysts.* Applied Catalysis A: General, 2007. **328**(1): p. 58-67.
6. Infantes-Molina, A., et al., *Nickel and cobalt phosphides as effective catalysts for oxygen removal of dibenzofuran: role of contact time, hydrogen pressure and hydrogen/feed molar ratio.* Catalysis Science & Technology, 2015. **5**(6): p. 3403-3415.
7. Iino, A., et al., *Kinetic studies of hydrodeoxygenation of 2-methyltetrahydrofuran on a Ni2P/SiO2 catalyst at medium pressure.* Journal of Catalysis, 2014. **311**: p. 17-27.
8. Mortensen, P.M., et al., *A review of catalytic upgrading of bio-oil to engine fuels.* Applied Catalysis A: General, 2011. **407**(1-2): p. 1-19.
9. Zhao, C., et al., *Aqueous-phase hydrodeoxygenation of bio-derived phenols to cycloalkanes.* Journal of Catalysis, 2011. **280**(1): p. 8-16.
10. Boullosa-Eiras, S., et al., *Catalytic hydrodeoxygenation (HDO) of phenol over supported molybdenum carbide, nitride, phosphide and oxide catalysts.* Catalysis Today, 2014. **223**: p. 44-53.
11. Nie, L. and D.E. Resasco, *Kinetics and mechanism of m-cresol hydrodeoxygenation on a Pt/SiO2 catalyst.* Journal of Catalysis, 2014. **317**: p. 22-29.
12. de Souza, P.M., et al., *Role of Keto Intermediates in the Hydrodeoxygenation of Phenol over Pd on Oxophilic Supports.* ACS Catalysis, 2015. **5**(2): p. 1318-1329.
13. Kay Lup, A.N., et al., *A review on reactivity and stability of heterogeneous metal catalysts for deoxygenation of bio-oil model compounds.* Journal of Industrial and Engineering Chemistry, 2017. **56**: p. 1-34.
14. Kung, H.H., *Chapter 4 Surface Coordinative Unsaturation.* Studies in Surface Science and Catalysis, 1989. **45**: p. 53-71.
15. Popov, A., et al., *IR study of the interaction of phenol with oxides and sulfided CoMo catalysts for bio-fuel hydrodeoxygenation.* Catalysis Today, 2011. **172**(1): p. 132-135.
16. Liu, H., et al., *Selective phenol hydrogenation to cyclohexanone over a dual supported Pd-Lewis Acid Catalyst.* Science, 2009. **326**: p. 1250-1252.
17. Rensel, D.J., et al., *Investigating the multifunctional nature of bimetallic FeMoP catalysts using dehydration and hydrogenolysis reactions.* Applied Catalysis A: General, 2016. **524**: p. 85-93.
18. Mortensen, P.M., et al., *Screening of Catalysts for Hydrodeoxygenation of Phenol as a Model Compound for Bio-oil.* ACS Catalysis, 2013. **3**(8): p. 1774-1785.
19. Cecilia, J.A., A. Infantes-Molina, and E. Rodriguez-Castellon, *Hydrodechlorination of polychlorinated molecules using transition metal phosphide catalysts.* J Hazard Mater, 2015. **296**: p. 112-9.
20. Kim, S.-S., et al., *Conversion of Kraft Lignin Over Hierarchical MFI Zeolite.* Journal of Nanoscience and Nanotechnology, 2014. **14**(3): p. 2414-2418.
21. Wang, L., et al., *Hydrodeoxygenation of Dibenzofuran Over SBA-15 Supported Pt, Pd, and Ru Catalysts.* Catalysis Letters, 2014. **144**(5): p. 809-816.

22. Lee, H.W., et al., *Catalytic hydrodeoxygenation of 2-methoxy phenol and dibenzofuran over Pt/mesoporous zeolites.* Energy, 2015. **81**: p. 33-40.
23. Wang, Y., et al., *Hydrodeoxygenation of dibenzofuran over noble metal supported on mesoporous zeolite.* Catalysis Communications, 2011. **12**(13): p. 1201-1205.
24. Infantes-Molina, A., et al., *Pd-Nb binfunctional catalysts supported on silica and zirconium phosphate heterostructures for O-removal of dibenzofurane.* Catalysis Today, 2016. **277**: p. 143-151.
25. Wang, L., et al., *Hydrodeoxygenation of dibenzofuran over SiO2, Al2O3/SiO2 and ZrO2/SiO2 supported Pt catalysts.* Catalysis Science & Technology, 2015. **5**(1): p. 465-474.
26. Rana, M.S., et al., *Origin of Cracking Functionality of Sulfided (Ni) CoMo/SiO2–ZrO2 Catalysts.* Journal of Catalysis, 2000. **195**(1): p. 31-37.
27. Xinghua, Z., et al., *Aqueous-phase catalytic process for production of pentane from furfural over nickel-based catalysts.* Fuel, 2010. **89**(10): p. 2697-2702.
28. Massoth, F., et al., *Catalytic Hydrodeoxygenation of Methyl-Substituted Phenols: Correlations of KineticParameters with Molecular Properties.* J. Phys. Chem. B, 2006. **110**: p. 14283-14291.
29. Resasco, D.E., *What Should We Demand from the Catalysts Responsible for Upgrading Biomass Pyrolysis Oil?* The Journal of Physical Chemistry Letters, 2011. **2**(18): p. 2294-2295.
30. Romero, Y., et al., *Hydrodeoxygenation of benzofuran and its oxygenated derivatives (2,3-dihydrobenzofuran and 2-ethylphenol) over NiMoP/Al2O3 catalyst.* Applied Catalysis A: General, 2009. **353**(1): p. 46-53.
31. Yang, Y., A. Gilbert, and C. Xu, *Hydrodeoxygenation of bio-crude in supercritical hexane with sulfided CoMo and CoMoP catalysts supported on MgO: A model compound study using phenol.* Applied Catalysis A: General, 2009. **360**(2): p. 242-249.
32. Berenguer, A., et al., *Evaluation of transition metal phosphides supported on ordered mesoporous materials as catalysts for phenol hydrodeoxygenation.* Green Chem., 2016. **18**(7): p. 1938-1951.
33. Echeandia, S., et al., *Synergy effect in the HDO of phenol over Ni–W catalysts supported on active carbon: Effect of tungsten precursors.* Applied Catalysis B: Environmental, 2010. **101**(1-2): p. 1-12.
34. Infantes-Molina, A., et al., *Effect of Ir and Pt Addition on the HDO Performance of RuS2/SBA-15 Sulfide Catalysts.* Topics in Catalysis, 2015. **58**(4-6): p. 247-257.
35. Cecilia, J.A., et al., *Oxygen-removal of dibenzofuran as a model compound in biomass derived bio-oil on nickel phosphide catalysts: Role of phosphorus.* Applied Catalysis B: Environmental, 2013. **136-137**: p. 140-149.
36. Infantes-Molina, A., et al., *Nickel and cobalt phosphides as effective catalysts for oxygen removal of dibenzofuran: role of contact time, hydrogen pressure and hydrogen/ feed molar ratio.* Catal. Sci. Technol., 2015. **5**: p. 3403-3415.
37. Cecilia, J.A., et al., *Enhanced HDO activity of Ni2P promoted with noble metals.* Catal. Sci. Technol., 2016. **6**(19): p. 7323-7333.

6. Fe phosphides for phenol HDO

6.1. Abstract

In the present chapter a series of iron phosphide catalysts supported on silica with an iron loading of 15wt% were synthesized and studied in the HDO of phenol. Unlike phosphides studied in chapters 4 and 5, these catalysts have been passivated after the reduction process, which implies a better protection of the phosphides. The amount of phosphorus varied in order to obtain iron phosphides with different stoichiometry. Thus, the synthesized catalysts will be referred to as P/Fe-x, where x is the P/Fe molar ratio employed, x= 0.5, 1, 2 and 3.

The catalytic activity was studied at 275ºC and at 0.5 and 1.5 MPa of hydrogen pressure. The textural and structural properties of the catalysts were studied by a wide range of techniques in order to evaluate the effects of the formed phase on the catalytic findings.

6.2. Characterization results

6.2.1 X-ray diffraction (XRD)

The identification of crystalline phases was performed by XRD and diffractograms of the passivated catalysts are represented in Figure 6.1. The measurements were carried out by using monochromatic Mo Kα radiation in order to diminish iron fluorescence. The diffraction pattern corresponding to P/Fe-0.5 sample identifies Fe_2P as unique crystalline phase with diffraction peaks located at 18.2, 19.9, 21.3, 23.7, 24.2 and 24.4º (PDF Nº:01-085-1725).

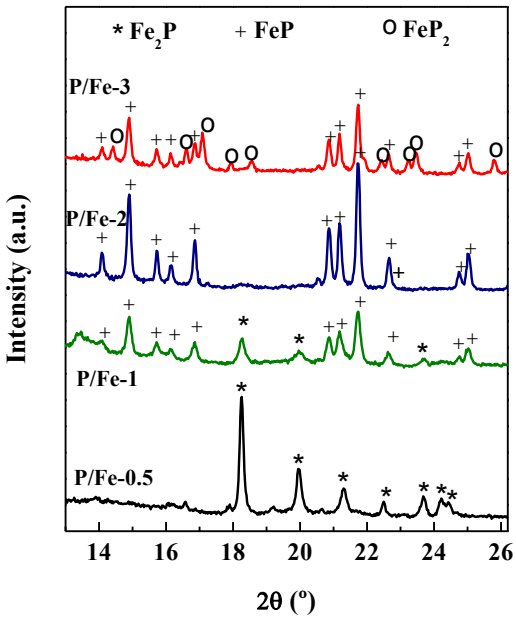

Figure 6.1. X-ray diffractograms of passivated catalysts

As phosphorus content increases in P/Fe-1 catalyst, diffraction peaks ascribed to the Fe_2P phase diminish and new ones emerge as a result of the formation of a phase richer in phosphorus such as FeP (PDF Nº: 01-078-1443). These peaks assigned to FeP phase are located at 14.1, 14.9, 15.7, 16.1, 16.9, 20.8, 21.1, 21.7, 22.6, 24.7 and 24.9º.The diffraction pattern of P/Fe-2 sample only shows a single phase, FeP, while the iron enriched phase, Fe_2P, eventually disappears. By increasing the P/Fe ratio to 3 in the catalyst with the greatest P content, the diffraction pattern of FeP phase is still dominant but new diffraction peaks appear at 14.4, 16.6, 17.1, 17.9, 18.5, 21.9, 22.4, 23.2, 23.4, 25.8 and 26.4º. These lines are attributed to the presence of a phase enriched in phosphorus, FeP_2 (PDF Nº: 03-065-6088), which coexists with the still present, FeP, but to a lesser proportion. The percentage of the various coexisting phases in P/Fe-1 and P/Fe-3 samples is included in Table 6.1. Therefore, in summary, the formation of phosphorus richer phosphides takes place as the P/Fe ratio increases.

Table 6.1 Crystalline phase, particle size and percentage of each phase

Catalyst	Crystalline phase	Size (nm)	Percentage (%)*
P/Fe-0.5	Fe_2P	41.2	100
P/Fe-1	Fe_2P	23.6	24
	FeP	26.6	74
P/Fe-2	FeP	42.8	100
P/Fe-3	FeP	36.5	66
	FeP_2	52.5	34

Semiquantitative analysis obtained from HighScore Plus Software from crystalline phases

The average particle size of the various phases present has also been determined by using the Scherrer's equation and the results are compiled in Table 6.1. These data show that Fe_2P phase presents a greater particle size in P/Fe-0.5 sample than in P/Fe-1 one, where this phase is therefore more dispersed. The particle size of FeP phase follows the order: P/Fe-1<P/Fe-3<P/Fe-2. Hence, samples which contain a mixture of phosphide phases such as P/Fe-1 (Fe_2P and FeP) and P/Fe-3 (FeP and FeP_2) present lower particle sizes of these coexisting phases.

6.2.2 Mössbauer spectroscopy

Mössbauer spectroscopy was performed in order to get further insight into the identification of both crystalline and amorphous iron phases present in the studied materials. The corresponding spectra are depicted in Figure 6.2 and Table 6.2 compiles the Mössbauer parameters, obtained from the fit of the spectra and the assignment of the various spectral components to the corresponding chemical species. The spectrum of the P/Fe-0.5 sample is composed of four

quadrupole doublets. The most intense ones correspond to the two crystallographic sites existing in the structure of the iron phosphide of composition Fe_2P [1]. The two minor doublets can be assigned to Fe(II) phosphate. Both the number of Fe(II) phosphates and the range of their Mössbauer parameters are large [2], therefore, in the absence of other complementary information, it is difficult to assign the obtained parameters to a particular Fe(II) phosphate species.

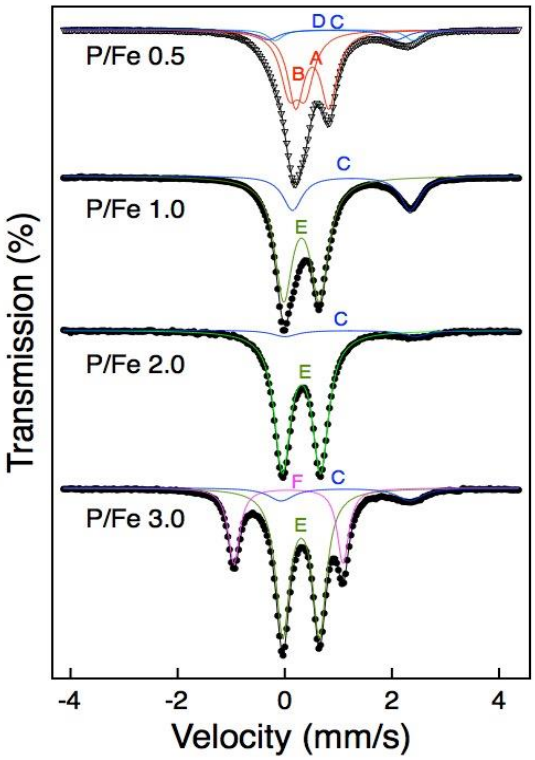

Figure 6.2 Mössbauer spectra of passivated phosphides

From the spectra of P/Fe-1 and P/Fe-2 samples the formation of an iron phosphide of composition FeP is deduced. In both cases, the major contribution is due to the FeP phase [1] as seen in Table 6.2. In both samples the minor contribution corresponds again to an unspecific Fe(II) phosphate**.** Finally, the catalyst P/Fe-3 also presents FeP (63%) as dominant phase with a contribution amount of 27% of the spectral area corresponding to the phosphorus rich FeP_2 phosphide [2]. The minor contribution is again ascribed to Fe(II) phosphate.

Table 6.2. Mössbauer parameters obtained from the corresponding spectra fitting

Catalyst	Component	δ (mms^{-1})	Δ (mms^{-1})	Area (%)	Assignment
P/Fe-0.5	A	0.52	0.62	46	Fe_2P
	B	0.23	0.30	38	
	C	1.11	2.58	7	Fe(II)phosphate
	D	0.88	2.41	9	
P/Fe-1	E	0.34	0.61	79	FeP
	C	1.14	2.40	21	Fe(II)phosphate
P/Fe-2	E	0.31	0.71	93	Fe_2P
	C	1.22	2.44	7	Fe(II)phosphate
P/Fe-3	E	0.31	0.69	63	FeP
	F	0.07	2.04	27	FeP_2
	C	1.13	2.40	10	Fe(II)phosphate

6.2.3 Textural properties and CO chemisorption

The textural parameters of the passivated catalysts and the support were obtained from N_2 adsorption-desorption isotherms. Table 6.3 includes the specific surface area and pore volume results, and Figure 6.3, shows the corresponding isotherms and pore size distribution graphs. The isotherms are all of type II, characteristic of solids with pores of diameters in the range of meso and macropores which are generally attributed to interparticle voids. As seen in Table 6.3, BET surface area values suffer a remarkable decrease in comparison with the bare support as a consequence of the incorporation of the active phases. This loss of specific surface area is attributed to the blockage of the surface pores with phosphorus species in excess [3, 4]. Regarding the pore size distribution, it is observed a bimodal distribution in all cases in comparison with pure silica, which does not show a well-defined distribution. An increase in the pore volume of the iron containing catalysts at high relative pressures is also observed, suggesting that the formation of pores of bigger size in the range of macroporous takes place. In this regard, all samples present a maximum close to 50 nm. However, pores of smaller size (22-27 nm) are also present, having a greater presence in the case of samples P/Fe-1 and P/Fe-2. In fact, P/Fe-1 presents the same proportion of both pore size ranges.

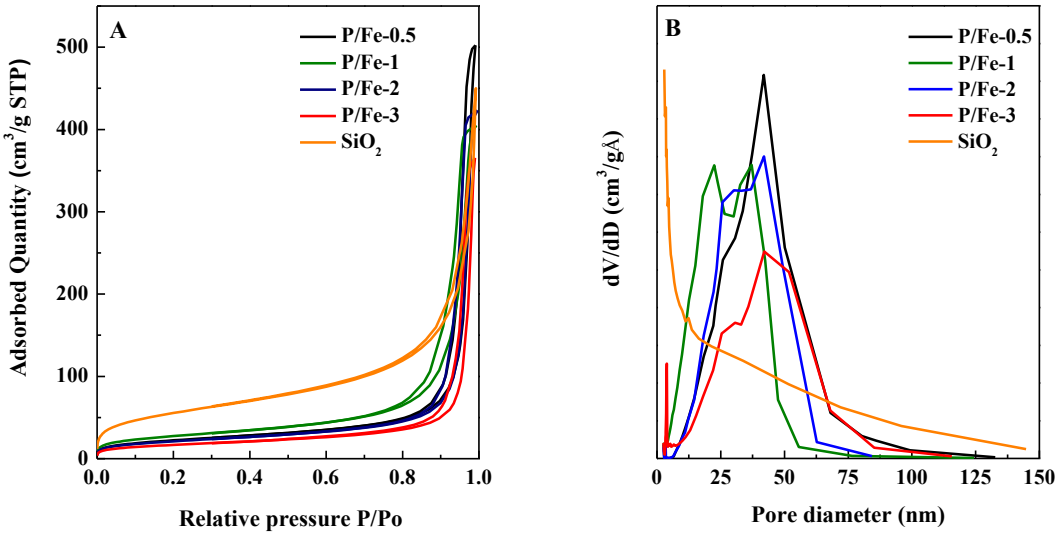

Figure 6.3 A) N_2 adsorption-desorption isotherms and B) pore size distribution by applying the BJH method to the desorption branch of the isotherm

Regarding now the CO chemisorption results, an estimation of the dispersion of the active phase may be performed. CO uptakes and dispersion values are compiled in Table 6.3. The calculated dispersion values from CO uptake data are low in all cases but in accordance with those found in literature for iron phosphide [5]. As it has been assumed in previous works [5], each CO molecule is adsorbed on one active site. From these results, it seems that FeP phase chemisorbs more CO than Fe_2P when comparing P/Fe-2 and P/Fe-0.5. But as the highest dispersion values are found in P/Fe-1 and P/Fe-3, the mixture of phases may also contribute to the presence of more available active sites. Furthermore, these dispersion data are in agreement with XRD results, which pointed out that P/Fe-1 and P/Fe-3 showed the lowest particle size and therefore likely greater dispersion. Moreover, the calculated dispersion are in accordance to XRD results, where samples with two different iron phosphide phases, P/Fe-1 and P/Fe3, show lower particle size.

Table 6.3. Textural properties and CO chemisorption results

Catalyst	S_{BET} ($m^2 \cdot g^{-1}$)	Vp ($cm^3 \cdot g^{-1}$)	CO uptakes ($\mu mol\ g^{-1}$)	Dispersion (%)*
P/Fe-0.5	82	0.77	4.6	0.17
P/Fe-1	100	0.62	12.2	0.45
P/Fe-2	76	0.64	6.6	0.25
P/Fe-3	61	0.56	4.8	0.82

Dispersion (%) = CO uptake (mmoles·g^{-1})/Metal loading (mmoles·g^{-1})

6.2.4 Transmission electron microscopy (TEM)

The estimation of the dispersion of the active phase over the support was carried out by HR-TEM and the micrographs of the various catalysts are depicted in Figure 6.4. In micrographs of samples P/Fe-0.5 and P/Fe-1 the distinction between the phosphide particles and the SiO_2 support is complicated. These micrographs are similar to those found in iron based catalysts reported by other authors [6]. Instead, the presence of phosphide particles is slightly more evident in samples with a greater P content, P/Fe-2 and P/Fe-3. In general, FexPy particles are dispersed on the SiO_2 matrix except in zones where local agglomeration hinders the particle size measurement.

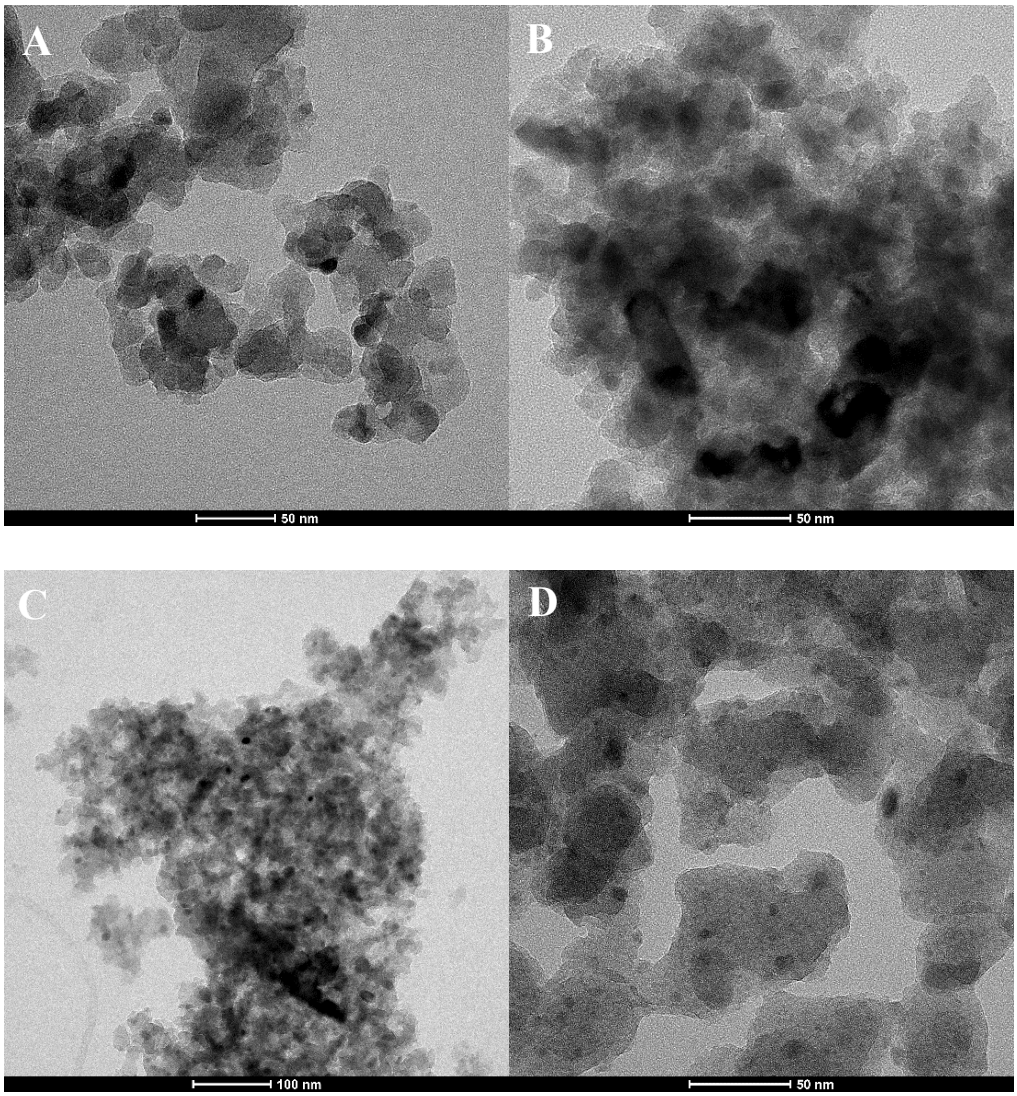

Figure 6.4 HRTEM images of A) P/Fe-0.5, B) P/Fe-1, C) P/Fe-2 and D) P/Fe-3

6.2.5 Fourier Transform infrared spectroscopy (FT-IR)

The hydroxyl groups were studied by FT-IR of the passivated samples after hydrogen activation in the OH-stretching region. The only sample which shows a representative contribution in this region is the sample P/Fe-0.5, depicted in Figure 6.5.A. The main band located at 3747 cm^{-1} is ascribed to the –OH stretching of isolated single silanols. The shoulder with a maximum located about 3720 cm^{-1} is assigned to the –OH stretching of silanol group that interacts with a vicinal pair [7]. Finally, the broad and weak band located at about 3700 cm^{-1} can be attributed to the –OH stretching of surface hydroxyl groups with intermediate acid properties possibly interacting with neighboring phosphate groups, clearly noticeable for Ni_2P and CoP based samples [8].

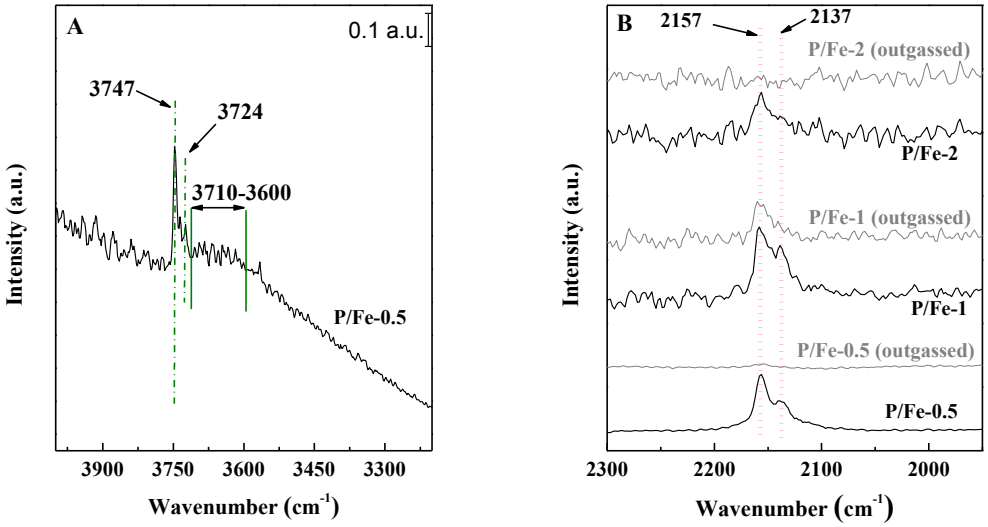

Figure 6.5 A) FTIR spectra in the OH-stretching region and B) after CO adsorption at -140ºC (black) and after CO outgassing at -140ºC (dark grey)

FT-IR measurements have also been performed to determine the kind of metal sites by using CO as target molecule. The spectra were recorded at low temperature, so the interaction between the CO molecule and the metal centers must be weak. From CO-adsorption profiles shown in Figure 6.5.B, two bands located at 2157 and 2137 cm^{-1} are observed. The first band is ascribed to the weak interaction of CO with the –OH groups located on the surface by H-bond, while the second band can be attributed to carbonyl species weakly coordinated to Fe-species partially reduced, likely superimposed to some liquid-like CO [8]. Both bands disappear when the temperature increases in all cases because of the weak interaction with CO molecule, with the exception of P/Fe-1 sample. This catalyst shows stronger interactions with CO since both contributions still remain after outgassing. On the contrary, the spectrum corresponding to P/Fe-3 sample is not shown due to the lack of noticeable bands. The high amount of phosphorus

present in this sample seems to be detrimental for IR analysis. From this figure, it is also observed that the contribution due to hydroxyl groups is more important for the three samples, while the contribution due to partially reduced iron decreases by increasing the amount of phosphorus present. This indicates that CO coordination with metallic sites is favored for iron-rich phosphides.

6.2.6 Ammonia temperature-programmed desorption (NH_3-TPD)

Total acidity of the reduced catalysts was measured by NH_3-TPD experiments. Table 6.4 includes the total amount of ammonia desorbed from 100 to 500 ºC and Figure 6.6 the desorption profiles.

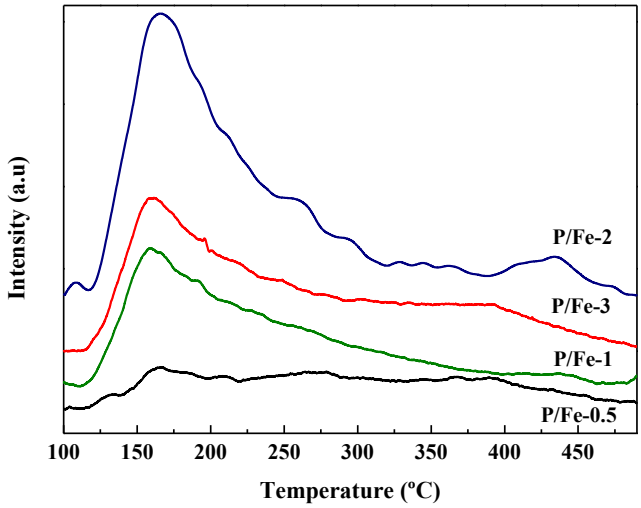

Figure 6.6. Ammonia temperature-programmed desorption profiles

Table 6.4 Total acidity values

Sample	Total acidity ($\mu molNH_3 \cdot g^{-1}$)
P/Fe-0.5	60
P/Fe-1	90
P/Fe-2	220
P/Fe-3	150

The desorption curves of all catalysts range from 100 to 300 ºC which is associated to a weak acidic character. The bare support desorbs (not shown) a negligible amount of ammonia indicating that the measured acidity is mainly due to the phosphide phases. Concretely, the total acidity increases remarkably with phosphorus content achieving its maximum value for the P/Fe-2 catalyst. Therefore, the acidity should be mainly related to the phosphorus content

present on the sample which is associated to –OH groups derived from surface oxidation as reported in literature [9, 10] and matching with previous IR analyses. The presence of these acid sites is necessary to favor the hydrogenolysis reaction of cyclohexanol to form cyclohexene and cyclohexane [3].

6.2.7 X-ray photoelectron spectroscopy (XPS)

The surface chemical composition of passivated catalysts was evaluated by XPS. The Si 2*p* and O 1*s* signals are centered at 103.5 eV and 532.9 eV, respectively, remaining unchanged in all catalysts (not shown). The Fe *2p* core level spectra show the coexistence of various species on the surface. Figure 6.7.A shows the Fe *2p* spectrum of the sample P/Fe-0.5 with the majority presence of iron(III) phosphate centered at 711 eV and a weak contribution owed to iron phosphide. The relative intensity of the signal corresponding to $P^{\delta-}$ rises (705 eV) with increasing the ratio P/Fe in both Fe *2p* and P *2p* spectra.

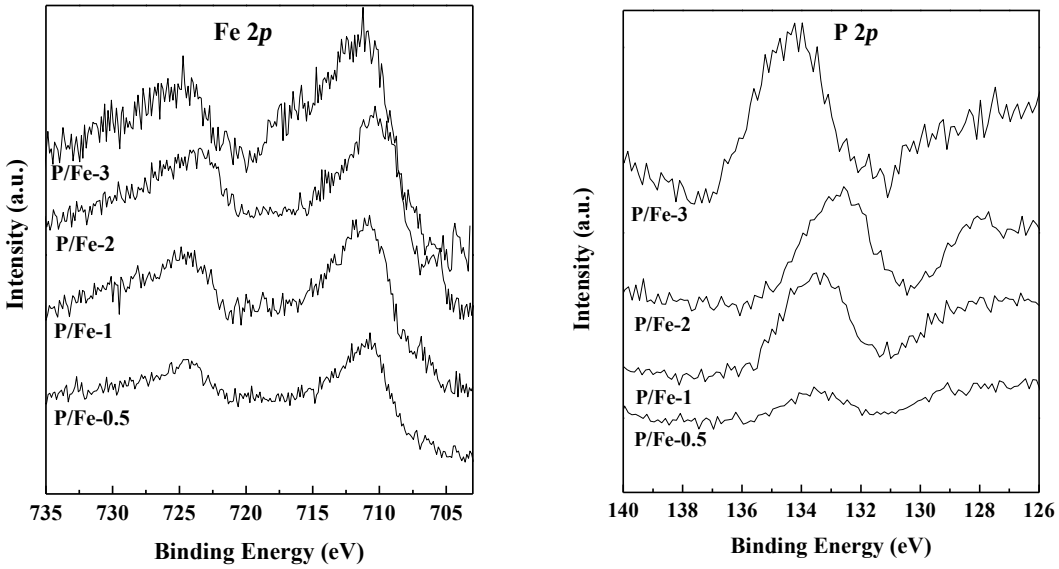

Figure 6.7 Fe *2p* and P *2p* core-level spectra of the passivated samples

Beside this, the evolution of the Fe 2*p* core level signal shows an increase of Fe(II) as the P/Fe rises, not only for the presence of a shoulder in the region of low binding energy but also for the modification of the signal owed to the presence of a shake-up satellite. The P 2*p* core level spectra of all catalysts present two contributions of the P $2p_{3/2}$ component centered at 133.2 and 128.2 eV which respectively correspond to PO_4^{3-} and $P^{\delta-}$ [11]. The phosphide species are present as Fe_2P, FeP and FeP_2 phases while phosphate species are originated in the passivation process. Table 6.5 compiles P/Fe and Fe/Si surface atomic ratios, calculated in order to elucidate the extent of surface exposure of both elements. Phosphorus exposure on surface increases steadily

with P/Fe ratio. On the contrary, iron exposed on surface becomes slightly lower although significant differences among the studied catalysts are not observed.

Table 6.5. Surface atomic ratios

Sample	Surface atomic ratio	
	P/Fe	Fe/Si
P/Fe-0.5	0.26	0.05
P/Fe-1	0.58	0.037
P/Fe-2	0.73	0.044
P/Fe-3	0.79	0.037

6.3. Catalytic results

The prepared catalysts have been tested in the HDO of phenol at 275 ºC under pressures of 0.5 and 1.5 MPa. A first comparison of the HDO conversion values working under both pressures is represented in Figure 6.8.A.

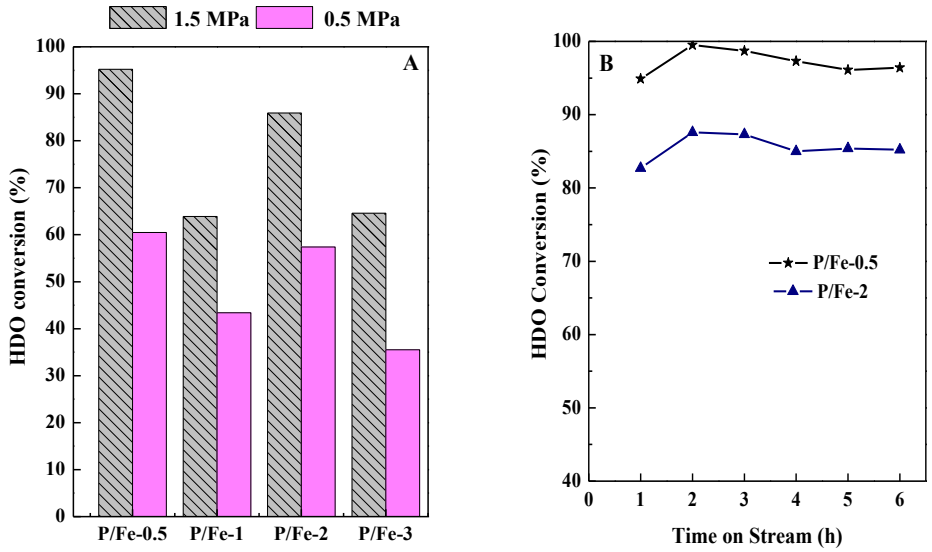

Figure 6.8. A) HDO conversion at ToS= 6h, 1.5 and 0.5 MPa, 275ºC, WHSV=0.3h^{-1} B) HDO conversion evolution at 1.5 MPa, 275ºC, WHSV=0.3h^{-1}

The results reflect the strong dependency of the pressure on the activity of the catalysts. Working at 1.5 MPa, all the catalysts displayed a good performance reaching conversion values exceeding 60 %. At 0.5 MPa the conversion values range from 40 to 60%. Under both pressures, P/Fe-0.5 and P/Fe-2 catalysts resulted to be the most active ones presenting greater HDO conversion values. The evolution of HDO conversion at 1.5 MPa with time on stream is represented in Figure 6.8.B. As seen in the representation, both catalysts display a growing

catalytic response during the first two hours on stream followed by a slight loss of activity which eventually remains steady during last two hours on stream.

Regarding the selectivity results, phenol hydrodeoxygenation can take place by direct deoxygenation route (DDO) [12], hydrogenation-dehydration route (HYD) [13] and tautomerization-deoxygenation route [14]. These proposed reaction pathways are included in Scheme 6.1 and have already been explained in chapter 4 and 5. And in agreement with the preceding chapters, the catalytic results seem to indicate that the reaction proceeds via hydrogenation-dehydration route (HYD).

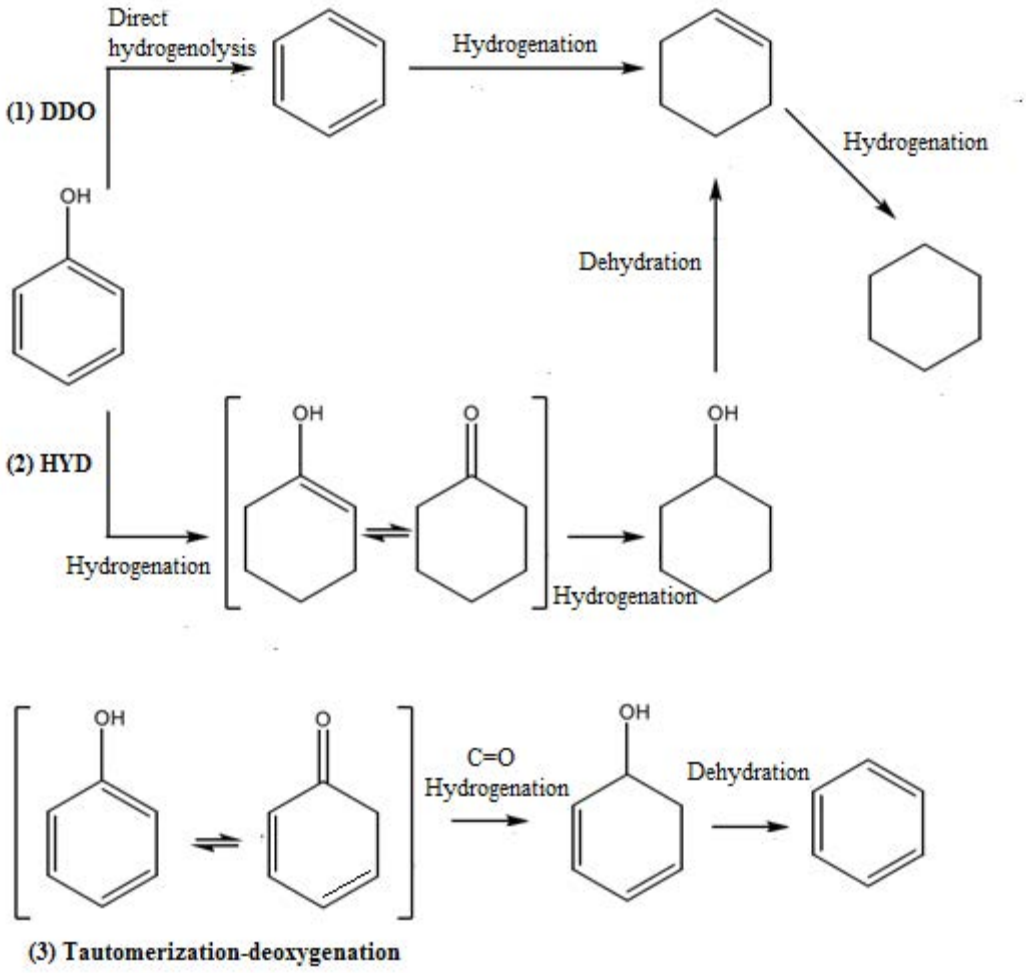

Scheme 6.1 Scheme of the reaction pathway in the HDO of phenol [15, 16]

Selectivity results under 1.5 and 0.5 MPa are shown in Figure 6.9.A) and B). The product selectivity is strongly dependent on the reaction pressure studied. Thus, at 1.5 MPa, the majority product is cyclohexane with selectivity values higher than 80%. Benzene and cyclohexene are also obtained but in much lesser extent. Instead, working at 0.5 MPa, the selectivity to cyclohexene increases conspicuously, being the most important product in the case of P/Fe-3

sample. These results point out that all tested catalysts react via hydrogenation of the aromatic ring followed by dehydration of cyclohexanol to obtain cyclohexane, cyclohexene and in a minority, benzene.

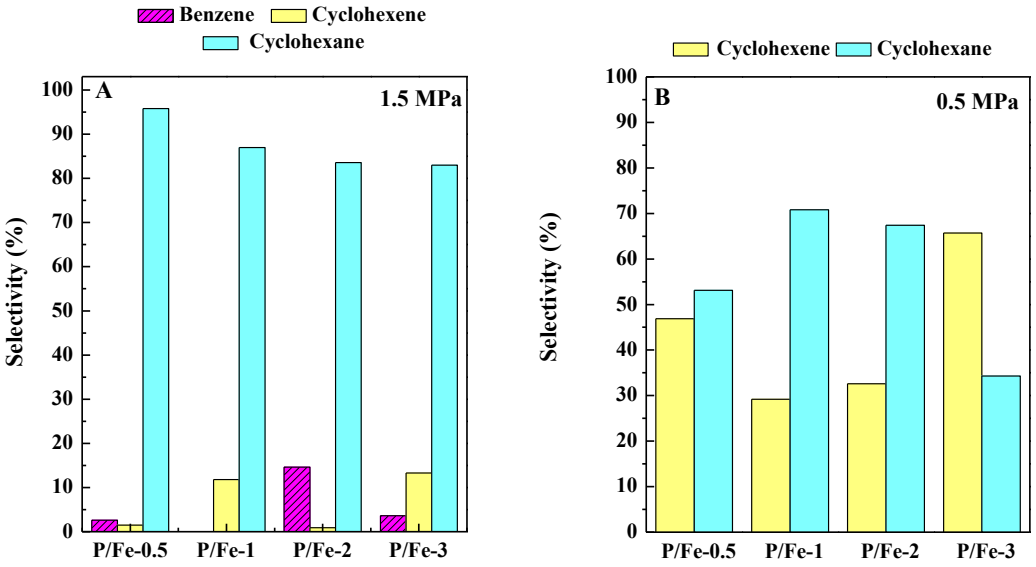

Figure 6.9. Selectivity plots at A) 1.5 MPa and B) 0.5 MPa after ToS=6h, 275 ºC, WHSV=0.3 h^{-1}

Regarding the proposed mechanisms in literature for metallic phosphides it has been suggested that coordinatively unsaturated metal sites (CUS) can act as Lewis sites while surface oxygen behaves as Lewis basic site [17]. As seen in Scheme 6.2, phenol is adsorbed by a heterolytic dissociation between the hydrogen of its –OH group on the oxygen sites on the oxide surface layer, leading to the formation of phenoxide species [18]. These phenoxide species are stabilized by the presence of coordinatively unsaturated metal sites (CUS) that act as Lewis acid centers [17]. Other authors have pointed out that phenol adsorption can also proceed by the existence of Lewis acid sites (Fe^{3+}) or by the presence of defects in the grain boundary that are favored in small crystals by their interaction with the aromatic ring [19, 20]. In the next step, the hydrogen adsorbed on metallic species hydrogenates the aromatic ring to form cyclohexanone which is rapidly transformed into cyclohexanol. Finally, the hydroxyl group of cyclohexanol interacts with the metal sites favoring the dehydration to cyclohexene and a subsequent hydrogenation to form cyclohexane [20].

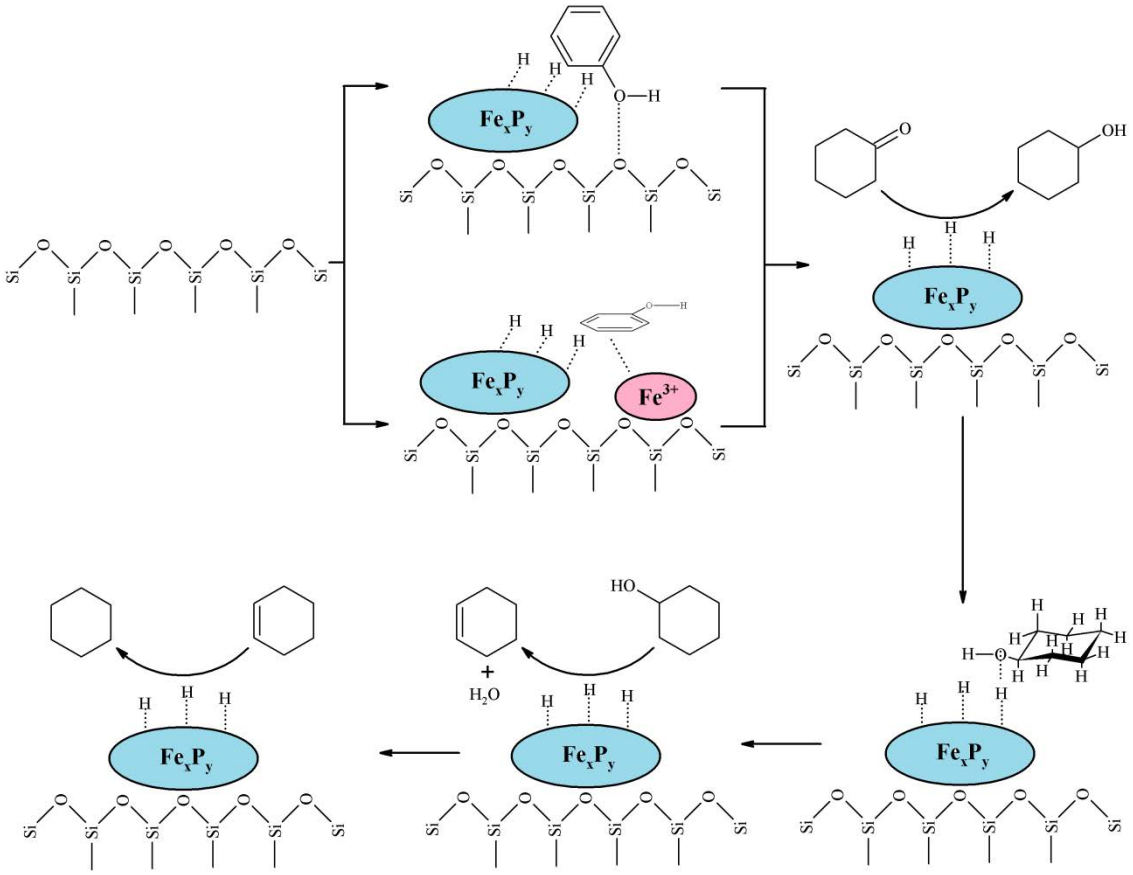

Scheme 6.2. Proposed mechanism for phenol HDO over FexPy catalysts

Previous studies evaluated the catalytic performance of iron based catalysts supported on silica and carbon using guaiacol as target molecule, at atmospheric pressure and high contact times [21, 22]. The research reported the formation of benzene and phenol, discarding the hydrogenation of the aromatic ring. In the present study, the catalysts were studied at higher H_2 pressure and lower contact time favoring the formation of dearomatized products. These data suggest that the hydrogenation of the aromatic ring is favored by the presence of H_2-pressure, but also iron plays an important role. In this sense, it is well reported in literature the hydrogenation of benzene to form cyclohexane under H_2-pressure using Fe-based catalysts [23, 24].

6.4. Discussion

The manuscripts devoted to the use of iron in hydrotreating reactions are scarce due to the low activity of iron in these reactions. However, its abundance, non-toxicity and low cost make it a good candidate to face the challenges in HDO catalysts design [25]. Rezaei et al.[26] reported that iron is an effective metal for the selective conversion of lignin-derived phenolics into aromatic hydrocarbons when it is combined with acidic supports. Iron is an oxophilic metal that may strongly interact with the carbonyl group facilitating its selective hydrogenation to the

corresponding alcohol [27]. The tuning among metallic and acidic sites can govern the reaction pathway as reported by Rezaei [27] when using iron catalysts supported on MCM-41 and promoted with Re and Zr to incorporate the acidic function. This bifunctional requirement is accomplished in transition metal phosphides. As the use of iron phosphide in HDO reactions is scarce, variating the phosphorus/iron molar ratio is going to lead to the formation of iron phosphide with different stoichiometry. Therefore, the metal and phosphorus surface exposure and so the acidity of the material is going to vary as a function of the phosphide phase formed. From the catalytic results presented here, it seems clear that the presence of higher phosphorus content worsens the conversions results. In that sense, it has been reported that the incorporation of phosphorus modifies the electronic density of the metal and also diminishes its exposure on the surface limiting the amount of available active sites leading, therefore, to poorer conversions [3, 28, 29]. In the present research, by increasing P/Fe molar ratio iron phosphides richer in phosphorus are formed: $Fe_2P \rightarrow FeP \rightarrow FeP_2$, iron surface exposure decreases and acidity improves. Furthermore, the P/Fe molar ratio employed determines the presence of unique or mixed phases in the corresponding catalyst. All these factors determine the catalytic respond of the tested catalysts. In this regard, samples containing unique phases such as P/Fe-0.5 and P/Fe-2 present the highest conversion values at both pressures. Fe_2P phase is present in P/Fe-0.5 sample and FeP in P/Fe-2 one. If catalytic results of all tested samples are lumped together the catalytic activity of the iron phosphide phases follows the trend: $Fe_2P > FeP > FeP_2$. This trend is in agreement with TOF values, included in Table 6.6. The activity per active site of the P/Fe-0.5 catalyst notably highlights over the rest of studied catalysts under both pressures. As previously observed from conversion values, P/Fe-0.5 and P/Fe-2 are those more active.

Table 6.6. Turnover frequency values

Sample	TOF (s^{-1})x10^3	
	1.5 MPa	**0.5 MPa**
P/Fe-0.5	147	45
P/Fe-1	18	10
P/Fe-2	66	29
P/Fe-3	50	21

TOF results can also be correlated with catalysts properties such as acidity and metal exposure as shown in Figure 6.10. Figure 6.10.a represents iron surface exposure versus TOF finding that both are directly related. Thus, the sample with the greatest iron exposure, P/Fe-0.5 (Fe_2P as unique phase), is the most active in the studied reaction. Its greater metal exposure is also observed from CO-IR experiments. In addition, the acidity also plays an important role in the

catalytic activity of the samples as shown in Figure 6.10.b where it is represented versus TOF values. Except for the P/Fe-0.5 catalyst the tendency is clear, the higher acidity the better activity per active site. If only samples containing FeP phase are considered, P/Fe-1, P/Fe-2 and P/Fe-3, the corresponding FeP particle size is directly correlated with TOF values regardless the reaction pressure evaluated (Figure 6.10.c). Thus, the higher the particle size, the better the activity. However, it should be kept in mind that P/Fe-2 sample only possesses the FeP phase; instead, in P/Fe-1 and P/Fe-3 samples coexist Fe_2P and FeP_2, respectively, with FeP one.

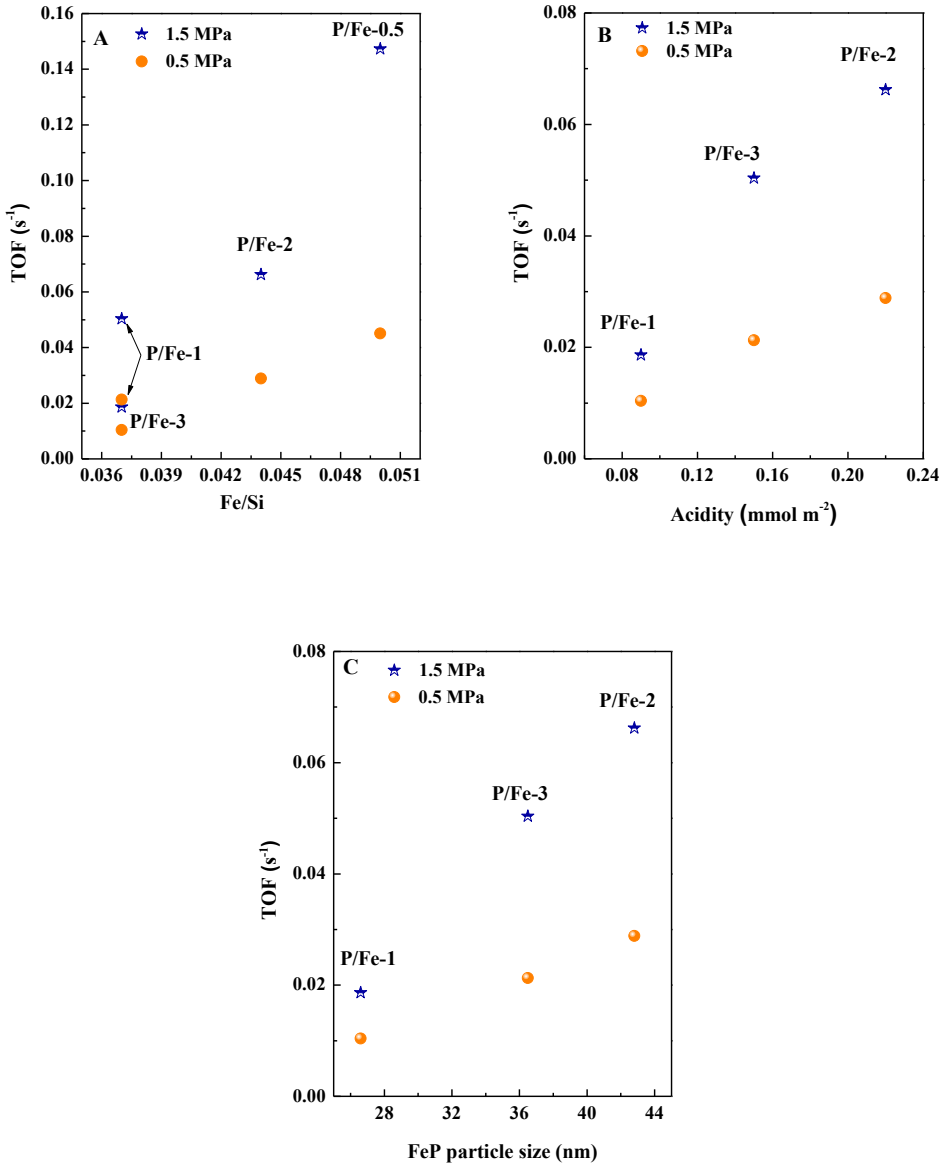

Figure 6.10. Dependency of TOF with A) iron surface exposure, B) acidity and C) FeP particle size

Therefore, iron phosphide stoichiometry, particle size, surface exposure of the iron and the catalyst acidity are directly correlated with catalytic activity. These results are at odds with

those found for iron phosphide supported on activated carbon in the hydrodesulfurization reaction of dibenzotiophene, where FeP was more active than Fe_2P [30]. In the case of HDO reactions, the oxophilic character of iron could justify why Fe_2P phase, presenting greater iron surface exposure, provides more active sites to interact with oxygen from the molecules of the feed.

Taking into account the selectivity data, all the samples follow the hydrogenation/hydrogenolysis route. Only the sample with the highest acidity values leads to the formation of a noticeable amount of benzene about 15%. However, the weak nature of those sites does not favor the hydrogenolysis route, where after the first hydrogenation of the carbonyl group forming cyclohexadienols, they must be dehydrated in acidic sites to form aromatic hydrocarbons [31]. As suggested by other authors, the strength of those sites is clue in order to favor the dehydration reaction to occur and to prevent catalyst deactivation [32]. Further research is required in this regard for a better understanding of the reaction mechanism in the HDO of iron phosphides and should be focused on the nature and strength of the acid sites.

6.5. Conclusions

The main conclusions drawn from this chapter are:

- The amount of phosphorus incorporated during the synthesis led to the formation of iron phosphides with different stoichiometry. As it increased, the obtained phosphides varied from an iron-rich to a phosphorus-rich phosphide ($Fe_2P \rightarrow FeP \rightarrow FeP_2$).
- The synthetized catalysts presented one or two phases depending on the starting P/Fe molar ratio. And so the activity of the catalyst depends on the iron phosphide formed. The observed trend was: $Fe_2P > FeP > FeP_2$.
- The activity per active site was related to the iron surface exposure, the particle size and the acidity of the catalysts.
- These results highlight the importance of the application of a cheap and abundant phase such as iron in HDO reactions.

6.6. References

1. Wäppling, R., et al., *Mösbauer study of phosphides containing iron* Journal of solid state chemistry, 1971. **3**: p. 276-292.
2. Dyar, M.D., et al., *Mössbauer parameters of iron in phosphate minerals: Implications for interpretation of martian data.* American Mineralogist, 2014. **99**: p. 914-942.
3. Rodríguez-Aguado, E., et al., *CoxPy Catalysts in HDO of Phenol and Dibenzofuran: Effect of P content.* Topics in Catalysis, 2017.
4. Rodríguez-Aguado, E., et al., *Ni and Fe mixed phosphides catalysts for O-removal of a bio-oil model molecule from lignocellulosic biomass.* Molecular Catalysis, 2017. **437**: p. 130-139.
5. Alvarez-Galvan, M.C., et al., *Metal phosphide catalysts for the hydrotreatment of non-edible vegetable oils.* Catalysis Today, 2017.
6. Song, L., S. Zhang, and Q. Ma, *Synthesis of an iron phosphide catalyst based on sulfides and hydrodesulfurization property.* Chemical Engineering Journal, 2015. **281**: p. 281-285.
7. Roosmalen, A.J.v. and J.C. Mol, *An Infrared study of the silica gel surface. 1. Dry Silica Gel.* The Journal of Physical Chemistry 1978. **82**: p. 2748-2751.
8. Infantes-Molina, A., et al., *Nickel and cobalt phosphides as effective catalysts for oxygen removal of dibenzofuran: role ofcontact time, hydrogen pressure and hydrogen/feed molar ratio.* Catalysis Science and Technology, 2015. **5**: p. 3403-3415.
9. Li, K., R. Wang, and J. Chen, *Hydrodeoxygenation of Anisole over Silica-Supported Ni2P, MoP, and NiMoP Catalysts.* Energy & Fuels, 2011. **25**(3): p. 854-863.
10. Pan, Z., et al., *Deoxygenation of methyl laurate to hydrocarbons on silica-supported Ni-Mo phosphides: Effect of calcination temperatures of precursor.* Journal of Energy Chemistry, 2015. **24**(1): p. 77-86.
11. Cecilia, J.A., et al., *Influence of the silica support on the activity of Ni and Ni2P based catalysts in the hydrodechlorination of chlorobenzene. Study of factors governing catalyst deactivation.* Journal of Molecular Catalysis A: Chemical, 2013. **368-369**: p. 78-87.
12. Boullosa-Eiras, S., et al., *Catalytic hydrodeoxygenation (HDO) of phenol over supported molybdenum carbide, nitride, phosphide and oxide catalysts.* Catalysis Today, 2014. **223**: p. 44-53.
13. Zhao, C., et al., *Aqueous-phase hydrodeoxygenation of bio-derived phenols to cycloalkanes.* Journal of Catalysis, 2011. **280**(1): p. 8-16.
14. Nie, L. and D.E. Resasco, *Kinetics and mechanism of m-cresol hydrodeoxygenation on a Pt/SiO2 catalyst.* Journal of Catalysis, 2014. **317**: p. 22-29.
15. de Souza, P.M., et al., *Role of Keto Intermediates in the Hydrodeoxygenation of Phenol over Pd on Oxophilic Supports.* ACS Catalysis, 2015. **5**(2): p. 1318-1329.
16. Kay Lup, A.N., et al., *A review on reactivity and stability of heterogeneous metal catalysts for deoxygenation of bio-oil model compounds.* Journal of Industrial and Engineering Chemistry, 2017. **56**: p. 1-34.
17. Kung, H.H., *Chapter 4 Surface Coordinative Unsaturation.* Studies in Surface Science and Catalysis, 1989. **45**: p. 53-71.
18. Popov, A., et al., *IR study of the interaction of phenol with oxides and sulfided CoMo catalysts for bio-fuel hydrodeoxygenation.* Catalysis Today, 2011. **172**(1): p. 132-135.
19. Rensel, D.J., et al., *Investigating the multifunctional nature of bimetallic FeMoP catalysts using dehydration and hydrogenolysis reactions.* Applied Catalysis A: General, 2016. **524**: p. 85-93.
20. Mortensen, P.M., et al., *Screening of Catalysts for Hydrodeoxygenation of Phenol as a Model Compound for Bio-oil.* ACS Catalysis, 2013. **3**(8): p. 1774-1785.
21. Olcese, R.N., et al., *Gas-phase hydrodeoxygenation of guaiacol over Fe/SiO2 catalyst.* Applied Catalysis B: Environmental, 2012. **115-116**: p. 63-73.
22. Olcese, R., et al., *Gas-phase hydrodeoxygenation of guaiacol over iron-based catalysts. Effect of gases composition, iron load and supports (silica and activated carbon).* Applied Catalysis B: Environmental, 2013. **129**: p. 528-538.

23. Yoon, K.J., et al., *Benzene Hydrogenation over Iron. 1. Specific Activities and Kinetic Behavior over Unsupported Iron and Iron Dispersed on Si02, Al203, Carbon, and Doped Carbon* Industrial Engineering Chemical Product Research Development, 1983. **22**: p. 519-526.
24. Yoon, K.J. and M.A. Vannice, *Benzene Hydrogenation over Iron. II. Reaction Model over Unsupported and Supported Catalysts.* Journal of Catalysis, 1983. **82**: p. 457-468.
25. Ruddy, D.A., et al., *Recent advances in heterogeneous catalysts for bio-oil upgrading via "ex situ catalytic fast pyrolysis": catalyst development through the study of model compounds.* Green Chem., 2014. **16**(2): p. 454-490.
26. Rezaei, P.S., H. Shafaghat, and W.M.A.W. Daud, *Aromatic hydrocarbon production by catalytic pyrolysis of palm kernel shell waste using a bifunctional Fe/HBeta catalyst: effect of lignin-derived phenolics on zeolite deactivation.* Green Chemistry, 2016. **18**(6): p. 1684-1693.
27. Sirous-Rezaei, P., et al., *Mild hydrodeoxygenation of phenolic lignin model compounds over a FeReOx/ZrO2 catalyst: zirconia and rhenium oxide as efficient dehydration promoters.* Green Chemistry, 2018. **20**(7): p. 1472-1483.
28. Wang, X., P. Clark, and S.T. Oyama, *Synthesis, Characterization, and Hydrotreating Activity of Several Iron Group Transition Metal Phosphides.* Journal of Catalysis, 2002. **208**(2): p. 321-331.
29. Cecilia, J.A., et al., *Gas phase catalytic hydrodechlorination of chlorobenzene over cobalt phosphide catalysts with different P contents.* J Hazard Mater, 2013. **260**: p. 167-75.
30. Yuan, Y., et al., *Preparation of Fe 2 P and FeP catalysts for the hydrotreating reactions.* Catalysis Communications, 2017. **100**: p. 202-205.
31. Zhu, X., et al., *Bifunctional transalkylation and hydrodeoxygenation of anisole over a Pt/HBeta catalyst.* Journal of Catalysis, 2011. **281**(1): p. 21-29.
32. Zhu, X., et al., *Efficient Conversion of m-Cresol to Aromatics on a Bifunctional Pt/HBeta Catalyst.* Energy & Fuels, 2014. **28**(6): p. 4104-4111.

7. Au NPs on mesoporous TiO_2 for CO photo-PROX

7.1. Abstract

The present chapter studies the photo-response behaviour of Au NPs supported on a mesoporous TiO_2 in the preferential oxidation of CO in a H_2-rich stream, under simulated solar light irradiation at room temperature and atmospheric pressure. The TiO_2 mesoporous supports were prepared by a sol-gel type method and calcined at different temperatures to obtain anatase/rutile mixed phases. Au nanoparticles (0.5 wt%) were supported on TiO_2 by a deposition-precipitation method with NaOH. The photocatalysts were studied by several characterization techniques in order to evaluate the effect of their structural, chemical and optical properties on the catalytic response.

7.2. Characterization results

7.2.1 X-ray diffraction (XRD)

Identification of crystalline phases of the catalysts after the deposition-precipitation process was accomplished by X-ray powder diffraction and results are included in Figure 7.1. Sample Au/MT400 shows a diffraction pattern characteristic of anatase phase (JCPDS, PDF card no. 73-1764) with broad peaks which indicate the formation of small crystallites as a consequence of the synthetic methodology used. In sample Au/MT500, calcined at a higher temperature, the diffraction profile is also ascribed to anatase phase but peaks are narrower and more intense, indicating an improved crystallinity. When increasing calcination temperature to 600ºC, sample Au/MT600, the intensity of the diffaction peaks also become sharper and new peaks associated to rutile phase appear (JCPDS, PDF card no. 21-1276). The rise in intensity can be explained either as improved crystallinity or particles agglomeration, both consequences of the higher calcination temperature.

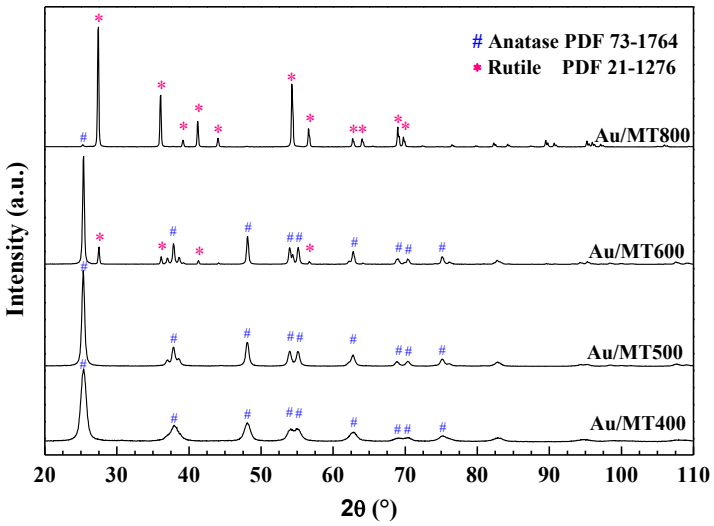

Figure 7.1. X-ray powder diffractograms of Au/MTX catalysts

The appearance of rutile phase is also a result of the calcination temperature and constitutes about 9.8% of the total amount of crystalline phases as calculated from XRD. If calcination temperature increases to 700ºC, the XRD pattern is fully superimposable to that of the sample calcined at 600ºC, that is why this sample was not studied. However, when the calcination takes place at 800ºC, sample Au/MT800, it is observed an almost complete transformation from anatase to rutile phase, which eventually constitutes about 98.8% of the total amount of crystalline phases identified by XRD. Table 7.1 compiles the relative amount of titania phases present in each sample and the average particle size. The crystalline size of the identified phases has been estimated from the FWHM of anatase (101) and rutile (110) by using the Scherrer equation. As mentioned before, an increased average particle size with increasing temperature is observed. The calculated average size of anatase crystallites is 9.5 nm in MT400, 19.7 nm in MT600 and 33.4 nm in MT700. Rutile crystals are found 40.1 and 44.1 nm for MT600 and MT800, respectively. XRD analysis of all samples before gold deposition-precipitation process was also carried out and no differences were found. That is to say that after gold incorporation the proportion and intensity of the identified phases remained unchanged and gold species were not discerned in the diffractograms of Au/MTX catalysts. This last fact may suggest that gold is present as highly dispersed nanoparticles in the pores of the support. But as gold content is below the XRD detection limit, other techniques such as TEM have to be employed to assert the authenticity of this statement. Table 7.1 also includes the gold content determined by AAS.

Table 7.1. Relative amount of titania phases and average crystallite size

Sample	Average crystallite size (nm)[a]	Anatase (%)	Rutile (%)	Au loading[b] (wt%)
MT400	9.5 (A)	100	-	-
Au/MT400	9.5 (A)	100	-	0.5
MT500	19.7 (A)	100	-	-
Au/MT500	19.7 (A)	100	-	0.54
MT600	33.4 (A)/40.1 (R)	91.2	8.8	-
Au/MT600	33.4 (A)/40.1 (R)	91.2	8.8	0.47
MT800	44.1 (A)/9.5 (R)	1.2	98.8	-
Au/MT800	44.1 (A)/9.5 (R)	1.2	98.8	0.49

[a] *Determined by Scherrer equation.*

[b] *Determined by elemental analysis.*

7.2.2 Textural properties

The porous nature of the prepared materials before and after gold incorporation has been evaluated by N_2 adsorption-desorption experiments and the results are included in Table 7.2. Figure 7.2 represents the isotherms of fresh supports before the deposition-precipitation process along with the pore diameter distribution.

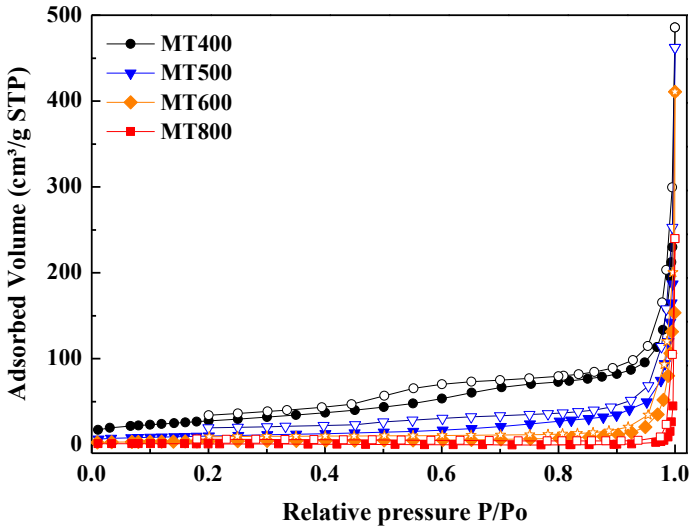

Figure 7.2 N_2 adsorption–desorption isotherms at -196 °C of the supports calcined at 400, 500, 600 and 800 ºC

Table 7.2 Textural parameters of MTX and Au/MTX catalysts

Sample	S_{BET} $(m^2 \cdot g^{-1})^a$	Vp $(cm^3 \cdot g^{-1})^b$
MT400	101	0.25
Au/MT400	100	0.24
MT500	37	0.15
Au/MT500	37	0.14
MT600	15	0.08
Au/MT600	14	0.07
MT800	5	0.01
Au/MT800	4	0.01

[a] *N_2 isotherms at -196 ºC were used to determine the specific surface area through BET equation*
[b] *Specific pore volume calculated at P/Po =0.98*

The isotherm of the support calcined at 400ºC, MT400, is of type IV presenting a hysteresis loop characteristic of ordered mesoporous materials according to the IUPAC classification. It

presents a specific surface area of 101 $m^2 \cdot g^{-1}$ with a narrow pore diameter distribution centered at 5 nm and a total pore volume of 0.25 $cm^3 \cdot g^{-1}$. By contrast, for the rest of supports, specific surface area values suffer a significantly decrease as well as the mesoporous texture when increasing the calcination temperature. Additionally, after gold deposition-precipitation on the support specific surface area slightly decreases in all the Au/MTX series.

7.2.3 Transmission electronic microscopy (TEM)

Distribution, morphology and size of gold nanoparticles have been evaluated by HR-TEM. Micrographs show well dispersed Au nanoparticles in all the prepared materials, becoming more homogeneously distributed and smaller in size by increasing the temperature. Average particle size distribution has been measured by statistical evaluation of particle sizes from selected regions of different micrographs and histograms are included in Figure 7.3.

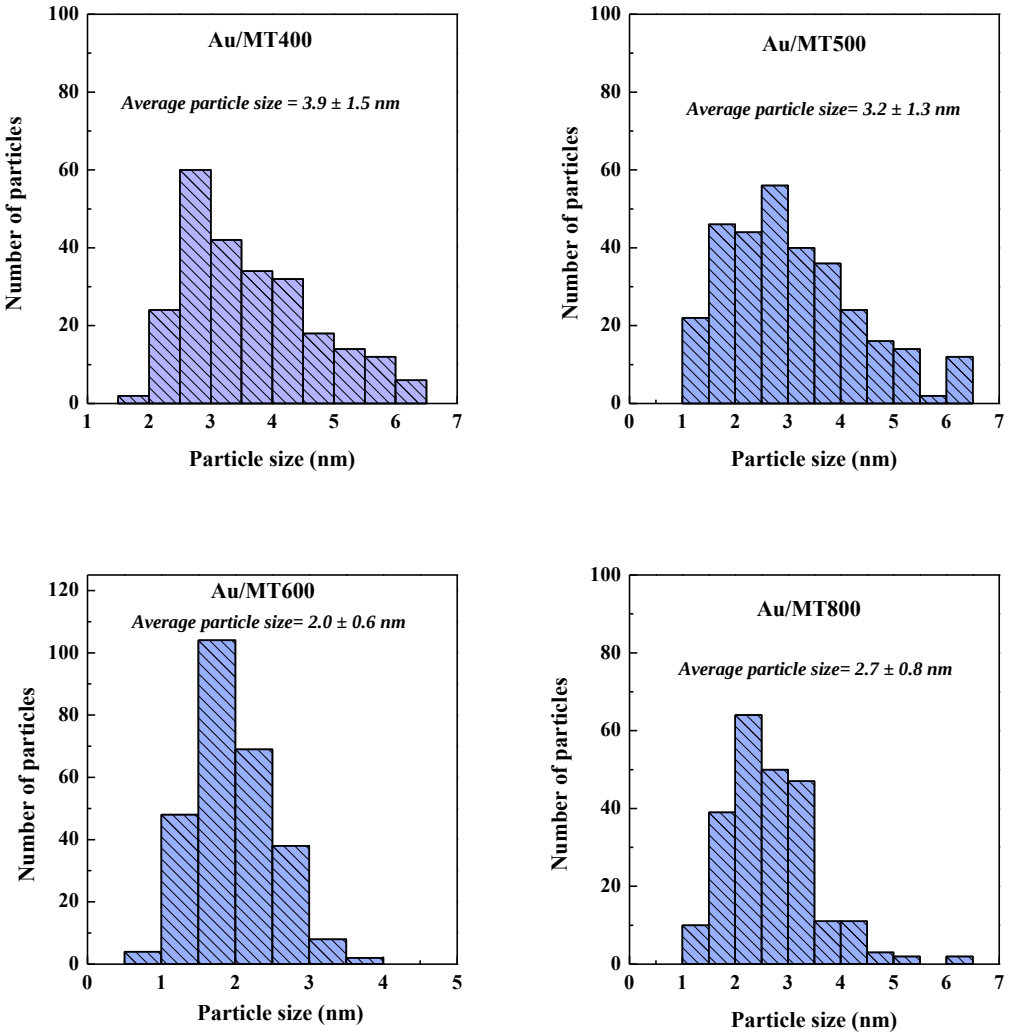

Figure 7.3 Gold particle size distribution of the fresh catalysts

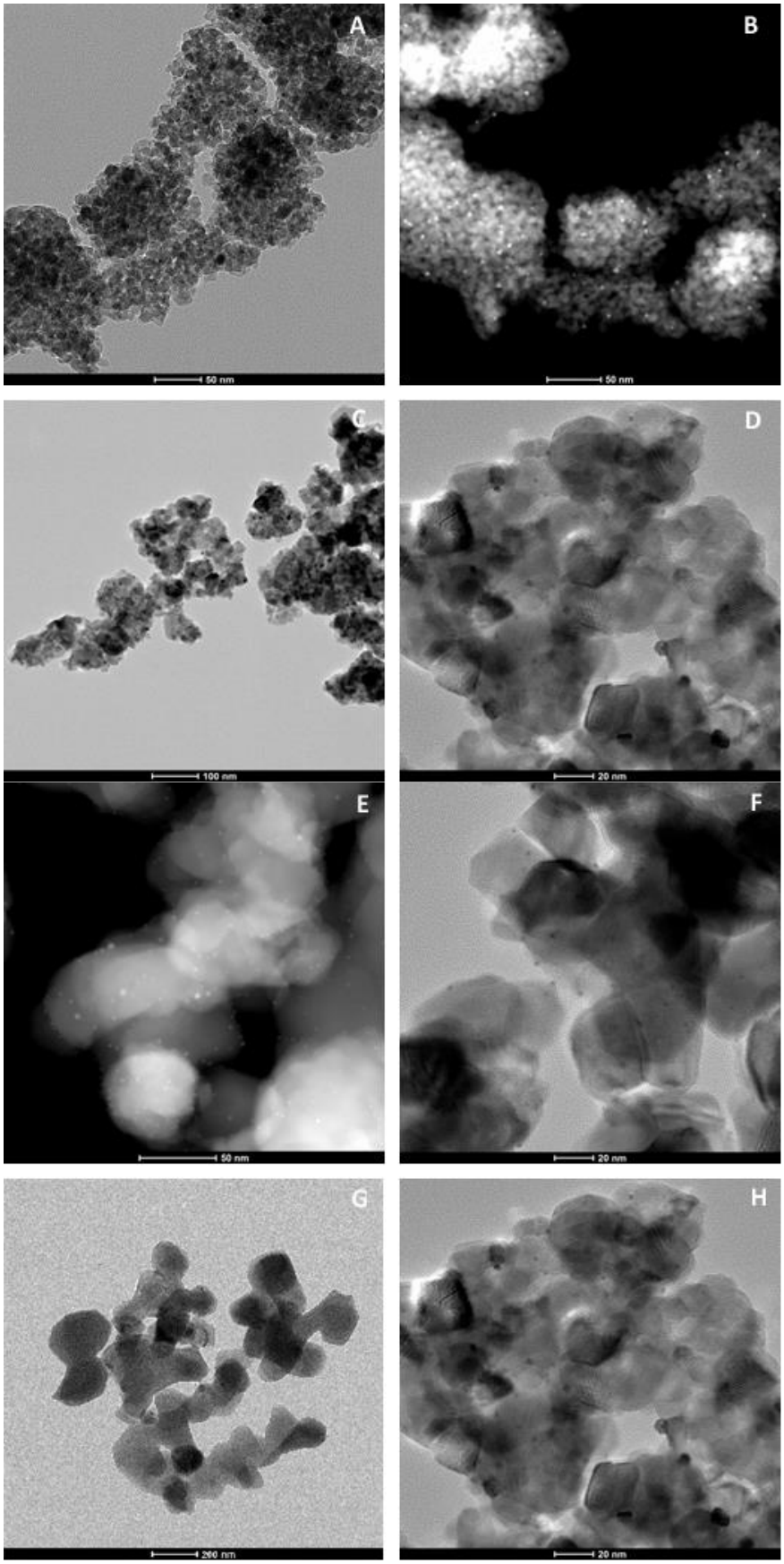

Figure 7.4. TEM images of A-B) Au/MT400; C-D) Au/MT500; E-F) Au/MT600; G-H) Au/MT800 (Note: Figures B and E are in STEM mode)

As aforesaid, samples calcined at 400 and 500 ºC present a broader particle size distribution with an average particle size about 5 nm. The coexistence of larger and smaller particles in both samples is clearly noticeable in their corresponding micrographs as well. Figure 7.4 shows HR-TEM micrographs of the studied materials before catalysis. Au/MT600 sample exhibits a narrow sixe distribution and the lowest particle size among the studied samples, about 2 nm. Au/MT800 sample presents a different morphology if compared to the other samples, presenting an average particle size smaller than that of Au/MT400 and Au/MT500 but bigger than that of Au/MT600. These results point to that the properties of the support are playing an important role in the particle size and its distribution. Anyhow, in all cases mean particle size is smaller than 5 nm which is required for highly photoactive CO-PROX catalysts [1]. TEM analyses were also performed after the catalytic test and no significance differences were observed as seen in the example of Figure 7.5.

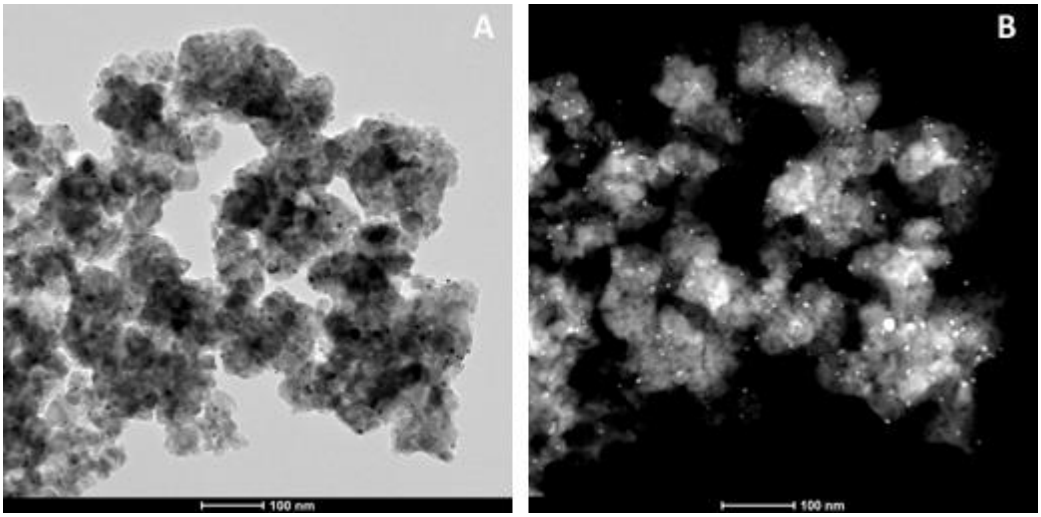

Figure 7.5. TEM A) and STEM B) micrographs of Au/MT500 after one cycle of CO-PROX photocatalytic reaction

7.2.4 Diffuse Reflectance UV-Vis spectroscopy (DRUV-Vis)

The photo-responsive behavior of the samples was studied by DRUV-Vis spectroscopy. Figure 7.6 shows the absorption peaks within the UV-Vis range of the studied material after incorporation of gold. All supports and Au/MTX series of materials exhibit an absorption peak below 400 nm assigned to the intrinsic absorption of TiO_2. Additionally, Au/MTX catalysts show a broad band in the visible region located between 400 and 700 nm with the maximum positioned between 570 and 585 nm, which is attributable to the LSPR effect of Au nanoparticles loaded on TiO_2. This is justified because it is known that Au/TiO_2 systems display a broad band between 450 and 600 nm characteristic of the LSPR effect of Au NPs and that the intensity and wavelength of this band are dependent on the metal loading and the size and shape

of nanoparticles [2]. Indeed, Au/MTX prepared materials are slightly pink-violet in color which is another qualitative sign of the existence of Au nanoparticles. Figure 7.6 shows that the intensity and position of the LSPR band is slightly shifted in each studied Au/MTX sample. Since the Au loading is the same in all samples (about 0.5 wt% as measured by AAS), the different intensities of the LSPR band cannot be attributable to the amount of gold present in each catalyst. Therefore, it is reasonable to suppose that the position of the band depends on the different particle sizes as previously observed from TEM micrographs, but also to the proportion of anatase-rutile phases presents in each sample. Since in fact, it is known that LSPR peak position can also depend on the solvent in which the nanoparticles are dispersed [3]. For unsupported spherical gold nanoparticles of a fixed size, a red linearly dependency with the increase of the solvent refractive index was registered [4]. Refractive indices of anatase and rutile minerals are 2.49 and 2.61, respectively and Kamura et al. [5] reported a red shift of about 40 nm in the LSPR peak of Au NPs of comparable size loaded in Au/anatase and Au/rutile materials. Our results show a shift of about 12 nm between the Au LSPR peak of the anatase containing catalysts (Au/MT400, Au/MT500, Au/MT600) and that containing only rutile phase (Au/MT800).

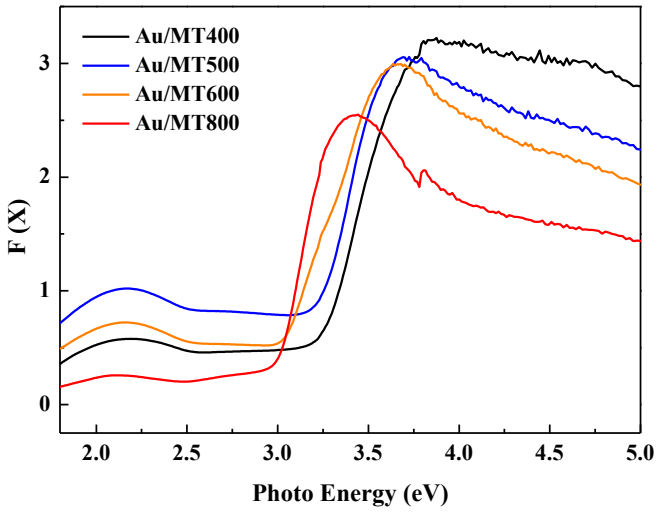

Figure 7.6. Diffuse reflectance UV-Vis spectra of the Au/MTX fresh catalysts

The band gap values have also been calculated and compiled in Table 7.3. As expected, band gap values of bare titania decrease with increasing calcination temperature of the support [6, 7], with the crystallinity and rutile content [8]. It is also worth noting that after gold incorporation the band gap of bare MTX titania is slightly reduced as found by other authors [6, 9]. The presence of Au nanoparticles is found to decrease the band gap of pristine titania calcined at different temperatures, as seen in Table 7.3, being more remarkable in Au/MT600 sample (0.13 eV lower). These results indicate that there is a stronger interaction between Au NPs and TiO_2

in Au/MT600 sample, predicting some important implications for its photocatalytic activity which will be discussed further on.

Table 7.3. Band gap values before and after gold deposition

Sample	Band gap (eV)
MT400	3.17
Au/MT400	3.12
MT500	3.13
Au/MT500	3.09
MT600	3.03
Au/MT600	2.90
MT800	2.97
Au/MT800	2.96

DRUV-Vis experiments were also carried out after one cycle of photoactivity in CO-PROX and the recorded spectra remain unaffected confirming the stability of these catalysts under solar simulated light in the operating conditions, as seen in Figure 7.7.

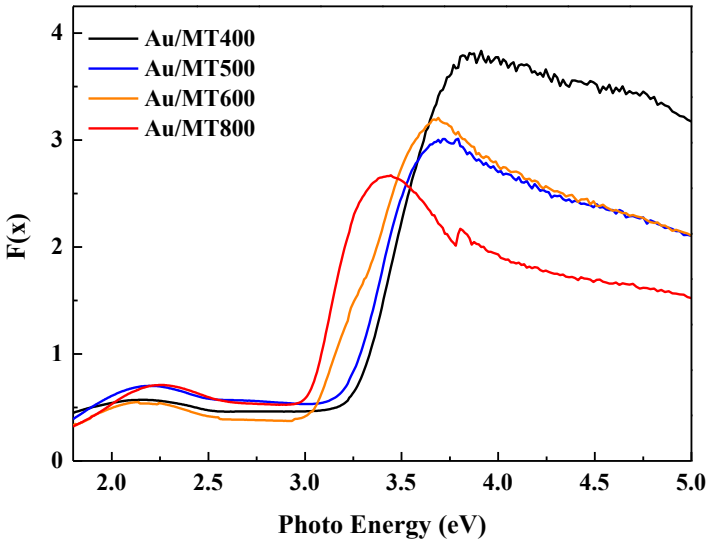

Figure 7.7. DRUV-Vis spectra of the Au/MTX catalysts after one cycle of CO-PROX photoactivity under simulated solar light irradiation

7.2.5 X-ray photoelectron spectroscopy (XPS)

The surface atomic composition of the prepared materials and the chemical state of their constituent elements has been studied by XPS analysis. Table 7.4 compiles the Au 4*f* binding energy values of fresh and spent catalysts along with the corresponding Au/Ti atomic ratios which give us an idea of the gold exposure on the surface. The Ti *2p* core-level spectra, Figure 7.8.A, present two contributions at 458.7 and 464.4 eV which respectively correspond to the Ti $2p_{3/2}$ and Ti $2p_{1/2}$ components. First one is attributed to Ti^{4+} which is the only observed oxidation state on surface [10]. It should also be noted that the maximum is slightly shifted to lower energy values in the case of the sample calcined at 800 ºC pointing out that rutile is present as the majority phase [11, 12]. This fact was also observed by XRD. Considering now the O 1*s* core-level spectra, Figure 7.8.B, two contributions are present in all the catalysts. The first one is centered at 529.9 eV and corresponds to the lattice oxygen reported for bare titania. A second contribution located at 531.7 eV is ascribed to surface oxygen [13]. As reported by some authors [1], surface oxygen can be consumed during the induction period which is not our case. Again, the O 1*s* core-level signal of Au/MT800 catalyst is slightly shifted to lower binding energy value, which is ascribed to the presence of the rutile phase [11].

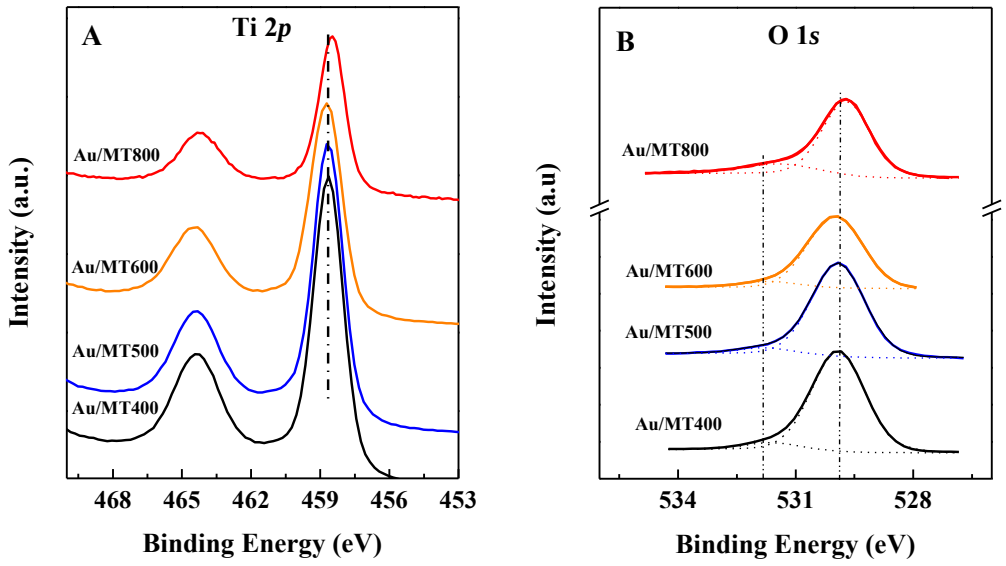

Figure 7.8. A) Ti *2p* and B) O *1s* core-level spectra of fresh catalysts

Table 7.4. Au *4f* binding energy values (eV) and Au/Ti atomic ratio of fresh and spent Au/MTX catalysts

Sample	Au $4f_{7/2}$	Au $4f_{5/2}$	Au/Ti
Au/MT400	83.3	85.2	0.004
Au/MT400Spent	83.3	85.2	0.004
Au/MT500	83.3	85.1	0.016
Au/MT500Spent	83.2	85.0	0.014
Au/MT600	83.4	84.9	0.011
Au/MT600Spent	83.2	84.9	0.012
Au/MT800	83.3	84.9	0.032
Au/MT800Spent	83.6	85.4	0.032

It is worth noting that as seen in Figure 7.9, the Au 4*f* core level signal shows two contributions centered at 83.4 and 87.1 eV which respectively correspond to the doublet Au $4f_{7/2}$ and Au$4f_{5/2}$. These contributions are asymmetric due to small energy electron-hole excitation near Fermi energy (E_F) of metal and typical of Au(0). However, there are also two low intensity contributions at higher binding energy ascribed to $Au^{\delta+}$ [1, 14] . Taking this into consideration, it may be deduced that gold mainly exists in a metallic state finding a minor contribution of partially positive charged gold.

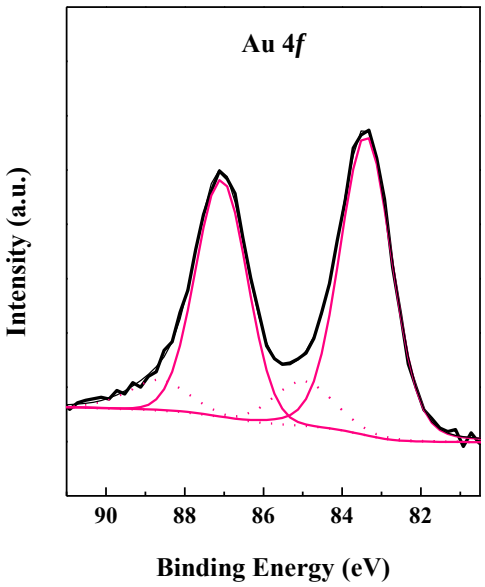

Figure 7.9. Au 4f core-level spectrum of Au/MT600 sample

7.3 Catalytic study

The photocatalytiv activity of the prepared catalysts in the CO-PROX reaction in excess of hydrogen under dark and simulated solar light irradiation has been studied. Results in terms of conversion and selectivity are depicted in Figure 7.10 A) and B).

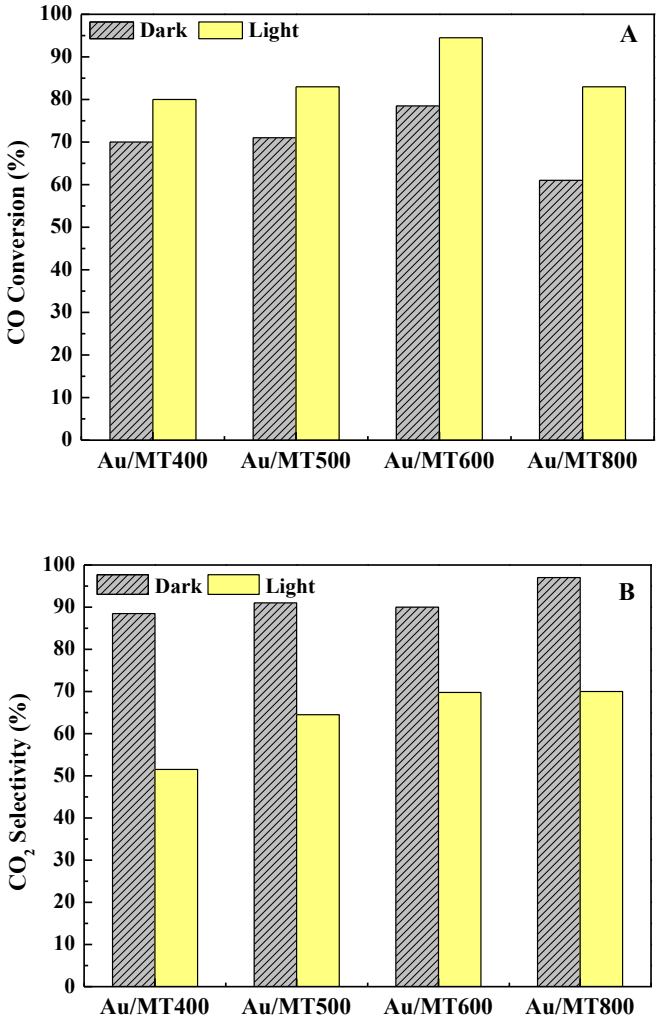

Figure 7.10. Conversion A) and selectivity B) values after one cycle of reaction under dark and light irradiation mode

Considering the very low temperature at which the catalytic reaction is performed (30 ºC), the samples display a very high activity and selectivity in oxidizing carbon monoxide both under dark and solar light. It is worth noting that the photocatalytic response of the bare MTX titania supports under both modes was found negligible. As seen in Figure 7.10.A conversion values are higher under the light irradiation mode reaching up to 96% whereas under dark mode conversion values reach up to 78%. Both results are attained by Au/MT600 sample which therefore is considered the most active catalyst. However, the rest of the catalysts also display

good results achieving up to 84% of conversion for Au/MT500 and Au/MT800 samples and up to 80% for Au/MT400 sample.

Regarding now the selectivity results after one cycle of reaction, it is observed the opposite trend. In all cases, selectivity to CO_2 is quite superior working under dark mode reaching values that range from 87 to 98 %. However, under simulated solar light irradiation, selectivity to CO_2 ranges from 50 to 70 %. These results evidence that the oxidation reaction of hydrogen to form water is encouraged under light mode since being more active promotes secondary undesirable reactions [15]. That is why in order to compare the performance of the various catalysts, activity data has been expressed in terms of TOF of CO oxidation and TOF of H_2 oxidation. Results are included in Table 7.5.

Table 7.5. Catalytic performances of Au/MTX catalysts as TOF of CO oxidation, H_2 oxidation and selectivity to CO_2 under dark and simulated sun light irradiation

Sample	TOF of CO oxidation ($mmol \cdot g_{cat} \cdot h^{-1}$)		TOF of H_2 oxidation ($mmol \cdot g_{cat} \cdot h^{-1}$)		CO_2 Selectivity (%)	
	DARK	LIGHT	DARK	LIGHT	DARK	LIGHT
Au/MT400	4.5	5.1	1.7	6.0	87	53
Au/MT500	4.6	5.4	1.0	4.5	92	65
Au/MT600	5.0	6.2	1.3	4.0	90	69
Au/MT700	4.6	5.7	0.4	3.9	97	70

λ = 2; CO (1.25%), O_2 (1.25%) and H_2 (50%) balanced with He.; T = 30ºC; [a] GHSV = 22000 h^{-1}

From this data it is deduced that all catalysts display similar catalytic response since TOF values are very close. However, Au/MT600 shows to be the most active one under simulated light irradiation reaching the greatest TOF of CO oxidation (6.2 mmol g_{cat}^{-1} h^{-1}) and the lowest TOF of H_2 oxidation (4 mmol g_{cat}^{-1} h^{-1}).

7.4. Discussion

Literature data indicate that the activity of Au/TiO_2 systems is ascribed to several factors such as: the size of gold nanoparticles, chemical state/environment, the pH of the precursor solution used during the synthesis, the gold loading and the synthetic method applied [16-20]. Overall, low metallic loadings lead to the formation of very small Au-NPs in size which are better dispersed on the support and display a lower capacity of sintering during both reaction modes. A homogeneous distribution of gold nanoparticles on the titania surface is therefore required in order to obtain a high rate of CO_2. It is also necessary a direct contact at the interface that allows the electron transfer from TiO_2 to gold nanoparticles. That way electron-hole separation can be enhanced as well as the transfer of the trapped electron to the adsorbed oxygen acting as

electron acceptor. When increasing the amount of noble metal, the chance of the photoelectron to find the hole also increases. In addition, electrons can be accumulated inducing an electric field that attracts holes. Au-NPs then are considered to be the recombination center between electrons and holes by induction of the light irradiation. Under the synthetic conditions employed here, the metallic loading has been estimated by elemental analysis being around 0.5 wt%. The mean particle size has also been measured being lower than 5 nm, which has been reported to be highly active in CO-PROX reactions [1]. Concretely, the most active among all the studied catalysts shows an average particle size close to 2 nm with a sharp distribution, as demonstrated by HR-TEM measurements. As was also found by other authors, CO conversion in hydrogen rich stream follows the same tendency as in the mean particle size, since smaller gold particles usually present more active coordination sites like edges and corners [15]. In our study a clear correlation between particle sizes and TOF values is observed when these two factors are compared.

As aforementioned, the Au/MT400 sample shows the lowest catalytic response among the studied catalysts. This striking result is not expected if considering that this sample presents a high specific surface area that normally leads to a better dispersion of the active phase. However, photoactive powders with high surface area are known to present a large number of defects sites that can favor the recombination of electrons and holes resulting in a poor photoactivity [21]. The crystallinity and the polymorph type of the titania are other key factors affecting the catalytic results. In that sense, several authors have reported that amorphous titania displays a negligible performance in CO-PROX reactions under light irradiation, proving that crystallinity of the support is a critical factor that has to be taken into account [22]. Regarding the type of polymorph, anatase phase displays better activities than rutile based catalysts, mainly due to the slightly more negative conduction band bottom of anatase polymorph [23].

Kowalska et al. [24] studied the influence of the aforementioned parameters in the CO-PROX under visible light, and they found that the larger the gold particle size is the wider the absorption wavelength range is, allowing a larger number of photons to be absorbed. Awake et al. [25] observed negligible visible light-induced activity of a gold-modified fine particulate titania sample. The opposite dependence, that is an increase in photo-efficiency under visible light irradiation with decrease in gold particle size, has also been reported [26], though gold was deposited in two types of titania supports. After all, the TiO_2 photoactivity was found to remarkably increase with the decreasing size accordingly. Therefore, a compromise among polymorph type, crystallinity, porosity and gold particle size have to be achieved. It should also be noticed that the interaction between AuNPs and TiO_2 reduces the band gap energy of the titania favoring a better photocatalytic response and also enhancing the charge separation between electrons (e^-) and holes (h^+). However, in our samples, where the amount of gold and

the preparation method used are the same, the relative band gap energy decrease is related to the polymorph type or the mixed polymorphs used as support by increasing surface to volume ratio of spherical Au-NPs. As shown in Table 7.5 , sample Au/MT600, is the most active catalyst in the CO-PROX reaction under solar light displaying the lowest band gap energy (2.9 eV) among the studied catalysts, most probably due to the very small size of the Au-NPs (2 nm). Furthermore, it has been observed a high decrease on the band gap (0.13 eV) between the pristine titania and the correspondent gold-loaded catalyst in this sample, Au/MT600. The strong metal-support interaction can be associated to the presence of both anatase and rutile polymorphs (91.2 % A and 9.8% R) and their relatively big crystallite size (33.4 nm A and 40.1 nm R). In addition, to study plasmon-induced charge-transfer mechanisms between excited gold nanoparticles and titania, Du et al. [2] reported that larger TiO_2 particles resulted in longer charge recombination times because of the longer diffusion length of electrons in larger TiO_2 particles. However, in our samples, where the amount of gold and the preparation method used are the same, the relative band gap energy decrease is related to the polymorph type or the mixed polymorphs used as support.

Wu et al. [27] studied a biphase photocatalyst containing 12-15% of rutile and 85-88% of anatase. This catalyst resulted very active in gas-phase photocatalytic oxidations. This positive effect was related to the interaction between the two titania phases, therefore, a synergetic effect between relatively large anatase and rutile particles can be supposed to explain the most outstanding behavior of the catalysts containing both phases as it is the case of Au/MT600. The difference between the Fermi levels of anatase and rutile enable the electrons to flow from one phase to the other, reducing the charge recombination accordingly. Recently, Scanlon et al.[12] carried out computational analyses of both polymorphs to explain how the simultaneous presence of both phases improved photocatalytic activity, showing how photogenerated conduction electrons flow from rutile to anatase lowering the effective band gap of composite materials, and facilitating efficient electron-hole separation.

Our results seem to be in line with the aforementioned results. Au/MT500 and Au/MT800 catalysts containing pure anatase (100% A) and almost pure rutile phase (98.8% R), respectively, display a lower photocatalytic performance than Au/MT600 despite presenting a larger surface enrichment of gold species. In addition, both samples present quite small-sized Au-NPs (3.2 and 2.7 nm respectively) and band gap values (3.09 and 2.96 eV) very close to the bare titania supports which have been reported to be suitable for the studied reaction. So, the previous argument gains weight in explaining the attained results highlighting the importance of presenting a mixture of both polymorphs. Finally, the catalyst also presenting pure anatase phase, Au/MT400, shows the lowest conversion values which can ascribed to the larger size of gold nanoparticles (3.9 nm) and the higher band gap energy value (3.12 eV).

According to the literature, gold supported catalysts exhibit COPROX conversion values relatively similar in the absence or presence of light [28]. Although an increase of the reaction rate by a factor of 1.05 under UV irradiation was reported [29]. The mechanism suggested by these authors considers that electrons separated from holes in titania by UV irradiation disseminate to Au and then to adsorbed oxygen at the interface. In the presence of visible light the mechanism is essentially the same. Under our operational conditions, a factor 1.1-1.2 between the light (UV-Vis irradiation) and dark mode irradiation is observed. The selectivity was found higher in dark conditions for all the studied catalysts. Similar results have been reported by Yang et al [30, 31].

Even though, under simulated sunlight, the selectivity to CO_2 was found quite high, being Au/MT600 (69%) and Au/MT800 (70%) the most selective catalysts among all the series of materials. But it is also true that a severe drop in selectivity compared to dark conditions was observed as well. Mukherjee et al. [32] studied the photocatalytic dissociation of hydrogen enabled by hot electrons generated by small AuNP surface plasmon decay. The authors proved that visible light induces the appearance of surface plasmons on AuNPs that decay into hot electrons. Hot electrons transfer into a Fesh back resonance of a hydrogen molecule interacting with the AuNP surface, triggering its dissociation. In our case, it is possible to speculate that under visible light irradiation, hydrogen molecules can dissociate on the gold nanoparticles surface and react with oxygen or with hydroxyl groups adsorbed at the interface between Au and TiO_2 giving water as reaction product. The decrease in selectivity of all the samples varies between 23 and 39%. Au/MT600 show the slightest decrease in selectivity coupled with a very good conversion to CO_2 (96%), the highest among the studied catalysts.

7.5. Conclusions

The main conclusions extracted from the present chapter are:

- All catalysts resulted very active in the preferential oxidation of CO under simulated solar light and ambient conditions in spite of the low metal loading (0.5 wt%).
- The photocatalytic response is ascribed to the very small Au NPs (2-5 nm) highly dispersed on the support. Therefore, able to strongly interact with TiO_2 surface, improving the catalytic sites able to coordinate to CO and O_2.
- Au/MT600 sample, containing 91.2 % A and 9.8% R polymorphs, achieved the highest activity in dark and under simulated solar light irradiation. The simultaneous presence of both polymorphs seems to reduce the recombination of charge carriers enhancing the photocatalytic activity.

7.6. References

1. Deng, X.-Q., et al., *Visible-light photocatalytic oxidation of CO over plasmonic Au/TiO2: Unusual features of oxygen plasma activation.* Applied Catalysis B: Environmental, 2016. **188**: p. 48-55.
2. Du, L., et al., *Plasmon-Induced Charge Separation and Recombination Dynamics in Gold-TiO2 Nanoparticle Systems: Dependence on TiO2 Particle Size.* Journal of Physical Chemistry, 2009. **113**: p. 6454-6462.
3. Yang, J., et al., *Organic solvent dependence of plasma resonance of gold nanorods: A simple relationship.* Chemical Physics Letters, 2005. **416**(4-6): p. 215-219.
4. Mock, J.J., D.R. Smith, and S. Schultz, *Local Refractive Index Dependence of Plasmon Resonance Spectra from Individual Nanoparticles.* Nano Letters, 2003. **3**: p. 485-491.
5. Kimura, K., et al., *TiO2Crystal Form-Dependence of the Au/TiO2Plasmon Photocatalyst's Activity.* The Journal of Physical Chemistry C, 2012. **116**(12): p. 7111-7117.
6. Debeila, M.A., et al., *The influence of gold on the optical properties of sol–gel derived titania.* Materials Science and Engineering: A, 2005. **396**(1-2): p. 70-76.
7. Monticone, S., et al., *Quantum size effect in TiO nanoparticles: does it exist?* Applied Surface Science, 2000. **162-163**: p. 565-570.
8. Chen, X. and S.S. Mao, *Titanium Dioxide Nanomaterials: Synthesis, Properties, Modifications, and Applications.* Chemical Reviews, 2007. **107**: p. 2891-2959.
9. Li, F.B. and X.Z. Li, *Photocatalytic properties of gold/gold ion-modified titanium dioxide for wastewater treatment.* Applied Catalysis A: General, 2002. **228**: p. 15-27.
10. Simonsen, M.E., et al., *Surface properties and photocatalytic activity of nanocrystalline titania films.* Journal of Photochemistry and Photobiology A: Chemistry, 2008. **200**(2-3): p. 192-200.
11. Tuichai, W., et al., *High-performance giant-dielectric properties of rutile TiO 2 co-doped with acceptor-Sc 3+ and donor-Nb 5+ ions.* Journal of Alloys and Compounds, 2017. **703**: p. 139-147.
12. Scanlon, D.O., et al., *Band alignment of rutile and anatase TiO(2).* Nat Mater, 2013. **12**(9): p. 798-801.
13. Górska, P., et al., *TiO2 photoactivity in vis and UV light: The influence of calcination temperature and surface properties.* Applied Catalysis B: Environmental, 2008. **84**(3-4): p. 440-447.
14. Hernández, J.A., et al., *Insight into the Deactivation of Au/CeO2 Catalysts Studied by In Situ Spectroscopy during the CO-PROX Reaction.* ACS Catalysis, 2015. **5**(7): p. 4003-4012.
15. Quinet, E., et al., *On the mechanism of hydrogen-promoted gold-catalyzed CO oxidation.* Journal of Catalysis, 2009. **268**(2): p. 384-389.
16. Imai, H., M. Daté, and S. Tsubota, *Preferential Oxidation of CO in H2-Rich Gas at Low Temperatures over Au Nanoparticles Supported on Metal Oxides.* Catalysis Letters, 2008. **124**(1-2): p. 68-73.
17. Sangeetha, P., L.-H. Chang, and Y.-W. Chen, *Preferential Oxidation of CO in H2 Stream on Au/TiO2 Catalysts: Effect of Preparation Method.* Industrial and Engineering Chemistry Research, 2009. **48**: p. 5666-5670.
18. Valden, M., X. Lai, and D.W. Goodman, *Onset of Catalytic Activity of Gold Clusters on Titania with the Appearance of Nonmetallic Properties.* Science, 1998. **281**.
19. Wen-Yueh Yu, C.-P.Y., Jiunn-Nan Lin, Chien-Nan Kuo and Ben-Zu Wan*, *Preparation of Au/TiO2 for catalytic preferential oxidation of CO under a hydrogen rich atmosphere at around room temperature.* Chemical Communications, 2005: p. 354-356.
20. Rossignol, C., et al., *Selective oxidation of CO over model gold-based catalysts in the presence of H.* Journal of Catalysis, 2005. **230**(2): p. 476-483.
21. Zhang, Z., et al., *Role of particle size in nanocrystalline TiO2-based photocatalysts.* Journal of Physical Chemistry, 1998. **102**: p. 10871-10878.

22. Ohtani, B., Y. Ogawa, and S.-i. Nishimoto, *Photocatalytic Activity of Amorphous-Anatase Mixture of Titanium(IV) Oxide Particles Suspended in Aqueous Solutions.* Journal of Physical Chemistry, 1997. **101**: p. 3746-3752.
23. Fujishima, A., X. Zhang, and D. Tryk, *TiO2 photocatalysis and related surface phenomena.* Surface Science Reports, 2008. **63**(12): p. 515-582.
24. Kowalska, E., et al., *Visible-light-induced photocatalysis through surface plasmon excitation of gold on titania surfaces.* Phys Chem Chem Phys, 2010. **12**(10): p. 2344-55.
25. Awate, S.V., et al., *Effect of Gold Dispersion on the Photocatalytic Activity of Mesoporous Titania for the Vapor-Phase Oxidation of Acetone.* International Journal of Photoenergy, 2008. **2008**: p. 1-13.
26. Rodríguez-González, V., et al., *MTBE visible-light photocatalytic decomposition over Au/TiO2 and Au/TiO2–Al2O3 sol–gel prepared catalysts.* Journal of Molecular Catalysis A: Chemical, 2008. **281**(1-2): p. 93-98.
27. Wu, C., et al., *Investigation on the synergetic effect between anatase and rutile nanoparticles in gas-phase photocatalytic oxidations.* Catalysis Today, 2004. **93-95**: p. 863-869.
28. Yoshida, Y. and Y. Izumi, *Recent Advances in the Preferential Thermal-/Photo-Oxidation of Carbon Monoxide: Noble Versus Inexpensive Metals and Their Reaction Mechanisms.* Catalysis Surveys from Asia, 2016. **20**(3): p. 141-166.
29. Dai, W., et al., *The promoted effect of UV irradiation on preferential oxidation of CO in an H2-rich stream over Au/TiO2.* Journal of Power Sources, 2009. **188**(2): p. 507-514.
30. Yang, K., et al., *Superior preferential oxidation of carbon monoxide in hydrogen-rich stream under visible light irradiation over gold loaded hedgehog-shaped titanium dioxide nanospheres: Identification of copper oxide decoration as an efficient promoter.* Journal of Power Sources, 2015. **284**: p. 194-205.
31. Yang, K., et al., *Comparative study of Au/TiO2 and Au/Al2O3 for oxidizing CO in the presence of H2 under visible light irradiation.* Journal of Catalysis, 2014. **317**: p. 229-239.
32. Mukherjee, S., et al., *Hot electrons do the impossible: plasmon-induced dissociation of H2 on Au.* Nano Lett, 2013. **13**(1): p. 240-7.

8. Au NPs on TiO_2 nanorods for CO photo-PROX

8.1. Abstract

In the present chapter gold nanoparticles with a metal loading of 1wt% were precipitated-deposited on titania nanostructures. Titania supports were synthesized by two hydrothermal methods markedly acid and basic, resulting in nanorods shaped nanostructures. The catalysts were labelled as AuTNRaX and AuTNRbX, where "a" and "b" refer to the acid or basic treatment which supports have been subjected and "x" refers to the calcination temperature, 500 and 700ºC.

These materials were tested in the photo-PROX of CO in excess of hydrogen, at room temperature and atmospheric pressure and also were characterized by a wide range of techniques as those applied in the previous chapter.

8.2. Characterization results

8.2.1 X-ray diffraction (XRD)

XRD of the synthesized catalysts are shown in Figure 8.1. In the XRD spectra of the catalysts from the acid treatment, AuTNRa5 and AuTNRa7, Figure 8.1.A, all the diffraction peaks are characteristic of the rutile phase of TiO_2 for both calcination temperatures (JCPDS 01-072-1148). The presence of crystalline anatase is discarded. In Figure 8.1.B, the diffraction pattern of AuTNRb5 and AuTNRb7 catalysts uniquely correspond to the anatase phase (JCPDS 01-089-4921), also for both calcination temperatures.

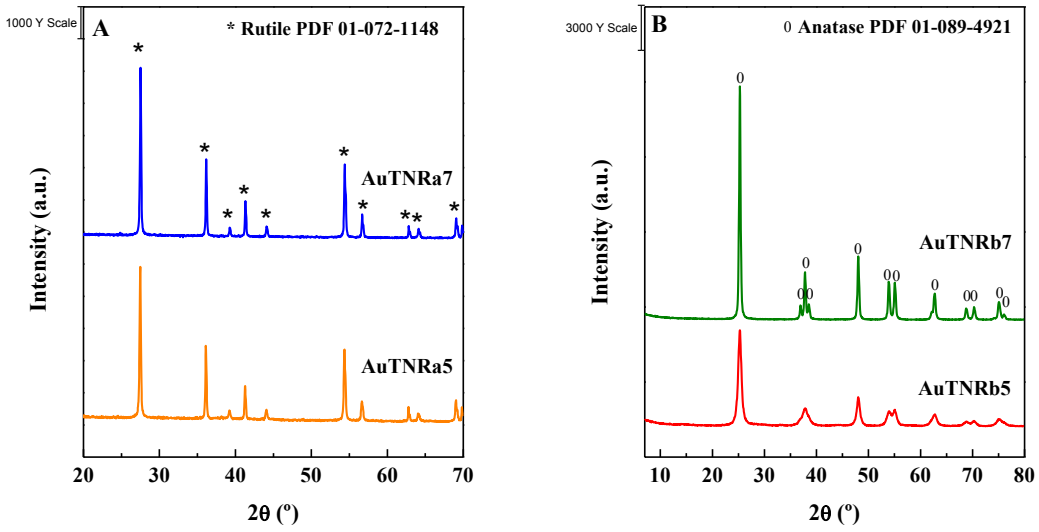

Figure 8.1. X-ray diffractograms of AuTNR catalysts: A) acidic hydrothermal treatment and B) basic hydrothermal treatment

In any of the series of materials, identification of gold was possible since it is present as highly dispersed nanoparticles, as will be shown in HRTEM micrographs. The very low gold loading also hinders its identification. Now, if the XRD profiles are compared all the peaks present a relatively equal intensity with a mild increase at higher calcination temperatures, being sharper in the case of the samples from the acid treatment.

TiO_2 crystallite size, calculated from Scherrer equation is listed in Table 8.1 showing two main trends: samples prepared from the acid treatment present a higher titania particle size. And, within each series of materials, the higher temperature the higher the particle size.

8.2.2. Textural properties

The textural properties of the bare supports and the corresponding Au catalysts were obtained by N_2 adsorption-desorption at -196ºC. Table 8.1 concretely includes the specific surface area and the pore volume values, revealing two uneven trends after the hydrothermal treatments. After the basic treatment, the supports show an increase on their surface area which in turn slightly diminishes at higher calcination temperatures. However, titania nanorods from the acidic synthetic approach present a much lower specific surface area than the titania P25 precursor (~50 m^2g^{-1}) and this parameter decreases with the thermal treatment. After gold incorporation, the specific surface area remains almost unaffected in all the catalysts with the exception of that of sample AuTNRa7, which slightly increases.

Table 8.1. TiO_2 crystallite size, textural parameters and gold content

Sample	TiO_2 crystallite size (nm)[a]	S_{BET} ($m^2 \cdot g^{-1}$)[b]	Vp ($cm^3 \cdot g^{-1}$)[c]	Au loading (wt%)[d]
TNRa5	64.1	42	0.38	-
AuTNRa5	64.1	40	0.38	1.2
TNR7	81	9.0	0.028	-
AuTNRa7	81	15	0.050	1.0
TNRb5	12	145	1.00	-
AuTNRb5	12	144	0.52	1.0
TNRb7	36.5	40	0.40	-
AuTNRb7	36.5	40	0.07	0.7

[a] *Determined by XRD*
[b] *N_2 isotherms at -196 ºC were used to determine the specific surface areas through the BET equation*
[c] *Specific pore volume calculated at P/P_0=0.98*
[c] *Determined by XRF*

The Au content (wt.%) determined by XRF, also included in Table 8.1, is close to the nominal value of 1 wt% Au with the exception of AuTNRa7, with a gold loading lower than the nominal one.

8.2.3. Raman Spectroscopy

The Raman spectroscopy technique allows us to get further insight about local microstructure and atomic arrangement. In the Raman spectra of the samples from the acidic approach, Figure 8.2.A, three one-phonon Raman scattering bands of rutile titania are located at approximately 143, 436 and 608 cm^{-1}, which correspond to the spectra of TiO_2 rutile single crystals [1]. These three bands are respectively assigned to B_{1g}, E_g and A_{1g} modes, respectively [1]. An additional band at around 250 cm^{-1} is ascribed to second order scattering of rutile crystals. Figure 8.2.B, corresponding to the spectra of the samples from the basic treatment, show several vibrational bands ascribed to the anatase polymorph. Specifically, five Raman-active fundamentals in the vibrational spectrum are noticeable: three E_g modes centred around 144, 197, and 639 cm^{-1} one B_{1g} mode at 519 cm^{-1} and one A_{1g} mode at 513 cm^{-1} [2].

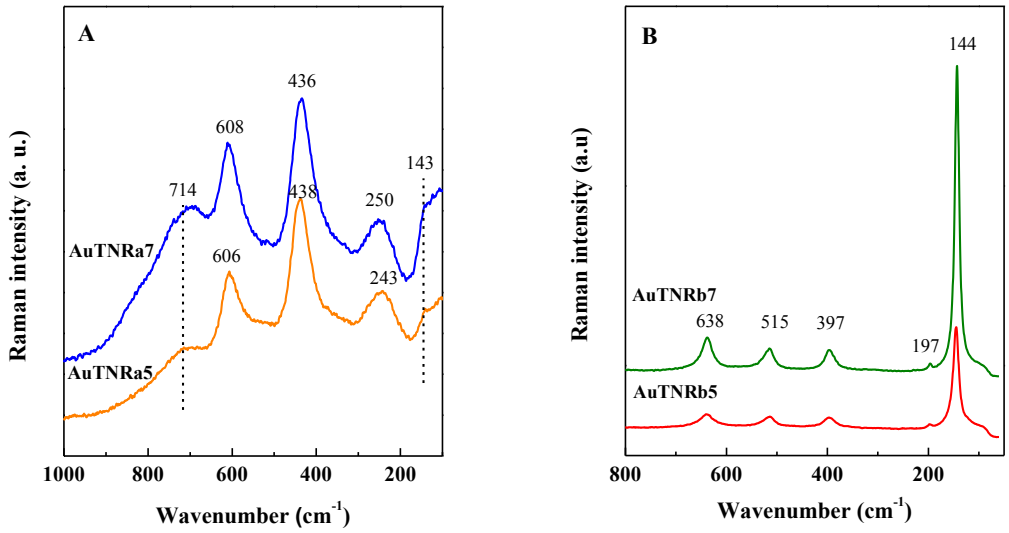

Figure 8.2. Raman spectra of A) AuTNRa and B) AuTNRb based samples

As reported in literature, the Raman peaks broaden and suffer a systematic frequency shift when the particle size decreases. In the case of AuTNRa samples, the spectra are quite similar. The most important feature is that the contribution at 714 cm^{-1} is much more evident in the sample treated at 700 ºC. This band is related to rutile phase and observed for titania nanotube structures. Its higher intensity in the sample treated at 700 ºC could be related to its higher particle size [3].

The differences between the spectra of AuTNRb samples are more evident. Thus, the intensity of the spectrum corresponding to AuTNRb7 is much stronger than for AuTNRb5 sample. The TiO_2 crystallite size, determined from XRD measurements, is three times higher for AuTNRb7 and explains this fact. The Raman data are in accordance with XRD. Samples prepared from a process in an acid medium give rise to the formation of rutile, whereas if the synthetic route followed is alkaline, the polymorph formed is anatase.

8.2.4 Small-angle X-ray scattering (SAXS)

Small-angle X-ray scattering measurements were performed in order to get more information about Au nanoparticles [4]. SAXS is a phenomenon originated by particles embedded in a matrix of different electron density. If the particle size is nanometric the scattering angle lies within the range 0 to 8 degrees at the lambda of Cu radiation. Figure 8.3 shows that the smaller the particles are, the higher the scattering angles. In both acid and basic media, it seems that samples treated at 700 ºC have a bimodal distribution while for those treated at 500 ºC the distribution is monomodal. The sizes of nanometric aggregates obtained by SAXS are of the order of the particle sizes measured by TEM, as will see below.

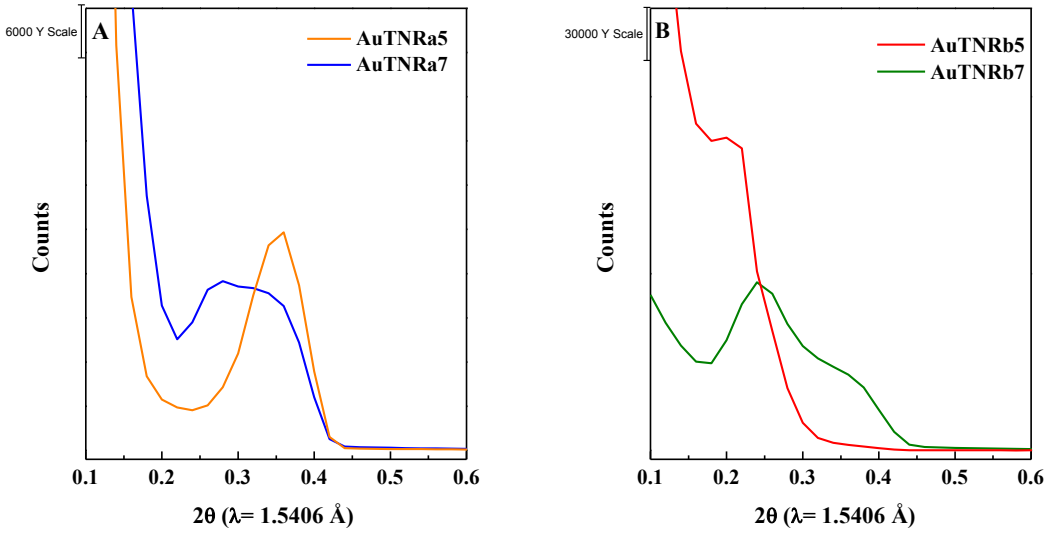

Figure 8.3. SAXS pattern of A) AuTNRa and B)AuTNRb based samples

8.2.5 High resolution transmission electron microscopy (HRTEM)

High resolution TEM micrographs were recorded in order to elucidate the particle size and morphology of both gold and titania structures. The micrographs corresponding to AuTNRa samples show very well defined titania nanorod structures with highly disperse gold nanoparticles on their surface. The length and diameter of the nanorods obtained at both calcination temperatures were calculated from the corresponding micrographs. Both length and

diameter increase with the calcination temperature: AuTNRa5 (L=269 nm, D=45 nm) < AuTNRa7 (L=350 nm, D=80 nm). And the average length to diameter ratio for each sample is 5.9 and 4.3, respectively. This fact along with the higher amount of gold on its surface points out that AuTNRa5 sample presents greater accessibility to reach active sites during the reaction. Gold particle size distribution was also measured from selected regions of TEM micrographs of the catalysts calcined at both temperatures, as shown in Figure 8.4. The histograms of AuTNRa samples exhibit a relatively narrow particle size distribution, mainly constituted by the coexistence of particles from 2 to 5 nm. The average particle size is close to 2 nm in AuTNRa5 and around 3.5 nm for AuTNRa7, which is reported to be a suitable size for the CO preferential oxidation [5]. The obtained data match well with those obtained by SAXS measurements.

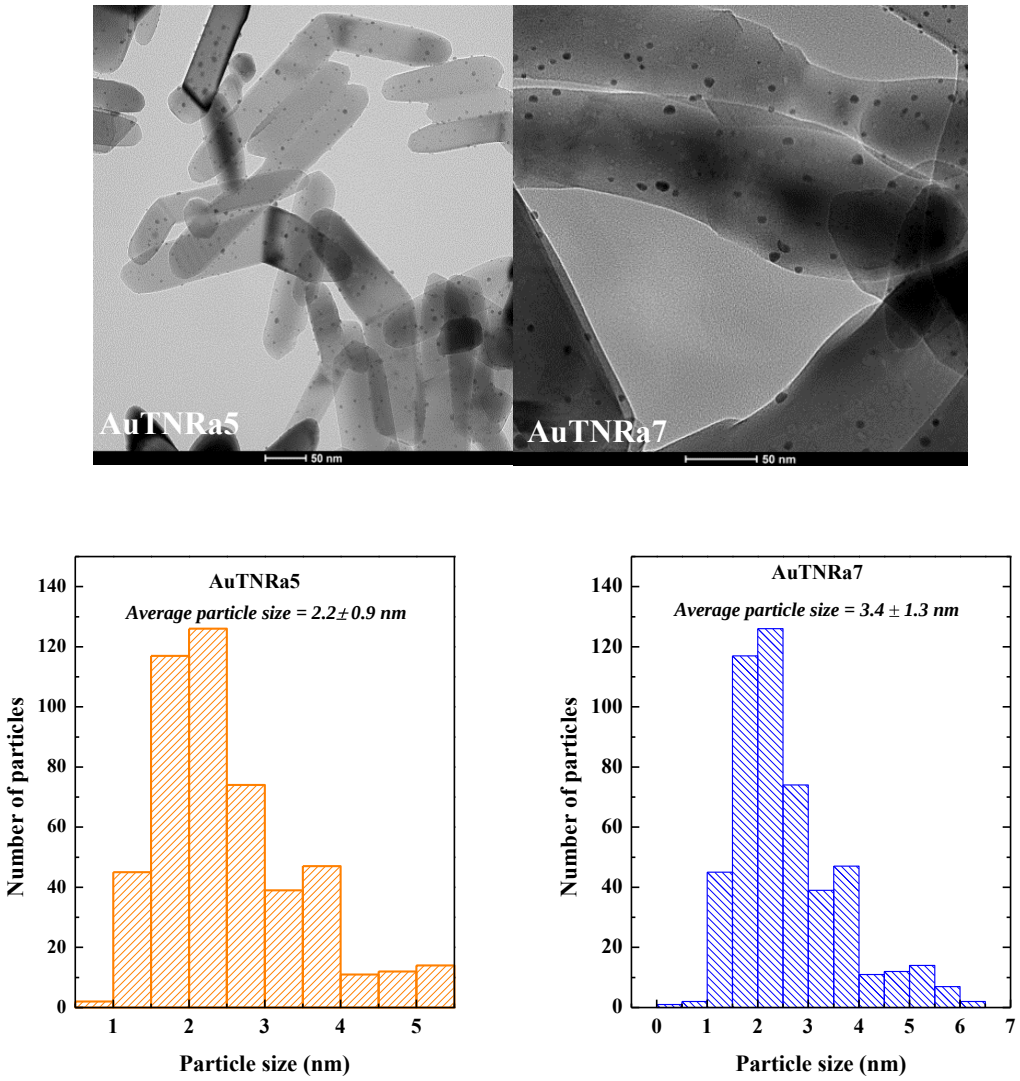

Figure 8.4. HRTEM micrographs and particle size distribution of AuTNRa samples

Micrographs and histograms of the samples prepared from the basic hydrothermal procedure are included in Figure 8.5. In this case, the titania nanorods are worse defined, finding some

deformed nanorods and spherical and irregular anatase structures as well. Furthermore, in both series of materials titania nanorods slightly deteriorate with calcination temperature. Nevertheless, the samples partially retain the peculiar morphology. As it is not possible to identify the presence of such small Au nanoparticles from HRTEM micrographs, the corresponding micrographs in STEM mode have been also included. Histograms of AuTNRb samples also show a narrow distribution of particles size, mainly from 1 to 4 nm, with an average size of approximately 2 nm in both cases. Therefore, gold nanoparticles deposited on titania from the basic treatment seem to exhibit a smaller size and a higher dispersion than those from the acidic approach.

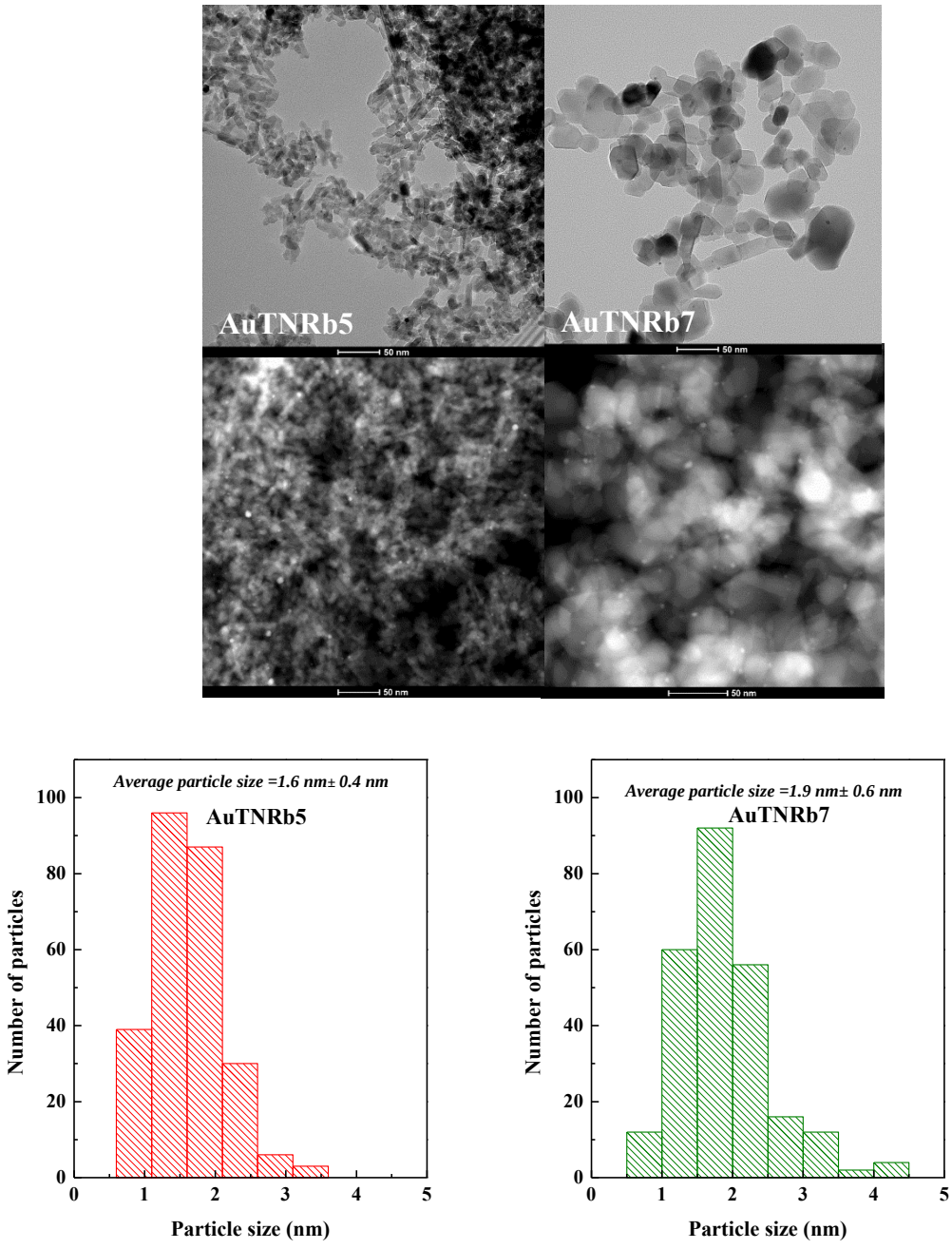

Figure 8.5. HRTEM and STEM micrographs and particle size distribution of AuTNRb samples

In order to get further insight into the differences in the photocatalytic response of AuTNRa5 and AuTNRa7 samples, high resolution images of both samples provide information about the interaction among Au NPs and TNRa5 and TNRa7 supports. As shown in HRTEM images (Fig.8.6 and Fig.8.7) nanostructured rutile phase presents more defects in AuTNRa7 sample than in AuTNRa5, and can be appreciable that, in the first sample, Au NPs are composed of both Au and Au_2O_3. Gold oxide has a crystalline structure very different from that of rutile. The particles of gold that grew on deformations due to the defects produced by the treatment at 700°C of pure rutile phase, are less linked to the $(TiO_6)^{8-}$ octahedra sharing their edges [6]. As a consequence, larger Au metallic particles are formed. Instead, less rutile defects are present on AuTNRa5 sample and the nanoparticles are mainly as Au^0. The mobility of Au particles on rutile as a support then seems to depend on the defects on it, on the shape of the border of the nanorods, and on the strength of the link between the defects and the gold particle seeds [7].

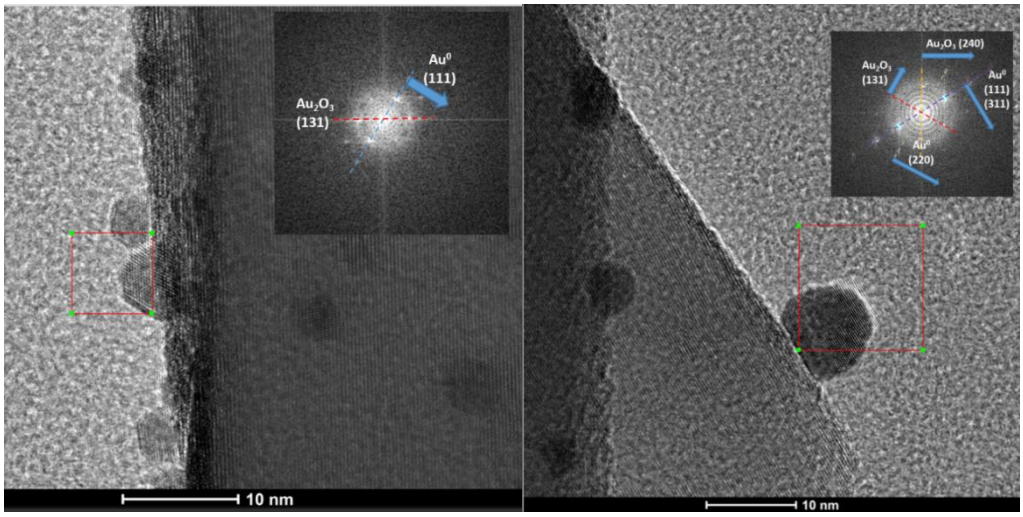

Figure 8.6. HRTEM micrograph of AuTNRa7 sample

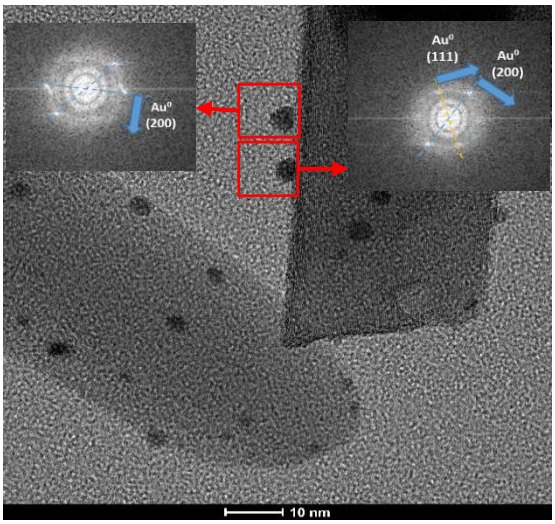

Figure 8.7. HRTEM micrograph of AuTNRa5 sample

8.2.6 Diffuse Reflectance UV-Vis spectroscopy (DRUV-Vis)

The photo-responsive behavior of the samples was studied by DRUV-Vis spectroscopy. Figure 8.8 shows the photo-response of the bare nanorods and AuTNR photocatalysts. In all the spectra, an absorption peak in the UV region below 400 nm is assigned to the intrinsic absorption of TiO_2. After incorporation of gold nanoparticles, the absorption peaks suffer a slight shift to higher wavelengths as a result of the interaction of gold NPs with titania

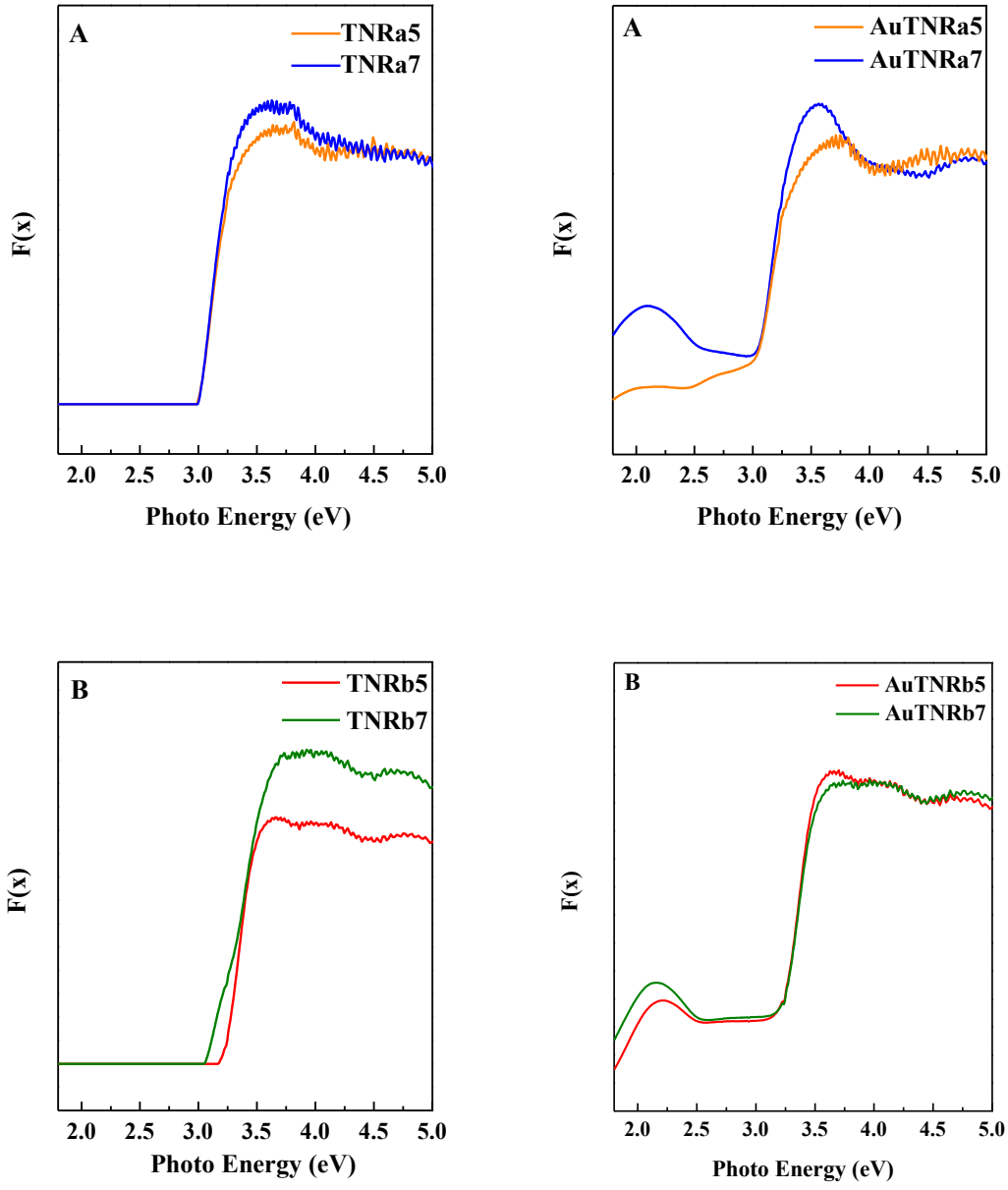

Figure 8.8. DRUV-vis spectra of A) titania bare nanorods (TNRa) and AuTNRaX samples and B) TNRb and AuTNRbX samples

In addition to titania absorption band, DRUV-Vis spectra exhibit a broad band in the visible region, located between 450 and 700 nm and due to the SPR phenomenon from Au NPs. The

SPR peak generated by the incident visible radiation on a metallic nanoparticle has generally a position and an intensity that depend on the metal loading and the shape and size of metal NPs as well as on the dielectric constant of the surrounding medium [8]. As calculated by XRF, the gold loading is different in the AuTNRa samples, which should be reflected in the intensity of the peaks. The sample AuTNRa7 exhibits a more intense and presents a lower gold content. The LSPR peak position is slightly shifted to minor wavelengths with increasing calcination temperature confirming the increase in the particle size also pointed by SAXS and TEM techniques. However, for the AuTNRb catalysts the position and intensity of the LSPR peak barely changes with the calcination temperature. The maximum is centred around 576 nm in AuTNRb7 and at 566 nm for AuTNRb5. It should be pointed that the particle size is similar in these catalysts which corroborates these findings. Now, if both families are compared, it is shown as well that the position of LSPR peak is slightly shifted to minor wavelengths in rutile-containing catalysts, i.e. AuTNRa samples, since it is reported that the different refractive index of both polymorphs affects the position of the LSPR band [9].

The optical band gap, Eg, of titania supports and the AuTNR catalysts was estimated from the linear extrapolation of $(\alpha h\nu)^{½}$ versus photon energy (hν) curves, where *h* is Planck's constant and ν is the frequency (s^{-1}). Eg values are compiled in Tab 8.2. As reported in the literature, the band gap of pristine rutile is lower than that of anatase polymorph [10]. After gold incorporation the band gap values decrease in both AuTNRa and AuTNRb samples, facilitating the absorption in the UV-vis region. These results point to the existence of a strong interaction between gold nanoparticles and the titania support. However, this cannot be regarded as a key factor that ensures a good performance under simulated sunlight since other factors such as crystallinity, calcination temperature and particle size have to be taken into consideration as well.

Table 8.2. Band gap energy values

Sample	Binding Energy (eV)
TNRa5	2.95
AuTNRa5	2.88
TNRa7	2.98
AuTNRa7	2.92
TNRb5	3.21
AuTNRb5	3.11
TNRb7	3.18
AuTNRb7	3.10

AuTNRb5 and AuTNRb7 samples, in which the support was prepared in basic conditions and calcined at 500 and 700 °C, respectively, and AuTNRa7, in which the support was prepared in acidic conditions and then calcined at 700 °C, show an LSPR peak more defined than in

AuTNRa5 sample. Experimentally [11], size dependence is observed as the plasmon band is strongly damped for small particles and even can disappear completely for nanoparticles with sizes lower than 2 nm. Very small nanoparticles in the size range below 2 nm are better treated as molecular clusters with discrete electronic states, and the assumption of a delocalized free electron gas is no longer valid [12]. Metal particles below about 2 nm are also called 'artificial big atoms' and are to be considered as connection between metal nanoparticles and small molecular clusters since they show typical quantum size behaviour, even at room temperature owing to the existence of discrete electronic energy levels and the loss of overlapping electronic bands[13].

8.2.7 X-ray photoelectronic spectroscopy (XPS)

The chemical composition of the catalysts surface as well as the chemical state of the constituent elements was determined by XPS. The Ti 2*p* and O 1*s* core-level spectra are represented in Fig. 8.9 and Figure 8.10, respectively.

Ti 2*p* spectra show two components located at approximately 458.6 and 464.2 eV, and assigned to the doublet Ti $2p_{3/2}$ and Ti $2p_{1/2}$, respectively, remaining almost unaffected regardless of the calcination temperature. The strong peak at low binding energy of 458.6 eV corresponds to Ti^{4+}, the dominant state on surface [14].

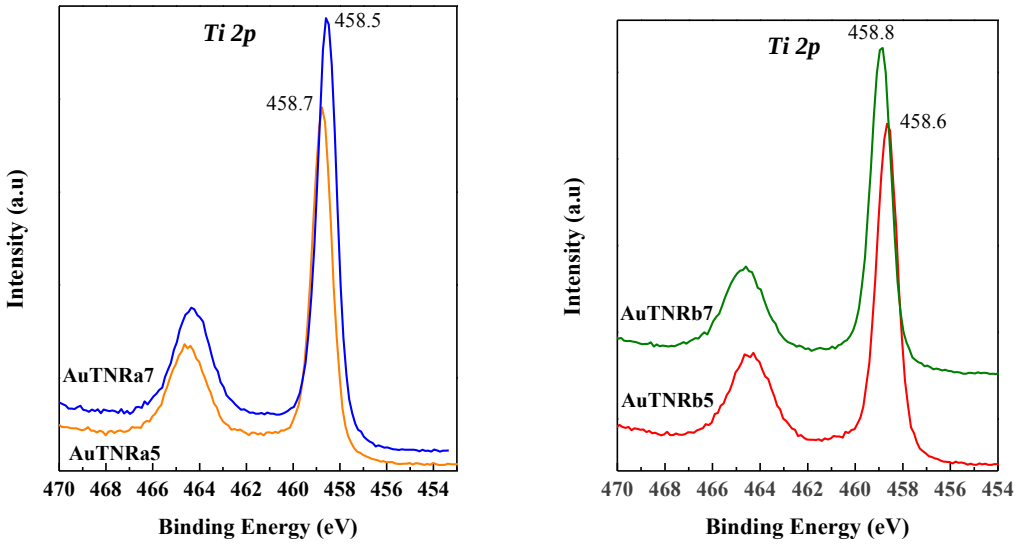

Figure 8.9. Ti *2p* core-level spectra

The O 1*s* spectra were decomposed and two contributions are observed in all cases. The main one is centred at 529.9 eV, which corresponds to lattice oxygen (92%) in titanium dioxide [15]. Another contribution and much less important is found at around 531 eV in both series of materials, due to surface oxygen. No major changes are observed in these spectra.

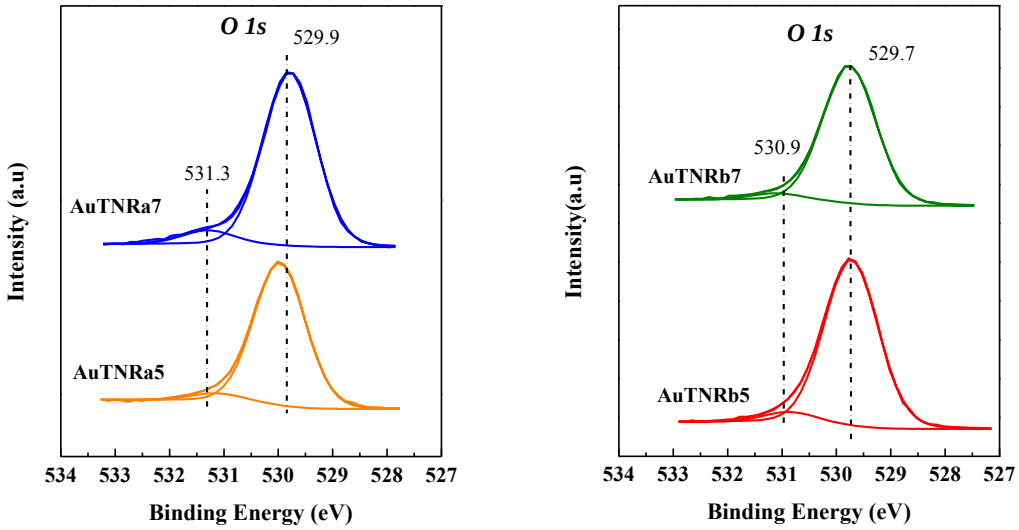

Figure 8.10 O *1s* core-level spectra

The details of the Au 4*f* photoelectron core level spectra are shown in Figure 8.11. The two main peaks of the doublet Au $4f_{7/2}$ and Au $4f_{5/2}$ appear at *ca.* 83.2-83.6 and 87.1 eV, respectively, and are ascribed to Au^0 [16]. Two less intense contributions at 85.2 eV and 88.8 eV are ascribed to Au^+ or $Au^{\delta+}$ which leads to deduce that gold exists mainly in a metallic state but the existence of a small cluster $Au^{\delta+}$ is also possible [17]. In addition, it is also found that the Au $4f_{7/2}$ component suffers a negative shift of 0.6 eV in comparison with that observed in Au metal. Meanwhile, the signal Ti $2p_{3/2}$ corresponding to Ti^{4+} is positively shifted by 0.2 eV in comparison with the binding energy of pure rutile. These results point out that there is an electron transfer from Au NPs to TiO_2 via *d-p* feedback bond as a result of the strong interaction between the active phase and the support [18].

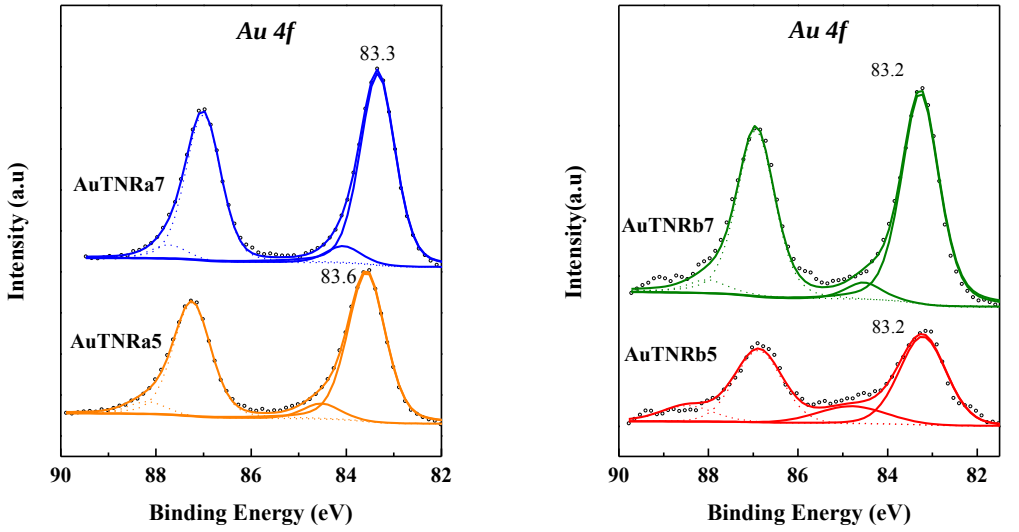

Figure 8.11. Au 4f core-level spectra

The relative abundance of Au^0 as well as the Au/Ti atomic ratio of the samples are compiled in Table 8.3. As seen from this Table, AuTNRa5 and AuTNRa7 catalysts present a mayor exposure of gold on the surface than samples prepared from the alkaline conditions.

Table 8.3. Relative abundance of Au^0 (atomic concentration %) and Au/Ti atomic ratio

Sample	%Au	%Au(0)	$\%Au^{\delta+}$	Au/Ti
AuTNRa5	5.83	90.6	9.4	0.0270
AuTNRa7	5.53	91.8	8.2	0.0270
AuTNRb5	0.86	79.0	21	0.0038
AuTNRb7	1.60	91.0	9.0	0.0078

Au nanoparticles are supposed to be mainly located on the outer surface of titanium dioxide nanorods. Thus, the analysis performed with a surface sensitive technique such as XPS, shows very high Au loading values for samples AuTNRa5 and AuTNRa7 compared to the basic ones. This indicates that gold nanoparticles are more uniformly distributed decorating the surface of the titania, probably thanks to the higher surface areas.

8.3 Catalytic results

The performance of the studied catalysts in the reaction of CO preferential oxidation in excess of hydrogen at room temperature and atmospheric pressure under dark and solar light irradiation is shown in Figures 8.12.A and 8.12.B. TOF values ($mmol \cdot g_{cat}^{-1} \cdot h^{-1}$) of CO and H_2 oxidation are listed in Table 8.4.

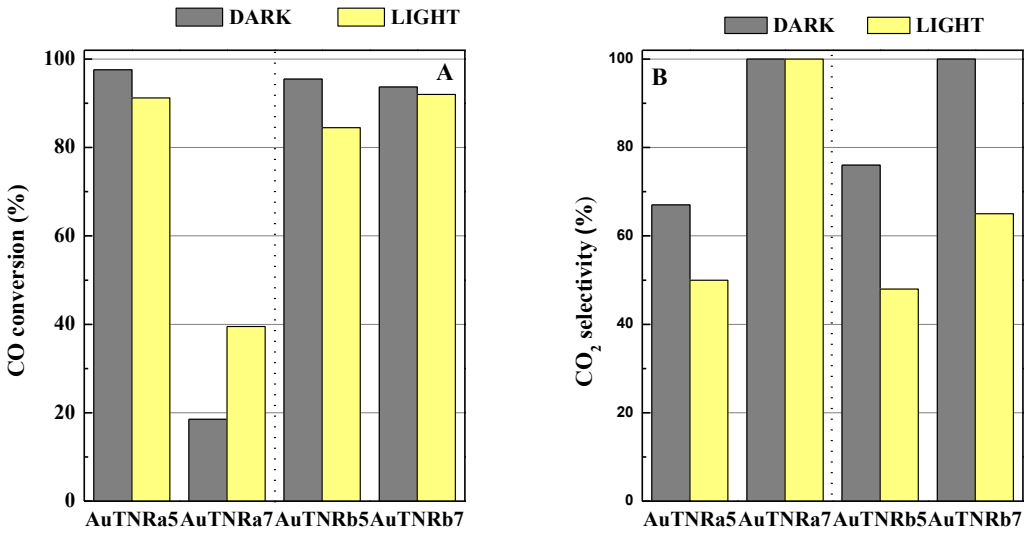

Figure 8.12. A) CO conversion and B) CO_2 selectivity for the photo-PROX reaction

Table 8.4. Turnover frequency values of CO and H_2 oxidation under dark and simulated sunlight irradiation

Sample	TOF of CO oxidation[a] (mmol $g_{cat}^{-1} \cdot h^{-1}$)		TOF of H_2 oxidation[a] (mmol $g_{cat}^{-1} \cdot h^{-1}$)	
	DARK	LIGHT	DARK	LIGHT
AuTNRa5	6.3	5.9	4.2	6.4
AuTNRa7	1.2	2.5	0	0
AuTNRb5	6.1	5.4	3.1	6.7
AuTNRb7	6.0	5.9	0	4.5

[a] *GHSV=22000 h^{-1}; λ=2; 1.2 % CO, 1.2% O_2 and 50.0% H_2 (vol.%, He balance); T=30 °C.*

The photocatalytic response of the bare TNR supports, synthesized both by acidic and basic hydrothermal conditions, was also investigated in dark mode and under solar light irradiation, and their responses were found negligible (not shown). Catalysts from the basic synthetic approach, AuTNRb, achieve conversion values that largely exceed 80% under both modes. In particular, AuTNRb5 sample reaches a CO conversion of about 96% in dark and 85% under light conditions, while AuTNRb7 catalyst exhibits values of 94% and 92% respectively. However, selectivity values are rather lower under solar light irradiation than in dark conditions. Considering now the AuTNRa samples, it appears that the conversion value of AuTNRa5 sample under solar light is far superior if compared to AuTNRa7 sample. However, the latter can be considered more active as a photocatalyst since it achieves CO_2 selectivity values of 100% under both modes, whilst AuTNRa5 catalyst only achieves 50% of selectivity. This is ascribed to its superior activity that promotes undesired secondary reactions like the competitive oxidation of hydrogen to water. As previously reported, the size-dependency is a key factor affecting the mechanism of the reaction: smaller gold particles have more low-coordination sites (LCS) like edges and corners providing more active sites for CO adsorption but also for water formation [19].

8.4. Discussion

Catalytic data indicate that by comparing AuTNRa samples (Fig.12.A and Tab.8.4), that calcined at 500 °C is the most active in the CO-PROX both under dark and light irradiation conditions due to the larger metallic surface exposed. This is reflected on its CO oxidation turnover frequency (TOF) values of 6.3 and 5.9 mmol g_{cat}^{-1} h^{-1} in dark and under light irradiation, respectively. However, this catalyst presents H_2 oxidation TOF values of 4.2 and 6.4 g_{cat}^{-1} h^{-1} under dark and light modes, respectively. Therefore, AuTNRa5 is also the least selective, since the formation of water is favoured by the presence of small Au nanoparticles giving rise to LCS phenomenon. Distorting the geometry of a cluster when it is adsorbed on a support will change its reactivity, and this has been invoked as a possible cause for the activity

of the metallic clusters. Therefore, the presence of a certain amount of non-crystalline gold particles of colloidal dimensions, as found by SAXS and DRUV-Vis measurements, and the low LSPR effect of gold, as shown by DRUV-vis spectrum, make the behaviour of this catalyst different from the AuTNRa7 one, being less active under simulated solar light irradiation [20]. AuTNRa7 catalyst, in which Au NPs have larger dimensions, is by far less active than AuTNRa5 sample in the CO conversion both under dark and light conditions but, in this case, the gold LSPR effect shown by this catalyst enhances the reactivity under simulated solar light irradiation compared to dark conditions, as can be inferred by CO oxidation TOF values, 1.2 and 2.5 mmol g_{cat}^{-1} h^{-1}, respectively (Tab.8.4).

Considering now the Au-containing samples based on titania nanorods obtained by alkaline conditions, AuTNRb5 and AuTNRb7 (Fig. 11), both show to be very active in dark conditions reaching CO conversion values of about 95% with CO oxidation TOF values of 6.1 and 6.0 mmol g cat^{-1} h^{-1}, respectively. Light exposure seems to be however slightly detrimental in the conversion of CO to CO_2 lowering the CO oxidation turnover frequency to 5.4 and 5.9 mmol g_{cat}^{-1} h^{-1}, respectively. As in the above discussed case, the very small size of gold particles (about 1.6 and 1.9 nm) makes these two catalysts very active in dark conditions. For AuTNRb5 catalyst the light exposure decreases the CO conversion promoting the undesired and competitive reaction of H_2 oxidation, while in AuTNRb7, light exposure seems not to significantly affect the CO conversion and CO_2 selectivity.

Consequently, it is suggested that AuTNR catalysts with gold particle size of about 2 nm or less are definitely very active in the CO-PROX in excess of hydrogen at ambient conditions. When Au nanoparticles exhibit larger sizes, as in the case of AuTNRa7, the catalyst behaves in a quite different way: less active in oxidizing CO to CO_2, but with an enhanced preferential CO conversion under solar irradiation with respect to dark mode. Noteworthy is that this sample, which behaves as a real photocatalyst, reaches a 100% of CO_2 selectivity.

8.5. Conclusions

The main findings extracted from the present study are:

- The reported method for the preparation of gold nanoparticles (1.0 wt%) on nanorod-like TiO_2 structures leads to active catalysts in the preferential CO oxidation in excess of H_2.
- Titania supports, synthesized by acid and basic hydrothermal methods give rise to rutile and anatase polymorphs, respectively. Those supports seem to play a different role in dispersing and growing gold nanoparticles.
- Gold particle size was found to depend on both the surface area and the type of polymorph of titania support. Thus, AuTNRa samples in which rutile nanorods are the

support, present Au NPs with an average particle size of 2 and 3.5 nm. Whereas AuTNRb samples, in which anatase is the support, show average size of 1.6 and 1.9 nm.

- An increment in the titania and Au particle size is observed by increasing the calcination temperature.
- The use of this type of nanostructured materials, very active in the CO-PROX reaction at ambient conditions under both studied modes (dark and light), may efficiently remove carbon monoxide from syngas in transportation applications.

8.6. References

1. Porto, S.P.S., T.C. Fleury, and T.C. Damen, *Raman spectra of TiO2, MgF2, ZnF2, FeF2, and MnF2.* Physical Reviews, 1967. **154**: p. 522-526.
2. Zayadi, R.A. and F.A. Bakar, *Comparative study on the performance of Au/F-TiO2 photocatalyst synthesized from Zamzam water and distilled water under blue light irradiation.* Journal of Photochemistry and Photobiology A: Chemistry, 2017. **346**: p. 338-350.
3. Morgan, D.L., E.R. Waclawik, and R.L. Frost. *Relationship of Titania Nanotube Binding Energies and Raman Spectra*. in *2006 International Conference on Nanoscience and Nanotechnology*. 2006.
4. Laggner, P., et al., *In-situ SAXS on Transformations of Mesoporous andNanostructured Solids* Studies in Surface Science and Catalysis, 2007. **160**: p. 661-665.
5. Haruta, M., *Size and support dependency in the catalysis of gold.* Catalysis Today, 1997. **36**: p. 153-166.
6. Bokhimi, X., et al., *Local order in titania polymorphs.* International Journal of Hydrogen Energy, 2001. **26**: p. 1279-1287.
7. Bokhimi, X., R. Zanella, and C. Angeles-Chavez, *Rutile-Supported Ir, Au, and Ir−Au Catalysts for CO Oxidation.* Journal of Physical Chemistry C, 2010. **114**: p. 14101-14109.
8. Zhang, L., D.A. Blom, and H. Wang, *AuCu2O CoreShell Nanoparticles: A Hybrid Metal-Semiconductor Heteronanostructure with Geometrically Tunable Optical Properties.* Chemistry of Materials, 2011. **23**: p. 4587-4598.
9. Kimura, K., et al., *TiO2Crystal Form-Dependence of the Au/TiO2Plasmon Photocatalyst's Activity.* The Journal of Physical Chemistry C, 2012. **116**(12): p. 7111-7117.
10. Chen, W.-T., et al., *Effect of TiO2 polymorph and alcohol sacrificial agent on the activity of Au/TiO2 photocatalysts for H2 production in alcohol–water mixtures.* Journal of Catalysis, 2015. **329**: p. 499-513.
11. Moretti, E., et al., *One-pot mesoporous Al–Ce–Cu oxide systems as catalysts for the preferential carbon monoxide oxidation (CO-PROX).* Catalysis Communications, 2009. **10**(5): p. 522-527.
12. Alvarez, M.M., et al., *Optical Absorption Spectra of Nanocrystal Gold Molecules.* Journal of Physical Chemistry, 1997. **101**: p. 3706-3712.
13. Schmid, G. and D. Fenske, *Metal clusters and nanoparticles.* Philosophical transactions of the royal society A, 2010. **368**: p. 1207-1210.
14. Simonsen, M.E., et al., *Surface properties and photocatalytic activity of nanocrystalline titania films.* Journal of Photochemistry and Photobiology A: Chemistry, 2008. **200**(2-3): p. 192-200.
15. Stoch, J., J. Lercher, and S. Ceckiewicz, *Correlations between XPS binding energies and composition of aluminasilicate.* Zeolites, 1992. **12**: p. 81-85.
16. Hernández, J.A., et al., *Insight into the Deactivation of Au/CeO2 Catalysts Studied by In Situ Spectroscopy during the CO-PROX Reaction.* ACS Catalysis, 2015. **5**(7): p. 4003-4012.
17. Deng, X.-Q., et al., *Visible-light photocatalytic oxidation of CO over plasmonic Au/TiO2: Unusual features of oxygen plasma activation.* Applied Catalysis B: Environmental, 2016. **188**: p. 48-55.
18. Li , H.X., et al., *Mesoporous Titania Spheres with Tunable Chamber Stucture and Enhanced Photocatalytic Activity.* J.Am. Chem.Soc, 2007. **129**: p. 8406-8407.
19. Quinet, E., et al., *On the mechanism of hydrogen-promoted gold-catalyzed CO oxidation.* Journal of Catalysis, 2009. **268**(2): p. 384-389.
20. Chretien, S., S. Buratto, and H. Metiu, *Catalysis by very small Au clusters.* Current Opinion in Solid State and Materials Science, 2007. **11**(5-6): p. 62-75.

9. CONCLUSIONS

According to the proposed objectives and the results obtained and described in chapters 4-6, it can be concluded:

1. A series of phosphides of the iron triad (Fe, Co and Ni) supported on commercial silica, and bimetallic Ni-Fe phosphides have been synthetized using dihydrogenophosphite salts as precursors showing a good dispersion of the active phases over the support.
2. Characterization results revealed that the initial Phosphorus/Metal molar ratio determines the stoichiometry of the formed phosphide phase, the acidity, the particle size and metal surface exposure and consequently the catalytic performance. An excess of P induces the formation of phosphorous rich phosphides that are less active in these reactions.
3. The catalytic activities indicated that for nickel and iron the metal rich phosphides, Ni_2P and Fe_2P, led to better catalytic results; while for cobalt, cobalt monophosphide, CoP, achieved the greatest HDO conversion values.
4. The selectivity results showed that all phosphides follow the hydrogenation-dehydration (HYD) route, obtaining cyclohexane as the majority product after phenol HDO and bycliclohexane after DBF HDO; although iron phosphides were those presenting better results to partial hydrogenated products such as cyclohexene.
5. All the catalysts were more active to hydrogenated products at higher hydrogen pressures.

The main conclusions extracted from the proposed objectives and the catalytic findings of chapters 7 and 8 are:

1. *Gold nanoparticles deposited on mesoporous titania supports*
   a) The samples synthesized by a sol-gel procedure and calcined at different temperatures presented good activity in the preferential oxidation of CO under simulated solar light irradiation at ambient conditions.
   b) The calcination temperature of the titania support was key to obtaining both anatase and rutile polymorphs. This was achieved at 600 ºC, and the corresponding catalyst presented the suitable particle size of highly dispersed gold nanoparticles with a strong interaction with the support and providing catalytic sites able to adsorb CO molecules.
2. *Gold nanoparticles deposited on titania nanorods*

a) The nanorods and titania polymorph formed depended on the acidic and basic hydrothermal synthesis followed. From an acidic synthesis, well defined rutile nanorods were formed and from the basic one, anatase was the main phase and the obtained nanorods were less structured.

b) Regardless of the synthesis procedure followed, the titania calcination temperature influenced the Au particle size obtained, being the sample calcined at 700 ºC and obtained from the acidic hydrothermal synthesis (AuTNRa7), the one with the highest particle size.

c) Catalytic results showed that all samples reached high CO conversion values (>80%) except for the sample AuTNRa7, which conversely, resulted to be highly selective to CO_2 (100%). In the rest of the catalysts, the high photoactivity led to a decrease in the selectivity towards CO_2 as a result of the competitive oxidation reaction of H_2 to H_2O.

APPENDIX

List of symbols and acronyms

A	Anatase
AAS	Atomic absorption spectroscopy
B	Benzene
BCH	Bycliclohexane
BCH-3-en-2-ol	1-1`bi(cyclohexan)-3-en-ol
C	Conversion (%)
CH	Cyclohexane
CH=	Cyclohexene
CHB	Cyclohexylbenzene
CHO	Cyclohexanol
CO-PROX	Preferential CO oxidation
C-PE-CH	Cyclopentylcyclohexane
C-PE-ME-CH	Cyclopentylmethylcyclohexane
CUS	Coordinatively unsaturated metal sites
DBF	Dibenzofuran
DDO	Direct deoxygenation
D_P	Pore diameter (nm)
DRUV-Vis	Diffuse reflectance ultraviolet-visible spectroscopy
E_B	Binding Energy (eV)
E_C	Kinetic Energy (eV)
EDX	Energy- dispersive X-ray spectroscopy
FID	Flame ionization detector
FT-IR	Fourier transform infrared spectroscopy
FWHM	Full width at half maximum
GC	Gas chromatograph
GHSV	Gas hourly space velocity (h^{-1})
H_2-TPD	Hydrogen temperature-programmed desorption
H_2-TPR	Hydrogen temperature-programmed reduction
HDN	Hydrodenitrogenation
HDO	Hydrodeoxygenation
HDS	Hydrodesulfurization
HHDBF	2,3,4,4a,9a, hexahydrodibenzofuran
HHV	Higher heating value
HRTEM	High resolution transmission electron microscopy

HYD	Hydrogenation
LCS	Low-coordination sites
LHSV	Liquid hourly space velocity
LSPR	Localized surface plasmon resonance
NH_3-TPD	Ammonia temperature-programmed desorption
NP_S	Nanoparticles
P	Pressure (Pa, Bar)
PDF	Powder diffraction file
PEM	Proton exchange membrane or polymer electrolyte membrane
PEMFC	Proton exchange membrane or polymer electrolyte membrane fuel cell
Photo-PROX	Preferential photo-oxidation
R	Rutile
RWGS	Reverse water gas shift
S	Selectivity (%)
SAXS	Small-angle X-ray scattering
S_{BET}	Specific surface area ($m^2 \cdot g^{-1}$)
STEM	Scanning transmission electron microscopy
T	Temperature (ºC, K)
TCD	Thermal conductivity detector
THDBF	2,3,4,9, tetrahydrodibenzofuran
TMC	Transition metal carbide
TMN	Transition metal nitride
TMP	Transition metal phosphide
TMS	Transition metal sulfide
TOF	Turn over frequency number (s^{-1})
ToS	Time on stream
V_P	Pore volume ($cm^3 \cdot g^{-1}$)
W	Catalyst weight (g)
WGS	Water gas shift
WHSV	Weight hourly space velocity (h^{-1})
wt%	Weight percentage
X	Conversion (%)
XPS	X-ray photoelectron spectroscopy
XRD	X-ray diffraction
XRF	X-ray fluorescence spectroscopy

List of Figures and Schemes

5. Co phosphides for phenol and dibenzofuran HDO

6. Fe phosphides for phenol HDO

List of Tables

7. Au NPs on mesoporous TiO_2 for CO photo-PROX

8. Au NPs on TiO_2 nanorods for CO photo-PROX

ARTICLES

Molecular Catalysis 437 (2017) 130–139

Contents lists available at ScienceDirect

Molecular Catalysis

journal homepage: www.elsevier.com/locate/mcat

MCAT

Research Paper

Ni and Fe mixed phosphides catalysts for O-removal of a bio-oil model molecule from lignocellulosic biomass

E. Rodríguez-Aguado, A. Infantes-Molina*, D. Ballesteros-Plata, J.A. Cecilia, I. Barroso-Martín, E. Rodríguez-Castellón*

Departamento de Química Inorgánica, Cristalografía y Mineralogía (Unidad Asociada al ICP-CSIC), Facultad de Ciencias, Universidad de Málaga, Campus de Teatinos, 29071 Málaga, Spain

ARTICLE INFO

Article history:
Received 30 March 2017
Received in revised form 9 May 2017
Accepted 9 May 2017
Available online 25 May 2017

Keywords:
Hydrodeoxygenation
Phenol
Nickel phosphide
Iron phosphide
Bifunctional catalyst

ABSTRACT

Silica-supported catalysts based on mono and bimetallic nickel and iron phosphides with different Ni:Fe molar ratios (1:0, 3:1, 2:1 and 0:1) were synthesised and tested in the hydrodeoxygenation (HDO) reaction of phenol, a model molecule present in bio-oil derived from pyrolysis of biomass. Tests were performed in a fixed bed reactor under hydrogen pressure (1.5 and 3 MPa) for different contact times. Freshly reduced catalysts were characterised by physisorption of N_2 at −196 °C, CO chemisorption, X-ray diffraction, transmission electronic microscopy, temperature-programmed desorption of ammonia and hydrogen, and X-ray photoelectron spectroscopy. Characterization results revealed that the presence of Ni increased their ability to activate hydrogen and the number of active sites, while the presence of Fe favored the spillover process. By increasing the amount of Ni, the surface became enriched with P, and this was associated with the presence of surface P-OH groups that provided Brönsted acid sites to activate O-containing compounds as well as surface hydrogen species that minimised deactivation by coke deposition. Ni-containing phases presented higher HDO capabilities than FeP ones, but generated some O-containing intermediates. In contrast, the FeP catalyst transformed all phenol molecules into O-free compounds (cyclohexane and mainly cyclohexene).

1. Introduction

Biomass is an abundant, carbon-neutral renewable energy resource that has gained special attention for its use in the production of clean biofuels as well as high added value products which can be obtained on a relatively short time scale with current infrastructures [1,2]. Lignocellulosic biomass, which is mainly composed of cellulose, hemicellulose and lignin, is a very promising feedstock for providing environmentally friendly renewable energy and chemicals for the transportation sector at reasonable costs. Lignin is the most similar to petroleum in composition and structure. It can be easily transformed into phenolic derived compounds through fast pyrolysis [3], but an upgrading is required to avoid undesired properties in terms of reactivity, catalyst deactivation and lower heat of combustion values if these O-containing compounds are to be used as fuel substitutes [4].

Hydrodeoxygenation (HDO) is an effective method for upgrading liquid fuels derived from pyrolysed biomass [5]. HDO normally occurs via elimination of oxygen as water and hydrogenation-hydrocracking of large molecules. This reaction is usually carried out at high temperatures under high hydrogen pressure, and the products obtained are in the diesel range [6]. Thus, during HDO, bio-oil is exposed to moderate temperatures and high pressures of hydrogen in the presence of heterogeneous catalysts. Under these conditions, O-containing intermediates are converted to hydrocarbon products that, once separated from water, lead to a product that can be directly used as biofuel [4]. However, there are many challenges to effectively apply this process. It requires a high degree of oxygen removal; low hydrogen consumption; catalysts designed to work effectively at relatively low pressures and mild temperatures without coke formation; and, finally, the use of non-toxic catalytic systems containing low cost active phases [7]. Common model compounds used to evaluate the catalytic performance of HDO reactions are furan compounds derived from cellulose and hemicellulose, and phenolic compounds derived from lignin [4]. Among them, phenol has been identified as a persistent oxygen-containing compound in bio-oil. Therefore, phenol is a good a representative probe molecule with which to test the HDO reaction.

* Corresponding authors.
E-mail addresses: aguadoelena5@gmail.com (E. Rodríguez-Aguado), ainfantes@uma.es (A. Infantes-Molina), castellon@uma.es (E. Rodríguez-Castellón).

http://dx.doi.org/10.1016/j.mcat.2017.05.008
2468-8231/

Top Catal
DOI 10.1007/s11244-017-0791-3

ORIGINAL PAPER

Co_xP_y Catalysts in HDO of Phenol and Dibenzofuran: Effect of P content

E. Rodríguez-Aguado[1] · A. Infantes-Molina[1] · J. A. Cecilia[1] · D. Ballesteros-Plata[1] · R. López-Olmo[1] · E. Rodríguez-Castellón[1]

Abstract Cobalt phosphide catalysts supporting on SiO_2 presenting different Co_xP_y stoichiometry were proved in hydrodeoxygenation (HDO) of two different model molecules present in biomass derived bio-oil such as phenol (Ph) and dibenzofuran (DBF). To investigate composition effects a series of cobalt phosphide catalysts presenting different initial P/Co atomic ratio were prepared. The catalysts were characterized by a range of techniques (N_2 physisorption, XRD, TEM, NH_3-TPD and XPS) and tested for DBF and Ph HDO activity and selectivity. Characterization results evidenced good textural properties, high dispersion of the active phase, as well as the presence of acid sites after P and Co incorporation. The highest activity was observed for catalysts containing an intermediate P/Co content were the CoP phase was the predominat one. Those catalyst containing Co_2P or CoP_2 phases were less active in these reactions.

Keywords Hydrodeoxygenation · Dibenzofuran · Phenol · Cobalt phosphide · Bifunctional catalyst

1 Introduction

The increase of the world population together with the larger demand for fuels has caused a progressive depletion of fossil fuels. This fact has provoked the research and development of alternative energy sources to replace the traditional fossil fuels. Among them, biomass is a sustainable feedstock and the unique alternative energy source to the petroleum, from which fuels and chemicals can be obtained. Lignocellulosic biomass is an abundant and non-food competing feedstock which enables an effective conversion to liquid biofuels and energy storage in a carbon-neutral cycle [1, 2], suitable with current infrastructures on a relatively short time scale [3]. One of the most promising alternatives to cope with that purpose is the conversion of biomass into bio-oil through fast pyrolysis followed by upgrading via removal of oxygen-containing species by hydrodeoxygenation (HDO) reactions [4]. Pyrolysis bio-oils are easier to handle and transport, also presenting lower sulfur and nitrogen content if compared with the petroleum feedstock. However, their higher oxygen (35–50 wt%) and water (15–30 wt%) contents [5] provide them deleterious properties [6]. In practice, a variety of functional groups including carboxylic acids, aldehydes, esters, alcohols, ethers, ketones, phenolics, sugars and furans are present in more than 400 oxygenated compounds in bio-oil [6]. This wide range of compositions hinders the subsequent upgrading if considering the highly reactive molecules that require careful choice of the operating conditions to avoid thermal pathways, leading to undesirable destructive side reactions. Using diluted model oxygenated compound solutions for HDO study will give more precise chemical information, and avoid the previously mentioned drawbacks. Therefore, two molecules derived from the pyrolysis of lignin, such as phenol and dibenzofuran are selected in the present study

Electronic supplementary material The online version of this article (doi:10.1007/s11244-017-0791-3) contains supplementary material, which is available to authorized users.

✉ A. Infantes-Molina
ainfantes@uma.es

✉ E. Rodríguez-Castellón
castellon@uma.es

[1] Departamento de Química Inorgánica, Cristalografía y Mineralogía (Unidad Asociada al ICP-CSIC), Facultad de Ciencias, Universidad de Málaga, Campus de Teatinos, 29071 Málaga, Spain

Published online: 08 May 2017

Catalysis Today xxx (xxxx) xxx–xxx

Contents lists available at ScienceDirect

Catalysis Today

journal homepage: www.elsevier.com/locate/cattod

Iron phosphides presenting different stoichiometry as nanocatalysts in the HDO of phenol

E. Rodríguez-Aguado[a], A. Infantes-Molina[a,*], D. Ballesteros-Plata[a], J.F. Marco[b], E. Moretti[c], E. Finocchio[d], J.A. Cecilia[a], E. Rodríguez-Castellón[a,*]

[a] Departamento de Química Inorgánica, Cristalografía y Mineralogía (Unidad Asociada al ICP-CSIC), Facultad de Ciencias, Universidad de Málaga, Campus de Teatinos, 29071 Málaga, Spain
[b] Instituto de Química Física Rocasolano, CSIC, Madrid, Spain
[c] Dipartimento di Scienze Molecolari e Nanosistemi, Università Ca' Foscari Venezia, INSTM Venice Research Unit, Mestre Venezia, Italy
[d] Dipartimento di Ingegneria Civile, Chimica e Ambientale, Universita degli Studi di Genova, Génova, Italy

ARTICLE INFO

Keywords:
Iron phosphide
HDO
Heterogeneous catalysis
Silica
Phenol

ABSTRACT

Iron phosphide catalysts supported on silica with an iron loading of 15 wt% were synthesized and studied in the hydrodeoxygenation (HDO) of phenol. The amount of phosphorus varied in order to obtain iron phosphides with different stoichiometry. Catalysts containing Fe_2P, FeP and FeP_2 phases were obtained. The textural and structural properties of the prepared catalysts were evaluated by using different experimental techniques such as N_2 adsorption-desorption at -196 °C, X-ray diffraction (XRD), Mössbauer spectroscopy, high resolution transmission spectroscopy (HRTEM), infrared spectroscopy (IR) of adsorbed CO at low temperature, X-ray photoelectron microscopy (XPS) and NH_3 thermoprogrammed desorption (NH_3-TPD). The catalytic activity was studied at 275 °C and at 15 and 5 bar of hydrogen pressure in the hydrodeoxygenation reaction of phenol. Characterization results evidenced that the initial P/Fe ratio employed in the synthesis not only governed the stoichiometry of the iron phosphide, but also the particle size, metallic surface exposure and acidity. The catalysts presenting unique phases were those presenting better activity in the HDO reaction of phenol. Moreover, Fe_2P phase presented better results than FeP in terms of HDO conversion.

1. Introduction

Increasingly awareness on polluted atmospheric environment combined with depletion of fossil fuels and increased reliance on unconventional crude oil resources which need to be highly purified, are prompting many researchers to address this problematic. Thus, new approaches on hydrotreating processes are being tackled as well as the search of new catalytic materials for processing fossil fuel feedstocks [1]. In this sense, fast pyrolysis of solid lignocellulosic biomass has drawn considerable attention for the production of liquid biofuels as this type of biomass is renewable and easily available [2–4]. Indeed, this process can be efficiently applied to commercial plants without investing a high amount of capital. However, the obtained bio-oil must be upgraded to ensure the removal of a wide variety of oxygenated compounds. The removal of oxygen can be tackled by means of hydrodeoxygenation, which is regarded as an effective method to improve the effective H/C ratio [5,6]. During HDO, oxygenated compounds are converted to hydrocarbons under hydrogen pressure and in the presence of heterogeneous catalysts. Currently, HDO faces several challenges, which have to be solved to expand its use in the already existing biorefineries [7,8]. In this respect, the consumption of low levels of hydrogen along with the obtainment of a high degree of deoxygenation is one of the most important challenges. Therefore, the catalyst design is a key factor to cope with that purpose. Typically, catalysts used in the HDO reactions are constituted by a metal with good hydrogen transfer properties supported on a high surface area oxide support. Conventional sulfide catalysts such as CoMoS and NiMoS, used in petroleum hydrodesulfurization, have been used in HDO reactions; however, the oxidation of the sulfide species by the presence of H_2O, obtained as by-product in the HDO reaction, and the formation of carbonaceous deposits cause a strong deactivation of the active phase [9,10]. Catalysts based on noble metals have also been widely studied but their high activity does not offset their high cost. That is why alternative catalysts as those constituted by transition metal phosphides have attracted great attention in recent years since they have much lower costs and their electronic structure is close to that of noble metals [11,12]. Concretely, transition metal phosphides have resulted to be very active in hydrotreating reactions also showing high

* Corresponding authors.
E-mail addresses: ainfantes@uma.es (A. Infantes-Molina), castellon@uma.es (E. Rodríguez-Castellón).

https://doi.org/10.1016/j.cattod.2018.05.023
Received 17 December 2017; Received in revised form 5 May 2018; Accepted 10 May 2018

Catalysis Today xxx (xxxx) xxx–xxx

Contents lists available at ScienceDirect

Catalysis Today

journal homepage: www.elsevier.com/locate/cattod

Sustainable photo-assisted CO oxidation in H_2-rich stream by simulated solar light response of Au nanoparticles supported on TiO_2

Elisa Moretti[a,*], Elena Rodríguez-Aguado[b], Antonia Infantes- Molina[b], Enrique Rodríguez-Castellón[b,*], Aldo Talon[a], Loretta Storaro[a]

[a] Dipartimento di Scienze Molecolari e Nanosistemi, Università Ca' Foscari Venezia, INSTM Venice Research Unit, Via Torino 155/B, 30172 Mestre Venezia, Italy
[b] Departamento de Química Inorgánica, Cristalografía y Mineralogía (Unidad Asociada al ICP-CSIC), Facultad de Ciencias, Universidad de Málaga, Campus de Teatinos, 29071 Málaga, Spain

ARTICLE INFO

Keywords:
CO preferential oxidation
Photocatalysis
Solar light response
Titania
Gold nanoparticles

ABSTRACT

In this study the photo-response behaviour of Au/TiO_2 systems in the preferential CO oxidation in a H_2-rich stream (CO-PROX) was investigated by the first time under simulated solar light irradiation at room temperature and atmospheric pressure. Au nanoparticles, with an average size of 2–5 nm, were precipitated-deposited on a mesoporous TiO_2, previously synthesized by sol-gel type procedure and thermally treated at different temperatures to obtain anatase/rutile mixed phases. Structural, chemical and optical properties were studied by means of AAS, N_2 physisorption, XRD, HR-TEM, DRUV–vis and XPS, investigating the effects of TiO_2 polymorphs (anatase, rutile and combination thereof). All samples, containing a very low amount of noble metal (0.5 wt%), resulted very active in the photocatalytic CO-PROX at ambient conditions, attaining very high CO conversion and CO_2 selectivity values. The Au/TiO_2 sample containing both anatase/rutile polymorphs in the support displayed the highest activity, both in dark and under simulated solar light, due to the simultaneous presence of these two titania crystalline phases, capable to lower the effective band gap of the composite system (2.90 eV) and improving the photocatalytic activity in the studied reaction. This kind of materials may provide a sustainable and feasible approach to selectively oxidize CO in H_2-rich stream under solar light irradiation and ambient conditions.

1. Introduction

In recent years, the photocatalytic processes have been extensively studied and applied to pollutant degradation [1–3] and environmental remediation, such as water/air purification and contaminant degradation [4–6].

This kind of processes displays many advantages, first of all, they can be carried out by sunlight, an inexhaustible and clean energy source, and in ambient conditions (temperature and pressure) [7].

Among the variety of semiconductor catalysts, titanium dioxide, TiO_2, is considered by far as one of the most promising solutions to cut down the environmental pollution, since it exhibits strong oxidizing ability, super-hydrophilicity, chemical stability, self-cleaning property and transparency to visible light [5,8]. In fact, as a n-type semiconductor, it is largely used in photocatalysis and photodegradation of organic pollutants in a variety of environmental applications [9,10]. Furthermore, titania based photocatalysts, if used in the synthesis of fine organic chemicals that are unstable at high temperatures, could achieve a good selectivity to the desired products through a green approach because only sunlight driven. Last but not least, titania is a cheap, non-toxic, widely diffuse material that can be also easily synthesized by soft chemistry processes (e.g sol-gel method), with the possibility to finely tune its physico-chemical properties.

Many studies have been carried out to show that the photoactivity of TiO_2 depends on a large number of parameters including the crystal structure [11], the ratio between anatase and rutile phases, particle size distribution, specific surface area and mean pore size [12,13].

The use of this material is however limited by its band gap energy, that can vary from 3.0 to 3.2 eV depending on the polymorph, and requires near UV wavelengths (387.5 nm) for efficient excitation. In consideration that sunlight reaching the Earth's surface contains less than 5% of ultraviolet light while visible light (wavelength 400–700 nm) accounts for 43% of the incoming solar energy, the development of materials with a visible-light photoresponse, using the less energetic but more abundant visible light, is one of the current challenges in photocatalysis.

* Corresponding authors.
E-mail addresses: elisa.moretti@unive.it (E. Moretti), castellon@uma.es (E. Rodríguez-Castellón).

http://dx.doi.org/10.1016/j.cattod.2017.09.048
Received 24 June 2017; Received in revised form 14 September 2017; Accepted 24 September 2017

Elsevier Editorial System(tm) for
International Journal of Hydrogen Energy
Manuscript Draft

Manuscript Number: HE-D-18-03679R1

Title: Au nanoparticles supported on nanorod-like TiO2 as catalysts in the CO-PROX reaction under dark and light irradiation: effect of acidic and alkaline synthesis conditions

Article Type: Full Length Article

Section/Category: Catalysts / Electrocatalysts / Photocatalysts

Keywords: CO preferential oxidation, photocatalysis, simulated solar light, titania nanorods, gold nanoparticles.

Corresponding Author: Dr. Elisa Moretti, Ph.D.

Corresponding Author's Institution: Ca' Foscari University of Venice

First Author: Elena Rodríguez-Aguado

Order of Authors: Elena Rodríguez-Aguado; Antonia Infantes-Molina; Aldo Talon; Loretta Storaro; Laura León-Reina; Enrique Rodriguez-Castellon; Elisa Moretti, Ph.D.

Abstract: Gold nanoparticles precipitated-deposited on titania nanostructures (1.0 wt% nominal loading) were studied in the preferential CO oxidation in excess of H2 at room temperature and atmospheric pressure, both in dark and under simulated solar light irradiation. Titania supports were synthesized by means of two hydrothermal methods markedly acid and basic, giving rise to rutile nanorods and anatase deformed nanorods structures, respectively. Characterization techniques such as N2 physisorption, XRD, XPS, DRUV-vis, HRTEM and XRF were performed in order to study the chemical, structural and optical properties of the catalysts. Well defined rutile nanorods structures were obtained from the acidic treatment allowing a regular distribution of gold nanoparticles and resulting quite active in the CO-PROX reaction. In particular the sample from the acidic synthetic approach calcined at 700 °C displayed the best results as it was highly selective to CO2 under both dark and simulated solar light irradiation.

Ms. Ref. No.: HE-D-18-03679R1
Title: Au nanoparticles supported on nanorod-like TiO2 as catalysts in the CO-PROX reaction under dark and light irradiation: effect of acidic and alkaline synthesis conditions
International Journal of Hydrogen Energy

Dear Dr. Moretti,

I am pleased to inform you that your paper "Au nanoparticles supported on nanorod-like TiO2 as catalysts in the CO-PROX reaction under dark and light irradiation: effect of acidic and alkaline synthesis conditions" has been accepted for publication in the International Journal of Hydrogen Energy.

Thank you for submitting your work to International Journal of Hydrogen Energy.

For further assistance, please visit our customer support site at http://help.elsevier.com/app/answers/list/p/7923 Here you can search for solutions on a range of topics, find answers to frequently asked questions and learn more about EES via interactive tutorials. You will also find our 24/7 support contact details should you need any further assistance from one of our customer support representatives.

Yours sincerely,

Mohammad Mahdi Najafpour, PhD
Assistant Editor
International Journal of Hydrogen Energy